Friction under microscope with trapped ions in optical lattices

by

Alexei Bylinskii

Bachelor of Applied Science in Engineering Science,
University of Toronto (2009)

Submitted to the Department of Physics
in partial fulfillment of the requirements for the degree of

Doctor of Philosophy

at the

MASSACHUSETTS INSTITUTE OF TECHNOLOGY

February 2016

Signature redacted

Author .....
Department of Physics
Sept 25, 2015

Signature redacted

Certified by.....
Vladan Vuletic
Professor of Physics
Thesis Supervisor

Signature redacted

Accepted by.....
Nergis Mavalvala
Professor, Associate Department Head for Education

Friction under microscope with trapped ions in optical lattices

by

Alexei Bylinskii

Submitted to the Department of Physics
on Sept 25, 2015, in partial fulfillment of the
requirements for the degree of
Doctor of Philosophy

Abstract

In recent years, cold-atom experiments have moved towards atomic systems with increasingly stronger interactions. One goal is to emulate condensed-matter phenomena in an ultimately controlled system by studying the motion of atoms in optical lattices. Trapped ions are the epitome of a strongly-interacting cold-atom system, but until now have been limited to simulating spin systems. In this thesis work, a toolbox is developed for combining trapped ions with optical lattices and for studying problems of atomic crystals in periodic potentials. One such problem of tremendous technological and economic importance is friction - a ubiquitous phenomenon that is poorly understood even at the atomic level (nanofriction), where stick-slip processes are known to be the dominant source of dissipation and wear.

Friction is studied in this thesis work with unprecedented spatial resolution and control at the individual-atom level in the synthetic frictional interface between crystals of trapped ions (moving object) and an optical lattice (rigid corrugated substrate). These experiments address, at the atomic scale, four quintessential questions about friction: the dependence of friction on the load (corrugation depth), on material properties (object-substrate lattice mismatch), on the contact area (number of atoms at an atomically smooth contact) and on velocity and temperature. In particular, we observe the elusive regime of superlubricity - the vanishing of stick-slip friction - for ion crystals mismatched to the lattice. With increasing load, we observe superlubricity to break and stick-slip friction to reappear as a result of a long-theorized sliding-to-pinned structural transition known as the Aubry transition. Although these effects were initially predicted to occur in the infinite-atom limit, we find them to arise already at the level of two or three atoms in our system.

The presented results could potentially lead to ways of engineering friction in nanomaterials or even at the macroscopic scale, and the system can further be used to study quantum many-body physics of solids in periodic potentials, potentially relevant to friction and surface physics at the nanoscale and at cold surfaces.

Thesis Supervisor: Vladan Vuletic
Title: Professor of Physics

Figure 0-1: Superlubricity of interacting graduate students in a periodic potential.

Acknowledgments

One of the most valuable lessons that I learnt in my PhD is the following: it doesn't matter what you do, but who you do it with. Science is a mentally tough endeavor that often makes you lose the sense of purpose. Ultimately, it is the people around you who put meaning back into this activity: through what your learn from them, through what you teach them, and through the fun that you have with them in the process (Fig.0-1).

For me, first and foremost two people from my PhD years have made these years unforgettable: Dorian Gangloff and Vladan Vuletic.

Vladan is an amazing physicist and experimentalist, and I hope to carry away with me some of his incredible physical intuition. Most importantly, I will never forget his unwavering positivity and excitement that always ignited my confidence in the work we were doing.

Dorian has been my partner in crime throughout the last five years (see Fig.0-2), and I cannot imagine a better teammate and friend. We have managed to stay on the same wavelength throughout, and the process of bouncing ideas, learning from each other, devising and setting up experiments, taking data late into the night, and writing papers together has been incredibly enjoyable and fruitful.

Figure 0-2: Running the lab with Dorian in "A symphony in Yb+ for dancing atoms" (https://www.youtube.com/watch?v=7c9dfxBAaJU).

Dorian and I had the pleasure of sharing the toughest period in this experiment with Leon Karpa - our postdoc, who exhibited exemplary patience as we wrestled to cool an ion in the optical lattice and demonstrate first signatures of single-site optical trapping of an ion.

As a junior PhD student, I had the opportunity to learn from the senior students who started the ion trapping effort in Vladan's group: Marko Cetina and Andrew Grier. Marko merits a special thank you from me: besides teaching me many tricks in the lab, his thorough design and implementation of the experimental chamber and ion trap have helped ensure a working experimental machine for most of my PhD.

In the past year, Ian Counts has been of tremendous help in running the experiments and pushing forward necessary upgrades to take the experimental machine to the next level. I also want to thank Wonho Jhe and Rajibul Islam; in the short time that I have had the opportunity to interact with them, they have brought some valuable insight to the experiment and to me personally. I am confident that with these new additions to the team, the next level will be exciting and not so far away.

I want to thank the motivated undergrads that I've had the opportunity to mentor and also learn from: Po Samutpraphoot and QinQin Yu. I also want to thank the whole Vuletic group, and in particular, fellow graduate students Kristin Beck,

Hao Zhang, Boris Braverman, Akio Kawasaki for being valuable learning resources throughout the years. The same goes for many members of the CUA from labs down the hallway.

I want to thank MIT CUA professors for their valuable advice, inspiration, and the physics I have learnt from them: Isaac Chuang, Wolfgang Ketterle and Martin Zwierlein.

Finally, I want to thank my parents, to whom I am forever grateful for giving me the opportunities throughout my life that brought me here, my parents-in-law, who have become my second family, and my beloved wife Zoya, who makes my life a dream regardless of whether experiments in the lab work or not.

Contents

Chapter 1

Introduction: new possibilities with ions in optical lattices

Advances in the trapping, cooling and quantum control of neutral atoms and trapped atomic ions in the last decades has offered scientists a glimpse into the thermodynamics and dynamics of coupled few-atom and many-atom systems, having both fundamental importance and applications in the form of quantum information processing [1] and quantum simulation [2]. Trapped ion systems and neutral atom systems have approached this process from different angles. Using techniques developed by Paul and Demhelt (leading to their 1989 Nobel Prize in Physics), ions can be trapped in vacuum for hours even at room temperature, owing to the strong nature of the Coulomb forces exerted by the trapping electric fields. The steepness, good harmonicity and stability of the resulting trapping potentials have enabled exquisite control of the motional degrees of freedom of trapped ions [3]. The same strong, long-range Coulomb forces between the ions a) result in trapped Wigner crystals of these ions with individual-ion optical addressability, and b) are used to mediate strong interactions between the internal degress of freedom (qubit states) of separate ions. As a consequence, trapped ions have conveniently been utilized as stationary, reconfigurable arrays of controllable qubits for quantum computation or metrology (the subject of the 2012 Nobel Prize in Physics awarded to Wineland). By contrast, taming the motional degrees of freedom of neutral atoms has been more challenging

due to shallow trapping potentials, requiring various clever cooling techniques (the subject of the 1997 Nobel Prize in Physics awarded to Chu, Cohen-Tannoudji and Phillips) and culminating in the discovery of the Bose-Einstein condensate (the subject of the 2001 Nobel Prize in Physics awarded to Ketterle, Cornell and Wieman). The shallow trapping potentials and weak interatomic interactions mean that neutral atoms in the trap act like a gas (unlike a solid Wigner crystal of ions), whose quantum properties at cold temperatures are of great interest and have been a major research focus in the neutral atom community. Furthermore, quantum gases can be studied in the very versatile periodic potentials of optical lattices [4], simulating electrons in crystal lattices in solids, with great promise for better understanding exotic quantum materials. With the achievement of atomic Mott insulators in optical lattices [5] and single-site resolution and control [6, 7, 8, 9, 10, 11], neutral atoms have entered the territory of bottom-up control traditionally available to trapped ions - but with larger numbers and much weaker, shorter-range interactions.

In this context, the effort described in this thesis it to study the physics of arbitrarily strongly interacting atoms in optical lattices - ions, allowing us to simulate a qualitatively different class of problems in solid-state physics: that of solids in periodic potentials. This encompasses friction between two objects at the atomic scale (the focus of this thesis), the surface science of adsorbed monolayers, the operation of molecular motors, etc. - in general, any kind of mechanical interaction between two short or extended atomic arrays. This new direction for atomic physics hinges on combining trapped ions with optical lattice potentials, pioneered by the groups of Walther [12], Schaetz [13, 14], Drewsen [15], and the experiments in this thesis [16, 17]. In this thesis, we have been concerned with studying and controlling the motional degrees of freedom of ions in the periodic optical-lattice potential, culminating in fundamental studies of atomic-scale friction. In the future, these new features will be combined with the quantum control toolbox for trapped ions [18] and with cavity QED [19, 20], leading to very rich hamiltonians involving both internal and external degrees of freedom of the ions, with possibilities to study spin-dependent friction [21], quantum superpositions of crystalline structures [22, 23], interacting bosons and

quantum magnetism [24] among other fascinating new regimes. Furthermore, returning to the context of quantum information processing with ions, ions in optical lattices could be used as a platform [25] to a) trap two- and three-dimensional arrays of qubits [26] without micromotion that often causes heating in the usual radio-frequency traps, and b) to bring qubits closer to each other (potentially down to the wavelength scale!) for scalability and faster quantum gates while avoiding the "anomalous" heating in proximity to planar traps [27, 28, 29, 30].

Trapping, cooling and studying ions in an optical lattice are associated with a number of challenges: a) operating a versatile and micromotion-compensated trap in the presence of a high-intensity lattice beam (and additionally in our case, operating such a trap together with an optical cavity used to generate the lattice), b) generating a deep optical-lattice potential that exerts forces on the ions that overcome the Coulomb forces, c) cooling the ions in such a deep optical potential and measuring their temperature and lifetime, and finally, d) tracking the position of the ions with sub-lattice-site (read: subwavelength) spatial resolution, and time resolution below the relaxation time scales. In part I of this thesis, I provide details on how we have addressed these challenges in our experiments, giving us the toolbox needed to study solids in periodic potentials, and in particular, the problem of friction.

I start part II of my thesis with a brief overview of friction: the motivations for studying this ubiquitous and economically relevant phenomenon, the atomistic models of friction, the current tools that exist for studying it at the nanoscale, and the advantages for studying it with trapped ions in optical lattices. In the remaining chapters part II, I describe experiments that we have done in our trapped-ion optical-lattice emulator, achieving unprecedented control and atom-by-atom resolution of a frictional interface and elucidating four long-standing questions about friction: 1) its dependence on normal load, 2) the effect of material (structural) properties, 3) the dependence of friction on contact area, and 4) its temperature and velocity dependence. Our experiments exhibit a fascinating transition from superlubricity to stick-slip friction, associated with the long-theorized Aubry transition which we directly observe here for the first time.

Part I

Trapped Ions in Optical Lattices: a new atomic physics toolbox

Chapter 2

A brief history and challenges

The first observation of lattice forces on an ion was reported in 1997 by Katori et. al. [12] as a suppression of ballistic oscillations in a shallow Paul trap and an onset of a diffusive regime. Based on the slowest measured diffusion constant, one can infer a 0.3μs maximum lifetime of the $^{24}Mg^{+}$ ion in a single lattice site for the deepest lattice employed (U/k_B = 1.5 mK = $300E_{rec}/k_B$, $\lambda/2$ = 140nm, where U is the optical lattice depth, $E_{rec} = \frac{h^2}{2m\lambda^2}$ is the photon recoil energy, λ is the optical lattice wavelength, and k_B is the Boltzmann constant). This lifetime corresponds to a single oscillation period of the ion in the lattice site and is only a factor of 2 longer than the transit time through the site in the bare Paul trap at the same temperature. This is consistent with the measured temperature being $k_BT \approx U$, which is in turn expected from the fact that the lattice itself was used for laser cooling (see subsection 6.1.1).

Holding an ion briefly with purely optical dipole forces was first achieved only recently in an optical dipole trap by Schneider et. al. in 2010 [13], and in an optical lattice in follow-up work by Enderlein et. al. in 2012 [14] ($^{24}Mg^{+}$ used again in both cases). In the first experiment, the RF trap was shut off for up to 2000μs with a greater than 50% chance of recapture. This optical trap lifetime corresponded to $\sim$ 330 transverse oscillation periods and $\sim$ 4 axial oscillations in the deep, $U/k_B = 38mK = 7600E_{rec}/k_B$ optical dipole trap. In the second experiment, the ion was held for 25μs without RF confinement in an optical potential of similar depth, but in an interfering counter-propagating beam configuration forming an opti-

cal lattice. These experiments have laid a foundation for all-optical micromotion-free ion trapping, relevant for quantum information processing with ions and for studying quantum collisions between ions and atoms [31, 32].

Another experiment by Linnet et. al. in 2012 [15] measured the effect of a deep ($U/k_B = 24mK = 75000E_{rec}/k_B$) intracavity optical lattice on the position distribution of a $^{40}Ca^+$ ion in a shallow Paul trap. During the 5μs of each experiment, the position distribution would go from the thermal Guassian in the harmonic trap, to a distribution peaked at the positions of lattice sites, as measured by fluorescence from a probe standing wave. This work was the first to demonstrate subwavelength confinement of an ion in an optical lattice, but with an undetermined and short lifetime (at most 5μs) and without site-by-site resolution or control.

In the experiments described in this thesis, we laser cool single $^{174}Yb^+$ ions, or chains of them, deep into an intracavity optical lattice ($T << U/k_B$, where $U/k_B = 0.05 - 2mK = 124 - 4960E_{rec}/k_B$) superimposed onto the Paul trap, achieving ion lifetimes in a single lattice site of up to 0.1 seconds ($10^4 - 10^5$ axial oscillations in a single site). We also develop techniques for subwavelength positioning and tracking of the individual ions with respect to the lattice, giving us the atom-by-atom, site-by-site resolution and control for studying friction with unprecedented microscopic control. In part I of my thesis, I describe in detail the system, the laser cooling and this control toolbox. Studying ions in an optical lattice is associated with the following challenges, which I address in the chapters that follow:

1) Operating a versatile and micromotion-compensated trap integrated with a high-intensity lattice beam or cavity (chapters 4,5).

2) Generating and calibrating a deep optical-lattice potential of comparable strength to the Coulomb potentials (chapter 5).

3) Cooling ions deep into the optical potential (chapter 6).

4) Measuring ion temperature in the lattice (section 6.4).

6) Measuring the positions of individual ions with sub-lattice-site spatial resolution and time resolution below the relaxation time scales (chapters 7,8).

Chapter 3

System overview

We trap and laser cool Yb^+ ions in 1-D chains along the linear microfabricated Paul trap (chapter 4), overlapped in vacuum with the mode of a 2.2cm-long optical cavity [33] (see Figs.3-1,3-2). The trap is loaded using a 2-step photoionization of the neutral Yb atoms in a thermal beam from a heated oven (section 4.4). The cavity can be used for fluorescence collection from the ions and fluorescence spectroscopy [33], as a quantum bus of photons connecting subchains of ions in the cavity mode [19], or it can be pumped with laser light to produce an intracavity standing wave - an optical lattice [16] (see chapter 5). Laser cooling beams (for Doppler cooling or Raman cooling - see chapter 6) and repumping laser beams are sent parallel to the trap chip surface to the center of the trap either through the optical cavity or from the side. Scattered fluorescence is collected by a large objective just outside the vacuum window and detected either by a electron-multiplying CCD camera, or by a pair of photomultiplier tubes (PMT).

After this brief system overview, the key system components are discussed detail in separate chapters: the microfabricated ion trap in chapter 4, the optical cavity and lattice in chapter 5, laser cooling in chapter 6 and imaging in chapter 7.

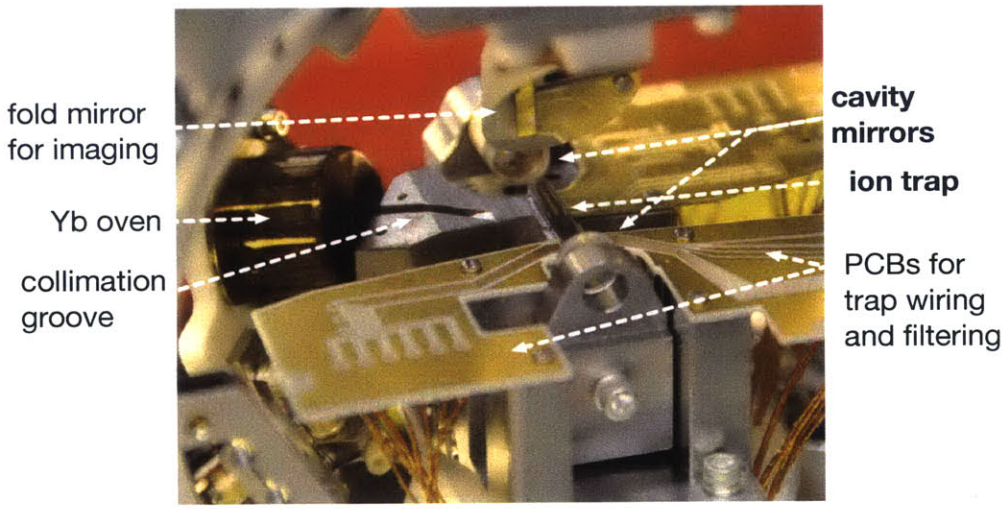

Figure 3-1: Photograph of the optical cavity integrated with a planar microfabricated ion trap inside the vacuum chamber. The cavity mirrors and the trap chip are mounted on a temperature-stabilized stainless steel block. One of the cavity mirrors can be translated by a piezo in order to tune the cavity resonance. Trap electrodes are wirebonded to the printed circuit boards (PCBs), where low-pass filtering occurs. Ions are loaded by photoionizing Yb atoms in a collimated flux coming from an oven. Ions are imaged through a 45° fold mirror by an objective outside the vacuum chamber with a working distance of 10 cm and numerical aperture (NA) 0.28.

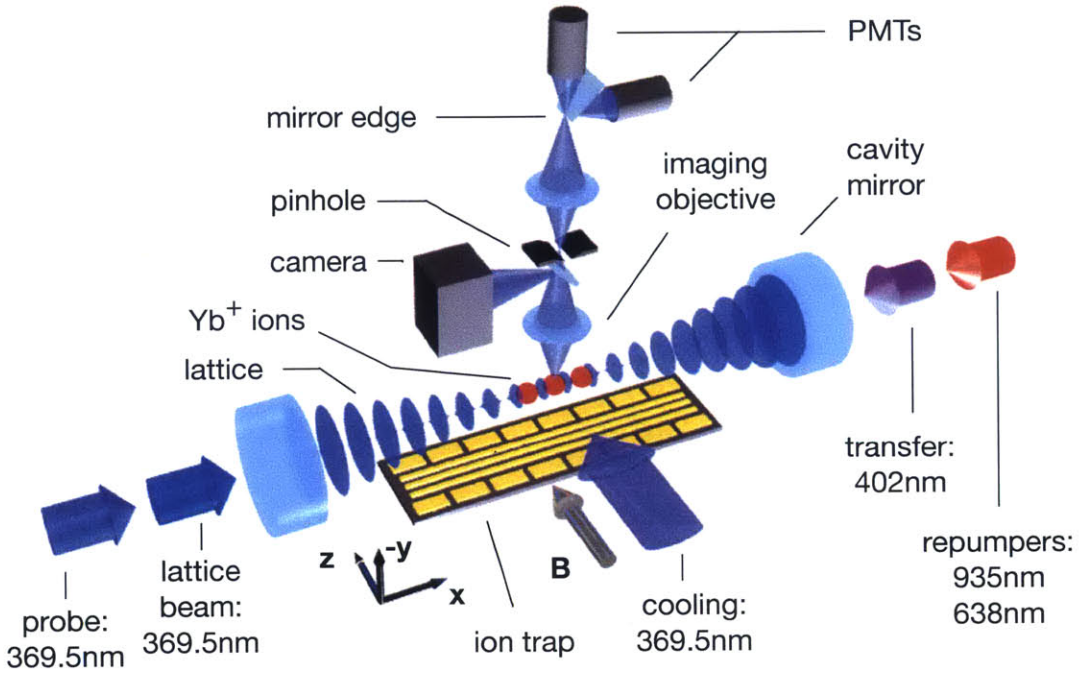

Figure 3-2: Diagram of the set-up. Chains of Yb^+ ions are trapped near the center of the cavity along the RF nodal line of the Paul trap, 134.5 μm from the trap electrodes. The intracavity optical lattice with lattice constant a =184.75 nm is produced by pumping the cavity with 369.5 nm light blue-detuned from the $^2S_{1/2}$–$^2P_{1/2}$ atomic transition by 12.6 GHz. A probe beam, red-detuned by $\sim$ 100 MHz also pumps the cavity, resulting in a standing wave that matches the lattice near the center of the cavity. Weak light for laser cooling, also red-detuned by $\sim$100 MHz hits the ions from the side. Ion fluorescence from scattered cooling light can be collected either by the imaging system shown (discussed further in chapter 7), or by the cavity, whose output can be fiber-coupled and detected by PMTs (not shown) [33]. Repumping lasers at 935.2 nm (to depopulate the $^2D^{3/2}$ state) and 638 nm (to depopulate the $^2F^{7/2}$ state) are sent through the other end of the optical cavity for easy alignment to the ions (but the cavity mirror reflectivity is near zero at those wavelengths). Finally, the cavity is stabilized by locking it to the 402 nm transfer laser, which does not affect the ions and is in turn locked to a reference cavity (not shown). All the 369.5 nm lasers are also locked to the reference cavity, which can be tuned via a piezo to tune the frequencies of the whole system (369.5 nm lasers, experimental cavity and optical lattice).

Chapter 4

Linear microfabricated Paul trap

4.1 Trap potentials

Our linear Paul trap is a microfabricated planar-electrode ion trap with gold electrodes on a quartz substrate [33, 34, 29], shown in Fig.4-1a. Radio-frequency (RF) voltage at $\omega_{RF} = 2\pi \times 16.160$ MHz and $V_{RF} \approx 100$ V amplitude is applied to two electrodes spanning the length of the trap (colored in green), while the rest of the electrodes are tied to ground at RF frequencies via capacitors [34]. This produces a transverse pseudopotential shown in Fig.4-1c, with a minimum at 134.5 μm from the electrode surface, typical radial trapping frequencies $\omega_{y,z} \approx 2\pi \times 1$ MHz, a Mathieu parameter $q \approx 0.2$ and a trap depth of 600 K along the weakest confinement direction away from the chip surface (-y). In practice, the trap depth is usually increased significantly by applying a DC quadrupolar field that provides additional confinement along the weak y-axis at the expense of deconfinement along the z-axis. This is achieved by applying a negative DC bias voltage of a few volts (typically -2V) to the RF electrodes. As a result of this DC quadrupole field, the y- and z- trapping frequencies differ on the order of ~100 kHz. In addition, we apply a tilted DC quadrupole in the transverse plane that results in rotated trap eigenaxes to ensure that both trap eigenaxes can be cooled by beams that come in parallel to the trap surface. The tilted quadrupole is produced by applying a positive and negative DC voltage (typically 0.5V) on the two RF electrodes and compensating the dipole field

using an opposite-polarity voltage on the large DC electrodes on the respective sides.

The trap is equipped with 24 large DC electrodes, controlled by a multichannel -30V to +30V 16-bit digital-to-analog converter (DAC) (with a 15Hz 3-pole low-pass output filter), for finely shaping the axial potential, and for compensating stray electric fields that lead to micromotion in the transverse plane (see subsection 4.3). Two pairs of these electrodes (indicated in Fig.4-1a) are also used to move the ions in the axial direction along the optical lattice in friction experiments. This is done at frequencies between 0.5Hz and 64kHz from an AC source, requiring the correction of the source waveform by the inverse filter function of the low-pass filter with corner at 2.1kHz near the trap chip, and of the high-pass filter with corner at 0.5 Hz, which AC-couples to the output of the DAC.

A split central electrode with a periodic structure, shown in Figure 4-1b, allows the axial trap to be sectioned into an array of 50 separate microtraps along the cavity mode, spaced by 160 μm, by applying a negative DC voltage to the inner periodic electrode and a positive DC voltage to the outer periodic electrodes. The ratio of outer-electrode voltage to inner-electrode voltage of -0.95 was chosen to cancel the displacement of the trap in the direction perpendicular to the chip surface (as measured by micromotion in that direction; see subsection 4.3). This way, the axial (x) vibrational frequency $\omega_0/(2\pi)$ at the positions of the microtraps can be precisely and conveniently adjusted in the range 20 kHz - 1 MHz with 0.1 kHz resolution enabled by the large dynamic range of the DAC (this is used to finely tune the matching of an ion crystal to an optical lattice as described in section 10.4). Note that axial frequencies at the low end of this range are plagued by slow drifts of the ion position on a typical scale of one lattice constant per hour, due to the weak confinement and drifting stray electric fields.

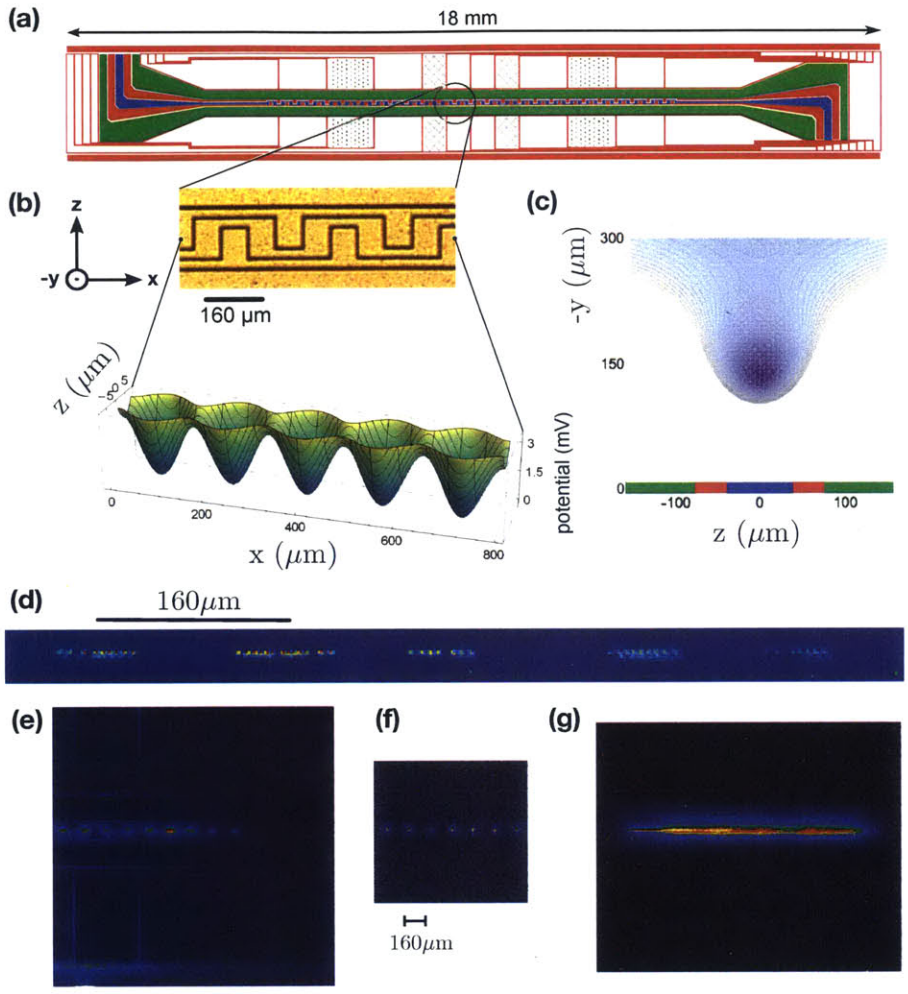

Figure 4-1: **(a)** Trap chip schematic. RF voltage is applied to the electrodes shown in green; the rest are grounded at RF. (Note that the central electrodes colored in blue and red could also be driven at RF by removing their capacitors, which are outside the vacuum chamber; this would allow moving the trap minimum to a different distance form the electrode surface.) The large rectangular electrodes are DC electrodes for axial potential shaping and micromotion compensation. The ions can be moved axially at AC by driving the two pairs of these electrodes filled with the dot pattern (for small displacements), or the two pairs filled with the dashed pattern (for large displacements). For the nominal $\omega_0/(2\pi) = 364$ kHz, the first set gives $0.022a$ displacement per +/-1mV on the two pairs (where $a = 184.75$ nm is the lattice constant), and the second set is 18 times more coarse. **(b)** Periodic electrodes for producing an axial array of microtraps. A close-up photograph of the periodic electrodes is shown (colored in blue and red in (a)) together with the potential that they produce at 134.5 μm from the surface. **(c)** Transverse pseudopotential produced by the RF. The equipotential contours are spaced by 5mV. **(d)** An image of Yb^+ ion chains (1-D crystals) loaded in the microtraps. **(e)** An image of Yb^+ 3-D crystals loaded in the microtraps, with trap electrodes illuminated in the background. **(f)** Single Yb^+ ions in microtraps. **(g)** A large elongated Yb^+ ion crystal with periodic potential off.

4.2 Trap characterization and modeling

The key parameters characterizing an ion trap, which is typically very harmonic even for large ion motional amplitudes, are the vibrational frequencies in the three directions $\{\omega_0, \omega_y, \omega_z\}/(2\pi)$ (the RF-free axial direction x and the two transverse directions $\{y, z\}$, respectively). These vibrational frequencies can be measured by "tickle spectroscopy". A small-amplitude AC voltage is applied to a set of electrodes that couples to the desired direction and the frequency ω_{tickle} of this excitation is swept. Vibrational resonances show up as heating and delocalization of the ion, seen as blurring of the ion image on the camera in the direction in question. Note that in practice, we usually apply this voltage to the RF electrodes at $\omega_{RF} + \omega_{tickle}$ and drive vibrational resonances using the beatnote with the RF trap drive. At large enough amplitude and weak enough cooling, ion motion in any of the three directions can be excited this way.

We must control precisely the axial vibrational frequency $\omega_0/(2\pi)$ to place the ions in a chain at well-defined spacings with respect to the optical lattice (see section 10.4). The typical width of the axial vibrational resonance that we observe is ~ 0.3 kHz under Doppler cooling at $\Delta/(2\pi) \approx 50$ MHz detuning, and the resonance typically does not drift by more than its width over the course of a day at the nominal vibrational frequency of $\omega_0/(2\pi) = 364$ kHz (with axial confinement produced primarily by the DC electrodes, and only a weak voltage < 500mV applied to the periodic electrodes for fine-tuning).

Radial vibrational frequencies $\omega_{y,z}$ of the Paul trap are usually held fixed, and from the corresponding measured vibrational resonances and the known trap RF frequency ω_{RF} one can calculate the trap Mathieu parameter as $q = 2\sqrt{2} \cdot \omega_{y,z}/\omega_{RF}$ and the RF voltage on the electrodes as $V_{RF} = q\frac{m\omega_{RF}^2}{2eC}$ (in the limit $\omega_x << \omega_{y,z}$ and with transverse DC quadrupolar fields set to zero). The constant $C = 1.7 \times 10^7 m^{-2}$ is a constant specifying the geometry of the RF electric fields at the trap center 134.5μm from the surface (C it is the curvature of the potential producing these fields).

The potential distribution above a planar trap (and the constant C) can be cal-

culated analytically as a superposition of contributions from all the electrodes, where the potential distribution above a rectangular electrode carrying voltage V_0 and the rest of the plane at ground is given by

$$\begin{aligned} V(x,y,z) = &\frac{V_0}{2\pi}\tan^{-1}\left(\frac{(l_x+2x)(l_z+2z)}{2y\sqrt{(l_x+2x)^2+(l_z+2z)^2+4y^2}}\right) \\ &+\frac{V_0}{2\pi}\tan^{-1}\left(\frac{(l_x-2x)(l_z+2z)}{2y\sqrt{(l_x-2x)^2+(l_z+2z)^2+4y^2}}\right) \\ &+\frac{V_0}{2\pi}\tan^{-1}\left(\frac{(l_x+2x)(l_z-2z)}{2y\sqrt{(l_x+2x)^2+(l_z-2z)^2+4y^2}}\right) \\ &+\frac{V_0}{2\pi}\tan^{-1}\left(\frac{(l_x-2x)(l_z-2z)}{2y\sqrt{(l_x-2x)^2+(l_z-2z)^2+4y^2}}\right) \end{aligned} \tag{4.1}$$

where $l_x \times l_z$ are the electrode dimensions. A voltage point source at the origin on a ground plane gives a potential distribution (obtained using the approach in ref. [35])

$$V(x,y,z) = V_0\frac{\pi y}{(x^2+y^2+z^2)^{3/2}} \tag{4.2}$$

Formula 4.1 then comes from integrating the point source location over the rectangular electrode region.

4.3 Micromotion compensation

If a DC electric field E_i displaces an ion from the null of the RF electric field quadrupole by $\delta_i = \frac{eE_i}{m\omega_i^2}$, the larger amplitude of the RF field at the new position results in an excess micromotion amplitude given by

$$u_i = \frac{1}{2}\delta_i q_i \tag{4.3}$$

where q is the Mathieu parameter and $i = \{z, y\}$ refers to one of the eigendirections in the RF plane. This excess driven motion can heat a trapped ion chain, so it is important to compensate the background electric field E_i, which can be appreciable

and also changing overtime in the vicinity of dielectric surfaces, such as the optical cavity mirrors, and in the presence of high-intensity light, such as the optical lattice, which can create charges on surfaces. In directions parallel to the planar trap (z), micromotion is compensated using the standard method [36] by detecting and minimizing the modulation of scattered fluorescence due to the micromotion-induced Doppler shifts of an addressing beam in the same direction.

Micromotion compensation in the direction perpendicular to the trap (y), however, is more tricky. The main issue with applying the traditional method is that the intense UV light addressing an ion's cycling transition causes charge build-up on the trap surface when shining directly on it ([37]). Because of close proximity of the trap surface to trapped ions in planar traps, this is detrimental to maintaining stable trapping potentials. This was verified to also be a problem for our trap and the 369.5 nm light used for the $^2\mathrm{S}_{1/2}-^2\mathrm{P}_{1/2}$ cooling transition in Yb^+. Instead, we probe micromotion-induced Doppler shifts orthogonal to the trap using a 935.2 nm laser beam which is used to repump the ion from the $^2D_{3/2}$ state via the $^3D[3/2]_{1/2}$ state (Fig.4-2a). This approach is motivated by the fact that lower-energy photons at 935.2 nm do not activate ionization processes on the trap surface that lead to charging (this approach was also taken at Oxford [38]). The linewidth of the $^3D[3/2]_{1/2}$ state is $\sim 2\pi \times 3.8$ MHz, with a dominant decay to the ground state [39]. This is narrow enough to resolve sidebands at $\omega_{RF} = 2\pi \times 16.160$ MHz put on the 935.2 nm transition by the micromotion. As the frequency of the 935.2 nm repumper is swept across the Bessel micromotion spectrum, the varying repumping efficiency modulates the population in the cycling manifold, and consequently the fluorescence collected at 369.5 nm, resulting in a frequency-domain Doppler spectrum of micromotion (Fig.4-2b). An additional advantage of this method is that a very small amount of 935.2 nm light ($\sim 100nW$, $\sim 500\mu$m focus) is sufficient to effectively repump the ion when it falls to $^2D_{3/2}$ from the $^2P_{1/2}$ state 0.5% of the time (the linewidth of the $^2P_{1/2}$ state is $2\pi \times 19.9$ MHz). This further mitigates any charging effect because very little light is directed at the ion trap surface, while maintaining the large fluorescence signal provided by cycling on the broad $^2S_{1/2}$-$^2P_{1/2}$ transition.

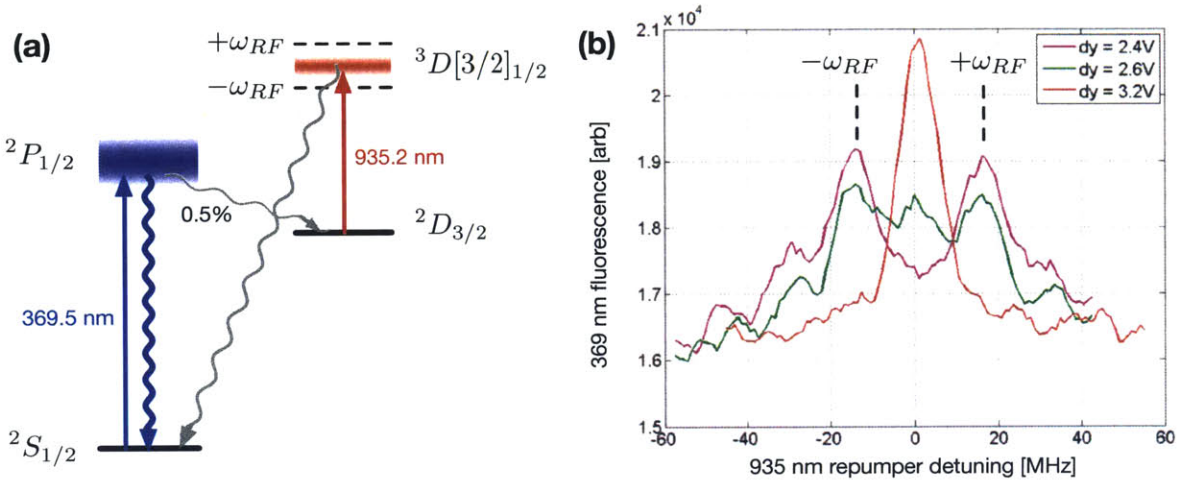

Figure 4-2: **(a)** A simplified atomic level scheme for $^{174}Yb^+$, showing the scheme for micromotion compensation of the trap direction perpendicular to the trap surface, using the 935.2 nm repumper to resolve RF sidebands. Fluorescence is detected at 369.5 nm, modulated by changing repumper efficiency as the repumper is swept through the micromotion spectrum. **(b)** A typical observed spectrum of micromotion in the perpendicular direction (y) for different values of the compensating voltage ("dy") applied to all the electrodes on the chip with respect to the vacuum chamber ground.

The micromotion modulation spectrum is characterized by the modulation depth

$$\beta = \pi q_y \frac{\delta_y}{\lambda} \tag{4.4}$$

where λ is the wavelength of the probing light (935.2 nm in our case). For a reasonably compensated ion, where $\beta << 1$, the ratio of the first sideband to the carrier gives

$$J_1^2(\beta)/J_0^2(\beta) \approx \frac{1}{4}\beta^2 \tag{4.5}$$

Combined with equations 4.4 and 4.3, this leads to a micromotion amplitude perpendicular to the trap given by

$$u_y = \frac{\lambda}{2\pi}\sqrt{2\frac{J_1^2}{J_0^2}} \tag{4.6}$$

where J_1^2 and J_0^2 are the measured values of the first sideband and the carrier in the

spectrum. Experimentally, sidebands can be suppressed down to a fraction of 1/20 of the carrier (limited by the signal-to-noise ratio of the measurement), corresponding to a residual micromotion amplitude of 47 nm (or 5% of the wavelength at 935.2 nm). For our typical trap parameters giving a vibrational frequency $\omega_y = 2\pi \times 1$ MHz and a Mathieu parameter $q_y = 0.2$, this gives a bound on the residual electric fields at $E_{stray} = 33$ V/m.

4.4 Deterministic trap loading

Yb^+ ions are produced by a two-step photo-ionization [33, 40, 41] of the effusive atom flux from a resistively heated oven. The flux is collimated, and to avoid coating the trap, angled away from the chip surface. The ionization is accomplished by resonant excitation on the 399 nm $^1S_0 - ^1P_1$ neutral Yb transition perpendicular to the oven flux, combined with one-photon ionization via 369 nm light built up in the cavity mode (see Figure 4-3). The intra-cavity intensity of the 369 nm light can be continuously controlled up to a maximum of 2 kW/cm^2, resulting in a loading rate of $\sim$2 ions/second. Addressing the coldest direction (perpendicular to the flux) of the atomic beam with the 399 nm light minimizes Doppler broadening and resolves the different Yb isotopes of interest, which are spaced by at least 250 MHz in frequency. This allows us to achieve isotopic purity of our ion samples in excess of 90% (see Figure 4-3b).

Our ability to control the loading rate and the shape of the axial potential permits the loading of a controlled number of ions into a long isotopically pure 1D crystal in the trapping region. By applying a DC periodic potential, we can split this crystal between the individual trap array sites with up to 20 ions per site. The crystal order of our sample resulting from the strong ion-ion repulsion pins each ion with respect to the applied periodic potential, causing the ion crystal to be split at defined positions and resulting in a deterministic loading of the microtrap array. By ramping the periodic potential up and down multiple times and counting the number of ions loaded into each array site, we collect statistics that show highly suppressed ion

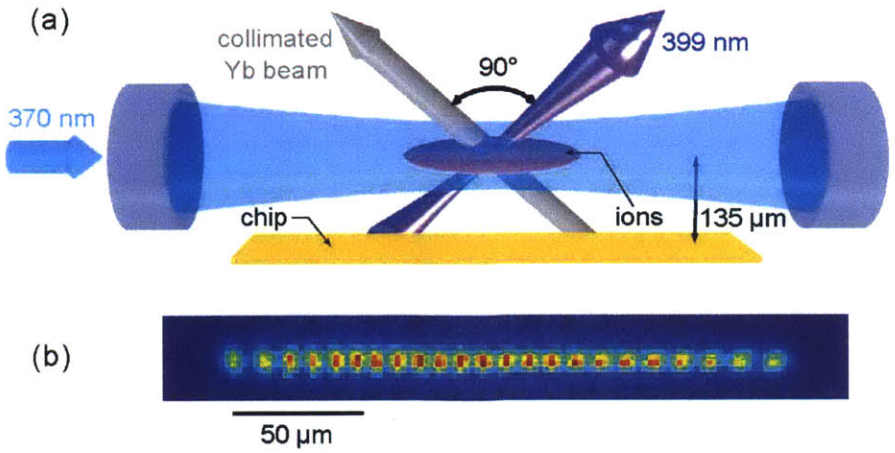

Figure 4-3: a) Trap loading configuration. 399 nm light perpendicular to the thermal atom beam excites the isotope of choice to the $^1P_1$ excited state, from which ionization to the continuum proceeds via the cavity-enhanced 369 nm light. b) Isotopically pure 1D crystal of 23 ions of $^{174}Yb^+$ in a harmonic potential. Ions of a different isotope would be off-resonant with the excitation light and would appear as dark gaps in the chain.

number fluctuations, as shown on Figure 4-4. This can be quantified using the Fano factor, which is defined as the ratio of the ion number variance to the mean number of ions loaded in each trap. This factor is unity for a Poisson process, which would be expected for weak interactions. We typically observe Fano factors less than 0.1.

The deterministically loaded array of microtraps that we demonstrated could be used for quantum information processing with cavity photons connecting the quantum ion registers at each microtrap [33, 19]. For friction studies at the level of a single-asperity nanocontact discussed in this thesis (part II), we always use a single microtrap holding a 1D ion crystal of deterministic size obtained by turning the 399 nm "loading" light off once the desired number of ions has been loaded. Future friction experiments in this system, however, could potentially explore multi-asperity friction by rubbing an array of ion chains, loaded into the different microtraps, against an optical lattice. In that case, the observed deterministic ion loading into the microtraps would come in handy again.

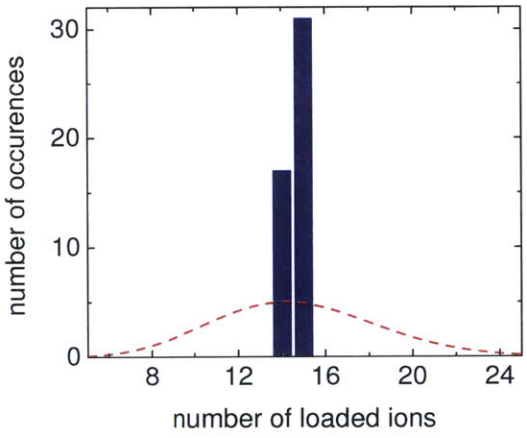

Figure 4-4: Typical ion number histogram for an array site after splitting a longer chain repeatedly with the periodic potential. The red dotted curve is the Poisson distribution with the corresponding mean. The Fano factor at this site is 1.6%. The Fano factor at any site of the array is <10%, limited by residual isotopic impurity.

Chapter 5

Optical cavity and intracavity lattice

The planar ion trap discussed in the previous chapter has been carefully integrated in vacuum with a cavity at the 369 nm optical wavelength (more details can be found in references [33, 34, 42]). The cavity can be used as a quantum interconnect between the ions trapped in the cavity for quantum information processing [19], or it can be used to generate a strong intracavity optical lattice for studying trapped-ion crystals in a periodic potential (i.e. friction, which is the focus of part II). Additionally, it can be used for collection of photons emitted by ions, for spectrometry on this emitted fluorescence [33], for measuring ion temperature (chapter 6.4), and finally, for measuring ions positions with sub-wavelength resolution (chapter 7) - a key tool ion our "friction microscope".

The near-confocal cavity, with its axis aligned with the RF nodal axis of the Paul trap, has a length of 2.2 cm, a TEM_{00} mode waist of $w_{cav} = 38\mu$m and a finesse of $F = \pi/(T + L) \approx 1.4 \times 10^3$ (latest measurement), dominated by loss L. The transmission coefficient for each mirror of $T = 1.8 \times 10^{-4}$ was quoted by Advanced Thin Films and we independently measured it to be $(2.9 \pm 0.2) \times 10^{-4}$. The finesse has degraded from the initial finesse of $F \approx 12.5 \times 10^3$ as a result of loss increase over time (accelerated during the bake), induced by depletion of oxygen from the outer-most dielectric layer Ta_2O_5. Our publication in reference [43] details a systematic study of this process and outlines a finesse recovery method with oxygen treatment.

5.1 Cavity for fluorescence collection and spectrometry

Photons scattered from the ions due to excitation by 369.5 nm light from the side of the cavity can be collected by the cavity (see Fig.5-1a). The number of these photons measured at the cavity output can be used to determine the coupling strength between the ions and the cavity, relevant for using photons as quantum interconnects, but also for the overlap between the trapped ions and a cavity-generated optical lattice for friction studies. In addition, as the cavity length is scanned via a piezo, the spectrum of the emitted fluorescence is obtained with a resolution of $\Delta\omega_{\text{res}} = 2\pi \times 7.5$ MHz given by the convolved linewidths of the drive laser $\Delta\omega_{\text{laser}}$ and of the cavity κ. Two spectra are shown in Fig.5-1b. The blue spectrum shows the energy-conserving scattering of monochromatic light from the 2-level atom, where the collected fluorescence at the peak is in good agreement with the expected value for ions trapped at the center of the cavity mode, testifying that the desired overlap betweens the ions and the cavity (i.e. the lattice) is achieved (more details can be found in our publication [33]). The red spectrum shows sidebands due to uncompensated micromotion in the direction of the side excitation beam (z). Note that this signal can also be used to effectively compensate micromotion in this direction parallel to the trap surface, or any micromotion along the cavity/lattice axis (x) due to stray RF fields.

The collected fluorescence also depends on the position of the ion relative to the lattice. For a perfectly localized ion at a cavity node, coupling is zero, and no fluorescence should be collected, while at a cavity antinode, maximal coupling should result in maximal collected fluorescence. Thus, the observed fluorescence at the cavity output can be used to determine an ion's position modulo half-wavelength $\lambda/2 =$ 184.75 nm with spatial resolution limited by photon shot-noise and temperature. At finite temperature, as the ion's thermal position distribution broadens, the contrast of the position-dependent fluorescence signal decreases, which can, in fact, be used to measure the ion's temperature. Fig.5-2 shows the modulation of fluorescence collected by the cavity as the ion, confined in a tight axial trap at $\omega_0 = 2\pi \times 1.14$ MHz, is moved

along the cavity axis. For friction experiments in a lattice, subwavelength position detection of ions and measurements of ion temperature are based on the same concept as presented here: ion fluorescence, this time collected from the side with the imaging system, is modulated by the position of the center of an ion's position distribution, and depends also on the width of this distribution (see chapter 7 and section 6.4).

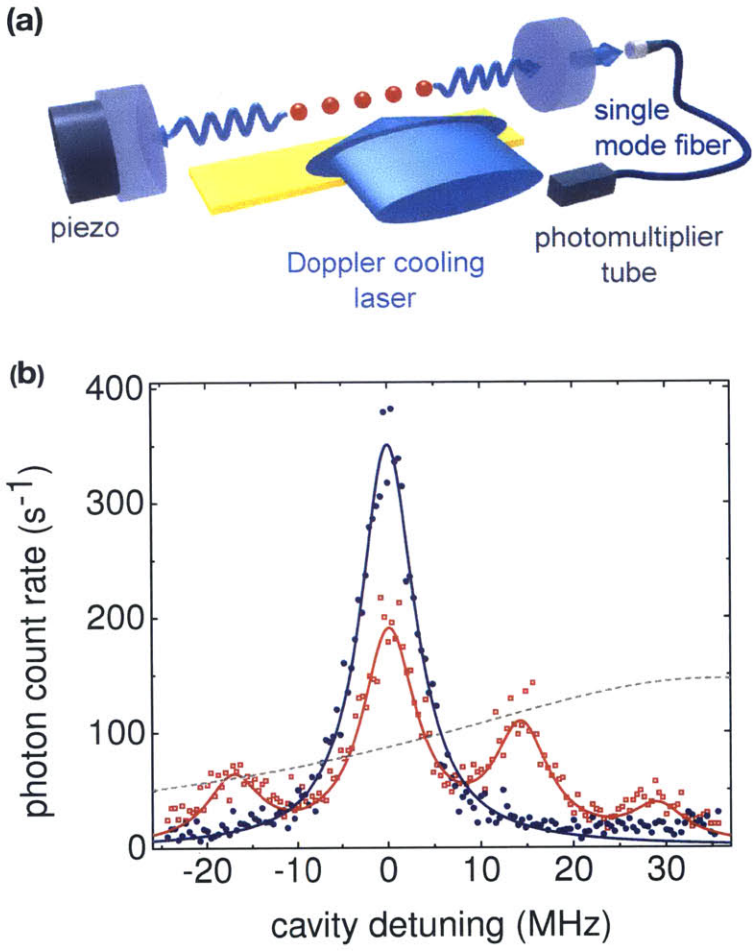

Figure 5-1: **(a)** Set-up for fluorescence collection and spectroscopy via the cavity. Doppler cooling light perpendicular to the cavity-trap axes is scattered into the cavity, which acts as a tunable spectrometer. The light exiting the cavity is coupled to a single-mode fiber and detected by a PMT. For results shown in this section, incident light is linearly polarized in the direction perpendicular to the cavity-trap axes, and collected photons are polarization-analyzed in the same direction. **(b)** Single-ion fluorescence spectra collected by the cavity for a well-compensated ion (blue) and an ion decompensated (red) in the direction of the Doppler cooling beam by a DC electric field of 65 V/m. The 1st-order micromotion sidebands show up clearly and a 2nd-order sideband is also visible on one side. The asymmetry in the spectrum is due to higher scattering rate on the side closer to atomic resonance; the grey dotted curve shows the calculated dependence of the photon scattering rate on the detuning.

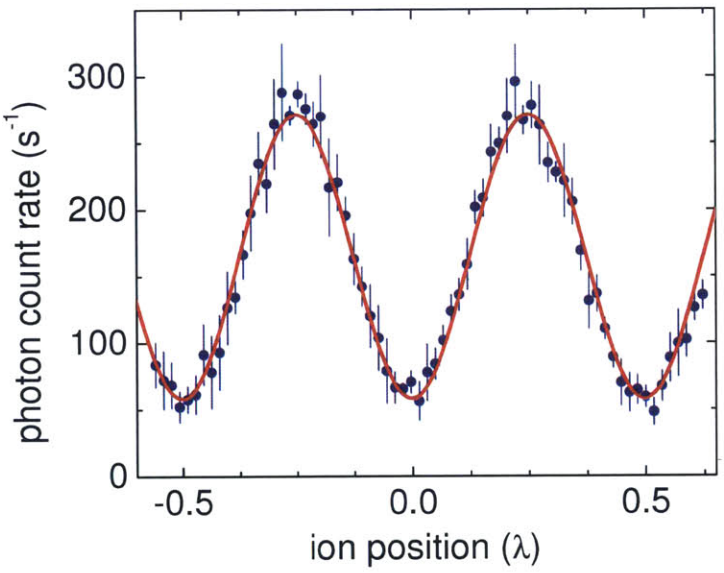

Figure 5-2: Fluorescence from a single Doppler-cooled ion collected by the cavity resonant with the cooling laser as a localized ion is transported along the cavity mode. The observed mode visibility is 65%, corresponding to an ion temperature of 1.6 T_D and a thermal RMS spread of the ionic position distribution of 27 nm. (Here $T_D = \frac{1}{2}\hbar\Gamma/k_B$ is the Doppler limited temperature.)

5.2 Intracavity optical lattice

For the optical lattice forces to dominate over the Coulomb forces in an ion trap, lattice confinement at a periodic potential minimum, or deconfinement at a maximum, must overcome the confinement of an ion at its position in an ion crystal by its neighbours. In other words, if ω_L is the lattice vibrational frequency given by

$$\omega_L^2 = -\frac{1}{m}\frac{\partial^2}{\partial x^2}\bigg|_{x=0}\left[\frac{1}{2}U(1+\cos(2\pi\frac{x}{a}))\right] = \frac{2\pi^2 U}{ma^2} \tag{5.1}$$

then we roughly want $\omega_L \gtrsim N\omega_0$. In other words, for axial trapping frequencies in the Paul trap on the scale of 100 kHz, and a few ions forming a chain in the trap, $\omega_L/2\pi$ on the scale of 1 MHz is desired. With $a = \lambda/2 = 184.75$ nm, this corresponds to lattice depths U/h on the scale of 30 MHz - larger than the linewidth of the $^2S_{1/2}$ - $^2P_{1/2}$ transition at $\Gamma = 2\pi \times 19.9$ MHz. This brings two challenges: generating such a deep optical potential and cooling the ions in it (see chapter 6). The optical potential is a result of the AC Stark shift of the ground-state energy, which is proportional to the optical intensity. When available laser power is limited, using a cavity can enhance the maximum intensity by a factor of $4F/\pi$ by exciting an intracavity standing wave. The depth of the optical lattice is then given by

$$U \approx \frac{1}{3} \times \frac{1}{2}\frac{I}{I_s}\frac{\Gamma^2}{\delta_L} \tag{5.2}$$

where I is the maximum intracavity intensity, $I_s = 50$ mW/cm^2 is the saturation intensity, δ_L is the detuning of the lattice and $\frac{1}{3}$ is the Clebsch-Gordan coefficient for the π-polarized optical transition $J = 1/2 \rightarrow J = 1/2$. With a few mW of laser power available to pump the cavity near 369 nm, even with the cavity-enhanced intensity, a relatively small detuning on the scale of 10 GHz is required to produce lattices of desired depth U. Since our cavity is resonant with Doppler cooling lasers, the lattice detuning must equal an integer number of cavity free spectral ranges of $\omega_{FSR} = 2\pi \times 6.4$ GHz. In the experiments described in this thesis, a lattice detuning of $\delta_L = +2\omega_{FSR}$ was used, blue-detuned relative to the 369.5 nm atomic transition.

Three independent ways have been used to calibrate the strength of the lattice potential actually experienced by the ions. The most indirect and least accurate way is to measure the cavity-transmitted power P_{out} of the laser used to make the optical lattice and to obtain the maximum intracavity intensity via the independently measured mirror transmission coefficient T and cavity waist w_{cav}:

$$I = \frac{P_{out}}{T}\frac{2}{\pi w_{cav}^2} \tag{5.3}$$

Then equation 5.2 can be used to calculate the lattice depth, assuming ions trapped at the center of the cavity waist, which was inferred to be the case (albeit with a large error margin) from measuring the fluorescence collection by the cavity (previous section).

A more accurate measurement is done by vibrational spectroscopy of a single ion trapped at a lattice site. This can be done by measuring the spacing of axial vibrational sidebands in the fluorescence spectrum of sideband-resolved Raman cooling (see chapter 6), or via tickle spectroscopy, where the ion's vibrational motion is excited by weakly modulating the lattice intensity and observing a fluorescence increase when the ion heats up (see Fig.5-3). Consider an ion placed at a lattice minimum (node), which can be done by observing its position-dependent fluorescence, either collected by the cavity from side beam excitation, as in Fig.5-2, or collected from the side using a close-detuned beam resonant with the cavity (which gives a similar signal). In this case, the lowest-order observed vibrational resonance is given by $\omega_{res} = \sqrt{\omega_0^2 + \omega_L^2}$, and ω_L can be extracted by doing and independent measurement of ω_0 via tickle spectroscopy with the lattice potential turned off (see chapter 4).

We found that tickle vibrational spectroscopy in the lattice results in a lattice vibrational frequency ω_L underestimated by 5%, by benchmarking the measured single-ion stick-slip friction force against the expected value from the Prandtl-Tomlinson model in the high-velocity, temperature-independent regime at $\eta = 4.6$ (see part II). We believe the latter to be the most accurate measurement of the lattice depth in our system, and subsequently use it for friction studies with multi-ion crystals.

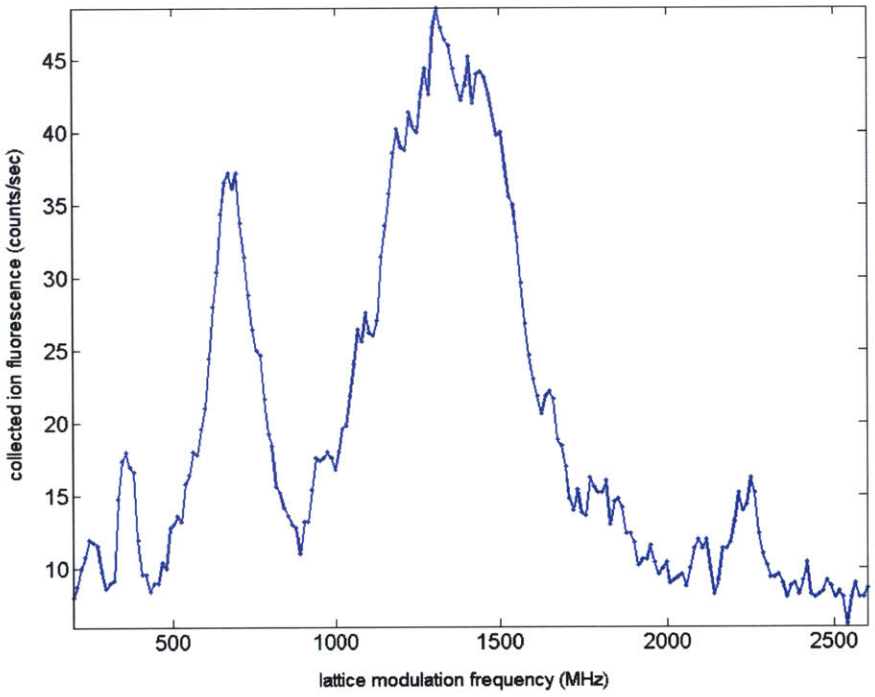

Figure 5-3: A typical vibrational spectrum of a single ion in a lattice, obtained by weakly modulating the lattice intensity and sweeping the modulation frequency. The narrow first-harmonic resonance at 700 kHz roughly gives the lattice vibrational frequency $\omega_L/2\pi$, which corresponds to a lattice depth $U = 2\pi\hbar \times 15$ MHz. The broad resonance around 1400 kHz corresponds to parametric heating at twice the vibrational frequency. The positions of the resonances scale as the square root of the lattice intensity, as expected from formula 5.1.

Chapter 6

Ground-state cooling of ions in a lattice

6.1 Challenges

6.1.1 The Doppler cooling problem

Cooling an atom deep into an optical lattice, such that $k_B T << U_L$, requires elaborate cooling methods, since the most basic Doppler laser cooling works poorly if one considers how an optical lattice destroys the conditions required to achieve the Doppler cooling limit.

Consider an optical transition in the atom with a large oscillator strength (for example the S-P transition in Yb^+ or a neutral Alkali atom). Given the natural linewidth Γ of the transition ($\Gamma = 2\pi \times 19.9MHz$ for the 369.5 nm $^2S_{1/2}$ - $^2P_{1/2}$ transition in $^{174}Yb^+$), the temperature limit $k_B T_D = \hbar\Gamma/2$ for Doppler cooling on this transition can be achieved at the optimal detuning of $\delta = \Gamma/2 = k_B T_D/\hbar$ of the laser from the transition [44, 45]. An optical lattice is a spatially periodic AC Stark shift of the ground-state energy that results in the desired periodic potential [44, 45]. The AC Stark shift results from an admixing of the excited states by the interaction of the atom with the standing wave of light, and the excited states are in turn shifted with opposite sign due to the admixing of the ground state. As a result, in general,

the optical transition is spatially modulated as well. In a 2-level system, the AC Stark shift of the optical transition is modulated between 0 and $\Delta_{AC} = 2U_L/\hbar$. Because of this, $k_B T << U_L$ cannot be achieved because, roughly speaking, that would require $\delta << \Delta_{AC}/2$ to achieve the Doppler limit, but δ is modulated by the Stark shifts at least up to the value Δ_{AC}.

This problem can be mitigated using a number of different schemes. One approach is to use a magic-wavelength optical lattice [44, 45], which results in equal AC Stark shifts of the ground state and the optically cycled excited state as a result of the admixing of other excited states. This cancels the spatially-dependent AC Stark shift of the optical transition used to cool the atom and the optimal detuning can be dialed in for reaching the Doppler cooling limit.

Another approach, which we take in our system, is to perform Raman cooling [46, 47, 48, 49]. In this approach, the far-detuned Raman transitions between ground-state sublevels are insensitive to the differential AC Stark shift between the ground and excited states, and the effective linewidth of these transitions and the corresponding Doppler cooling limit can be tuned via the scattering rate of a pumping beam, and can therefore be significantly reduced. Furthermore, with resolved-sideband Raman cooling where the red vibrational sideband is addressed by the narrow Raman transitions and where momentum diffusion is suppressed by the confinement, the ion can be prepared in its ground state of motion in a lattice site [50].

6.1.2 The temperature measurement problem

Time-of-flight temperature measurements, that work for neutral atoms by releasing the trap and converting momentum to position for imaging, do not work for trapped ions, because of poor number statistics, and because of the difficulty of switching off the trapping electric fields without adding energy to the ions. Making use of the tight confinement of ions in the trap, one way to measure temperature is via the asymmetry of response to excitation of red and blue motional sidebands, which works in the sideband-resolved regime. The asymmetry is strong when the occupation of the ground vibrational state is high, but the signal disappears for higher temperatures.

The temperature measurement scheme which we implement (see section 6.4), involves a direct measurement of the width of the ion's position distribution using a spatially structured probe (a close-detuned standing wave). This method does not require operation in the sideband-resolved regime or a large ground-state occupation.

6.2 Basics of Raman cooling

6.2.1 Raman-Doppler cooling

The idea behind Raman-Doppler cooling is to create an effective 2-level system in the ground-state manifold of the atom, with an effective linewidth and the corresponding Doppler cooling limit controlled by an optical pumping laser. Consider an atom with the ground state and the excited state having 2 sublevels each: $|g_1\rangle$, $|g_2\rangle$ and $|e_1\rangle$, $|e_2\rangle$, respectively (see Fig. 6-1). Optical pumping from $|g_2\rangle$ to $|g_1\rangle$ (by the beam with Rabi frequency Ω_c) limits the lifetime of state $|g_2\rangle$, resulting in a linewidth of this state given by the pumping rate Γ_p. Two laser beams (Rabi frequencies Ω_a and Ω_b) far-detuned from the excited state ($\delta_a >> \Gamma$) drive a stimulated 2-photon transition between $|g_1\rangle$ and $|g_2\rangle$ at a 2-photon detuning Δ_2 and a 2-photon Rabi frequency $\Omega_2 = \frac{\Omega_a \Omega_b}{2\delta_a}$.

The rate of photon scattering by a 2-level atom is given by

$$\gamma_{sc} = \frac{\Gamma}{2} \frac{2(\Omega/\Gamma)^2}{1 + 2(\Omega/\Gamma)^2 + (2\delta/\Gamma)^2} \tag{6.1}$$

This means that the scattering rate from the effective 2-level system $\{|g_1\rangle, |g_2\rangle\}$ is given by

$$\gamma_{sc} = \frac{\Gamma_p}{2} \frac{2(\Omega_2/\Gamma_p)^2}{1 + 2(\Omega_2/\Gamma_p)^2 + (2\Delta_2/\Gamma_p)^2} \tag{6.2}$$

The linewidth Γ_p is in turn given by the pump scattering rate

$$\Gamma_p = \frac{\Gamma}{2} \frac{2(\Omega_c/\Gamma)^2}{1 + 2(\Omega_c/\Gamma)^2 + (2\delta_c/\Gamma)^2} \tag{6.3}$$

(ignoring the Clebsch-Gordan coefficients for now) with the corresponding Raman-

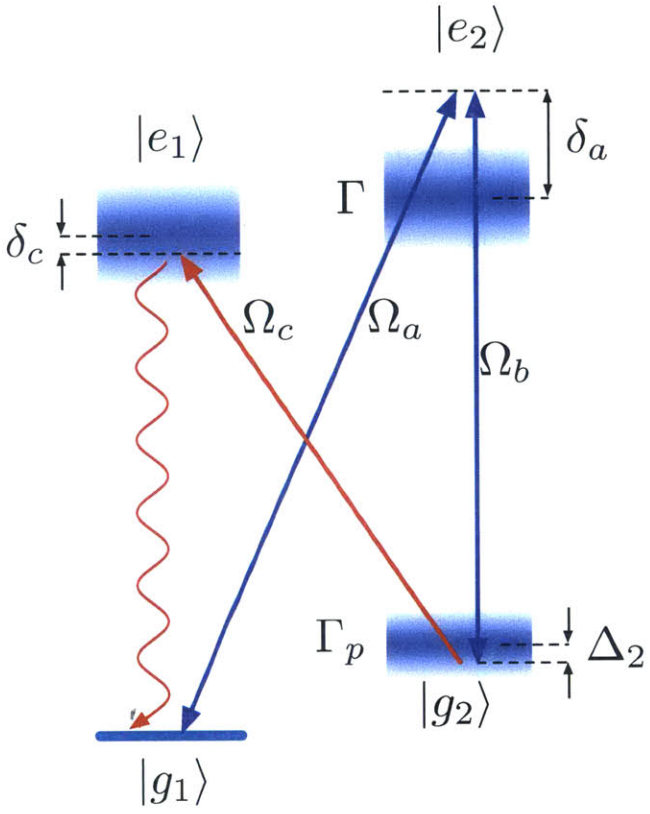

Figure 6-1: **Raman cooling basics.** Ground sublevels $|g_1\rangle$ and $|g_2\rangle$ form a 2-level system with a linewidth of Γ_p, driven at a 2-photon Rabi frequency $\Omega_2 = \frac{\Omega_a \Omega_b}{2\delta_a}$.

Doppler cooling limit $k_B T_{RD} = \hbar\Gamma_p/2$, tunable via the intensity of the pump beam Ω_c or its detuning δ_c.

To see the Doppler cooling mechanism in Raman-Doppler cooling, consider an atom moving at velocity $\vec{v}$. In the moving frame, each laser beam is Doppler-shifted by $-\vec{k} \cdot \vec{v}$ (where the wavevectors $\vec{k}$ of the beams have nearly equal magnitudes) and the 2-photon detuning is shifted by $-(\vec{k}_a - \vec{k}_b) \cdot \vec{v}$. Then the average force on the atom, due to the 2-photon Raman transitions as a result of absorbed and emitted photon recoil (in beams Ω_a and Ω_b respectively), is given by

$$\vec{F}_R(\vec{v}) = \hbar(\vec{k}_a - \vec{k}_b)\gamma_{sc}(\vec{v}) = \hbar(\vec{k}_a - \vec{k}_b)\frac{\Gamma_p}{2}\frac{2(\Omega_2/\Gamma_p)^2}{1 + 2(\Omega_2/\Gamma_p)^2 + \left(2\frac{\Delta_2 - (\vec{k}_a - \vec{k}_b)\cdot\vec{v}}{\Gamma_p}\right)^2} \tag{6.4}$$

Clearly, only the counter-propagating projections of the Raman beams contribute to this radiation pressure force. Fig. 6-2 shows this force on the moving atom as

a function of velocity for red ($\Delta_2 < 0$, Fig. 6-2B) and blue ($\Delta_2 > 0$, Fig. 6-2C) two-photon detunings. When $\Delta_2 < 0$, a large positive force decelerates atoms moving in the negative direction, leading to a cooling effect, whereas when $\Delta_2 > 0$, the opposite happens: a large positive force accelerates atoms moving in the positive direction, leading to heating. When cooling, there are also weak accelerating forces for positive velocities, but in a confining trap, they are overcome by the much stronger decelerating forces during the other half of an oscillation period. In order for the radiation pressure force to decelerate the atoms at all velocities, two additional beams can be added (Fig. 6-2D), identical to the first two Raman beams, but with their propagation directions switched (one can also switch their polarizations as shown in Fig. 6-2E). This results in a viscous cooling force for all velocities as shown in Fig. 6-2F.

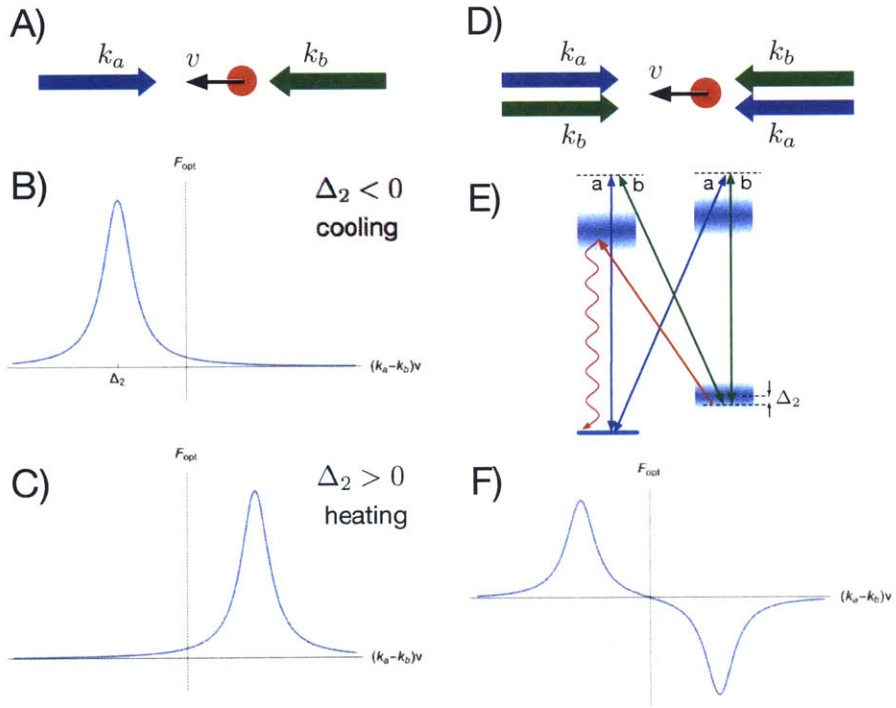

Figure 6-2: **Doppler cooling forces.**

Note that there is an additional radiation pressure force along $\vec{k}_c$ due to the optical pumping beam Ω_c, given by $\vec{F}_c(\vec{v}) = \hbar\vec{k}_c\gamma_{sc}(\vec{v})$. It can enhance or reduce the velocity-dependent forces in the Raman cooling direction of $\vec{k}_a - \vec{k}_b$ depending on whether the

component of $\vec{k}_c$ in this direction is parallel or anti-parallel. In addition, the pumping rate and effective linewidth Γ_p is dependent on velocity along $\vec{k}_c$ due to Doppler shifts:

$$\Gamma_p(\vec{v}) = \frac{\Gamma}{2} \frac{2(\Omega_c/\Gamma)^2}{1 + 2(\Omega_c/\Gamma)^2 + \left(2\frac{\delta_c - \vec{k}_c \cdot \vec{v}}{\Gamma}\right)^2} \tag{6.5}$$

This provides some standard Doppler cooling in the direction $\vec{k}_c$ if $\delta < 0$. (In the limit where the 2-photon transition saturates $\Omega_2 >> \Gamma_p$, basic scattering from the excited state is recovered $\gamma_{sc}(\vec{v}) \rightarrow \Gamma_p(\vec{v})/2$ and we get back to the original Doppler limit $k_B T_D = \hbar\Gamma/2$ along $\vec{k}_c$). Note that this velocity dependence of Γ_p does not affect the Raman cooling process in equation 6.4, where an effective Γ_p can be used as long as $\vec{k}_c$ is perpendicular to the Raman cooling direction, in which case Γ_p is uncorrelated with velocity in the Raman cooling direction, and the effective Γ_p to be used in equation 6.4 only depends on the width of the velocity distribution in the direction $\vec{k}_c$.

6.2.2 Raman sideband cooling

As the effective linewidth of 2-photon transitions Γ_p is reduced to lower the cooling limit, one enters the regime where it becomes smaller than the trap vibrational frequency ($\Gamma_p \lesssim \omega_0$) and vibrational sidebands are resolved. The picture of optically pumping down the ladder of vibrational energy eigenstates is more appropriate in this strong confinement regime, rather than the picture of momentum eigenstates and velocity-dependent scattering invoked thus far. The basic idea is that the stimulated 2-photon Raman transitions tuned to a red sideband remove vibrational quanta from the atom and change its internal state from $|g_1\rangle$ to $|g_2\rangle$, then the optical pumping closes the cooling cycle by bringing the atom back to $|g_1\rangle$ without changing the vibrational energy thanks to Lamb-Dicke confinement.

Depending on the 2-photon detuning Δ_2, the stimulated 2-photon Raman process can drive i) carrier transitions $|n\rangle \rightarrow |n\rangle$, which do not change the vibrational energy of the atom, when $\Delta_2 = 0$, ii) blue sideband transitions $|n\rangle \rightarrow |n + l\rangle$, which add l

vibrational quanta, when $\Delta_2 = +l\omega_0$, or ii) red sideband transitions $|n\rangle \rightarrow |n-l\rangle$, which remove l vibrational quanta, when $\Delta_2 = -l\omega_0$ (see Fig. 6-3). The spatial component $e^{i\Delta kx}$ of the electric field operator couples the vibrational levels via $\Delta kx = 2k(\frac{\hbar}{2m\omega_0})^{1/2}(a + a\dagger) = 2\eta_{LD}(a + a^\dagger)$. Here $\eta_{LD} = (\omega_{rec}/\omega_0)^{1/2} = (\frac{\hbar^2k^2}{2m}/(\hbar\omega_0))^{1/2}$ is the Lamb-Dicke parameter equal to the square root of the ratio of the photon recoil energy and the trap vibrational quantum (where x is the atom's external coordinate in the Raman cooling direction, $\Delta k = 2k$ is the photon momentum transferred by the Raman beams assuming that they are counter-propagating and a and $a^\dagger$ are the harmonic oscillator annihilation and creation operators). Under strong Lamb-Dicke confinement $\eta_{LD} << 1$ the coupling operator can be expanded in a Taylor series in η_{LD} as $e^{i\Delta kx} \approx 1 + i2\eta_{LD}(a + a^\dagger) - 2\eta_{LD}^2(a + a^\dagger)^2 + O(\eta_{LD}^3)$. The first term only couples carrier transitions, the second term can add or remove a single vibrational quantum (bringing out the prefactor $\sqrt{n+1}$ or $\sqrt{n}$) corresponding to first-order blue or red sidebands, respectively, the third term corresponds to second-order sidebands (bringing out the prefactor $\sqrt{(n+1)(n+2)}$ or $\sqrt{n(n-1)}$), and so on. The coupling *rate* of Raman transitions on a sideband l is therefore down from the carrier rate due to a factor on the order of $n^l\eta_{LD}^{2l}$. In other words, sideband transitions are strongly suppressed under Lamb-Dicke confinement when an atom is cold. However, they can still be driven selectively by the stimulated 2-photon Raman transitions by choosing the 2-photon Raman detuning as explained above. The pumping process, on the other hand, involves a spontaneously emitted photon predominantly on the carrier because of the Lamb-Dicke suppression of sidebands. (Note that absorption of the pump photon can remove vibrational quanta if $\delta_c < 0$, but the sidebands are not resolved since $\Gamma >> \omega_0$, and this corresponds to the additional Doppler cooling by the pump in the direction $\vec{k_c}$ described in the previous subsection).

For cooling, usually the 2-photon detuning is tuned to the first-order red sideband to remove one energy quantum $\hbar\omega_0$ per cooling cycle. If the 2-photon transition is not saturated ($\Omega_2 << \Gamma_p$), then

$$\gamma_{sc(|n\rangle \rightarrow |n-1\rangle)} \approx \frac{n\eta_{LD}^2\Omega_2^2}{\Gamma_p} \tag{6.6}$$

where Ω_2 here is the carrier 2-photon Rabi frequency. The cooling rate (ignoring pump absorption) is then

$$\frac{dE}{dt} = \hbar\omega_0\gamma_{sc(|n\rangle\rightarrow|n-1\rangle)} = n\hbar\omega_{rec}\frac{\Omega_2^2}{\Gamma_p} \tag{6.7}$$

and the cooling rate constant is

$$\frac{1}{\tau_{cool(RS)}} = \frac{1}{E}\frac{dE}{dt} = \frac{1}{n\hbar\omega_0}\frac{dE}{dt} = \frac{\eta_{LD}^2\Omega_2^2}{\Gamma_p} \tag{6.8}$$

We can rewrite this Raman sideband cooling rate constant (RS) and compare it to the Raman-Doppler cooling rate constant at optimal 2-photon detuning (RD):

$$\begin{aligned}\frac{1}{\tau_{cool(RS)}} &= \frac{\Gamma_p}{\omega_0}\omega_{rec}\left(\frac{\Omega_2}{\Gamma_p}\right)^2 \text{ , } \Gamma_p << \omega_0 \text{ , } \Delta_2 = -\omega_0 \\ \frac{1}{\tau_{cool(RD)}} &= 8\omega_{rec}\left(\frac{\Omega_2}{\Gamma_p}\right)^2 \text{ , } \Gamma_p >> \omega_0 \text{ , } \Delta_2 = -\Gamma_p/2\end{aligned} \tag{6.9}$$

One can see that for a fixed resonant saturation parameter $s_0 = 2(\frac{\Omega_2}{\Gamma_p})^2$, as Γ_p is lowered beyond $\Gamma_p \lesssim \omega_0$, entering the resolved-sideband regime, the optimal cooling rate constant starts to drop linearly.

Furthermore, the temperature limit begins to be limited by the trap frequency. It can be found by equating the cooling rate on the 2-photon resonant red sideband to the heating rate on the off-resonant (by $2\omega_0$) blue sideband. This gives $\frac{\bar{n}+1}{\bar{n}} = 1 + (4\frac{\omega_0}{\Gamma_p})^2 = e^{\frac{\hbar\omega_0}{k_BT}}$ and the following relations for the mean vibrational occupation and temperature at the Raman sideband cooling limit:

$$\begin{aligned}\bar{n} &= \left(\frac{\Gamma_p}{4\omega_0}\right)^2 \\ k_BT_{RS} &= \frac{\hbar\omega_0}{\ln(1+1/\bar{n})}\end{aligned} \tag{6.10}$$

In other other words, with better sideband resolution, sideband cooling allows a high-fidelity preparation of the motional ground state, but the absolute temperature only goes down logarithmically with reduced effective linewidth Γ_p.

6.3 Lattice-assisted Raman sideband cooling of $^{174}Yb^{+}$ in a lattice

We perform Raman cooling on the 369.5 nm $^2S_{1/2}$-$^2P_{1/2}$ cycling transition in $^{174}Yb^{+}$ that has an excited state linewidth of $\Gamma = 2\pi \times 19.9$ MHz (see Fig.6-3). The ground and the excited state both have total spin $J = 1/2$ with two magnetic sublevels. In the ground state, the two sublevels $|g_1\rangle$ and $|g_2\rangle$ correspond to the S= $\frac{1}{2}$ electron spin projections $m_s = -1/2$ and $m_s = +1/2$ on the quantization axis (z) defined by the externally applied magnetic field $\vec{B}$, with a Zeeman energy splitting given by

$$\Delta E_Z = \mu_B g_e \vec{S} \cdot \vec{B} \tag{6.11}$$

where μ_B is the Bohr magneton and g_e is electron's gyromagnetic ratio. This corresponds to a ground-state splitting of $\Delta E_Z = 2\pi\hbar \times 2.8$ MHz per Gauss of applied magnetic field. As described in the section 6.2, in order to cool, we drive stimulated 2-photon transitions (via a virtually excited $^2P_{1/2}$ state) between $|m_s = -1/2, n\rangle$ and $|m_s = +1/2, n' < n\rangle$, flipping an electron spin and removing motional quanta. The cooling cycle is closed via a pumping beam detuned from the 369.5 nm transition by $\delta_c \approx 100$ MHz and with a resonant saturation parameter near $s_0 \approx 2.5$. It drives a spontaneous 2-photon transition back to $|m_s = -1/2, n'\rangle$, which flips the electron spin again and spontaneously emits a photon, but maintains the new vibrational level n'. This gives an effective linewidth Γ_p to the $|m_s = +1/2\rangle$ sublevel on the scale of $2\pi \times 100 - 500$ kHz, near the edge of the sideband resolved regime for the typical vibrational frequencies between 400 kHz and 1 MHz.

The cooling rate is proportional to the 2-photon Rabi frequency squared $\Omega_2^2 = \left(\frac{\Omega_a \Omega_b}{2\delta_a}\right)^2$. To minimize heating due to spontaneous emission from the $^2P_{1/2}$ excited state, large detuning δ_a/Γ is desired, which must be compensated by a large intensity in at least one of the Raman beams (Ω_a or Ω_b) to achieve a desired cooling rate. The criteria of large intensity and far detuning coincide with the criteria for an optical lattice, and so we use the lattice itself, to drive at least the π-polarized leg of the

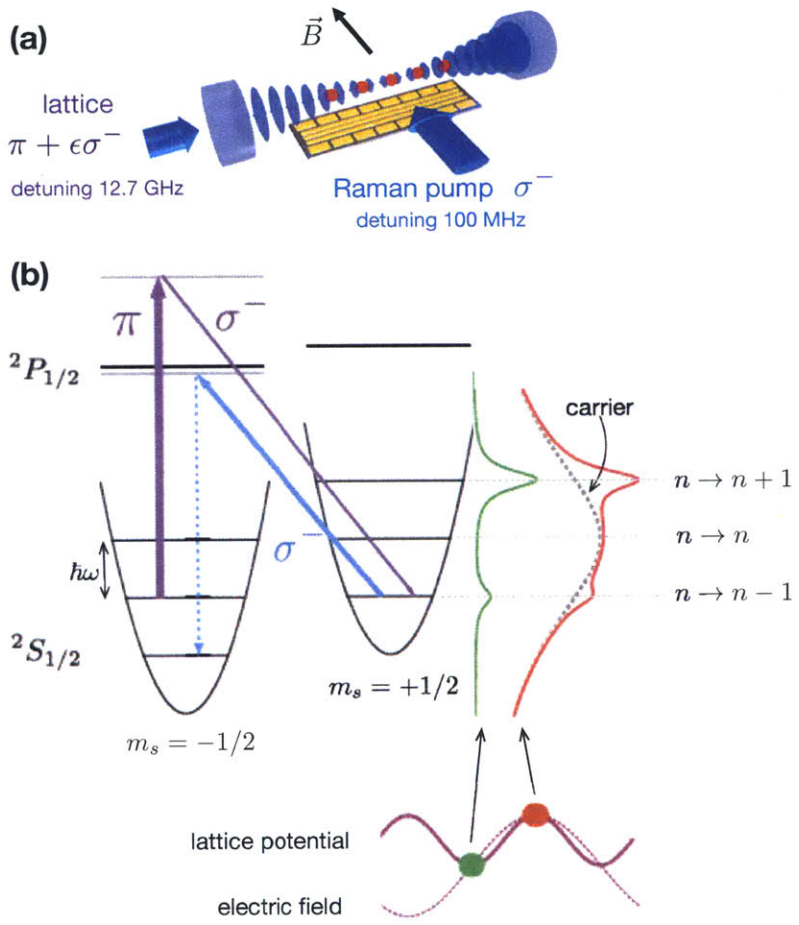

Figure 6-3: Raman cooling scheme for $^{174}Yb^+$. Two-photon cooling (π and σ^- beams shown in purple) is done on the effective two-level system formed by $m_s = \pm 1/2$ Zeeman sublevels of the ground $^2S_{1/2}$ level, with an effective linewidth set by the pumping rate (σ^- beam shown in cyan) to resolve vibrational sublevels at $\hbar\omega$. In (a), we show the cooling beam configuration used for friction experiments, where both the π and σ^- components of the 2-photon Raman transition are due to a lattice light, which is mostly linearly polarized (π), but with a small circular polarization impurity introduced to obtain the desired σ^- component. The momentum vector of both components, and therefore the Raman cooling, is along the lattice direction, the relevant direction for the 1D friction experiments. Some Doppler cooling is maintained along the orthogonal directions due to pump beam scattering and a DC quadrupolar tilt of the transverse trap axes. In (b), and illustration is shown of 2-photon scattering spectra for an ion placed at a lattice minimum (node, shown in green), and for an ion placed at a lattice maximum (antinode, shown in red). At the node, the carrier transition is suppressed. At the antinode, it is much stronger and broader than the sideband transitions, contributing to fluorescence even at a 2-photon detuning Δ_2 tuned to the red sideband $n \to n-1$. This gives the position-dependent fluorescence signal for tracking individual ions, as discussed in chapter 7.

stimulated Raman transition, as shown in Fig.6-3. The other leg of the Raman transition can either be driven by a separate σ-polarized beam, or by a small σ-polarized component of the lattice itself. In either case, the 2-photon Rabi coupling squared $\Omega_2^2 = \left(\frac{\Omega_\pi \Omega_\sigma}{2\delta_a}\right)^2$ is controlled by the intensity Ω_σ^2 of the σ component, since the detuning $\delta_a = 2\pi \times 12.6$ GHz is fixed at the lattice detuning and Ω_π^2 is fixed by the lattice depth at $\Omega_\pi^2 = 3 \times 2\delta_a U/\hbar$.

The 2-photon detuning Δ_2 is controlled via the magnetic field and the resultant Zeeman splitting:

$$\Delta_2 = -\Delta E_Z - (\omega_\sigma - \omega_\pi) - \Delta_{AC,p} \tag{6.12}$$

Here ω_π and ω_σ are the optical angular frequencies of the Raman beams. In the case where the π and σ components both come from the lattice, they are degenerate, and formula 6.12 reduces to $\Delta_2 = -\Delta E_z - \Delta_{AC,p}$. The shift $\Delta_{AC,p}$ is due to an AC Stark effect of the pumping beam, which changes with the pumping beam parameters and consequently with the chosen linewidth Γ_p of the 2-photon Raman transitions as

$$\Delta_{AC,p} = \tfrac{2}{3} \times 4\Gamma_p \frac{\delta_c}{\Gamma} \tag{6.13}$$

neglecting here for simplicity the effect of optical lattice Stark shifts on the pumping beam detuning δ_c.

Two representative Raman fluorescence spectra, obtained by scanning the z-component of the magnetic field B_z with the ion positioned at a lattice minimum, are shown in Fig.6-4 in the Raman-Doppler cooling regime (Fig.6-4a) and in the sideband-resolved regime (Fig.6-4b). In the Raman-Doppler regime, the fluorescence peak at $\Delta_2 > 0$ corresponds to ion heating, which results in increased fluorescence. The fluorescence dips close to zero at $\Delta_2 < 0$, corresponding to near ground-state cooling (see next section). Note the absence of the Rayleigh fluorescence peak at $\Delta_2 \approx 0$, which would correspond to carrier $n \rightarrow n$ scattering. This coupling is suppressed at the lattice minimum because the electric field coupling element $sin(kx) \approx kx + O((kx)^2)$ responsible for the Raman transitions has no x^0 term to give lowest-order coupling between motional levels of equal vibrational quantum number (see Fig. 6-3b).

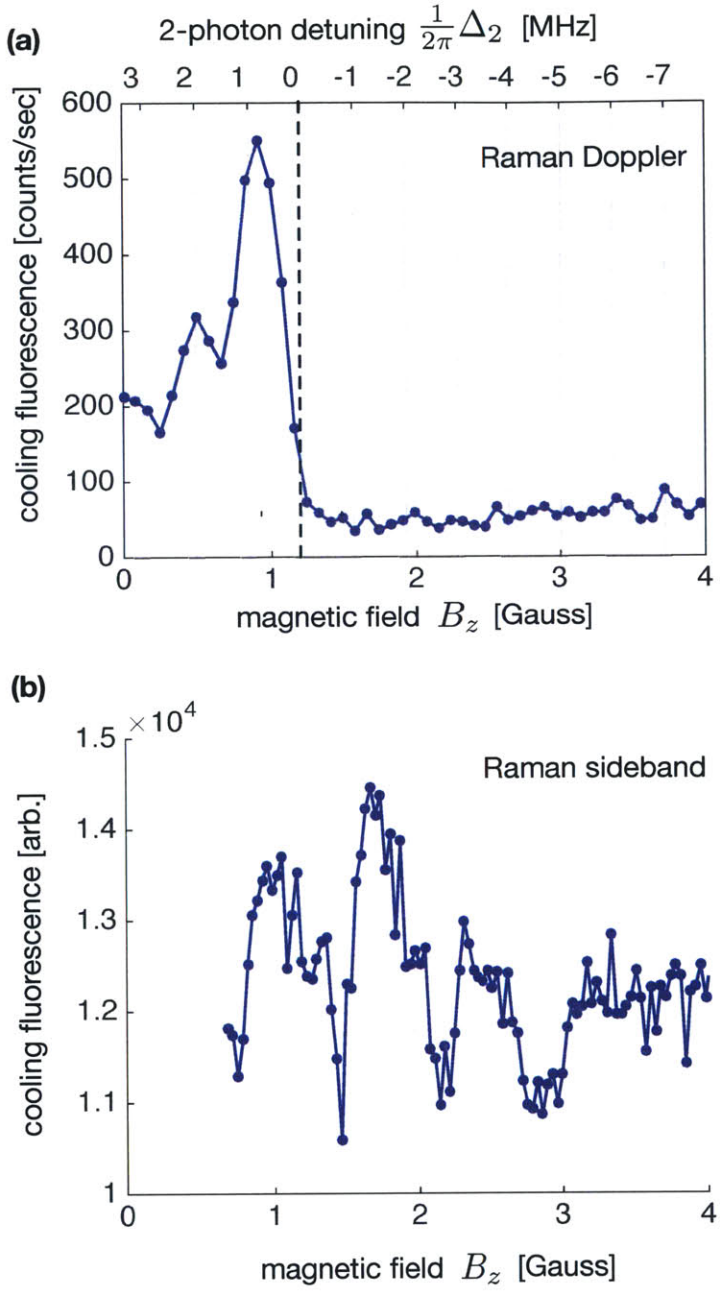

Figure 6-4: **(a)** A typical Raman spectrum of pump fluorescence versus magnetic field (or two-photon detuning Δ_2) in the Raman-Doppler cooling regime (at the edge of the sideband-resolved regime) with the beam configuration shown in Fig.6-3a. The dashed line indicates the approximate location of $\Delta_2 = 0$, where a carrier peak would appear if the Raman beams were running waves. For red-detuned Raman transitions (to the right of the dashed line) cooling is observed as a drop in fluorescence to a level of $\sim$ 50 photon counts per second detected on the PMT. **(b)** A sideband-resolved Raman spectrum of pump fluorescence versus magnetic field. Cooling resonances show up as dips in the observed fluorescence (collected by the electron-multiplying CCD camera.)

In our paper demonstrating initial trapping and cooling of ions in a lattice [16] (chapter 8), the stimulated 2-photon transitions were driven by the π-polarized lattice and separate σ-polarized beam. Ultimately, it was empirically found that the scheme with the σ component derived from the lattice was more robust for friction experiments and was subsequently used for these experiments. Consider this second scheme. The electric field matrix element that couples harmonic oscillator levels n and n' of the $|m_s = -1/2\rangle$ and $|m_s = +1/2\rangle$ ground sublevels is a multiplication of the electric fields from the two Raman legs, and when both of them are driven by the lattice standing wave, it gives

$$V_{n,n'} = \langle n|sin^2\big(k(x - x_c)\big)|n'\rangle \tag{6.14}$$

where x is the ion's motional coordinate in the lattice direction with respect to the center position of the ion x_c in the combined Paul trap and lattice potential, and $k = \frac{2\pi}{\lambda}$. Expansion of this for $kx \propto \eta_{LD} << 1$ gives

$$V_{n,n'} \approx \langle n|\ sin^2(kx_c) - kx\ sin(2kx_c) + (kx)^2 cos(2kx_c)\ |n'\rangle \tag{6.15}$$

The lowest-order term x^0 gives the $n \rightarrow n$ carrier coupling, which varies from zero at the lattice minimum $x_c = 0$ to largest at the lattice maximum $x_c = a/2 = \lambda/4$ (see Figs.6-3b and 6-5). The first-order $n \rightarrow n \pm 1$ sideband couplings (x^1 term) and the second-order $n \rightarrow n \pm 2$ sideband couplings (x^2 term) vary sinusoidally with half the period and out-of-phase with each other as a function of the ion's position x_c (Fig.6-5). Therefore, cooling on the first red sideband turns off at the lattice minima and maxima, and is most effective at the slope of the periodic lattice potential. Cooling on the second red sideband does the opposite, and works at lattice minima and maxima. In friction experiments, where ions are dragged through the lattice, to maintain cooling for all positions in the lattice at a fixed 2-photon detuning, we operate in the Raman-Doppler cooling regime near the edge of the sideband-resolved regime (Fig.6-4a), where first-order sideband cooling and second-order sideband cooling can both contribute. Furthermore, in this regime, the position-dependent variation of

carrier scattering, which dominates the collected fluorescence signal even though the 2-photon detuning is off-resonant, can be used to track the position of ions relative to the lattice with subwavelength resolution (see chapter 7).

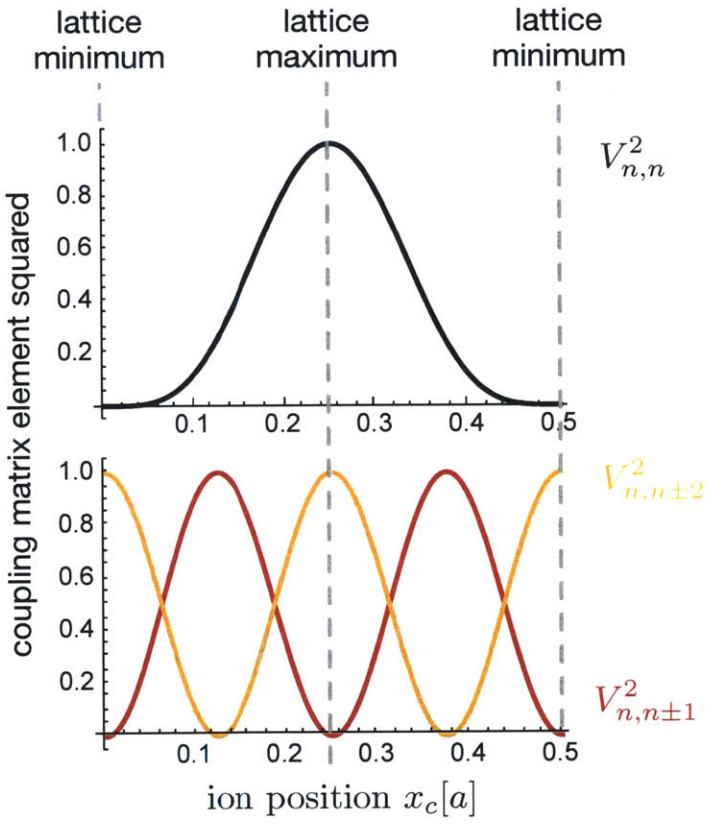

Figure 6-5: Variation of the vibrational coupling matrix elements (squared) with ion position relative to the lattice. The carrier $n \rightarrow n$ coupling varies from zero at lattice minima to unity at lattice maxima (black). Variation of fluorescence from carrier scattering can therefore be used to determine an ion's position relative to the lattice, with subwavelength resolution limited by photon shot noise (see chapter 7). The first-sideband coupling (red) goes from zero at lattice minima, to unity at the lattice slope, and back to zero lattice maxima. The second-sideband coupling (orange) does the opposite.

6.4 Temperature measurement and ground-state cooling

While the fluorescence in spectra in Fig.6-4 can be used to qualitatively infer the temperature of the ion (low fluorescence corresponds to low temperatures, and high fluorescence corresponds to high temperatures), the effects of temperature and of Raman coupling, which changes with the 2-photon detuning Δ_2 even at a fixed temperature, are convolved. For example, at large negative 2-photon detunings, cooling breaks down and temperature should increase again, but without cooling, no photons are scattered and the fluorescence is no longer representative of temperature.

To measure the temperature independently from cooling, we measure the width of the ion's position distribution in a lattice site using a "probe" standing wave in the cavity. The probe is detuned from the 369.5 nm transition by 100 MHz and resonant with the cavity 2 free spectral ranges away from the lattice-cavity resonance (which is 12.7 GHz detuned). This means that at the center of the cavity where the ions are trapped, the probe standing wave intensity pattern nearly coincides with the lattice intensity pattern (see Fig.6-6). A cold ion at the lattice minimum will be well localized at the node of the probe standing wave and will not scatter photons. A hot ion's position distribution will sample high-intensity regions of the probe standing wave and will scatter photons. Thus, scattered probe fluorescence is a measure of the ion's temperature.

To distinguish the scattered probe fluorescence from fluorescence from the pump in the cooling process, we run a sequence where we interleave cooling and probing. First, the ion is cooled for 160 μs (pump beam and cooling are on, probe beam is off), then cooling is turned off (pump beam off) and after 10 μs, the probe beam is turned on for 20 μs, during which fluorescence is collected, and after another 10 μs the cycle repeats. Fluorescence collected this way is plotted in (Fig.6-7a) as a function of the magnetic field (2-photon detuning) for cooling in the Raman-Doppler regime. Comparison with the fluorescence spectrum where cooling photons were collected (Fig.6-7b) reveals a much more pronounced cooling dip and fluorescence approaching

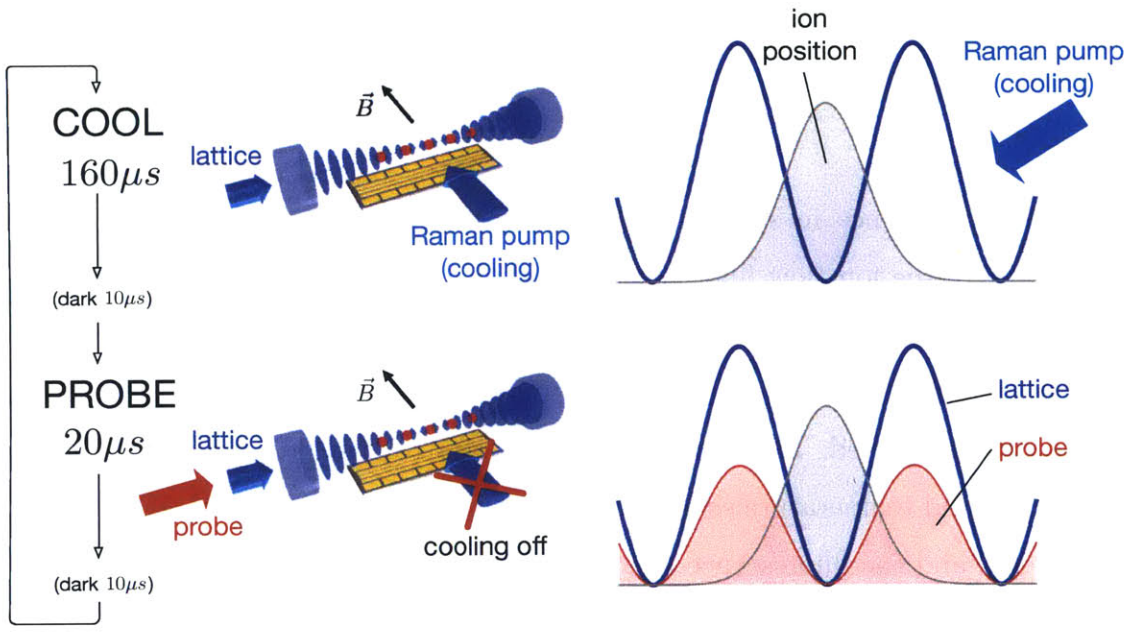

Figure 6-6: Experimental sequence to measure the temperature of an ion centered at a lattice site, using a near-resonant standing-wave probe in the cavity. The probe (red) is scattered at a rate proportional to the width of the ion's position distribution, shown in gray. The Raman pump beam, which closes the cooling cycle, is shut off during the probe period of 20 μs when probe fluorescence is recorded.

constant values corresponding to large temperatures for large 2-photon detunings on the cooling and heating sides. For low fluorescences, such as observed around the cooling dip, the probe fluorescence divided by largest fluorescence observed can be interpreted as k_BT/U, as explained below.

The position distribution of an ion in a thermal state is assumed to be a Guassian at an optical lattice site locally approximated as a harmonic oscillator with vibrational frequency $\omega_L = \frac{2\pi^2 U}{ma^2}$ where $a = \lambda/2$ is the lattice constant:

$$p(x) = \frac{1}{\sqrt{2\pi\sigma_x^2}} exp\left(-\frac{x^2}{2\sigma_x^2}\right) \tag{6.16}$$

The width of this distribution depends on temperature:

$$\sigma_x^2 = \frac{k_BT}{m\omega_L^2} \tag{6.17}$$

which results from the application of the equipartition theorem to the harmonic oscil-

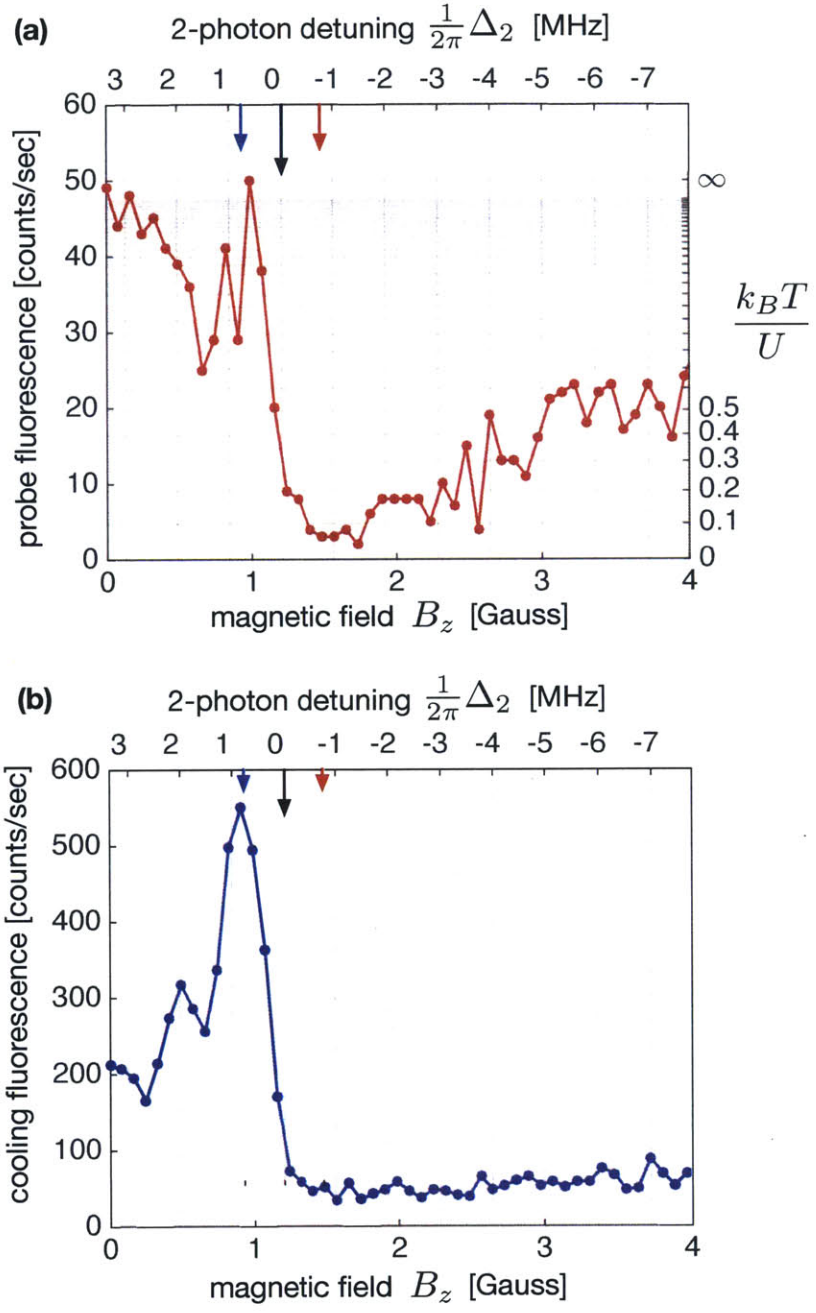

Figure 6-7: Probe fluorescence (top) and pump fluorescence (bottom) as the magnetic field (2-photon detuning) is scanned. The probe fluorescence is converted to temperature on the second vertical axis on the right, showing cooling deep into the optical lattice ($k_B T/U \approx 0.05$) at 2-photon detunings around the first-order and second-order red vibrational sidebands. (The blue, black and red arrows indicate detunings corresponding to the first-order heating sideband, the carrier, and the first-order cooling sideband, respectively.)

lator: $\langle \frac{1}{2} m\omega_L^2 \rangle = \frac{1}{2} k_B T$. The fluorescence as a result of probe beam scattering varies sinusoidally with the ion's position as

$$f(x) = f_0 \frac{1}{2}(1 - cos(2\pi x/a)) \tag{6.18}$$

where f_0 is the fluorescence at the antinode. The mean fluorescence given off by the ion is therefore

$$\begin{aligned} \langle f \rangle = \int_{-\infty}^{+\infty} p(x) f(x) dx &= f_0 \frac{1}{2}\big(1 - exp(-2\pi^2 \sigma_x^2/a^2)\big) \\ &= f_0 \frac{1}{2}\big(1 - exp(-k_B T/U)\big) \end{aligned} \tag{6.19}$$

This dependence of observed fluorescence on temperature is plotted in Fig.6-8. The fluorescence is linear in $k_B T/U$ for small temeratures and saturates at $\frac{1}{2} f_0$ at large temperatures. Expanding the expression for small $k_B T/U << 1$ in fact gives the fluorescence relative to the largest observed fluorescence $f_{max} = \frac{1}{2} f_0$ as

$$\langle f \rangle / f_{max} = k_B T/U \tag{6.20}$$

Based on this, the coldest point in the spectrum shown in Fig.6-7 gives $k_B T/U \approx 0.04$ - a value that can be routinely achieved in the system. For the lattice depth of $U = 2\pi\hbar \times 18$ MHz used in the measurement shown, this corresponds to a mean vibrational quantum number $\bar{n} \approx 0.5$. With a slightly different scheme for cooling and temperature measurement, and under optimized cooling conditions, a mean vibrational quantum number as low as $\bar{n} = 0.1 \pm 0.1$ has been achieved, as reported in our publication in reference [16]. This represents the preparation of an ion near its motional ground state in an optical lattice site.

Note that his temperature measurement is performed with the ion stationary at a lattice minimum; it breaks down for other ion positions. In friction experiments, where the ions are driven across the lattice, the effective time-averaged temperature was found to increase slightly, as determined by comparing observed friction forces

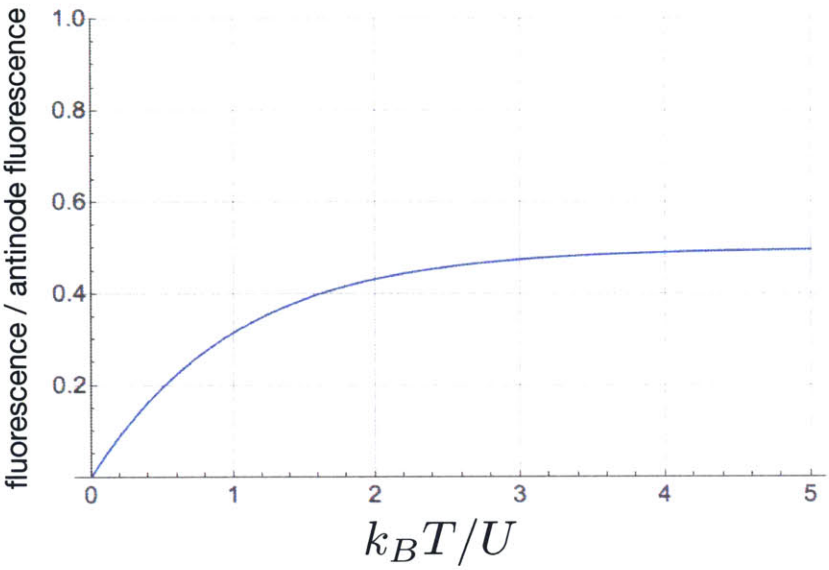

Figure 6-8: Expected dependence of probe scattering on temperature for an ion at a lattice minimum.

with Langevin simulations of the dynamics at finite temperature (see chapter 15).

6.5 Tuning temperature

Ion temperature depends on the balance of the laser cooling power and heating power from ambient electrical and optical noise. Deliberately increasing noise in the system leads to a higher temperature (which can be measured with the technique discussed in the previous section). We use two different ways to increase the ion temperature to study its effect on friction (chapter 15). One way is to increase recoil heating due to photons scattered from the Raman pump beam by introducing a π-polarized component to it via rotation of a quarter-waveplate. Another way is to "tickle" the ion by weakly modulating the lattice intensity via an acousto-optical modulator (also used for tickle spectroscopy as discussed in section 5.2). These two methods allow us to introduce noise in a controlled way to tune the temperature from $k_BT/U \approx 0.04$ in the absence of additional noise, to $k_BT/U \approx 1$ where our temperature measurement saturates (see Fig.6-8).

Chapter 7

Imaging and fast, subwavelength position tracking

A key ingredient in the trapped-ion optical-lattice emulator, particularly for atom-by-atom friction studies, is the microscope, i.e. the ability to 1) Image individual ions in the optical lattice; 2) measure their positions with sub-lattice-site (sub-wavelength) resolution; 3) track the position with time resolution faster than the relaxation time scales.

Imaging individual ions spaced by several micrometers in a chain can simply be done by diffraction-limited optics and a camera. To achieve fast time resolution on the scale of 1 ms or shorter, photomultiplier tubes (PMTs) are used instead of the camera (see Fig.7-1). To achieve subwavelength spatial resolution, two methods were employed in this thesis work. The first method is to split an ion's image between two PMTs and track the difference in detected fluorescence - a single-PMT version of this was used in our work [16] first demonstrating the cooling and trapping of a single ion in an optical lattice. The second method is to infer each ion's position from the fluorescence it emits, which is modulated by the ion's position with respect to a lattice period due to a position-dependent carrier scattering in our Raman cooling scheme (see chapter 6). In other words, the wavelength-scale structure of the lattice itself is used to probe the ion's position. This method gives a significant improvement in the signal-to-noise ratio, and scales better to ion numbers larger than 1, so we

subsequently used this method for all the studies of friction between the ions and the lattice.

7.1 Imaging setup

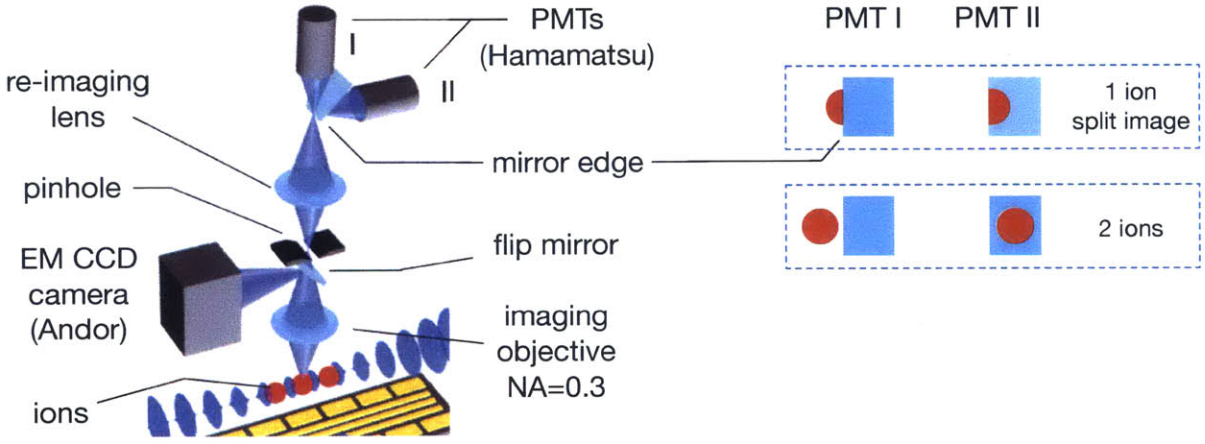

Figure 7-1: Ion imaging system. Two modalities of ion position tracking are shown on the right. The split-image modality can be used to measure the position of a single ion with subwavelength resolution by averaging the normalized difference signal from the two PMTs each observing one half of the ion's image, split by a sharp mirror edge. The position-dependent fluorescence modality gives a position resolution improvement by 2 orders of magnitude and allows measuring the positions of two ions simultaneously.

A summary of the imaging setup is shown in Fig.7-1. The ions are imaged to infinity by an aberration-corrected commercial objective (FAC30125-A from Thorlabs) outside the vacuum chamber, with numerical aperture $NA \approx 0.3$ and working distance of $\approx 10cm$ matched to its focal length. A field lens (Thorlabs LA4246-UV) immediately after the objective re-focuses the image with a magnification of 3.7 either onto the electron-multiplying CCD camera sensor, or onto a plane where a 25μm-diameter pinhole rejects stray fluorescence before getting re-imaged by another lens onto a sharp mirror edge that splits the image between two PMTs for detection. (The re-imaging lens is a conjugate achromatic matched lens pair from Thorlabs, MAP1075150-A, which magnifies the image by another factor of 2 with object and image focal lengths 75 and 150 mm respectively.) The roughness of the sharp mirror edge (obtained by breaking the mirror) was verified under microscope to be below 10

μm. The resolution of full imaging system was experimentally determined to be at $\Delta x_{res} = 1.8$ μm for the FWHM of the Airy disk - limited by aberrations to be a factor of 2.6 above the diffraction limit of 0.68 μm for the 369 nm fluorescence wavelength. This was determined using split-image position detection of an ion driven at a known amplitude (see next section).

7.2 Split-image position detection

The mirror with the sharp edge can be used to split the image of a single ion in half and send the two halves to the two PMTs (Fig.7-1). If $I(x - x_{ion})$ is the one-dimensional intensity profile of the image of the ion at position x_{ion}, then the signals detected by the two PMTs are $s_1 = \int_{-\infty}^{-x_{ion}} I(x)dx$ and $s_2 = \int_{-x_{ion}}^{+\infty} I(x)dx$. A balanced fluorescence signal, obtained as

$$s = \frac{s_2 - s_1}{s_2 + s_1} \tag{7.1}$$

can then be used to track the center position of the ion. For displacements of the ion image x_{ion} from the balanced point $s = 0$ much smaller than the width of the ion image,

$$\begin{aligned} x_{ion} &\approx s \times \left(\frac{\partial s}{\partial x_{ion}}\bigg|_{x_{ion}=0} \right)^{-1} \\ &= s \times \left(\frac{2I(0)}{I_T} \right)^{-1} \end{aligned} \tag{7.2}$$

where $I(0)$ is the peak 1D intensity of the ion image and I_T is the integrated total signal in the image. This gives the conversion from the observed balanced signal s from the PMTs to ion position x_{ion}. For a fixed total fluorescence from the ion (I_T), the sensitivity of this ion position detection $2I(0)/I_T$ is inversely proportional to the imaging system resolution; in fact $I(0)/I_T \sim \Delta x_{res}^{-1}$ with a prefactor of order unity that depends on the lineshape of $I(x)$. This gives a rough scale for the balanced signal as

$$s \sim \frac{1}{2} \frac{x_{ion}}{\Delta x_{res}} \tag{7.3}$$

Under ideal conditions, this signal is limited by photon detection shot noise and the minimum resolvable balanced signal is $\Delta s = \frac{1}{\sqrt{N}}$. This gives an ion position resolution of

$$\Delta x_{ion} \sim \frac{2\Delta x_{res}}{\sqrt{N}} \tag{7.4}$$

Thus, position resolution scales as the inverse of the integration time, $\Delta x_{ion} \propto t^{-1/2}$, reaching after sufficiently long integration arbitrary position resolution. In our publication [16], a position resolution substantially finer than the 369 nm wavelength was reported with this method, $\Delta x_0 = \lambda/40$.

7.3 Position detection via lattice-modulated fluorescence

The scale of ion position resolution in the split-image method in equation 7.4 is set by the aberration-limited imaging system resolution $\Delta x_{res} = 1.8\mu$m, which would be the ion position resolution upon the detection of a single photon. If instead the cavity standing wave is used to detect ion position, the position scale is roughly set by half the optical lattice period $a/2 = 92nm$. Consider carrier scattering fluorescence $f(x_{ion})$ in the Raman cooling scheme from chapter 6. It dominates the ion fluorescence and varies sinusoidally with the ion position relative to the lattice between zero and f_{max} with nearly perfect contrast. The maximum sensitivity of fluorescence to position is achieved half-way on the slope of a lattice site, where

$$\frac{\partial f(x_{ion})}{\partial x_{ion}} = \frac{\pi}{a} f_{max} \tag{7.5}$$

With detected fluorescence fluctuations limited by photon shot noise, the minimum resolvable fractional fluorescence difference is given by $\Delta f/(\frac{1}{2}f_{max}) = \frac{1}{\sqrt{N}}$, resulting in

$$\Delta x_{ion} = \frac{a/(2\pi)}{\sqrt{N}} \tag{7.6}$$

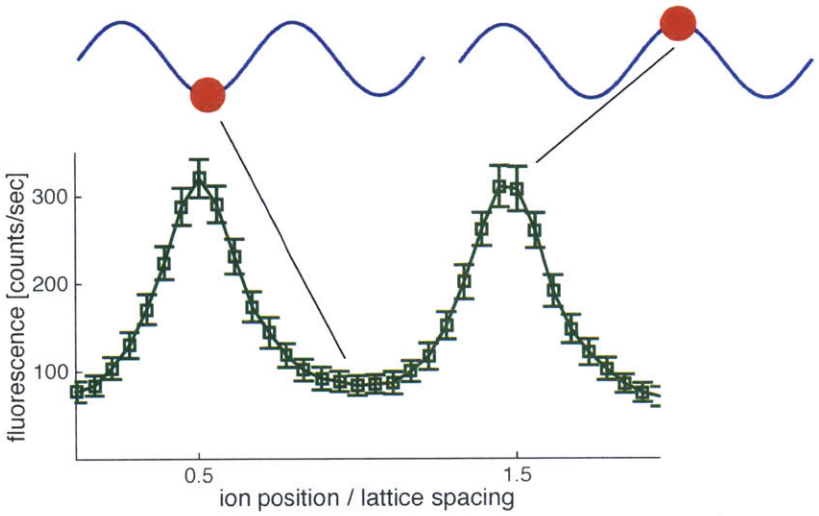

Figure 7-2: Fluorescence signal that reveals an single ion's position as it is moved through the lattice. At few hundred detected photon counts per second, the signal-to-noise ratio was obtained after only a few seconds of integration per point. Note that the shape of the signal is distorted from sinusoidal because the ion slips to a different local minimum before reaching the cavity maximum (see part II of this thesis).

Comparing this to equation 7.4 gives an ion position resolution for this method 123 times better than for the split-image method for equal integration times. In fact, using the cavity standing wave for ion position imaging is a type of super-resolution microscopy.

In addition, this method has several other advantages over the split-image method: it does not suffer from vibrations or drift of the imaging system, and scales better for multiple ions. In particular, the positions of two separate ions in an ion crystal can be tracked at once using the two PMTs which both had to be utilized for tracking a single ion in the split-image method (see Fig.7-1). This is important if correlation between the motion of different ions is of interest.

7.4 Time-resolved experiments

The fluorescence that reveals an ion's position is detected by PMTs with very fast time resolution and recorded using custom FPGA counters at sampling rates up to a few hundred megasamples per second (limited by the FPGA clock speed). Typical

experiments are performed at a 1 kHz repetition rate, and photons detected during each experiment fall into appropriate time bins with respect to the experiment start trigger. The experimental cycle can be divided into up to 300 bins, limited by the number of resources on the FPGA chip. This setup allows us to resolve the fastest time scales of ion motion and thermalization (including the RF micromotion frequency, which we also detect with this setup for compensation in the direction parallel to the trap).

Chapter 8

Long-lived lattice-site trapping of an ion

The combination of time-resolved split-image detection of ion position and Raman sideband cooling enabled us to demonstrate first long-lived localization of a single ion in an optical lattice site [16]. The initial experiment involved driving the ion with a time-varying electric field of varied frequency, which in the absence of the optical lattice moved the ion with an amplitude of two optical lattice sites in an axial Paul trap potential with vibrational frequency of $\omega_0 = 2\pi \times 130$ kHz. In the presence of an optical lattice with depth $U/h = 40$ MHz and a fast enough driving frequency (with period between 10 ms and 31 μs), we observed that ion motion was suppressed to an amplitude consistent with zero within a ± 20 nm experimental error after averaging a sufficient number of experimental repetitions (see Fig.8-1). At lower driving frequencies (100 ms period), only partial suppression of ion motion and a phase delay were observed, since thermal hopping was sufficiently fast to enable the ion's position distribution to follow the displacement of the axial Paul trapping potential. To find the time scale at which thermal hopping limits the lifetime of an ion at an optical lattice site, we varied the drive frequency and measured the amplitude of the driven ion motion. Fig.8-2 shows the best repeatedly observed amplitude suppression for each frequency, from which we infer an approximate lifetime on the order of 0.1 s, corresponding to an amplitude suppression of the driven motion by 30%.

In more recent experiments, where position was measured via position-dependent fluorescence in the lattice, thermal hopping across a lattice barrier was measured as a function of the barrier height. The ion would first be initialized in a lattice site, and then a force would be applied quickly to tilt this potential and lower the barrier separating the ion from the global minimum to a desired value. The ion would then be allowed to relax across this barrier, with its fluorescence decaying over time to the global minimum value (Fig.8-3). The fitted exponential time constant of this decay can be interpreted as the thermal activation or thermal hopping across the energy barrier. Thermal hopping time versus the height of the energy barrier was measured for several temperatures, and the results are shown in Fig.8-4. The dissipation time scale $\tau_c = \gamma^{-1}$, which is the time for an ion to be recooled after slipping across a barrier, can be found as the intercept of these curves with the $U_B = 0$ axis where the barrier height is zero. This measurement is the most direct measurement of the thermal relaxation time scales in the system, critical for understanding the thermal dynamics and velocity dependence of friction, discussed in chapter 15.

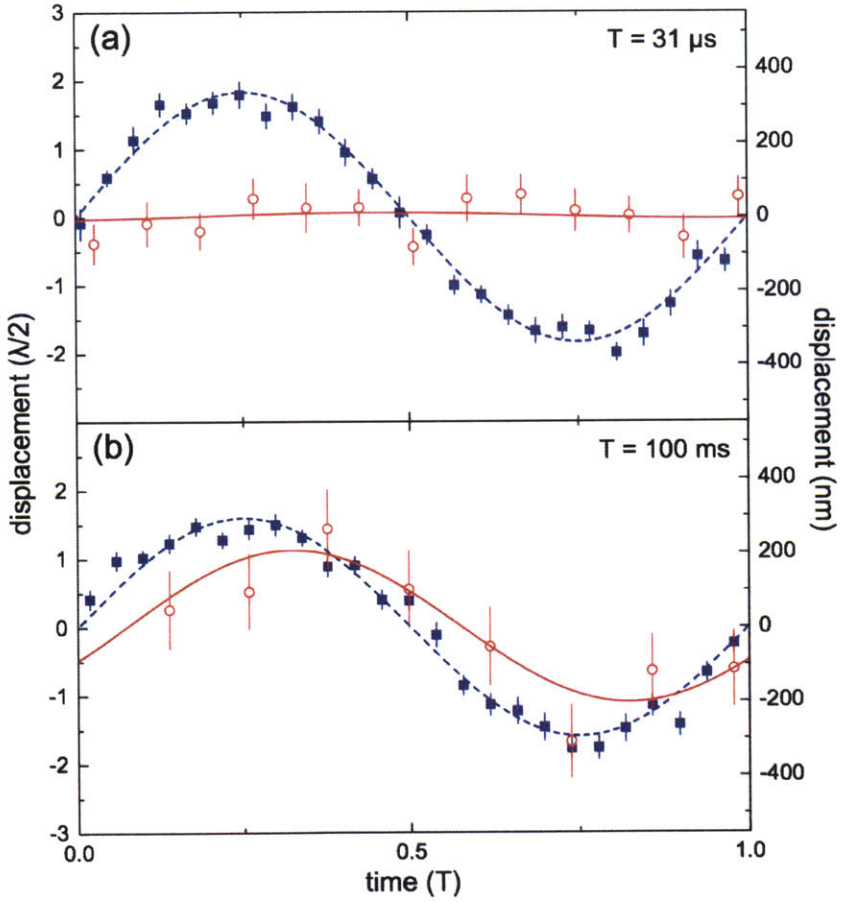

Figure 8-1: Ion displacement by a periodic electric field in units of the lattice site spacing, $\lambda/2 = 185$ nm, without optical confinement (squares) and in an optical lattice (circles). (a) The modulation with a period of T = 31 μs was applied for averaging durations of 150 s and 300 s respectively. The lines represent sinusoidal fits yielding amplitudes of $A = (340 \pm 10)$ nm in the Paul trap and $A^{(ol)} = (10 \pm 20)$ nm in presence of the optical lattice, respectively. (b) Corresponding measurements for a modulation period of T = 100 ms. The fit yields $A = (300 \pm 10)$ nm, $A^{(ol)} = (200 \pm 40)$ nm and a phase delay $\Delta\phi = (25 \pm 11)^\circ$ of the driven motion in the lattice.

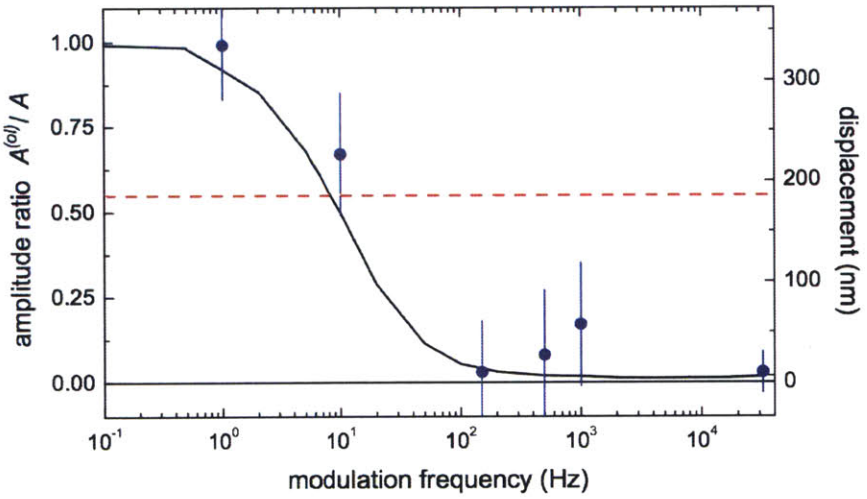

Figure 8-2: Normalized ion oscillation amplitude in the lattice, $A^{(ol)}/A$, as a function of the modulation frequency. The dashed line represents a displacement of $\lambda/2$. The results of a numerical simulation for the optical pumping rate of $\Gamma_p = 0.1\ \Gamma$ and a temperature $T \approx 250\ \mu$K are shown as a solid line.

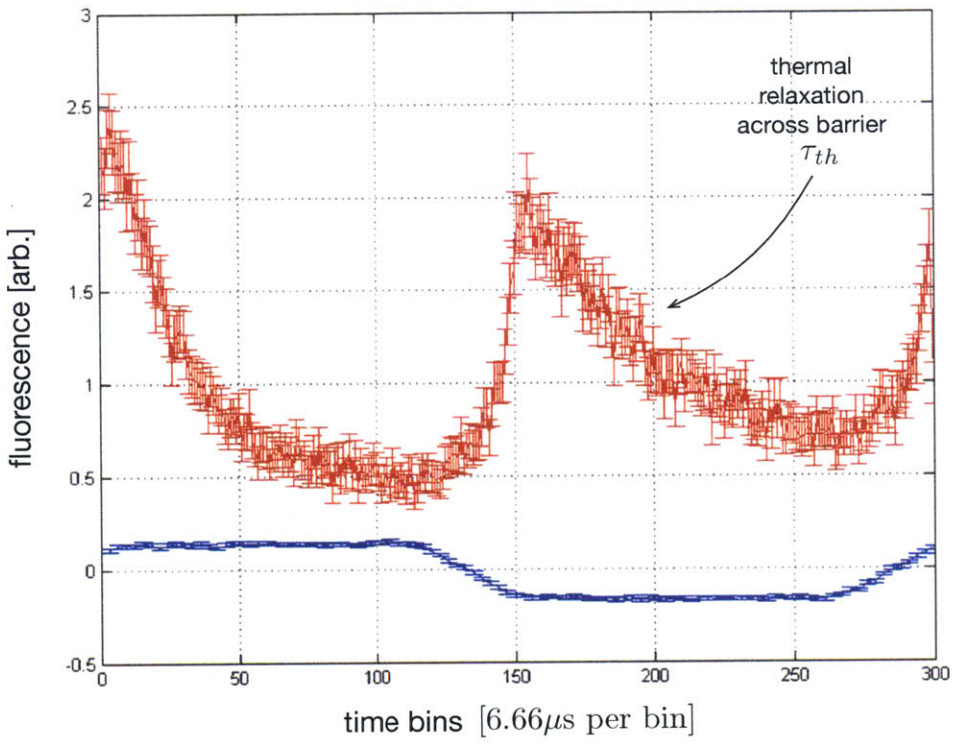

Figure 8-3: Measurement of thermal hopping time scale of an ion across an energy barrier of controlled height. The blue curve shows the experimentally measured position of the ion in the absence of an optical lattice. With the lattice on, the red curve is Raman pump fluorescence that indicates ion position relative to the lattice and its temperature. The ion is first initialized in a lattice site (0-120), then the potential is tilted to move the ion up the lattice slope (hence the increased fluorescence) and reduce the energy barrier to a desired value (120-150), then the ion thermally relaxes across the barrier during the wait time (150-270).

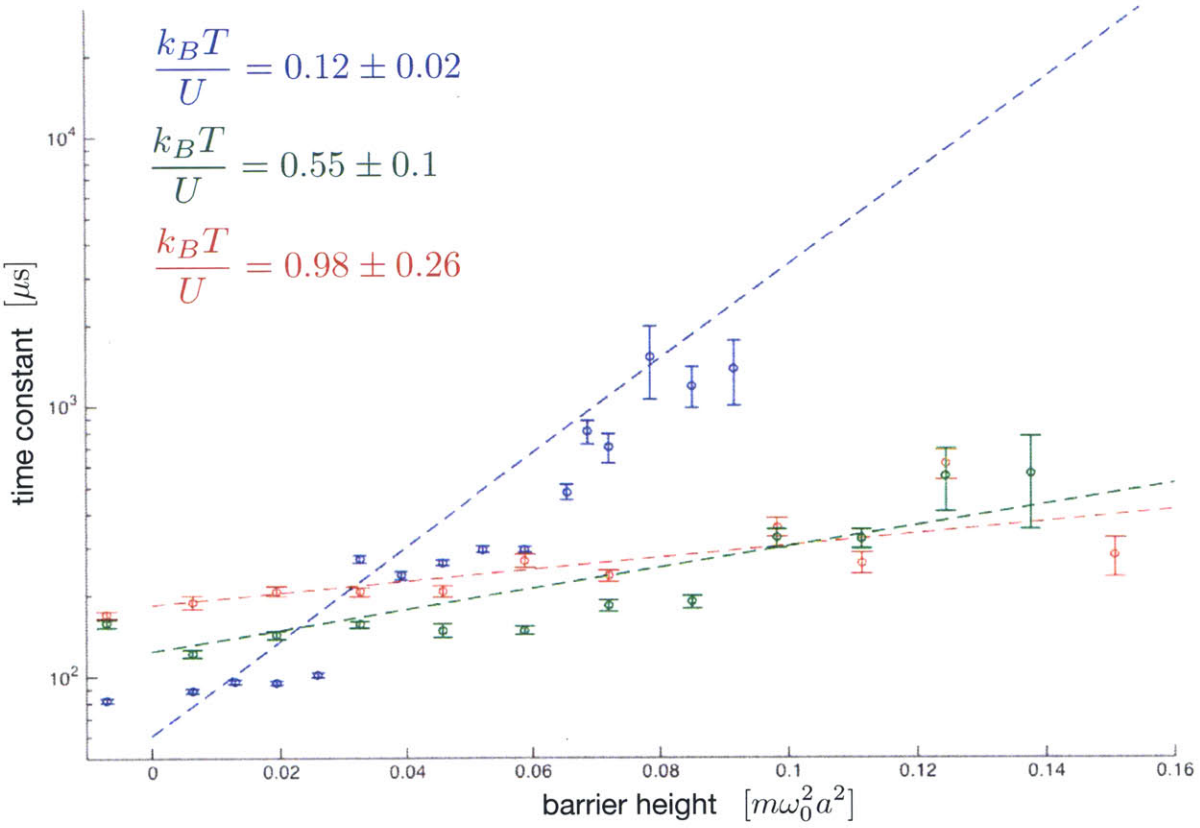

Figure 8-4: Measured thermal hopping time versus barrier height for three different temperatures. At the coldest temperature, an ion lifetime in a single lattice site (no tilt) can be extrapolated to yield ~100 ms, consistent with amplitude suppression measurements in Fig.8-2.

Part II

Friction and Surface Physics

Chapter 9

Friction from the macro-scale to the nano-scale: an introduction

Friction is the ubiquitous phenomenon of a non-conservative force resisting the motion of two objects relative to each other, of energy dissipation during such motion, and of the often associated surface wear. According to some estimates [51], about 6% of the gross national product is wasted due to frictional energy dissipation and wear (e.g. due to engine inefficiencies), which constitutes 1 trillion dollars annually in the USA today. Clearly, this is a problem of enormous technological and economic importance. Yet our ability to control friction remains modest, and our knowledge of it largely empirical. This is not surprising: at the macroscale, it is a complex emergent phenomenon. However, even at the atomic scale, friction is not yet fully understood. It is a highly nonlinear many-body problem, and friction happens at an interface between two objects, which is sandwiched between them hidden from access by experiments. Wolfgang Pauli nicely summed up the difficulty of studying friction, when he said "God made materials, but surfaces were the work of the Devil".

The commonly known phenomenological laws of macroscopic friction date back to Leonardo Da Vinci (1452-1519), Amontons (1663-1705) and Coulomb (1736-1806):

1. Friction force is directly proportional to the applied (normal) load.
2. Friction force in independent of the apparent contact area.
3. Friction is independent of the sliding velocity.

The proportionality of friction to normal load F_N and independence on the contact area and velocity can be summed up in the well-known formula

$$F_f = \mu F_N \tag{9.1}$$

where μ is an empirical material-dependent coefficient of friction.

It is now well understood that the first two laws arise from the multi-scale roughness of surfaces. Only a small fraction of the apparent contact area is actually in contact, and the contacts are made by a multitude of asperities at various length scales [51, 52, 53, 54, 55] (Fig.9-1). The friction force is proportional to the sum of all atomically smooth contact areas, which change under varying contact pressure as a result of elastic deformations of asperities. The mean contact pressure is given by the normal load divided by the true area of contact, and in the linear deformation regime this area, and consequently the friction force, will vary linearly with the normal load. The independence of friction on the apparent contact area naturally comes out of this picture: any increase in the apparent area is compensated by the decrease in the contact pressure, which reduces the contact area of each asperity, compensating for the increased number of asperities, and friction does not change.

Because of the crucial role of asperities as the fundamental elements determining macroscopic frictional behaviour, it is natural to ask about the frictional behaviour of a single asperity or a small collection of asperities in atomically smooth contact with a substrate - this is the domain of nanotribology, or nanofriction. At the level of a single atomically smooth contact, do the three phenomenological laws for macroscale friction apply? In other words, how does friction depend on the strength of interaction between an asperity and a substrate surface ("normal load"), on the number of atoms at the contact ("contact area") and on the relative velocity of the asperity and the substrate? As we shall see, at the atomic scale, the question of velocity is intimately connected to the thermal dynamics of the system and thus also becomes the question of temperature. Furthermore, studying friction at the atomic scale is posed to answer a fourth question only addressed empirically at the macro-scale,

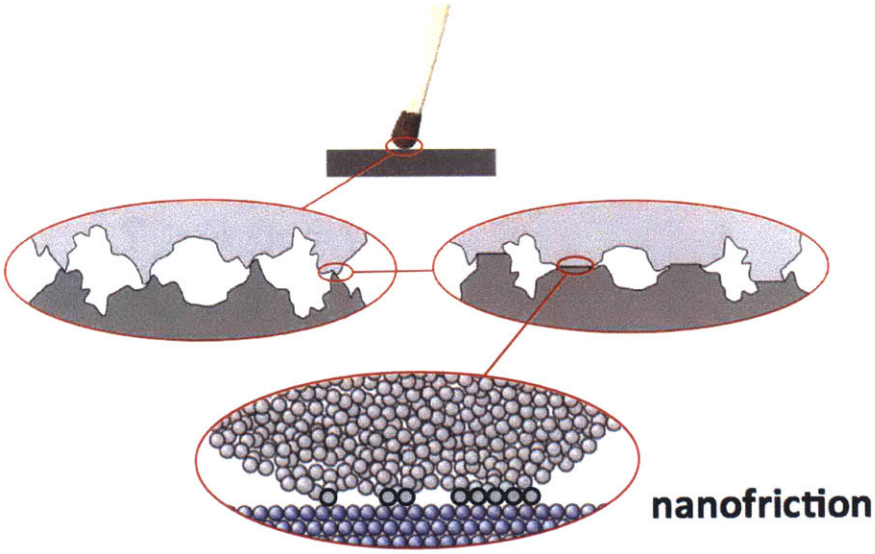

Figure 9-1: Multiscale roughness of contacting surfaces means that as we zoom in on an apparent contact at the end of an asperity, we find many asperities and contacts on a smaller scale, and so on until the atomic scale. The study of friction at the level of atomically-smooth contacts is known as nanotribology or nanofriction.

related to the material-dependent coefficient of friction μ: how does the structure of the nanocontact affect friction, and how does any structure effect depend on the contact size? For example, does the concept of incommensurability survive for finite, few-atom contacts? Thus, I present the four "pillars" of friction (Fig.9-2) - the four questions that I will address in this part of my thesis in the context of nanofriction, using our trapped-ion optical-lattice friction microscope:

1. Normal load. How does nanofriction depend on the normal load or substrate interaction strength? (chapter 12)

2. Material properties. How does nanofriction depend on the structural properties of the interface at the atomic scale? (chapter 13)

3. Contact area. How does nanofriction and the effect of structure depend on the size of an atomically smooth contact (true contact area)? (chapters 12, 13 and 14)

4. Velocity & temperature. How does nanofriction depend on sliding velocity and temperature? (chapter 15)

At the nanoscale, the dominant form of friction is stick-slip friction. Stick-slip friction is a non-linear phenomenon where two surfaces stick due to a static friction

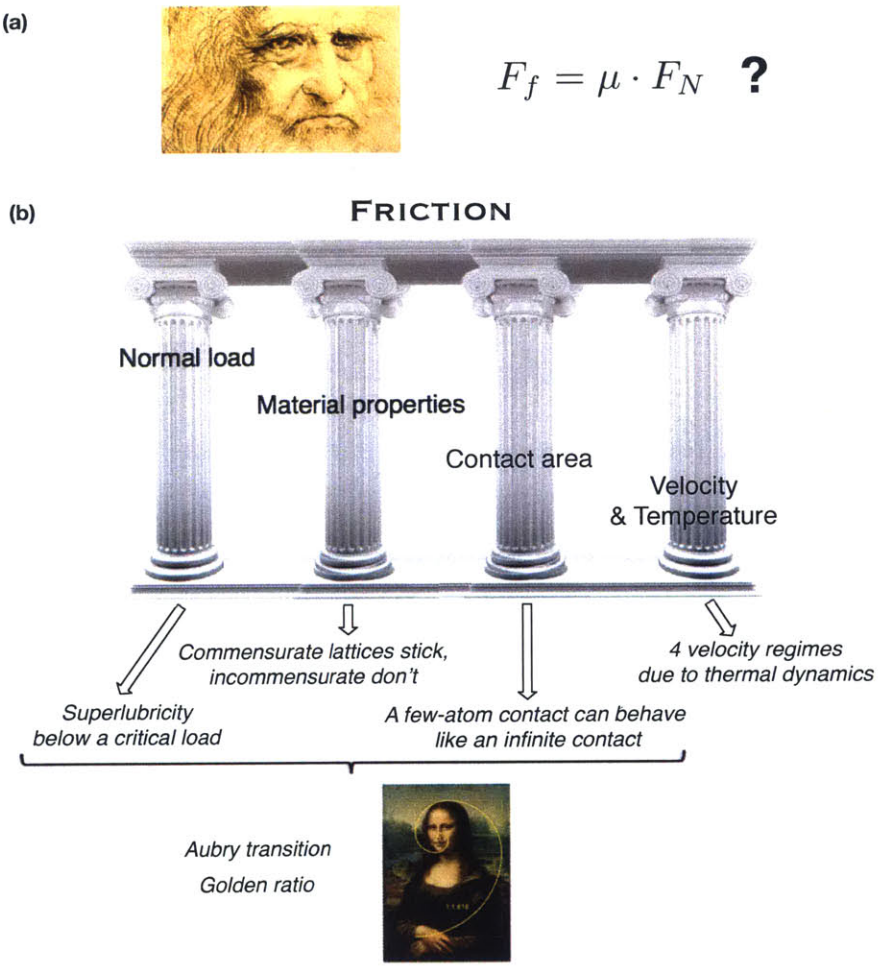

Figure 9-2: **(a)** The study of friction, also known as tribology, dates back to Leonardo Da Vinci, who first postulated the well-known empirical law that friction is proportional to the normal load on the surface. Does it apply at the atomic scale? We shall see in this part of my thesis that it doesn't. **(b)** The 4 pillars of friction, which can be used to organize the studies of friction, both at the macroscale and at the nanoscale. Below each pillar is summarized the key finding from experiments in the trapped-ion optical-lattice frictional interface. The first three are related to the Golden ratio (Da Vinci again!), and the Aubry transition, which we observe for the first time in our system).

force and accumulate potential energy under increasing applied shear force, then slip suddenly, releasing this energy as kinetic energy. As the released energy is dissipated, the surfaces stick again and the process repeats. Meanwhile, the large amount of released energy can cause surface damage known as wear. The stick-slip phenomenon turns out to be very general and spans many orders of magnitude from the nanometer length scales of biological molecules and atomic contacts [56, 57, 58] to the kilometer scales of earthquakes [59]. At familiar length scales stick-slip manifests in the familiar concepts of static friction and kinetic friction. To get an object at rest on a surface to move, one must apply a critical shear force known as the static friction force F_s. Once the object is moving, the force resisting motion is known as the kinetic friction force F_k, which is generally smaller than the static friction force $F_k < F_s$. The action of the kinetic friction force over the slip distance gives the dissipated energy:

$$\Delta W = F_k * \delta x_{slip} \tag{9.2}$$

At the atomic scale, a number of minimalistic models have been invoked to model stick-slip friction. The simplest is the single-atom model proposed by Prandtl and Tomlinson (PT) in 1928 and 1929 [60, 61]. In this model, a single atom at the tip of an asperity, held in the harmonic confining potential of this asperity, is driven across a sinusoidal potential of a rigid substrate crystal (Fig.9-3a). The PT model can also be applied to a multi-atom contact, assuming that each contact atom experiences a harmonic confining potential due to the mean field from the rest of the contact-layer atoms, or in the limit where interactions between contact-layer atoms are much weaker than the interactions with the substrate potential and the attachment to the bulk of the asperity. As we shall see in chapters 12-14, the PT model remains valid for multi-atom contacts even if the contact-layer atoms interact strongly with each other, as long as their spacing is matched or nearly matched to the lattice constant of the substrate. The PT model, however, fails to capture the effects of structural mismatch between the crystal of contact-layer atoms and the substrate crystal. A many-particle model, proposed by Frenkel and Kontorova (FK) in 1938 [62, 63], instead treats the contact

layer as an independent, infinite chain of atoms joined by springs (Fig.9-3b). Friction in this model is governed by the commensurability of the unperturbed chain and the substrate, and exhibits non-trivial dynamics due to kinks and other solitons [63], as well as many-body static and dynamic phenomena, such as the pinned-to-sliding phase transition predicted by Aubry in 1983 [64], and the related superlubricity - the vanishing of stick-slip friction [65]. Since nanocontacts have a finite number of contacting atoms and the mutually interacting contact-layer atoms are also attached to their asperity, the Frenkel-Kontorova-Tomlinson model (FKT) - a combination of PT and FK - is more appropriate for nanofriction (Fig.9-3c). As we shall see in chapter 10, we implement and study this model in our trapped-ion optical-lattice synthetic friction interface. In the context of these models, normal load can be interpreted as the depth of the substrate potential, the true contact area as the number of atoms in the chain, and the questions of material properties and interface structure reduce to the spacing mismatch between the atomic chain and the substrate.

Sensitive nanotribology apparatuses [67, 68, 69, 66, 70, 71], and in particular atomic force microscopy [67], are able to measure tiny shear forces and atomic-scale slips between atomically smooth surfaces comprising down to a few atoms [72, 66, 70]. This has enabled the observation of superlubricity of a nanocontact below a critical normal load [73] and at orientations of the contacting crystal lattices that result in mismatch [74, 75]. Most experimental observations of stick-slip in these systems can be qualitatively explained via variants of the PT or the FK models, but without direct access to the microscopic parameters or dynamics [76]. For example, the depth of the substrate potential and the asperity stiffness have to be inferred, the number of atoms at the nanocontact is usually not known, and the behaviour of individual atoms is not resolved. Velocity and temperature dependence of friction have also been studied [77, 78, 79, 80, 80, 81, 82, 83], but the experimental results have thus far not yielded a consistent picture that can be unambiguously linked to microscopic models [84, 85, 86, 87, 88].

One way to peek at individual-particle behaviour in friction, with independent control over the microscopic parameters, is by studying a synthetic frictional inter-

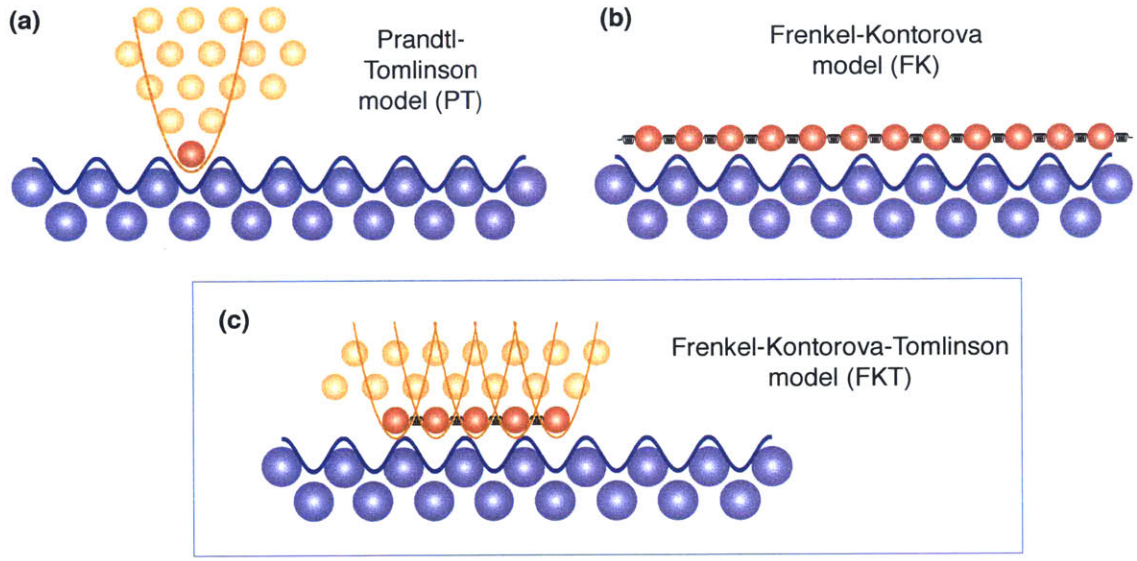

Figure 9-3: **Atomistic models of friction.** **(a)** The Prandtl-Tomlinson model is often invoked to interpret experimental results in single-asperity nanotribology with atomic force microscopes [66]. **(b)** The Frenkel-Kontorova model involves an infinite atomic chain on a substrate and can be used to understand some aspects of friction, such as commensurability of contacting surfaces. The physical situation of an independent chain, however, is perhaps more appropriate for the problem of adsorbed monolayers or long biomolecules on an ordered substrate surface. **(c)** The generalized Frenkel-Kontorova-Tomlinson model is a combination of the other two, involving a finite chain with additional external confinement by the asperity. It is most appropriate for modeling nanofriction, and also our trapped-ion optical-lattice frictional interface.

face - a nanofriction "simulator". One such interface, implemented with colloidal polystyrene beads on water and in an optical lattice, has confirmed some dynamical aspects such as the propagating kinks predicted by the FK model [89], and a number of other experiments have been proposed in this system [90]. The ultimate synthetic frictional interface, however, involves real atoms as opposed to macroscopic particles, and following a number of recent proposals [91, 92, 93, 94], we have implemented in this thesis a synthetic nanofriction interface using trapped atomic ions in an optical lattice [17] (chapter 10) able to resolve the stick-slip motion of the individual ions (chapter 11).

I will describe in this part of my thesis the experimental findings about nanofriction obtained from our trapped-ion optical-lattice interface, which can be summarized with regards to the 4 pillars of friction in Fig.9-2 as follows:

1. Below a critical normal load (lattice depth), superlubricity occurs (stick-slip friction vanishes).
2. Commensurate crystals stick, and incommensurate crystals don't - leading to structural superlubricity.
3. A few-atom contact can behave like an infinite-atom contact in the manifestation of structural superlubricity.
4. Four regimes of velocity-dependence of friction can be observed as a result of separated time scales of thermal dynamics.

Our results represent the first atom-by-atom demonstration of these four elusive effects. Furthermore, they represent the first observation of the Aubry transition - a structural transition of a Golden-ratio chain on a surface (chapter 14). Perhaps the most valuable lesson learned, is that all of these effects, some of which have traditionally been assumed to arise from many-body interactions (e.g. the Aubry transition), emerge already at the level of a few atoms - the size of the smallest asperities, the collective behaviour of which determines macro-scale friction. Therefore, perhaps some of the findings can be applied to engineer friction between materials - both at the nanoscale and at the macro-scale.

Chapter 10

Trapped-Ion Optical-Lattice Nanofriction Interface

10.1 A complementary system to condensed matter interfaces

In our system, we measure, atom-by-atom, friction between a trapped crystal of Yb^+ ions and the corrugated potential produced by the optical lattice (Fig.10-1). This idealized frictional interface captures many static and dynamic multi-atom phenomena thought to be of relevance at condensed matter surfaces and in friction processes at these surfaces on the nanoscale. The advantage of our trapped-ion optical-lattice frictional interface is the ability to study these phenomena with unprecedented resolution and microscopic control. For tribologists, our system can be viewed as a physical emulator or simulator of processes at condensed matter interfaces. For physicists, it is a microscope for such processes in an ultimate controlled lab environment. In any case, it can elucidate the mechanisms of friction and instruct ways to engineer materials with desired frictional properties.

In particular, the distinguishing capabilities of our nanofriction emulator/microscope are:

1) *Tracking of individual atoms at a frictional interface.* This is currently not possible

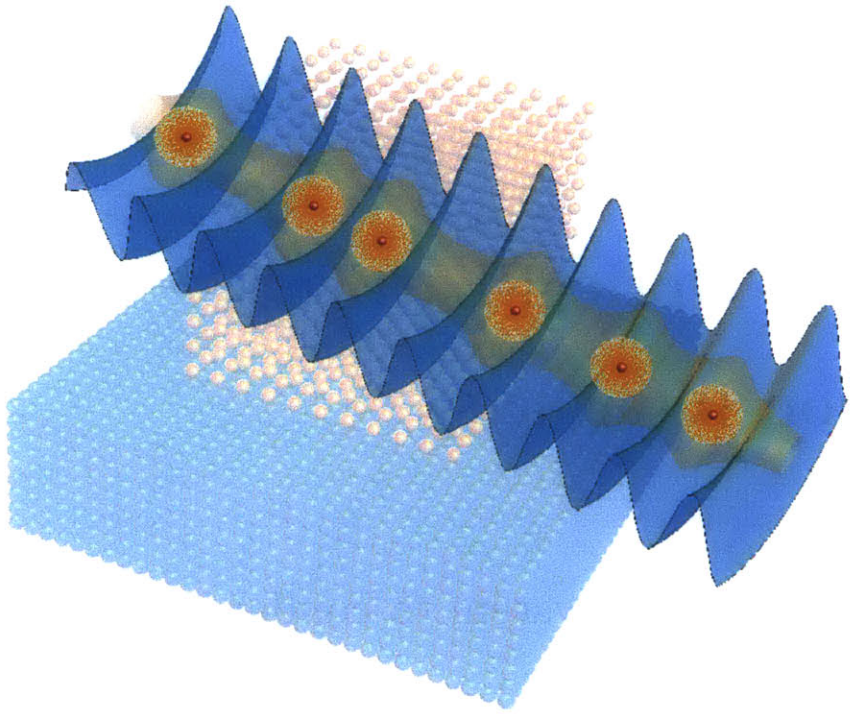

Figure 10-1: A crystal of atomic ions, strongly interacting via Coulomb forces (the object), is rubbed against the corrugated potential of an optical lattice (the substrate) to study, with individual-atom resolution, the physics of nanoscale friction.

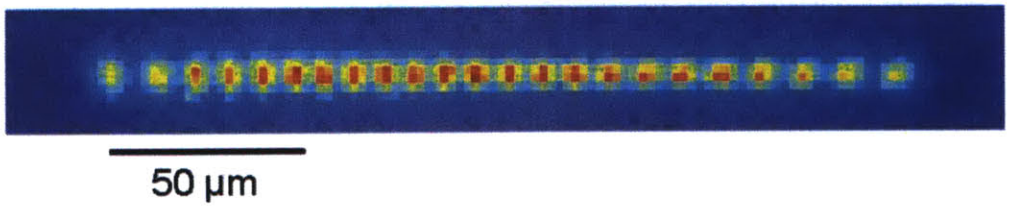

Figure 10-2: An image of a $^{174}Yb^{+}$ ion crystal in vacuum.

at a condensed matter frictional interface, because the interface is buried between the two objects in contact (with the exception of the simplest case where the interface consists of a single atom, which can be tracked with an atomic force microscope). In our system, the "interfacial" atoms form a chain in vacuum, spaced by several micrometers, and can be imaged directly with diffraction-limited optics (see Fig.10-2).

2) *Control of atom number at a frictional interface.* The size of a condensed matter nanocontact cannot be measured directly because of the reason above, and is difficult to infer - as a result, it is usually not known in nanotribology experiments [76]. In our system, a deterministic number of ions up to 10 or 20 can be loaded into the trap and seen directly on the camera [33] (see Fig.10-2).

3) *Control of atomic arrangement at a frictional interface.* Although the relative lattice spacing of two atomic lattices at an extended atomically flat contact can be controlled by choice of material and crystal orientation [75, 74], the arrangement of atoms is usually unknown at an asperity contact, since the asperity can be significantly deformed from the lattice structure of the bulk. This is important, since friction at the macroscale is believed to be governed by the collective behaviour of asperities on multiple length scales [51, 53, 54, 55, 52]. In our system, we can precisely tune the spacing between the ions in a chain to match it or mismatch it to the optical lattice.

4) *Control of interatomic interactions.* Although materials with a desired bulk modulus can be chosen, surface properties might be very different and poorly known, especially at the ends of asperities. In our system, interactions between ions are via Coulomb forces, and can be tuned by adjustments of ion spacings.

5) *Control of temperature and dissipation over a wide range.* Although temperature can be varied in condensed matter experiments, it is technically challenging to make nanotribology apparatuses work over wide ranges of temperature. Dissipation is an intrinsic property of the material, the microscopic mechanism of which is typically unknown [76]. In our system, both temperature and dissipation can be varied by tuning laser cooling parameters.

6) *Time resolution of dynamical processes higher than the fastest dissipation rate.*

Tribology experiments typically cannot time-resolve the dissipation processes. In our cold atom system, dissipation is significantly slower, determined by laser cooling, and we can both resolve it and control it as mentioned above.

7) *Possibility to observe quantum many-body effects.* Friction is typically thought of as a dissipative process far in the classical regime. This is due to the large number of degrees of freedom and fast decoherence rates (dissipation again) in condensed matter. Our cold ions are well isolated from the environment if the laser cooling is turned off, and coherent many-body processes can be observed. Several possibilities are explored in part III of this thesis.

10.2 The Frenkel-Kontorova-Tomlinson model.

Both our system and a condensed-matter nanocontact can be modeled by a generalized Frenkel-Kontorova-Tomlinson (FKT) model [95, 96] (Fig.10-3). In this model, an N-atom chain with an intrinsic spacing d interacts with a sinusoidal potential with lattice constant a and depth U. The model captures the physics of competing length scales and competing energy scales. The intrinsic chain spacing d competes against the lattice spacing a, embodied in the dimensionless ratio

$$r \equiv d(\text{mod } a)/a = (d/a)(\text{mod } 1) \tag{10.1}$$

The stiffness of the chain competes against pinning by the lattice. There are two components to the effective chain stiffness: the "internal" chain springs of stiffness g which couple the atoms together, and the "external" springs of stiffness K which couple the atoms to a rigid support (Fig.10-3c). (This support can be used to drag the atoms across the substrate in a friction scenario.) As a result, two more dimensionless parameters describe the competition of energy scales: the ratio η of maximum lattice curvature to external spring stiffness, and the ratio c of internal to external spring

stiffness:

$$\eta \equiv \frac{2\pi^2}{a^2} U/K = \omega_L^2/\omega_0^2$$
$$c \equiv g/K \tag{10.2}$$

In a nanocontact, the sinusoidal potential U represents the potential due to the atomic lattice of the substrate at its surface. The chain represents an atomic layer in contact with the substrate. The internal chain springs g represent next-neighbour atomic bonds in this contact layer, and the external confinement K corresponds to attachment of this layer to the bulk of the asperity (Fig.10-3a).

In our system, we literally have a chain of atoms (ions) interacting with a sinusoidal potential (optical lattice), resulting in an almost exact implementation of the FKT model (Fig.10-3b). The effective internal springs g between the ions are due to Coulomb forces and are, in fact, long-range (see section 10.3 below). K corresponds to confinement by the ion trap at the common-mode angular frequency $\omega_0 = \sqrt{K/m}$, where m is the mass of an ion. The ions self-organize in this trap at typical spacings d of a few micrometers, an order of magnitude larger than the optical lattice spacing $a = 184.75$ nm. However, the physics is periodic in the lattice spacing a, as evident from equation 10.1. Therefore, it suffices to precisely tune the spacing between the ions with sub-wavelength precision, which is done by controlling K (see section 10.4), while the absolute spacing can be kept significantly larger than a wavelength, allowing us to image this frictional interface with individual atom resolution using diffraction-limited optics (Fig.10-2).

There are two important limits of the FKT model. The limit $N = 1$ corresponds to the Prandtl-Tomlinson (PT) model of a single-atom contact [60, 61] (Fig.9-3a) and it is usually used to model the contact between an AFM tip and the substrate under study in nanotribology experiments [58, 66]. Our system with a single trapped ion is an exact implementation of the PT model. The opposite limit of an infinite chain $N \to \infty$ and no external confinement $K = 0$ corresponds to the Frenkel-Kontorova (FK) model [62, 63] (Fig.9-3b) used to model friction of extended contacts

and adsorbed monolayers among many other systems. As discussed in subsection 10.3 below, our system approaches this limit as more ions are trapped in a chain: as N increases, so does the ratio g/K and the chain stiffness begins to be dominated by the internal springs g rather than external confinement K. In general, our system with finite ion chains and the corresponding FKT model treat the general case of finite N and K, more appropriate for modeling asperities, which are believed to play a key role in macro-scale friction [51, 52, 53, 54, 55], and which have finite stiffness and might be several atoms in extent.

Finally, friction is a dissipative process, which can be modeled as coupling of the chain motion to a thermal bath at temperature T with rate constant γ (Fig.10-3c). Heat generated by friction is dumped to this bath. In a nanocontact, this bath is usually believed to be provided by the bulk vibrational degrees of freedom of the substrate and the asperity, but the detailed mechanism is not understood in condensed matter. In our system, dissipation is provided by continuous laser cooling of ions, and both the cooling rate and the equilibrium temperature can be controlled via laser cooling parameters. The effects of temperature and dissipation are discussed in detail in chapter 15.

To summarize, the total potential (external plus interaction potential) of the FKT model can be written down as follows

$$V_{FKT} = V_{ext} + V_{int} = \sum_{i=1}^{N} \left(\frac{1}{2} K (x_i - x_{i,0} - X)^2 + \frac{1}{2} U \big(1 + \cos(2\pi x_i / a)\big) \right) + \sum_{i=1}^{N-1} \left(\frac{1}{2} g (x_{i+1} - x_i - d)^2 \right) \tag{10.3}$$

where x_i are positions of chain atoms, $x_{i,0}$ are their intrinsic positions in the unperturbed chain at $U = 0$ and $X = 0$, and X is the displacement of the rigid support that can be used to drag the atoms across the substrate. In dimensionless units, where lengths are in units of a and taken modulo 1 (since the system is periodic in a), and

removing the energy offset, the potential becomes:

$$\frac{V_{FKT}}{Ka^2} = \sum_{i=1}^{N} \left(\tfrac{1}{2}(x_i - x_{i,0} - X)^2 + \tfrac{1}{4\pi^2}\eta \cos(2\pi x_i) \right) + \sum_{i=1}^{N-1} \left(\tfrac{1}{2}c(x_{i+1} - x_i - r)^2 \right) \tag{10.4}$$

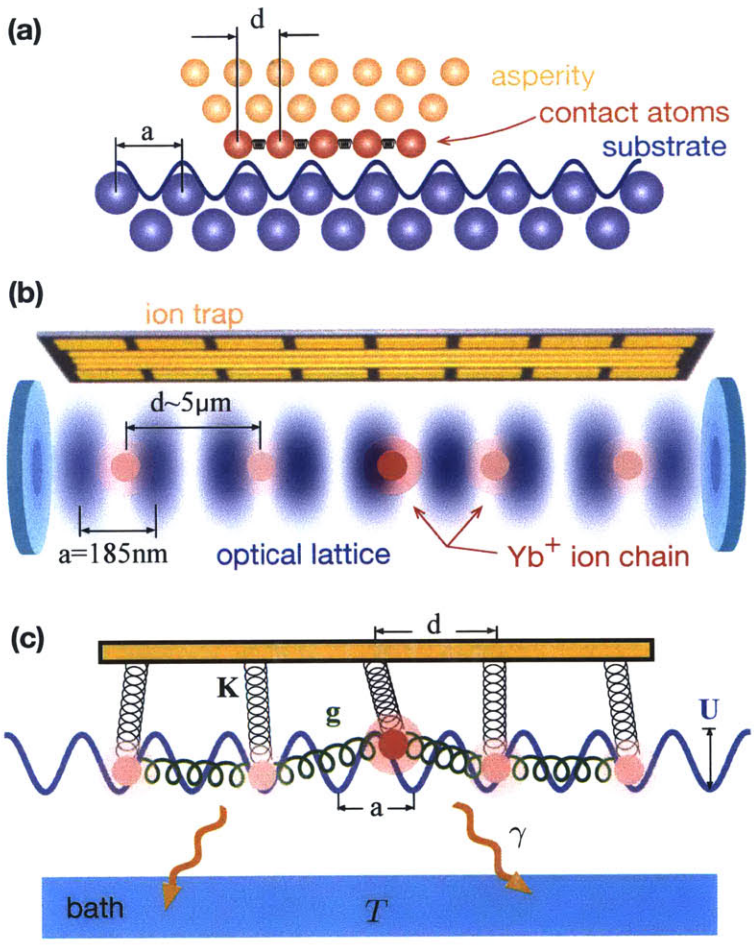

Figure 10-3: **(a)** A nanocontact can be modeled as a chain of atoms representing the contact-layer atoms of an asperity, attached to the asperity via harmonic springs, and subject to the lowest harmonic component of the periodic potential due to a rigid substrate crystal. **(b)** A nanocontact is emulated by a Coulomb crystal of trapped ions ("contact-layer atoms"), attached to the ion trap ("asperity") and subject to the cavity-generated optical lattice ("substrate"). **(c)** The Frenkel-Kontorova-Tomlinson model of systems in (a) and (b), additionally interacting with a thermal bath where frictional heat is dissipated (phonons for a nanocontact, and laser cooling for trapped ions).

10.3 Internal chain springs

The FKT potential in equation 10.3 is a good approximation to the total potential of the ion-lattice system:

$$V_{FKI} = V_{ext} + V_{Coul} = \sum_{i=1}^{N} \left(\frac{1}{2} K (x_i - X)^2 + \frac{1}{2} U \big(1 + \cos(2\pi x_i / a)\big) \right) + \sum_{i \neq j} \left(\frac{e^2}{4\pi\epsilon_0 |x_i - x_j|} \right) \tag{10.5}$$

To reiterate, the harmonic confinement by "external springs" K corresponds to the axial confinement in the linear Paul trap at angular vibrational frequency $\omega_0 = \sqrt{K/m}$ [33], which corresponds to the center-of-mass (COM) motion of the chain - its lowest-energy vibrational mode. The internal springs g in the FKT model roughly correspond to the highest-energy "Egyptian" vibrational mode of angular frequency ω_{max}, where neighbors move in opposite directions:

$$g \approx \frac{1}{4} m \omega_{max}^2 \tag{10.6}$$

To see this, consider the phonon dispersion relation for an infinite crystal of atoms with next-neighbor harmonic springs: $\omega = (4g/m)^{1/2} |\sin(\frac{\pi d}{\lambda_{ph}})|$ [97]. The maximum energy is reached at the edge of this crystal's Brillouin zone $\lambda_{ph} = 2d$. This phonon wavelength indeed corresponds to neighboring atoms moving out-of-phase and results in the relation 10.6 exactly. It turns out that this property largely survives for internal springs in the center of a finite, inhomogeneous Coulomb crystal of ions with long-range coupling, trapped in a harmonic potential, as can be seen in Fig.10-4 and Fig.10-5 .

Coulomb coupling for an ion pair separated by Δx falls off with dipole-dipole scaling as Δx^{-3} if the Coulomb forces are linearized around ion equilibrium positions by expanding them in $\delta x / \Delta x$. This is a good approximation because the largest changes in ion separation δx due to the optical lattice are on the order of the lattice spacing a, which is one to two orders of magnitude smaller than ion separations in our trapped chains: $\delta x / \Delta x \lesssim a / \Delta x \ll 1$. Changes in the Coulomb force due to δx

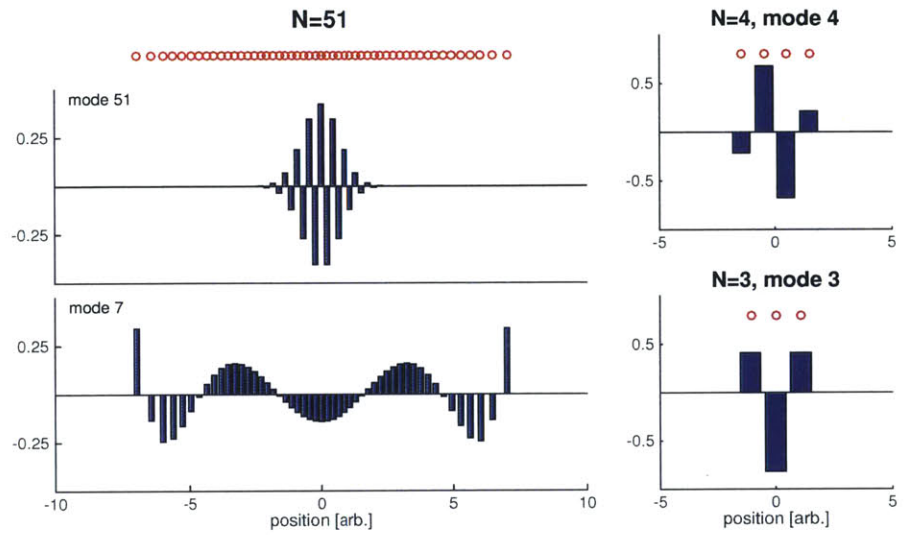

Figure 10-4: **Vibrational modes of finite ion chains.** In an infinite homogeneous chain, the highest-energy vibrational mode ω_{max} corresponds to the shortest-wavelength phonons: neighboring ions oscillating out of phase. *(Top left)* For finite N in a harmonic trap (N=51 shown), due to broken translational symmetry these short-wavelength phonons get localized towards the chain center, where the ions see the stiffest internal springs g directly related to the energy of these phonons. *(Bottom left)* A lower-energy vibrational mode is shown for comparison, exhibiting longer-wavelength phonons less stiff than the next-neighbor springs g. *(Top right and bottom right)* Even for a few-ion chain ($N = 4, 3$ shown), the highest-energy vibrational motion corresponds to the center ions moving out-of-phase, preserving the relationship $g \approx \frac{1}{4}m\omega_{max}^2$. (The ion positions on the x-axis are in units $(\frac{e^2}{4\pi\epsilon_0 m})^{1/3}\frac{1}{\omega_0^{2/3}} = x_2/2^{1/3}$, where x_2 is the separation of 2 ions in the trap with the given ω_0).

are then given by

$$\begin{aligned}\delta F_{Coul} &= \frac{e^2}{4\pi\epsilon_0}\Big((\Delta x + \delta x)^{-2} - \Delta x^{-2}\Big) \\ &\approx \frac{e^2}{4\pi\epsilon_0}\Big(\Delta x^{-2}(1 - 2\frac{\delta x}{\Delta x}) - \Delta x^{-2}\Big) \\ &= -2\frac{e^2}{4\pi\epsilon_0 \Delta x^3}\delta x\end{aligned} \tag{10.7}$$

This gives the effective spring constant for an ion pair as $g_{ij} = \frac{2e^2}{4\pi\epsilon_0|x_i - x_j|^3}$. In other words, for a homogeneous spacing d, beyond-next-neighbor contributions are reduced by 1/8, 1/16, etc - the sum of these forces to infinity contribute additional

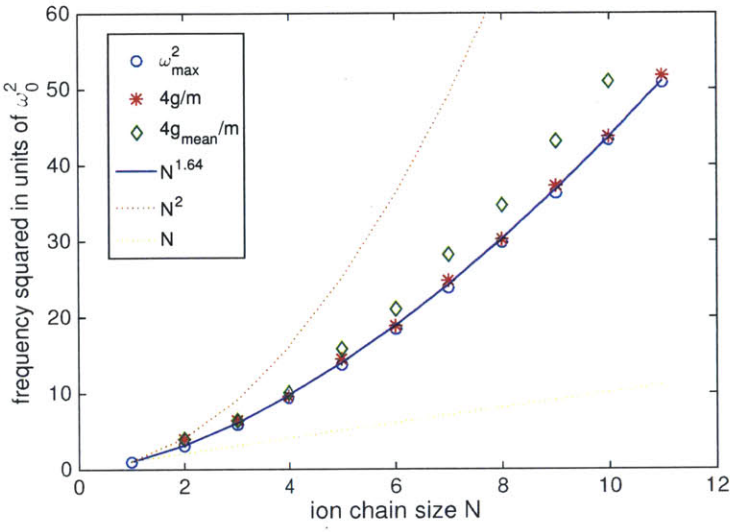

Figure 10-5: **Scaling of central internal springs g with the number of ions N.** The maximum vibrational mode energy and the internal spring $g = \frac{2e^2}{4\pi\epsilon_0 d_{min}^3}$ at the center of the chain both increase with N as $g/K \approx \frac{1}{4}(\omega_{max}/\omega_0)^2 \approx \frac{1}{4}N^{1.64}$. The additional confinement by the mean field of ions beyond the next-neighbors results in a slight deviation of g_{mean} from this behavior.

20% to the confinement of an ion in the mean field of an infinite crystal:

$$g_{mean} = \sum_{j=1}^{\infty} g_{1j} = g \sum_{j=1}^{\infty} \frac{1}{j^3} = g \cdot \zeta(3) \approx 1.2g \tag{10.8}$$

where g is the internal next-neighbor spring stiffness as defined for the FKT model. For finite N and inhomogeneous ion spacing d as in the ion trap (see section 10.4), g and g_{mean} vary with position in the chain and are largest in the center, where d is the smallest and most uniform (see Fig.10-6). As mentioned above and shown in Fig.10-5, in the center of even a few-ion chain, g agrees with $\frac{1}{4}m\omega_{max}^2$ as expected for an infinite chain. In our studies of the Aubry transition in finite chains (chapter 14), we focus on the superlubricity breaking and analyticity breaking of the center ion (odd case - corresponds to the symmetry-breaking transition known as the finite version of the Aubry transition[92, 98, 99, 63]) or the center two ions (even case).

As we add ions one by one into the trap at fixed ω_0, the ions get closer together (Fig.10-6) and the center-ion internal springs g scale together with ω_{max} as $\sim N^{1.64}$

(Fig.10-5). In effect, we use the ion number N to tune the FKT model parameter $g/K \approx \frac{1}{4}N^{1.64}$.

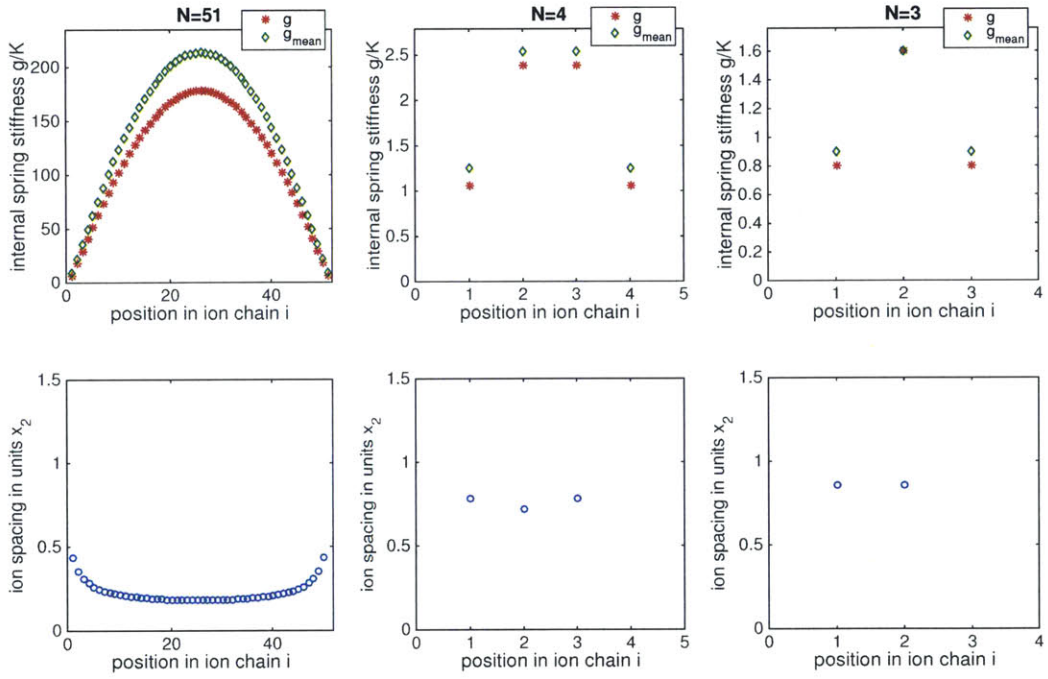

Figure 10-6: **Variation of internal springs g with position in the chain j.** Ion spacing d is the smallest and most uniform in the center of the chain, where the internal spring g attains its largest value and corresponds to the highest-energy vibrational mode. Note the special case of the edge ions: they only have a single neighbor, and as a consequence, the effective spring g is about a factor of 2 lower that for the next ion. As a result, in the finite-N transition from superlubricity to stick-slip, these boundary ions always get pinned first.

10.4 Control of ion spacings to tune lattice mismatch

The intrinsic ion positions $x_{i,0}$ unperturbed by the lattice are obtained by minimizing V_{FKI} in equation 10.5 at $U = 0$, which is a convex function and yields a unique set of ion positions [100, 101]. In the harmonic potential, the chain spacings are inhomogeneous (shown for $N = 51$, $N = 4$ and $N = 3$ in Fig.10-6). However, for a given N, the ratio of spacings is fixed and they all scale as $K^{-1/3}$. Therefore, we tune the harmonic confinement of the Paul trap to vary ion spacings on the scale of the

lattice constant a, giving us control over the matching between the ion chain and the lattice.

One sensible way to mismatch a finite chain to the lattice [17, 102] is to cancel the sum of lattice forces on the unperturbed chain such that $\sum_i^N \sin(\frac{2\pi}{a}(x_{0,i} - \phi) = 0$ for all ϕ, where ϕ represents the common displacement of unperturbed ion positions by moving the harmonic trap position X. The intuition behind this is that an infinitely stiff chain $g \to \infty$ that does not deform would not see the corrugated potential at finite U, and would slide frictionlessly because of this cancellation of lattice sticking forces. This leads us to define the matching parameter q as follows:

$$q = \max_\phi \left(\frac{1}{N} \sum_i^N \sin\left(\tfrac{2\pi}{a} x_{0,i} - \phi\right) \right) \tag{10.9}$$

Thus, q represents the normalized Peierls-Nabarro potential barrier to the displacement of the unperturbed (infinitely rigid) ion crystal. The value of q always falls between 0 and 1. $q = 1$ corresponds to the ion chain matched to the optical lattice, resulting in the largest possible value of such barrier because lattice forces add constructively. $q = 0$ corresponds to the chain mismatched to the lattice, resulting in a vanishing barrier (in the limit of an infinitely rigid ion crystal) because the lattice forces add destructively and cancel.

The easiest way to visualize this is with $N = 2$ trapped ions, as shown in Fig.10-7a. When the distance between the ions d is in registry with the lattice spacing (or "in phase"), giving $r = (d/a)(\text{mod } 1) = 1$, they always see the same slope of the lattice potential, resulting in a constructive addition of the lattice sticking forces. In particular, they see the maximum slope at the same time as the ion crystal position X is translated, giving $q = 1$, and this maximal sticking force on the crystal per ion is equal to that of a single trapped ion in this external potential. When the distance between the ions is perfectly out of registry (or "out of phase"), giving $r = (d/a)(\text{mod } 1) = 1/2$, the ions always see opposite slopes of the lattice potential, resulting in a destructive addition of lattice forces, and $q = 0$. At intermediate values of r, one obtains intermediate values $1 > q > 0$. Since the distance between the ions

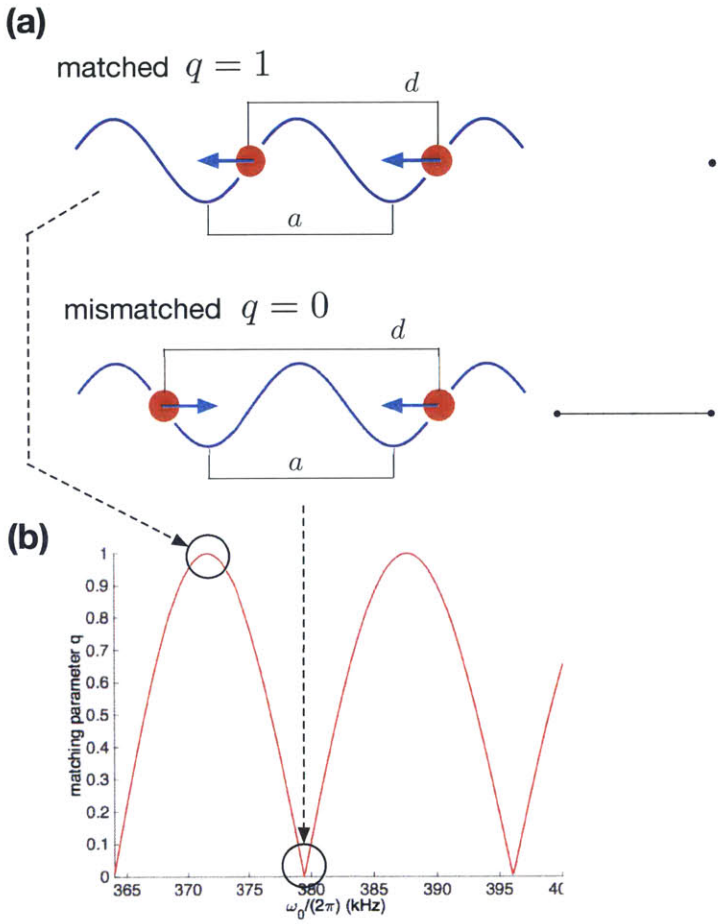

Figure 10-7: **(a)** The ions are matched to the lattice when the lattice forces add constructively, and mismatched when the lattice forces add desctructively. **(b)** The matching parameter q is tuned via the external harmonic confinement and is periodic with the trap vibrational frequency, as ions go in and out of registry with the lattice.

and consequently the value of r are tuned via K, as the axial vibrational frequency ω_0 of the Paul trap is varied, the calculated value of q quasi-periodically goes through maxima at $q = 1$ and minima at $q = 0$ (see Fig.10-7b).

For larger N, it is convenient to visualize the intrinsic arrangement of the ions with respect to the lattice by plotting their relative lattice phases $\theta_i = 2\pi x_{0,i}/a$ on the unit circle as shown for $N = 2$ in Fig.10-7a. The matched case of $q = 1$ corresponds to all ions being in registry, i.e. they all see the same lattice phase. An arrangement of $N = 5$ ions close to $q = 1$ is shown in Fig.10-8a. However, the mismatched case of $q = 0$ may be given by many different arrangements, two of which are shown for

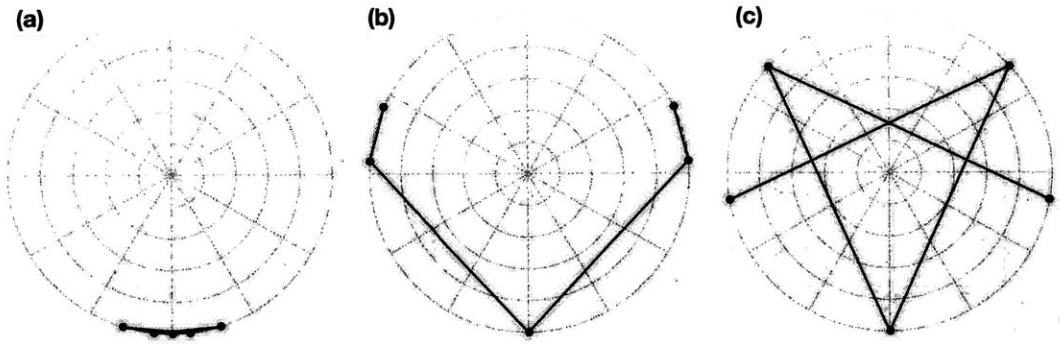

Figure 10-8: Calculated unperturbed positions of $N = 5$ ions with respect to the lattice plotted as phases $\theta_i = 2\pi x_{0,i}/a$ on a unit circle. The lines connect neighbouring ions. **(a)** In the near-matched case $q = 0.98$ as the ions are almost in registry (the phases modulo 2π almost coincide). **(b),(c)** For a mismatched case $q = 0$ multiple configurations of ions relative to the lattice are possible; (c) shows a $q = 0$ configuration where the ion spacing is close to the Golden ratio $r \approx (\sqrt{5} - 1)/2$.

$N = 5$ in Fig.10-8b,c. Incidentally, the second one corresponds to a dimensionless ion spacing r close to the golden ratio, which will become important in chapter 14.

The calculated values of q versus the axial vibrational frequency ω_0 (near the nominal value of $2\pi\times364$ kHz) for $N = 2 - 6$ and $N = 10$ are shown in Fig.10-9. Evidently, the single control parameter ω_0 is insufficient to control matching for large enough N. For example, by $N = 10$, $q = 1$ cannot be reached in the vicinity of the desired nominal vibrational frequency. However, up to $N = 6$, both the matched case $q = 1$ and the mismatched cases $q = 0$ can be dialed in by controlling ω_0 with sub-kHz precision, which is done via the snake electrode (see chapter 4).

The plots of q versus ω_0 and the intrinsic chain arrangements discussed above are calculated assuming a perfectly harmonic trap, with N and the measured values of ω_0 as inputs. In reality, even a small asymmetry in the Paul trap axial trapping potential can cause small changes of ion spacings, that are however considerable on the scale of the lattice spacing a. For that reason, we also measure the intrinsic arrangements and extract values of q experimentally. This is done by taking fluorescence images of the ion chain in a weak lattice at different positions X of the Paul trap. Under a weak perturbation from the lattice, combined with thermal averaging, the fluorescence of each ion as a function of X should peak when the ion's intrinsic position aligns with

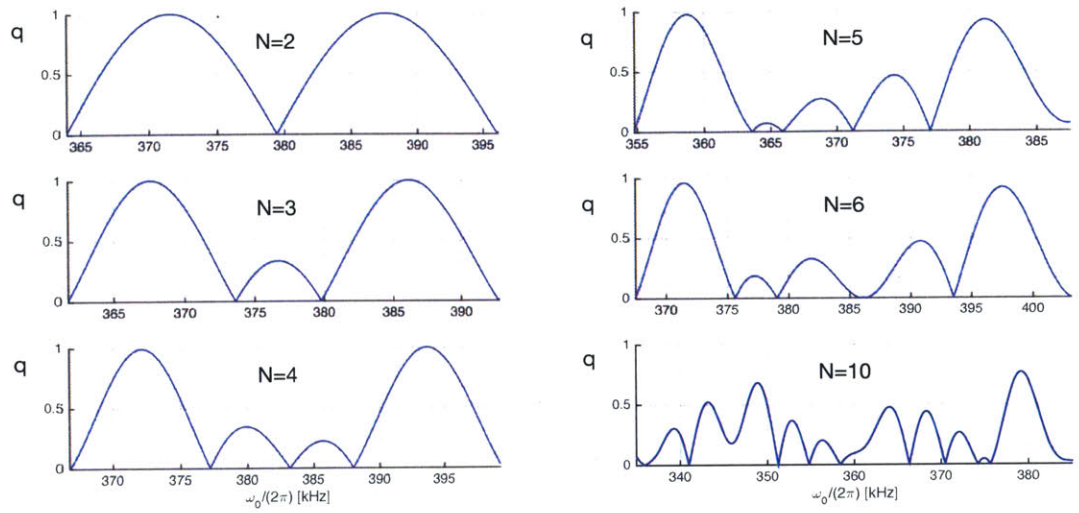

Figure 10-9: Calculated matching parameter q versus harmonic trap vibrational frequency ω_0 for ion chains of different size. Arbitrary control of q using ω_0 breaks down by $N = 10$, but works well up to $N = 6$, which is the largest ion number used in experiments in this thesis.

the lattice maximum. Such a set of 1D images versus X is shown in Fig.10-10 for $N = 6$. Denoting by X_i the trap positions where each ion's fluorescence peaks in this procedure, the experimental measurement of the matching parameter is given by:

$$q_{exp} = \max_{\phi}\left(\frac{1}{N}\sum_{i}^{N}\sin\left(\tfrac{2\pi}{a}X_i - \phi\right)\right) \tag{10.10}$$

The plot of measured q versus ω_0 closely agrees with the the calculation with no free parameters up to $N = 6$ (Fig.10-11), and is also very reproducible from one measurement day to another, meaning that the trapping potentials are stable and under control.

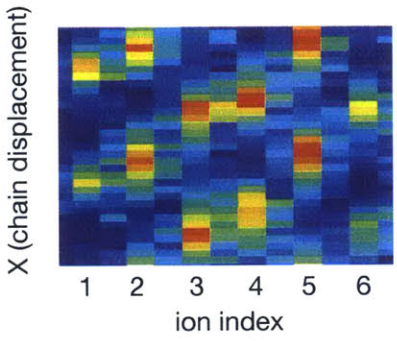

Figure 10-10: Experimental signal used to measure the matching parameter q_{exp} for $N = 6$ ions. Horizontal 1D images of the ion chain are shown stacked vertically for different trap positions X. Different ions experience maximum fluorescence at different trap positions X_i, corresponding to alignment of ion i with a lattice maximum.

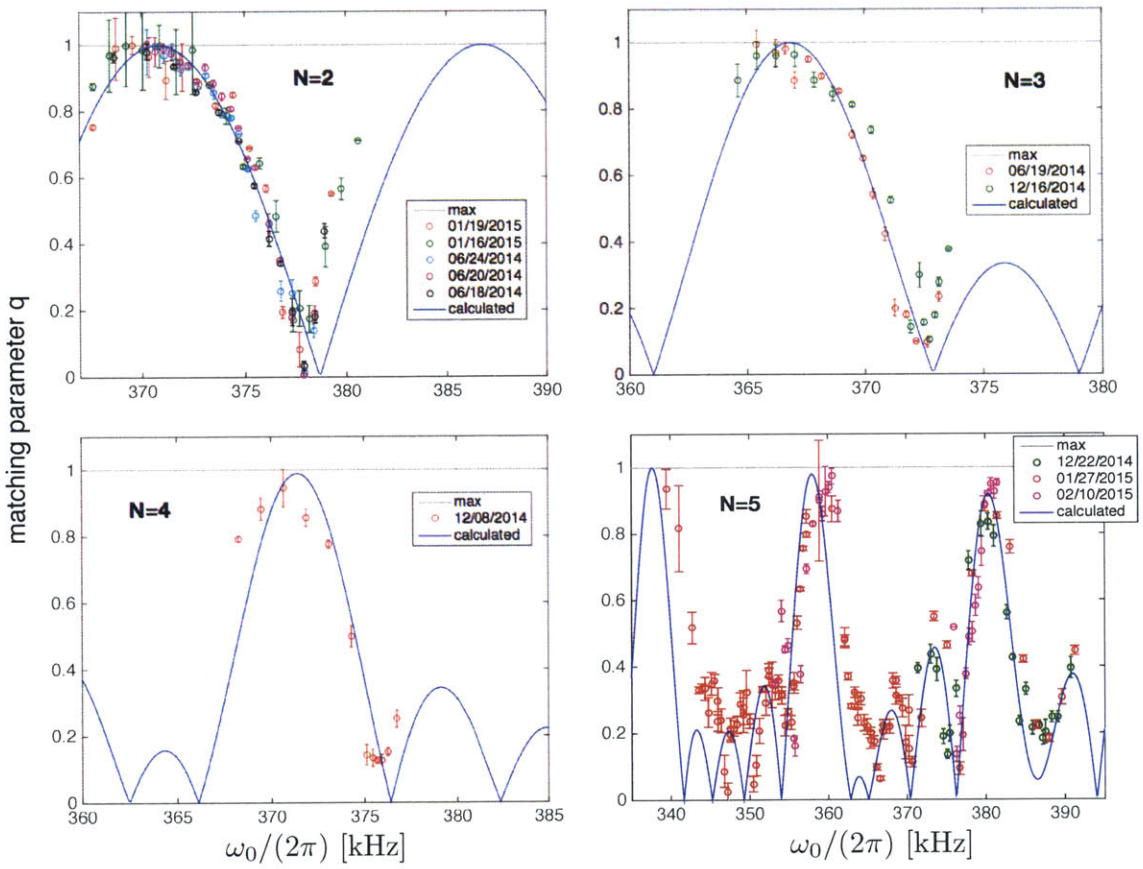

Figure 10-11: Measured matching parameter q_{exp} for ion chains of different size. Measurements agree well with calculations (blue line, no free parameters), and are reproducible on different days.

Chapter 11

Friction microscope: measuring stick-slip, atom-by-atom

One of the key advantages of studying nanofriction with trapped ions in optical lattices is the ability to track the sticking and slipping of each atom at this idealized frictional interface. In this chapter, I outline our experimental procedure for measuring stick-slip friction of individual ions in a 1D Coulomb crystal (chain) dragged through an optical lattice.

To study friction, we apply a known shear force to our nanofriction interface, which moves the ion chain over the corrugated lattice potential, and we track the position of each ion via the fluorescence that it emits (Fig.11-1). The applied shear force is a uniform electric force $F_{app} = eE$ due to a uniform electric field applied via two pairs of far away DC electrodes (see chapter 4). This force displaces the minimum of the axial harmonic trap of stiffness K by $X = F_{app}/K$, moving with it the ion chain. This is equivalent to translating the rigid support in the FKT model, resulting in a uniform shift of the intrinsic atom positions $x_{i,0} \rightarrow x_{i,0} + X$ (Fig.11-2b). We linearly ramp the applied shear force so that $X(t) = v \cdot t$ and the chain is "dragged" along the lattice at constant speed, and then we reverse the ramp to drag the chain at constant speed back to its initial position (Fig.11-3a).

The ions in a typical chain are separated by micrometers, and therefore can be individually resolved with diffraction-limited optics (the imaging setup is discussed

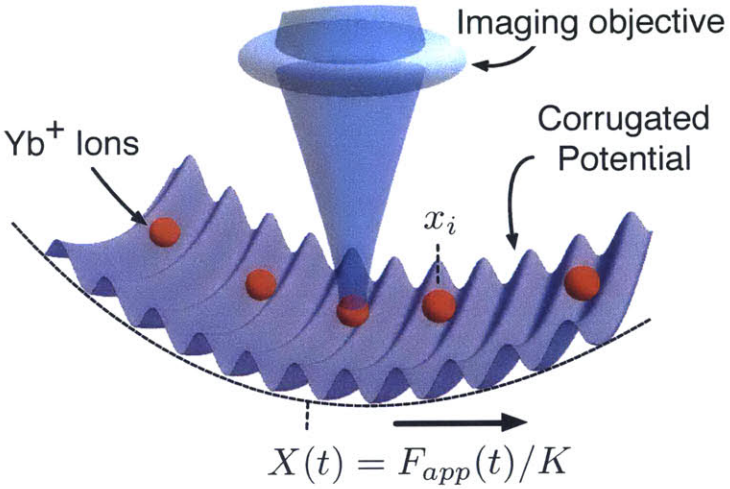

Figure 11-1: To measure friction, we ramp a uniform longitudinal electric force to translate the harmonic trap with the ion crystal over the corrugated lattice potential. The motion of each ion is tracked by monitoring its fluorescence.

in chapter 7). However, we are interested in observing the position of each ion with resolution finer than the optical lattice spacing of half the optical wavelength $a = \lambda/2 = 185$ nm (Fig.11-2a). This is enabled by the lattice itself, combined with the repumping laser in the cooling scheme (see chapter 7), acting as a subwavelength position probe. As a result, each ion's fluorescence is proportional to its lattice potential, i.e. the observed fluorescence is maximum at lattice maxima, and minimum at lattice minima. This modulation of fluorescence by the ion's position relative to the lattice can be inverted to extract the relative position from the observed fluorescence. Thus, in friction experiments, we move the ion chain along the lattice at speed v and observe the fluorescence from different ions peak when the respective ions reach a maximum value of the lattice potential before slipping. At low speeds v, the camera can be used to observe all the ions at once, while at high speeds, we use two PMTs to observe two ions at a time, and reconstruct the fluorescence traces of the entire chain with successive overlapping measurements.

This type of super-resolution microscope allows us to track the position of each ion with sub-lattice-constant resolution, enabling an ion-by-ion measurement of the stick-slip process. As the shear force is applied, each ion can stick to a lattice site until a critical shear force is reached that makes that position unstable, at which

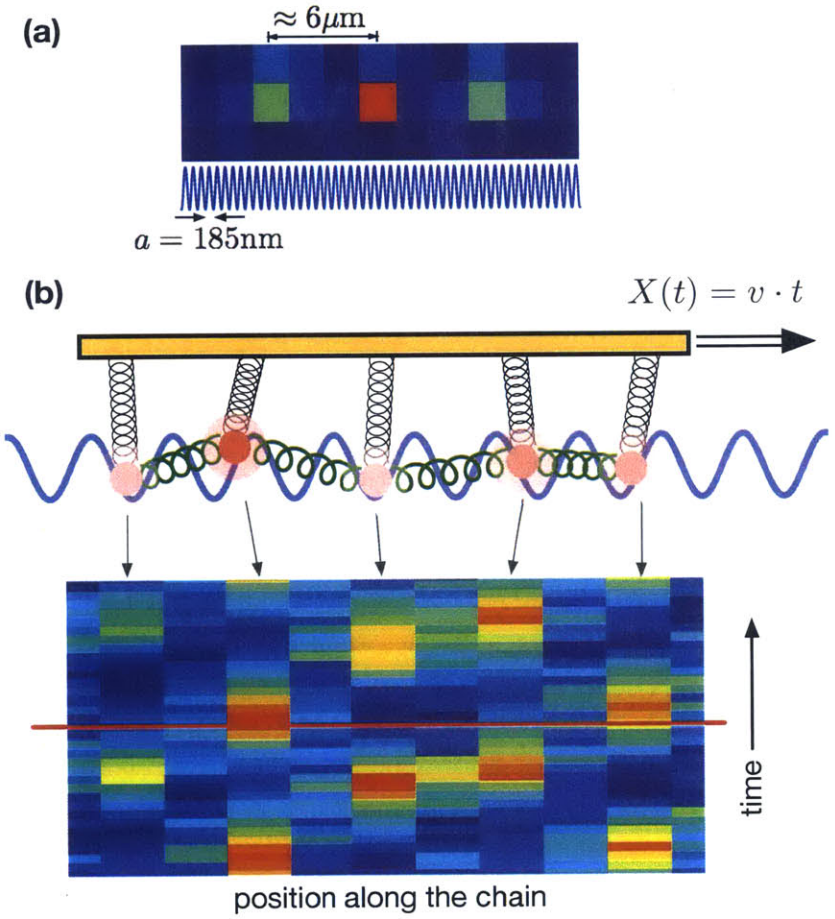

Figure 11-2: **(a)** A near-diffraction-limited image of a 3-ion crystal juxtaposed with a schematic of the lattice potential to illustrate that the lattice spacing is 1.5 orders of magnitude smaller than the typical ion spacing: $a/d \approx 1/30$. The large ion spacing allows for fluorescence to be collected from individual ions, and the value of the fluorescence indicates each ion's position relative to a lattice site. **(b)** As the trap is translated by ramping the electric force, different ions stick and slip at different times, with the slip events signaled by a fluorescence peak, since an ion reaches a maximum value of the lattice potential right before a slip. Horizontal 1D images of the ion chain are shown here stacked vertically versus time as the applied force is ramped.

point a fold catastrophe occurs [103], and the ion slips to a new minimum which is stable. Thus, bistability (or multistability) is the key ingredient in stick-slip, which is the process of switching between the multiple minima of the potential under the action of an applied force.

This process is visualized in Fig.11-3a for a single trapped ion in the Prandtl-Tomlinson bistable potential arising from the addition of the Paul trap axial confinement and the sinusoidal lattice potential with $\eta > 1$:

$$V_{PT}(x,t)/(Ka^2) = \frac{1}{2}(x - v \cdot t)^2 + \eta \frac{1}{4\pi^2}(1 + \cos(2\pi x)) \tag{11.1}$$

As the linear ramp of the applied force F_{app} displaces the harmonic potential to the right at speed v, the ion sticks to its initial site (#1), riding up the lattice potential and increasing in fluorescence (#2), until a critical maximum static friction force F_s is reached. At that point, the barrier vanishes and the initial minimum disappears, resulting in the fold catastrophe. The ion discontinuously slips from its initial site to the global minimum one site over (#3). The ion then dissipates the released energy ΔW via laser cooling, while localization in the lattice potential reduces its fluorescence again. The positions of fluorescence peaks in Fig.11-3b thus correspond to values or the applied force causing the ions to slip over consecutive lattice barriers during the forward ramp, then during the reverse ramp. Hysteresis can be clearly observed in the shift between the forward and reverse slips - this shift corresponds to twice the maximum static friction force $2F_s$. The fluorescence increase leading up to each slip is converted to the ion's position to reconstruct the force-displacement curve. When $X = F_{app}/K$ is moved by one lattice site a, this curve is a loop enclosing the area $2\Delta W$ equal to twice the energy dissipated after a single slip (since two slips occured: one on the way forward, and one on the way back) (Fig.11-3c).

Such hysteresis loops measured for individual atoms via their fluorescence therefore provide all the microscopic information about friction, atom-by-atom: the half-width of each loop is the static friction force F_s on that atom, the half-area of the loop is the energy ΔW which that atom dissipates in a single slip, and this dissipated

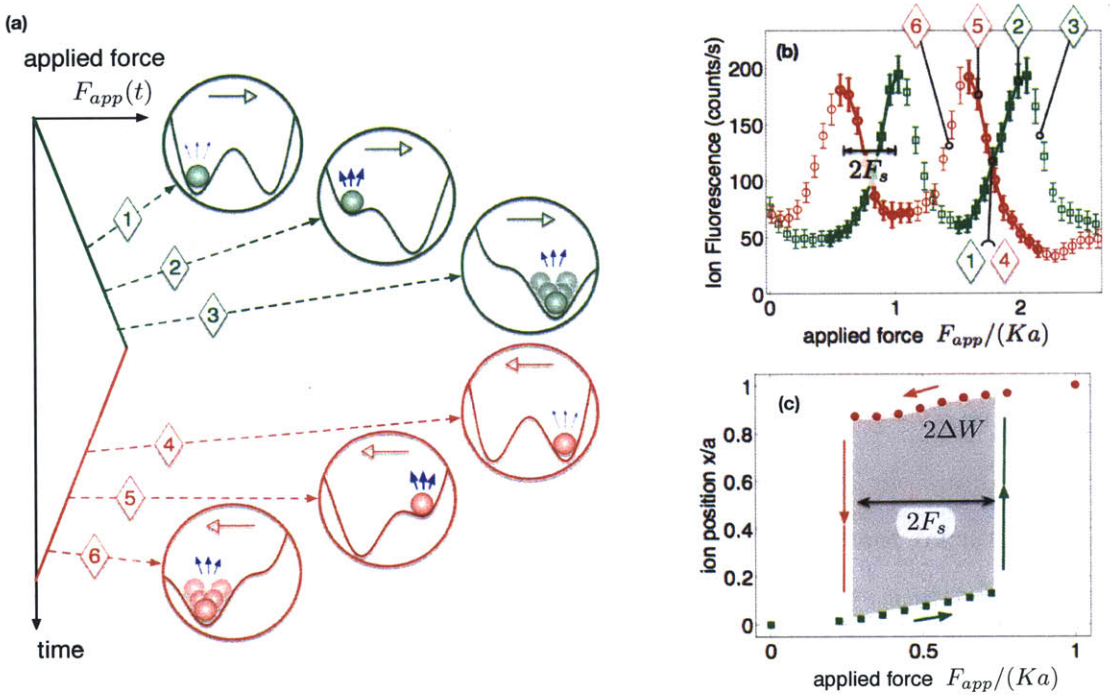

Figure 11-3: **(a)** Stick-slip results from bistability, illustrated here for a single ion. We linearly ramp a shear force causing the ion to jump between the minima, and we extract its position from its fluorescence, proportional to the lattice potential energy: (#1) ion initialized in the left site; (#2) the applied force pushes the ion up the lattice potential, eventually causing the slip; (#3) immediately after the slip, the ion is optically recooled and localizes to the right site; (#4),(#5),(#6) the force ramp reverses and the ion sticks at the right site before slipping back to the left. Slips are identified by maxima in the ion's fluorescence. **(b)** Fluorescence versus applied force measured during the forward transport (green squares) and reverse transport (red circles), showing hysteresis that is used to measure the static friction force F_s. The stages of the stick-slip process (#1)-(#6) correspond to the illustrations in (a). Only the bold data points indicate the ion's position before a slip and are used to reconstruct the force-displacement curve shown in (c) (immediately after the slip, fluorescence is high as a result of the released kinetic energy, and indicates temperature rather than the ion's position until it has cooled down again). **(c)** The force-displacement hysteresis loop encloses an area equal to twice the dissipated energy per slip ΔW.

energy per 1 lattice site of displacement is the kinetic friction force $F_k = \Delta W/a$. In addition, ΔW is proportional the the height U_B of the energy barrier to chain displacement, intuitively because it is the energy released when the chain falls off the top of the barrier by slipping (see section 12.2).

It is interesting to note that just like in most manifestations of friction at the macroscopic scale, the kinetic friction force is smaller than the static friction force $F_k < F_s$. This can be seen as follows: the half-area of the loop is $\Delta W \approx F_s \times \Delta x$, where Δx is the distance between the two minima in the bistable potential and also roughly the distance over which the ion slips. The ion is never stuck exactly at the lattice site, but gets pushed up the potential before each slip, so $\Delta x < a$, meaning that $F_k = \Delta W/a < \Delta W/\Delta x = F_s$.

A note about the definition of static friction force is in order. In our system, F_s is the external force field that needs to be applied to the atoms to force them over the barrier in a symmetric bistable potential. The actual reaction force exerted by an atom on the rigid support in the FKT model (Fig.11-2) is given by $F_{react} = (x_{i,0} + X) - x_i$. This critical reaction force just before the slip $F_{react,s}$ is commonly defined and measured in tribology experiments as the static friction force. It is always larger than the static force we have defined here: $F_{react,s} > F_s$, but $F_{react,s}$ goes to zero whenever F_s goes to zero, and therefore this does not affect any conclusions in this thesis (for example, the conclusions about superlubricity in the subsequent chapters). Of course, $F_{react,s}$ can also be extracted from the measured hysteresis loops, but our measurement of F_s comes directly from a very reliable measurement of the shift in the fluorescence peaks, and so we stick to discussing the static friction force in terms of our definition of F_s.

Chapter 12

Normal load dependence of friction and superlubricity

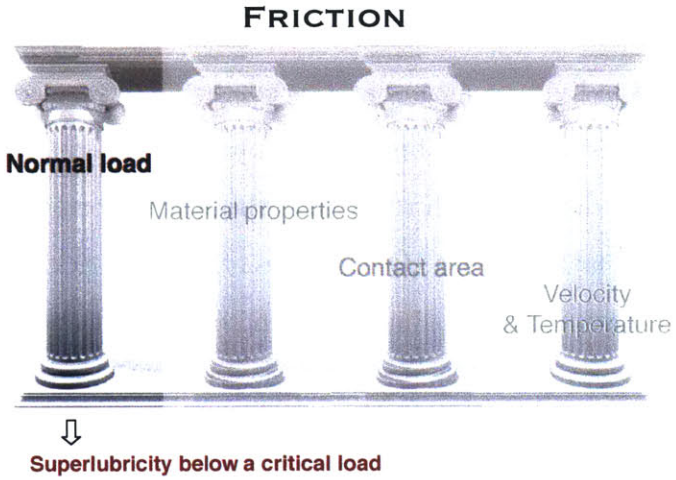

Figure 12-1: In this chapter, I explore the first and oldest pillar: the normal load dependence of friction, and show experimental observations of superlubricity.

The well-known empirical law of friction

$$F_f = \mu \cdot F_N \tag{12.1}$$

which states that friction is proportional to the normal load at the contact surface, does not hold even in the simplest atomistic model of friction involving a single atom on a periodic substrate, the Prandtl-Tomlinson model (PT) [60, 61], commonly used

to describe single-asperity nanocontacts and AFM experiments [58]. Stick-slip friction vanishes below a critical normal load in this model in a phenomenon termed superlubricity [65, 104]. In a multi-atom contact, as in the Frenkel-Kontorova-Tomlinson model (FKT), the critical normal load below which superlubricity appears depends on the matching of atomic lattices at the contact, in which case we refer to that regime as structural superlubricity (explored in more detail in chapter 13). In the limit of the Frenkel-Kontorova model, structural superlubricity can be associated with the sliding-to-pinned Aubry transition [64, 105, 106, 107, 63] (I explore this connection in chapter 14). Superlubricity is an elusive, but technologically and economically important regime, which does not seem to naturally occur on the macroscopic scale. Evidence for it has been seen mostly at the nanoscale using atomic force microscopes [75, 73, 74], but recently also at the microscale in sheared graphite [108] and at the macroscale in carbon nanotubes [109] and graphene stabilized by nanodiamonds [110]. Unfortunately, these condensed-matter experiments have limited access to all microscopic variables and individual atoms at the contact interface. In our experiments described here, we measure friction between trapped-ion chains and an optical lattice as a function of lattice depth, which represents the normal load, and observe superlubricity below a critical lattice depth. Our studies of superlubricity with atom-by-atom control provide detailed understanding of its microscopic mechanisms, including the effects of atomic lattice mismatch and contact size [17, 111], and the effects of velocity and temperature [112] - effects which I fully unravel by the end of part II of my thesis.

12.1 Observations of superlubricity and transition to stick-slip

Our measurements of friction as a function of lattice depth U for ion chains of $N = 1-5$ ions are shown in Fig.12-2. In a) ion chains are matched to the lattice, and in b) they are mismatched to the lattice. In both regimes, the vanishing of the measured static friction force, the mean force per ion $\overline{F_s}$, is apparent below a critical finite

lattice depth U_c. This zero-friction regime is superlubricity. Note that according to the empirical law in equation 12.1, which translates to $F_s \propto U$, there should be no superlubricity as any finite corrugation results in a finite friction force. Note also the difference between U_c in the matched and mismatched scenarios: a matched chain of any length N gives the same mean friction force per ion $\overline{F_s}$ as with a single trapped ion, whereas mismatching makes superlubricity more robust and U_c increases with N from the single-ion value $U_c^{(1)} = Ka^2/2\pi^2$.

12.2 Friction of a single trapped ion and the Prandtl-Tomlinson model

The occurence of superlubricity is most easily understood in terms of a single trapped ion ($N = 1$). This case is an exact implementation of the Prandtl-Tomlinson model (PT) [58, 60, 61], which assumes a single-atom contact between an asperity of stiffness K at equilibrium position X and a substrate producing a periodic potential with lattice constant a and depth U (Fig.12-3). In our system, $K = m\omega_0^2$ is the axial harmonic confinement of the ion in the Paul trap, where ω_0 is the axial vibrational frequency (nominally at $2\pi\times$364 kHz), X is the position of the minimum of the axial potential, U is the depth of the optical lattice (here varied in the range $2\pi\hbar \times (1.6 - 36.8)$ MHz) with lattice period $a = 184.75$ nm. In the absence of the Paul trap, the lattice would confine the ion at one of the sites, which for small oscillations around the energy minimum would result in a vibrational frequency ω_L given by

$$\omega_L^2 = -\frac{1}{m}\frac{\partial^2}{\partial x^2}\bigg|_{x=0}\left[\frac{1}{2}U(1+\cos(2\pi\frac{x}{a}))\right] = \frac{2\pi^2 U}{ma^2} \tag{12.2}$$

Thus, the total potential experienced by the atom is:

$$V_{PT}(x) = \frac{1}{2}K(x-X)^2 + \frac{1}{2}U\left(1+\cos\left(2\pi\frac{x}{a}\right)\right) \tag{12.3}$$

which in dimensionless units of Ka^2 for energy and a for position becomes

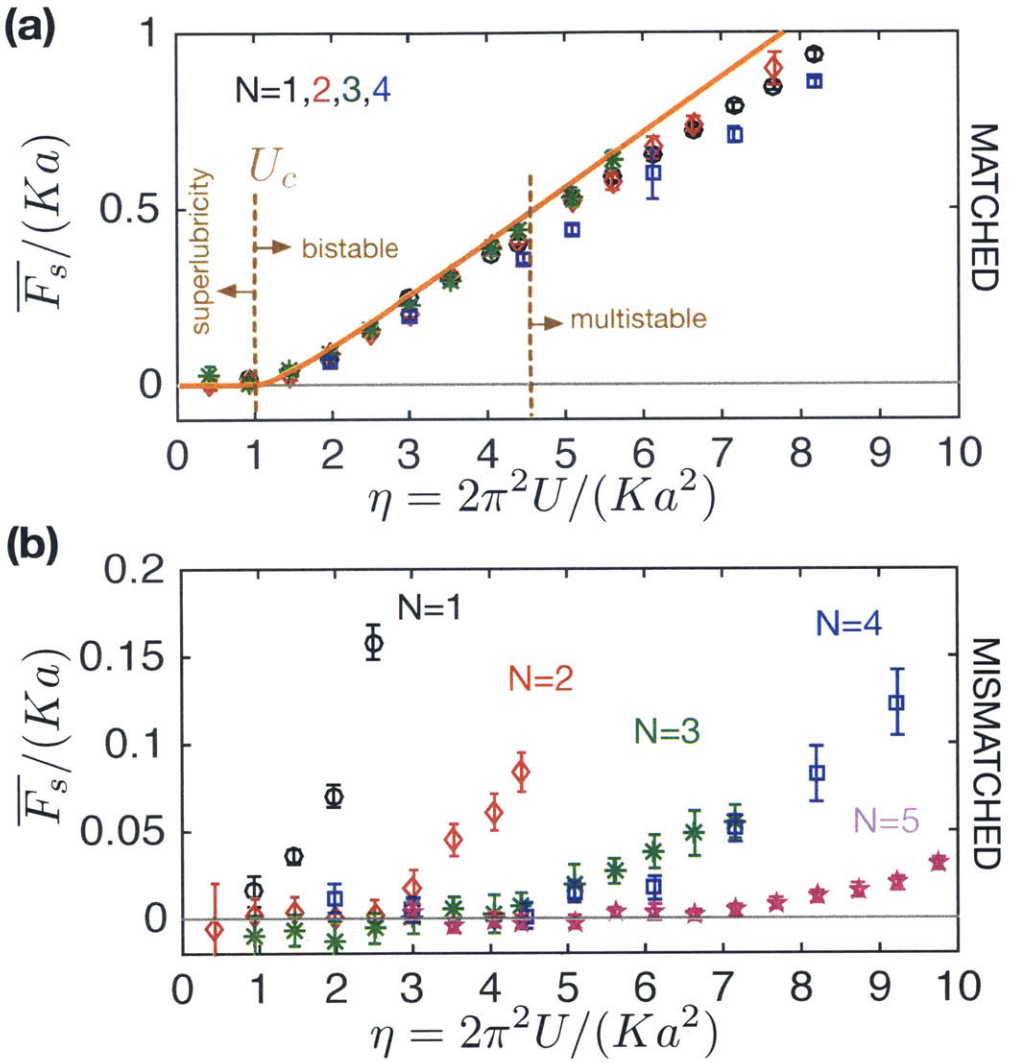

Figure 12-2: Summary of observed dependence of stick-slip friction on lattice depth U (or "dimensionless normal load" η). Superlubricity is observed when friction vanishes within experimental error. **(a)** For ion crystals of $N = 1 - 4$ matched to the lattice, superlubricity is observed below a critical value of the lattice depth U_c corresponding to $\eta = 1$, independent of the ion number. This is in agreement with the single-atom Prandtl-Tomlinson model (orange solid line), where the potential is monostable for $\eta < 1$ and bistable for $\eta > 1$. For $\eta > 1$ friction is observed to increase linearly with η, with no observable change in behaviour as the multistable regime is entered at $\eta \approx 4.6$, where multi-slip motion is expected to take place. **(b)** For ion crystals of $N = 1 - 5$ mismatched to the lattice, the stick-slip behaviour with normal load η changes drastically: superlubricity persists to larger and larger critical values of η as the size of the crystal N increases. In (a) and (b) the measured mean friction force per ion is plotted ($\bar{F}_s$), and error bars indicate statistical errors of 1 standard deviation.

$$V_{PT}(x) = \frac{1}{2}(x - X)^2 + \eta\frac{1}{4\pi^2}(1 + \cos(2\pi x)) \tag{12.4}$$

The dimensionless parameter η defines the topography of the potential landscape and is given by the ratio of maximum lattice curvature $m\omega_L^2$ to the curvature of the harmonic trap $m\omega_0^2$ (or equivalently, by the square ratio of the associated vibrational frequencies):

$$\eta = \frac{2\pi^2 U}{Ka^2} = \frac{\omega_L^2}{\omega_0^2} \tag{12.5}$$

Since η is proportional to the lattice depth U through this relation, it can be thought of as the dimensionless normal load.

The total potential in eqn. 12.4 is always monostable for $\eta < 1$, bistable for a range of X for $1 < \eta < 4.604$ and multistable for $\eta > 4.604$, as shown in Fig.12-4. The crossover from monostability to bistability happens at $\eta = 1$ because that is when the negative curvature at the lattice maximum overcomes the positive curvature of the harmonic trap, and creates a barrier. The global potential minimum bifurcates into two degenerate local minima (at distance x from the lattice maximum). Since stick-slip can be understood as a sudden switch induced by an applied force from a metastable potential minimum to a lower minimum, stick-slip requires bistability. Therefore, in the PT model stick-slip should be finite for $\eta > 1$ and should vanish for $\eta < 1$, resulting in superlubricity. This crossover at $\eta = 1$ (i.e. $U_c^{(1)} = Ka^2/2\pi^2$) for $N = 1$ is indeed observed in our experimental data in Fig.12-2a.

Recalling chapter 11, we measure the static friction force F_s as the electric force required to move the harmonic trap position X from the symmetric point $X = 0$ until the ions slips: $F_s = KX_{slip}$. By considering at which X the metastable initial minimum disappears, we obtain, in our dimensionless units where force is measured

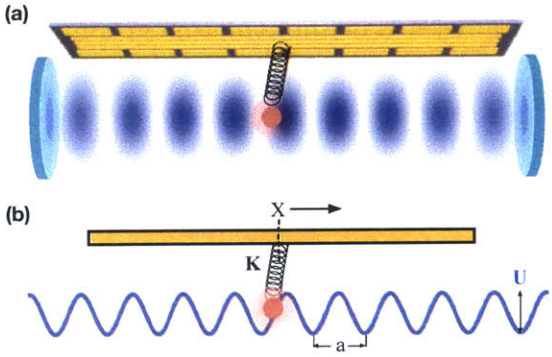

Figure 12-3: **(a)** Friction of a single trapped ion against the optical lattice potential. **(b)** The Prandtl-Tomlinson model of a single trapped ion in the lattice.

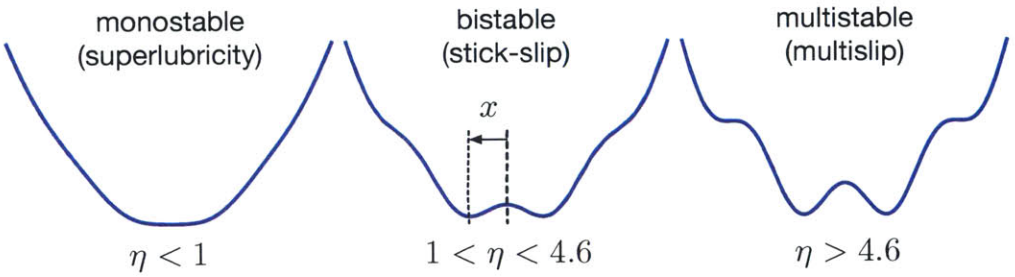

Figure 12-4: The Prandtl-Tomlinson potential results from the superposition of the harmonic trap potential and the sinusoidal lattice potential. It is monostable when the curvature of the harmonic trap dominates $\eta = \omega_L^2/\omega_0^2 < 1$, becomes bistable when the lattice curvature dominates $\eta = \omega_L^2/\omega_0^2 > 1$, and is multistable (more than two local minima) for $\eta > 4.6$.

in units Ka and distance in units a, for $\eta > 1$:

$$\begin{aligned} F_s = X_{slip} &= \frac{1}{2\pi}\Big(\eta \cdot \sin\big(\text{arcsec}(\eta)\big) - \text{arcsec}(\eta)\Big) \\ &= \frac{1}{2\pi}\Big(\sqrt{\eta^2 - 1} - \text{arcsec}(\eta)\Big) \end{aligned} \tag{12.6}$$

This exact result of the PT model agrees very well with our experimental curve of F_s versus η for the matched ion chains as can be seen in Fig.12-2a. Near $\eta \gtrsim 1$, F_s scales as $(\eta - 1)^{3/2}$ and for $\eta >> 1$, F_s scales linearly with η. A good approximation in the full range $\eta > 1$ turns out to be (see Fig.12-5):

$$F_s \approx \frac{1}{2\pi}\frac{(\eta - 1)^{3/2}}{\eta^{1/2}} \tag{12.7}$$

What is the relationship of this measurement of F_s to the dissipated energy ΔW and to the energy barrier U_B? Measurements of the ion fluorescence allow us to reconstruct the force-displacement hysteresis loop for this single-ion stick-slip process, as discussed in chapter 11. Let us revisit this loop in Fig.12-5. The measurement of the static friction force F_s comes from the width of this loop and the dissipated energy comes from the area $\Delta W \approx F_s \times \Delta x$ where Δx is the distance between the two degenerate minima of the bistable PT potential at the symmetric point $X = 0$. F_s is the shear force that needs to be applied to overcome the sticking force of the barrier between these minima, corresponding to the largest barrier slope. In a sinusoidal potential, the largest barrier slope is related to the barrier by $F_{max} = \pi U_B/\Delta x$. Taking this relationship for the PT potential,

$$U_B \approx \frac{1}{\pi}F_s\Delta x \approx \frac{1}{\pi}\Delta W \tag{12.8}$$

The height of the hysteresis loop $\Delta x/a$ scales as $(\eta - 1)^{1/2}$ near $\eta \gtrsim 1$ and for $\eta >> 1$, it saturates to unity since in that limit, the distance between the minima is equal to a. A good approximation is

$$\Delta x/a \approx \frac{(\eta - 1)^{1/2}}{\eta^{1/2}} \tag{12.9}$$

Combining this with equations 12.7 and 12.8, gives an approximate expression for the energy barrier U_B:

$$U_B \approx \frac{1}{2\pi^2}\frac{(\eta-1)^2}{\eta} \tag{12.10}$$

and since the depth of the lattice potential in dimensionless units is $\frac{1}{2\pi^2}\eta$, the ratio of barrier height to maximum barrier height (lattice barrier U) is

$$\frac{U_B}{U} \approx \left(\frac{\eta-1}{\eta}\right)^2 \tag{12.11}$$

In Fig.12-5, numerical results for F_s, Δx and U_B as a function of η are compared with the approximate formulae 12.7, 12.9, and 12.10 (left column), and with the experimental determinations of these quantities from the measured hysteresis loops (right column). It is evident that the measurement of F_s is robust and agrees well with the theory, but there is a slight discrepancy in the experimental measurement of Δx, which translates to a discrepancy in the experimental value of U_B. This can be attributed to finite temperature (see chapter 15) and to drifts of the fluorescence signal, to which the measurement of Δx is significantly more sensitive than F_s. For these reasons, we stick to measurements of F_s as the primary experimental signal.

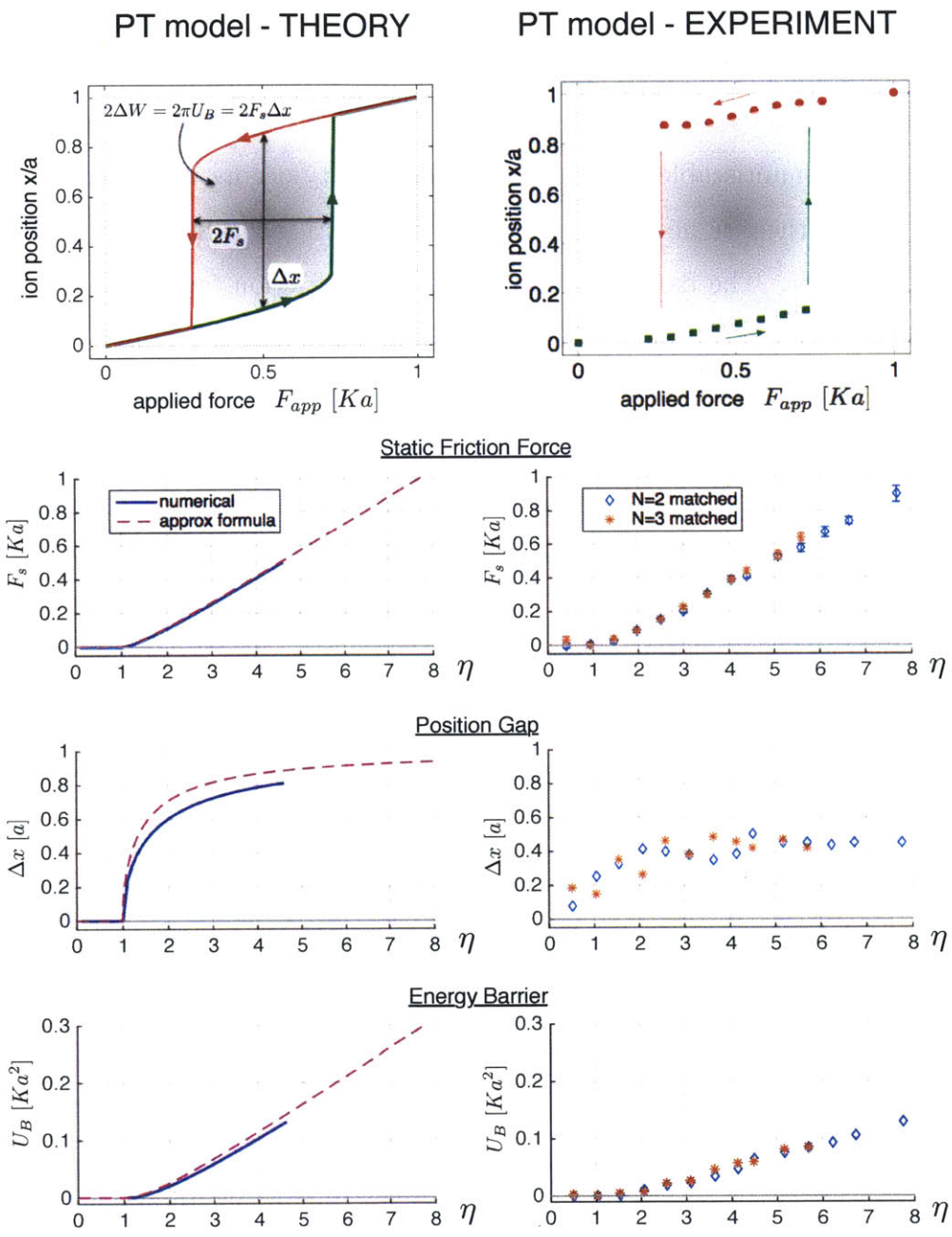

Figure 12-5: Theoretical (left) and experimental (right) hysteresis loops are shown corresponding to the stick-slip of a single ion in the optical lattice. The corresponding measurements of the static friction force F_s (from the width of the loops), of the height of the loops Δx, and of the resultant energy barrier U_B from equation 12.8 are plotted below (for $N = 2, 3$ ions matched to the lattice). The numerical plots of these quantities and the approximate formulae plotted on the left agree well for F_s and agree qualitatively for Δx and U_B.

12.3 Multi-ion contact (matched vs mismatched)

As discussed in detail in the previous section in the context of the PT model, the central concept differentiating finite stick-slip and superlubricity is an energy barrier in a bistable (or multistable) landscape. Superlubricity occurs when the potential is monostable and there is no energy barrier, whereas stick-slip friction increases with the energy barrier. The data showing very different friction forces for the matched cases and the mismatched cases (Fig.12-2) can be understood in terms of a reduction of the energy barrier - the Peierls-Nabarro barrier - due to the Coulomb forces between the ions in a chain mismatched to the lattice. This barrier reduction can be visualized in a 3D plot of the total potential of a 2-ion chain versus the coordinates x_1 and x_2 of the two ions (Fig.12-6). When the ions are matched to the lattice, all the ions always experience identical lattice sticking forces equal to the sticking forces on a single trapped ion in the PT model. As a result, the energy barrier per ion is unmodified compared to a single ion, and scales with η as in the PT model (Fig.12-5). When the ions are mismatched and experience opposite lattice sticking forces, their partial cancellation leads to a reduced barrier U_B.

The transition from superlubricity to stick-slip occurs when the stiffness of lattice confinement $\frac{2\pi}{a^2}U$ overcomes an effective stiffness of the ion chain s. For a single ion, or a matched chain, the competing chain stiffness is given by the common mode $s = K$. However, in the mismatched case, the internal springs g due to a higher-order motional mode also contribute to the competing chain stiffness $s(K, g) > K$ and a deeper lattice U is required to break superlubricity. This suggests defining the parameter $\tilde{\eta}$ in terms of the effective chain stiffness $s(g, K)$ equivalent to the PT parameter η reduced by a factor $\epsilon < 1$:

$$\tilde{\eta} = \frac{2\pi^2 U/a^2}{s(K, g)} = \epsilon\eta \tag{12.12}$$

Assuming the same form for $U_B(\tilde{\eta})$ and $F_s(\tilde{\eta})$ as in equations 12.10 and 12.7, this indeed leads to a reduced energy barrier and static friction force, as well as a transition from superlubricity to stick-slip at a larger value of η given by $1/\epsilon$:

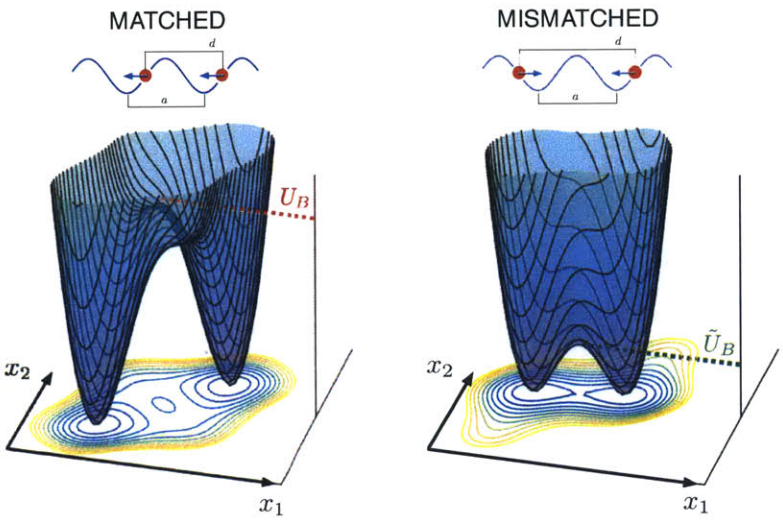

Figure 12-6: Total potential landscape (including Coulomb interactions) for a matched and a mismatched 2-ion chain showing a reduction of the PN energy barrier in the mismatched case.

$$\tilde{U_B} \approx \frac{1}{2\pi^2}\frac{(\tilde{\eta}-1)^2}{\tilde{\eta}} = \epsilon\frac{1}{2\pi^2}\frac{(\eta-1/\epsilon)^2}{\eta} \tag{12.13}$$

$$\tilde{F_s} \approx \frac{1}{2\pi}\frac{(\tilde{\eta}-1)^{3/2}}{\tilde{\eta}^{1/2}} = \epsilon\frac{1}{2\pi}\frac{(\eta-1/\epsilon)^{3/2}}{\eta^{1/2}} \tag{12.14}$$

The model 12.14 indeed fits well to the experimental data for mismatched ion chains with the single parameter ϵ (Fig.12-7a). Indeed, rescaling the η axis for each curve by its fitted value of ϵ, the curves collapse onto the same curve as a function of the rescaled normal load $\tilde{\eta}$, as shown in Fig.12-7b.

Numerical results at zero temperature show a transition from superlubricity to stick-slip at values of η in agreement with the fitted values of $\eta_c = 1/\epsilon$. However, F_s appears to increase with η for $\eta > \eta_c$ much more sharply in the zero-temperature numerical simulations, not following formula 12.14, indicating that the naive rescaling of the normal load that appears to hold experimentally for mismatched crystals, works partially due to finite temperature and thermolubricity, effects discussed in chapter 15.

To conclude this chapter, superlubricity occurs for dimensionless normal loads

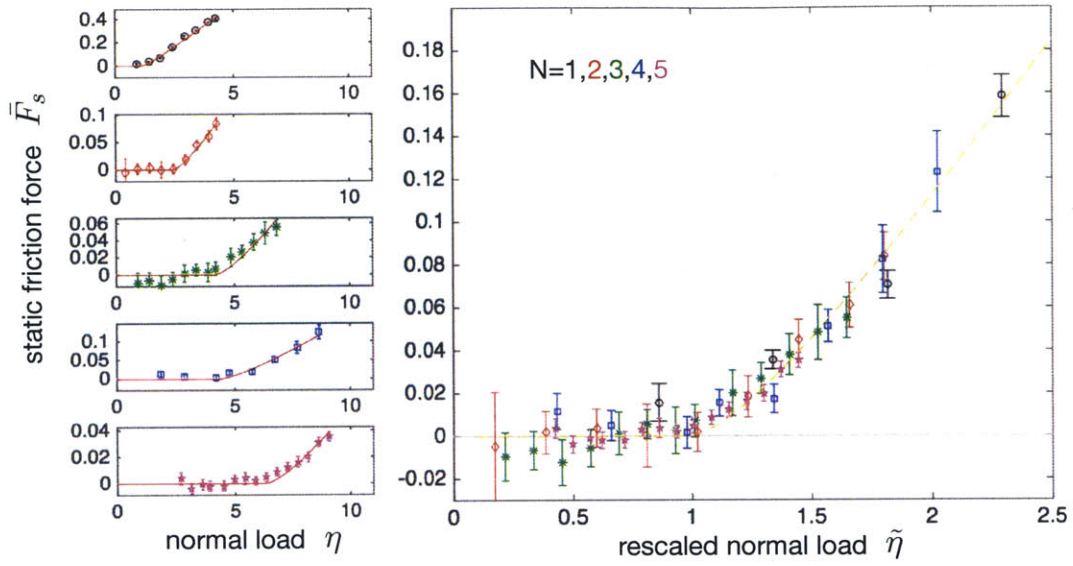

Figure 12-7: When in the mismatched cases the measured friction force F_s versus η is fitted with model 12.14 with the single parameter ϵ, the data for crystals of $N = 1-5$ ions collapses onto a single curve as a function of the rescaled normal load $\tilde{\eta} = \epsilon\eta$. This is consistent with the idea of PN barrier reduction by internal chain stiffness in the mismatched case.

$\eta < 1$ for a single ion or for an ion crystal of any N matched to the lattice, in which case the Prandtl-Tomlinson model explains the onset of stick-slip friction for $\eta > 1$ by the emergence of an energy barrier in a bistable total potential. This barrier is reduced by Coulomb interactions in the mismatched case, resulting in the extension of superlubricity to larger values of η, and the behaviour of the friction force with η under effects of finite temperature can be modeled by a single-particle Prandtl-Tomlinson model with a rescaled dimensionless normal load $\tilde{\eta}$. The mismatched case is considered in more detail in the next chapter on structural lubricity.

Chapter 13

Structural lubricity

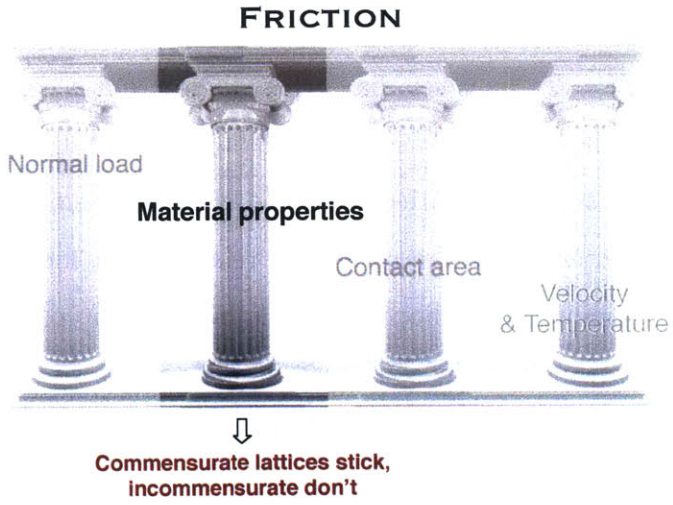

Figure 13-1: In this chapter, I explore the second pillar: the effect of structural mismatch on friction.

The question of how the microscopic structures of contacting surfaces interact at a frictional interface is perhaps the first one that comes to mind in the context of friction. In the empirical law for microscopic friction $F_f = \mu \cdot F_N$, it is embodied in the material-dependent friction coefficient μ, which is believed to be affected by surface roughness on multiple length scales in a complicated way [51, 53, 54, 55, 52]. For atomically smooth contacts at the nanoscale, as in a single asperity contact at the lowest scale of roughness, or as in nano-scale mechanical systems, a simple intuition might be expected to hold. When the atomic lattice constants of the contacting

surfaces are matched (in registry), the two atomic lattices can lock together and stick, resulting in large friction. When the lattice constants are mismatched, or in the extreme case incommensurate, the two lattices do not lock and the cancellation of sticking forces can significantly reduce friction. In fact, superlubricity can occur as a result of this structural effect. As discussed in chapter 12, the effect is to extend the superlubric regime to larger values of the critical normal load that breaks it.

Varying the lattice constants of surfaces in contact is difficult to do in condensed matter interfaces, requiring the use of different materials. One trick, that has been utilized to observe structural superlubricity in an atomic force microscope [75, 74], involves rotating one surface with respect to the other surface. Unfortunately, individual atoms cannot be accessed in such a system to verify the locking hypothesis and to study the microscopic behaviour of the friction process with varying degrees of structural lubricity. We do, however, have this single-atom access in our ion-crystal optical-lattice friction interface. This enables us to show that as the relative length scales of the two structures are varied from matched to mismatched, friction is reduced, and the character of this reduction is related to a localization of kinks as the atoms go from sticking and slipping simultaneously to crossing lattice barriers one at a time. This transition in a finite system is related to the commensurate-incommensurate transition in the infinite chain as in the Frenkel-Kontorova model, also known as the Frank-van-der-Merwe transition [63].

13.1 Observation of structural lubricity

Recall from section 10.4 that the ion chain spacing is inhomogeneous and that we define matching between the trapped ion crystal and the optical lattice in terms of the parameter q representing the normalized potential barrier to the displacement of the unperturbed (infinitely rigid) ion crystal:

$$q = \max_{\phi}\left(\frac{1}{N}\sum_{j}^{N}\sin\left(\tfrac{2\pi}{a}x_{0,j} - \phi\right)\right) \tag{13.1}$$

When we measure the frictional hysteresis of each ion in a matched ($q = 1$) crystal of $N = 1 - 6$ ions, we observe large hysteresis loops, with large values of the static friction force F_s and of the energy dissipated during a slip ΔW for each ion (Fig. 13-2a). The ions are observed in this case to stick and slip simultaneously. This explains the large F_s and ΔW as the simultaneous catastrophe (slip) of all the particles leads to a large amount of released energy. Furthermore, because the ions stick and slip simultaneously, only their common motional mode ω_0 participates in the process, which is identical for a single trapped ion in that harmonic potential. This is consistent with our observation (also discussed in chapter 12) that the measured friction force for each ion in the matched crystal of any size N is equal to that for a single trapped ion at the same value of $\eta = (\omega_L/\omega_0)^2$ which parametrizes the Prandtl-Tomlinson model. The other parameter, describing the internal chain stiffness g in the FKT model, drops out of the problem.

When we measure the frictional hysteresis of each ion in a mismatched ($q = 0$) crystal of $N = 1 - 6$ ions, we observe that the hysteresis loops are significantly reduced or vanish (Fig.13-2b). The ions are observed to pass the lattice maxima one at a time, in a staggered fashion. The reduction in friction can therefore be interpreted as additional confinement against slipping of each ion on top of a lattice barrier by its better pinned neighbours via the internal springs g, as the ion crystal is translated across the lattice. This stiffness against internal deformations with the energy scale of the highest vibrational mode can result in smooth translation of the entire chain along the lattice in a snake-like motion reminiscent of kinks.

13.2 Commensurate to incommensurate transition

As we vary the matching parameter q continuously from the matched case $q = 1$ to the mismatched case $q = 0$ by tuning the external harmonic confinement $K = m\omega_0^2$ (see section 10.4), the static friction force $\bar{F}_s$ and dissipated energy $\overline{\Delta W}$ drop quickly from the single-ion value at first, then approach slowly a much reduced value near $q = 0$ (Fig.13-3 and 13-4). This reduced value decreases with increasing chain size N

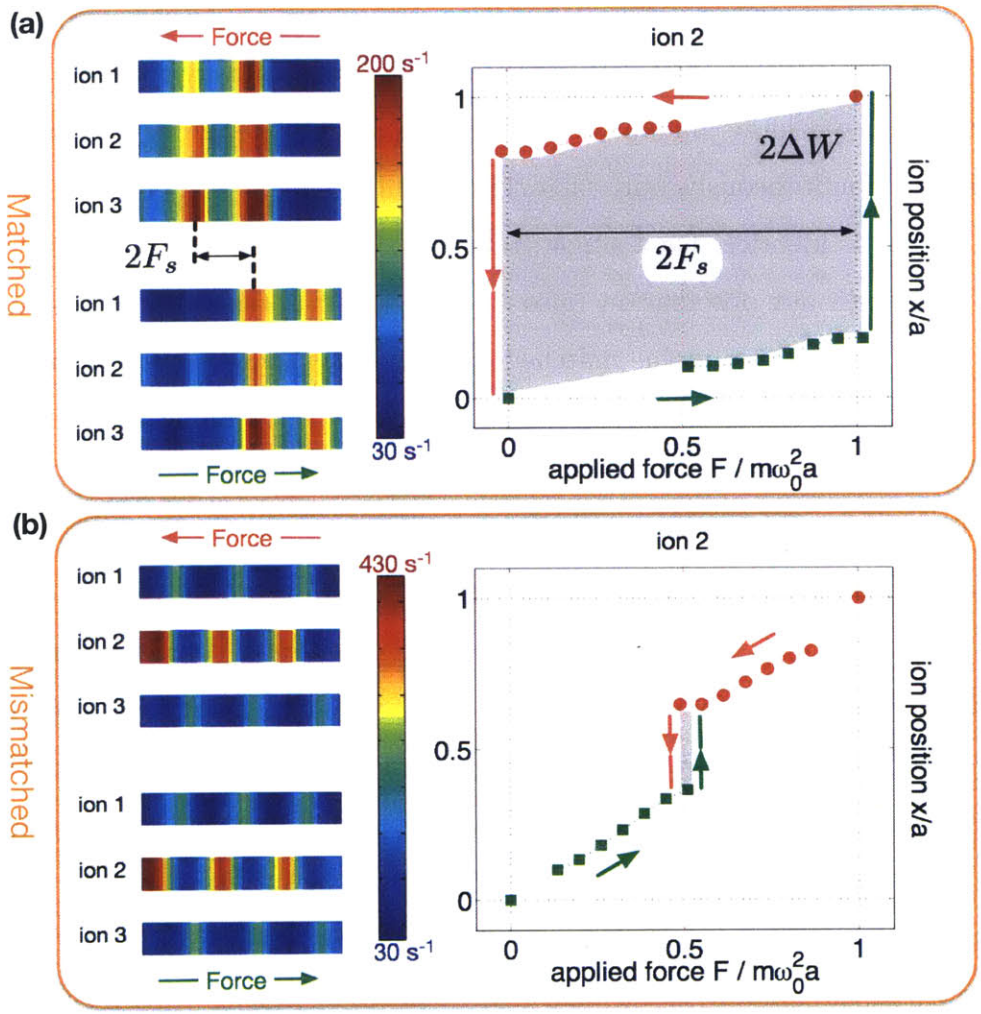

Figure 13-2: Changing friction in a 3-ion crystal from maximal to nearly frictionless (superlubric) by structural mismatch. In the matched case (top), the ions stick and slip synchronously during transport (the observed fluorescence for each ion expressed as a photon detection rate and indicated by the color, is maximum when the given ion slips over a potential barrier). The large hysteresis loop corresponds to large friction, shown here for the middle ion. In the mismatched case (bottom), the different ions slip in a staggered fashion and the friction and hysteresis loop nearly vanish. The results shown are taken at a value of the dimensionless normal load η just below 4.6.

at a fixed η, consistent with the measured curves of F_s vs η in chapter 12. This is also consistent with the fact that friction reduction comes from additional confinement by the internal springs g, which increase with growing N (section 10.3).

The observed 10-fold reduction in friction already for $N = 2$ ions and a 100-fold reduction for $N = 6$ ions is interesting because no energy scales were changed in the system. This lubricity is purely structural, coming from a slight tweak of ion separations on the scale of the optical wavelength. This lesson can be important in designing materials and nano-scale mechanical systems with ultra-low (or ultra-high, as needed) frictional coefficients.

The property of simultaneous or staggered crossing of lattice barriers can be captured by the degree of slipping synchrony

$$\xi = \max_{\phi}\left(\frac{1}{N}\sum_{j}^{N}\sin\left(\tfrac{2\pi}{a}X_j - \phi\right)\right) \tag{13.2}$$

defined analogously to the matching parameter q in equation 13.1, but with intrinsic ion positions $x_{j,0}$ replaced by trap positions X_j where each ion crosses the barrier or slips (the maximum fluorescence point). The slipping synchrony is basically the correlation of ion slipping times during the force ramp that translates the trap position X, and it is measured in the same way as the matching parameter (see section 10.4), but during the actual friction experiments (rather than in the limit of low lattice depth and slow driving). The synchrony varies between $\xi = 1$ for simultaneous slipping and $\xi = 0$ for maximally staggered slipping.

The measured degree of slipping synchrony (Fig.13-5) exhibits a transition from simultaneous slipping ($\xi = 1$) of the ion crystal for $q \gtrsim q_c$ to staggered slipping ($\xi < 1$) for $q \lesssim q_c$. This means that the first regime $q \gtrsim q_c$ can be viewed as single-particle stick-slip in the Prandtl-Tomlinson model with an effective value of $\tilde{\eta} = \frac{2\pi^2 U/a^2}{s(K,g,q)}$ that scales as $\tilde{\eta} \approx \eta\frac{1}{1-q_c}(q - q_c)$ to lowest order, where $s(K, g, q)$ is an effective chain stiffness (discussed also in chapter 12) with a q-dependent contribution from internal springs g due to Coulomb interactions. In the second regime $q < q_c$, a single ion can slip without forcing the rest to do the same, forming a kink that propagates one ion

at a time. In this regime, friction appears to be nearly independent of the matching parameter q.

These results point to an important conclusion about structural lubricity: it is robust to imperfect mismatch. Friction is low and independent of q for a large range of values $q < q_c$; as long as ions cross lattice barriers one at a time, the exact timing of these crossings or slips does not affect friction. In fact, the robustness to structural lubricity to mismatch is a feature of the finite system. This brings us to the next chapter, where I show observations of the Aubry transition in our finite system and discuss the questions of contact size and the concept of incommensurability in a finite system.

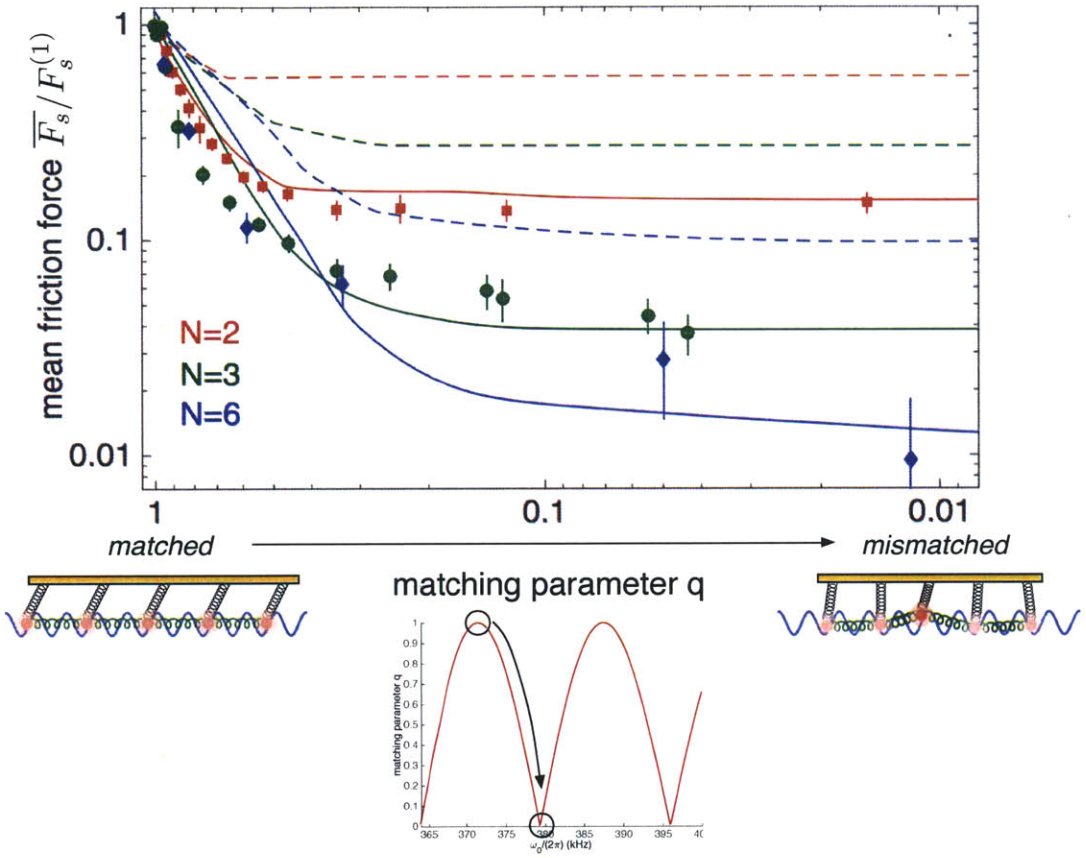

Figure 13-3: The dependence of static friction force on the structural mismatch q between the ion crystal and the optical lattice for different crystal sizes. The value of q is tuned from the matched case ($q = 1$) to the mismatched case ($q = 0$) by changing the trap vibrational frequency ω_0. The static friction force $\bar{F}_s$ is plotted, averaged over the ions and normalized to $F_s^{(1)}$ as measured for a single trapped ion. The results shown are taken at a value of the dimensionless normal load η just below 4.6. Error bars represent 1 standard deviation. Simulations are shown for zero temperature (red, green and blue dashed lines) and finite q-dependent temperature (red, green and blue solid lines), indicating that in the limit of low q structural lubricity and structural thermolubricity reduce the observed friction by similar factors in our data (see chapter 15).

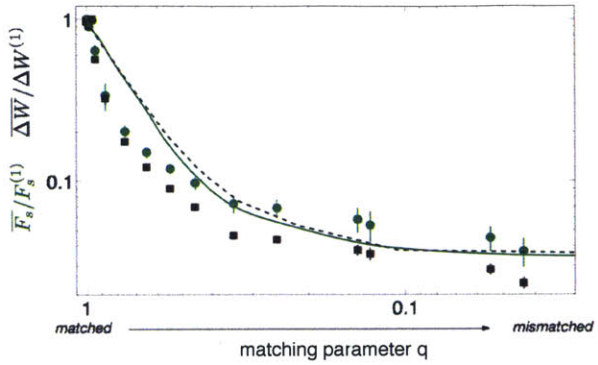

Figure 13-4: The dependence of mean dissipated energy $\overline{\Delta W}$ on the structural mismatch q between the ion crystal and the optical lattice for $N = 3$ ions. The results shown are taken at a value of the dimensionless normal load η just below 4.6.

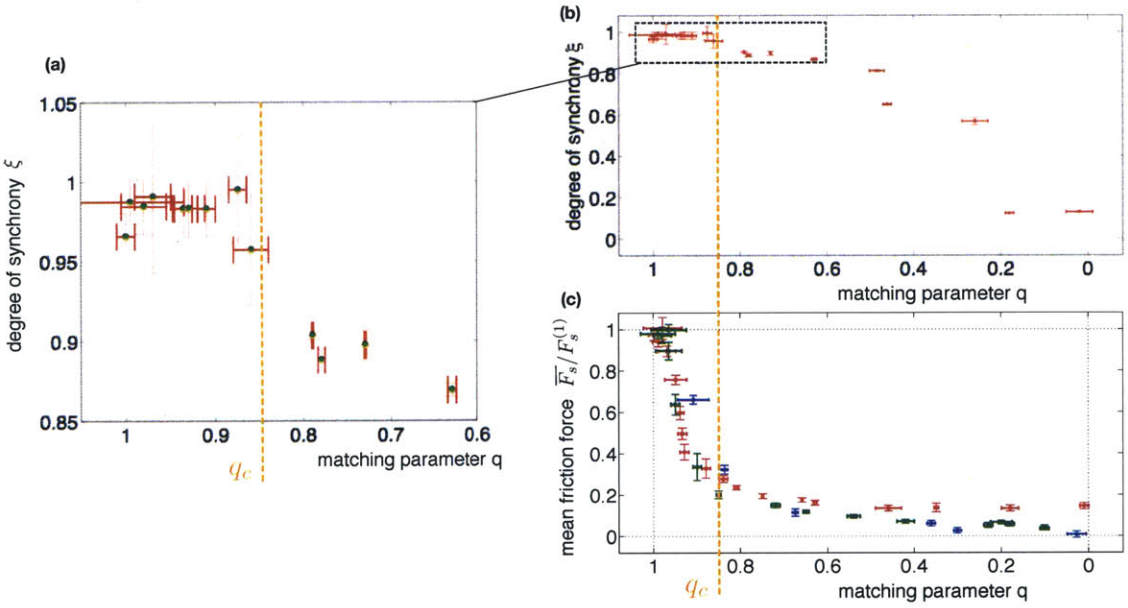

Figure 13-5: The measured degree of slipping synchrony as a function of matching parameter q, shown here for an $N = 2$ ion crystal at η just below 4.6. The results are compared to the measured friction force $\bar{F}_s/F_s^{(1)}$ from Fig.13-3, showing that for $q > q_c$ where the friction force drops linearly with q, synchrony is locked at $\xi = 1$: the ions slick and slip synchronously. Below q_c, staggered slipping sets in ($\xi < 1$), and friction becomes nearly independent of q. Here, q_c was loosely assigned to the point when synchrony breaks and ξ deviates from unity.

Chapter 14

Aubry transition

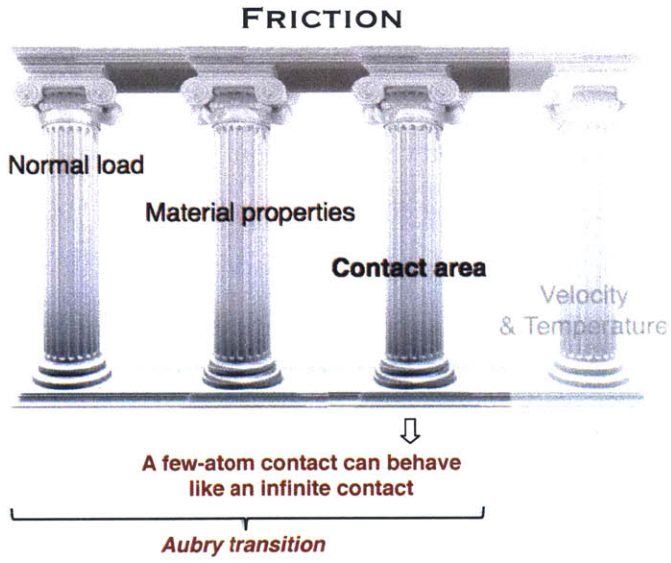

Figure 14-1: In this chapter, I tie together our findings about structural lubricity and superlubricity at low normal load to demonstrate the first observation of the Aubry transition. I wrap up with the related question of the third pillar: the dependence of friction on the true contact area (the number of atoms at the contact).

In chapters 12 and 13, I discussed our observations of superlubricity - the vanishing of stick-slip friction - between finite ion chains and the optical lattice below a critical normal load (lattice depth) and as a result of mismatch between the ion chains and the lattice. Superlubric behaviour - a dynamical frictional phenomenon - has been conjectured to be related to a translationally invariant sliding phase - a static property of the ground state of the infinite-chain Frenkel-Kontorova model, found by

Aubry [64, 105, 106, 107] to occur below a critical substrate corrugation depth when the chain is incommensurate with the substrate. Above the critical corrugation depth, he found that the infinite chain gets pinned and analyticity-breaking occurs in the atomic positions, which form an everywhere-discontinuous fractal "staircase" pattern relative to the substrate period (Fig.14-2). Although signatures of superlubricity have been observed at the nanoscale [73, 74], a clear connection to Aubry's sliding phase has never been made, and the Aubry analyticity-breaking transition has never been directly observed. One reason for this is that the transition as discussed by Auby happens in a very theoretical limit of a static, infinite, maximally incommensurate chain interacting only with a sinusoidal potential (without any external confinement). However, a realistic experimental scenario is dynamical (involving, for example, measurements of friction), and involves finite atom chains, which might additionally be attached to an external support, which provides external confinement and breaks discrete translational symmetry of the sinusoidal potential. The Aubry transition concept has been extended to finite chains as a reflection-symmetry-breaking transition due to the pinning of the center ion in an odd chain [92, 98, 99, 63]. Separately, it has been extended to infinite chains with finite external confinement, in which the frequency of the soft "sliding" mode is lifted to a finite value [93] and the critical pinning corrugation U_c is pushed to a larger value [95, 96]. Even though these modifications represent a more physical situation, quantitatively linking any observations of superlubricity and superlubricity breaking to the Aubry transition concept involves linking the dynamical processes to the static properties and having full control of microscopic parameters and individual atoms. Such experimental capabilities, achieved for the first time in our system, and the experimentally-guided conceptual connection between the statics and dynamics in our system, enable us to claim the first observation of the Aubry transition via superlubricity breaking. I discuss this milestone in this chapter.

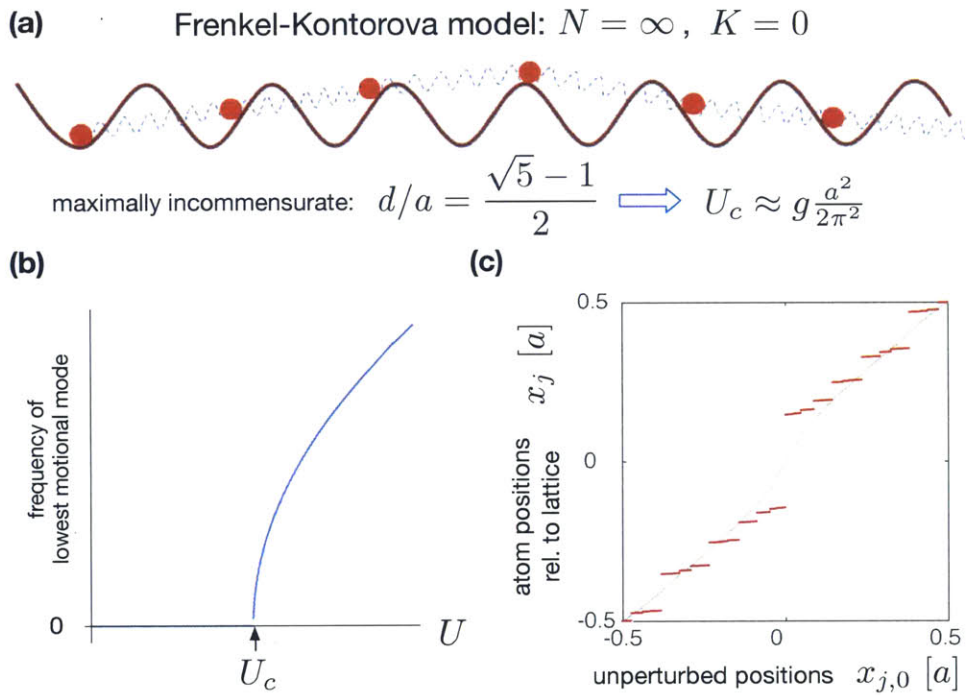

Figure 14-2: **(a)** The infinite-chain Frenkel-Kontorova model is where the Aubry sliding-to-pinned structural transition was predicted to occur. The largest value of the critical potential depth where pinning occurs is set by the stiffness of next-neighbour springs g, and occurs at the maximally incommensurate Golden ratio spacing of the chain relative to the periodic potential. **(b)** The sliding phase below the Aubry analyticity-breaking transition manifests itself as a soft (zero-frequency) motional mode, conjectured to be related to superlubricity. **(c)** The ground-state curve of allowed atomic positions relative to the substrate potential goes from continuous below the transition, to a fractal staircase with forbidden regions or gaps above the transition, earning the term "analyticity-breaking transition".

14.1 Static and dynamic manifestations of pinning

In general, both the static and dynamic properties of a chain of atoms in the periodic potential of a substrate lattice are governed by two competing length scales and two competing energy scales. The intrinsic chain spacing competes against the lattice spacing, and the stiffness of the chain competes against pinning by the lattice. When the spacings are mismatched and the atom chain is stiff, it is stable against pinning and favours its intrinsic arrangement, where atoms can take any positions with respect to the lattice period and there is a cancellation of lattice forces - the total potential landscape is monostable, without barriers. Dynamically, this means that the chain can be smoothly translated through the lattice, manifesting in superlubricity. If the depth of the lattice potential is increased, at the point when it overcomes the chain stiffness, the chain becomes unstable against pinning and the atoms reorganize towards lattice minima and avoid lattice maxima (Fig. 14-3), which become Peierls-Nabarro (PN) energy barriers in the a multistable total potential [63]. Dynamically, the finite force, required to move the chain over these barriers, manifests in stick-slip friction.

Consider for each atom j its position relative to the lattice period in the form of the displacement from the nearest lattice maximum x_j (Fig. 14-3). Since the pinning transition manifests in exclusion of atoms from lattice maxima, one can parametrize it via the disorder parameter $x_{min} = \min_j |x_j|$ giving the closest distance to a lattice maximum [113]. Consider first the infinite-chain limit. The atoms whose intrinsic positions coincide with lattice maxima $x_{j,0} = 0$, stay there below the pinning transition, giving $x_{min} = 0$. Above the transition, they displace left or right and $x_{min} > 0$ as a result of anti-confinement by the negative lattice curvature $\frac{2\pi^2}{a^2}U$ overcoming the confinement due to total chain stiffness (g and K), and creating a finite PN barrier there (Fig. 14-3). Analyticity breaking is the formation of discontinuities in the curve of an atom's relative position x_j in the ground state versus its unperturbed position $x_{j,0}$ as the position of the support X is varied. (Since all the atoms in an infinite chain are equivalent, this curve is identical for all j and coincides with the

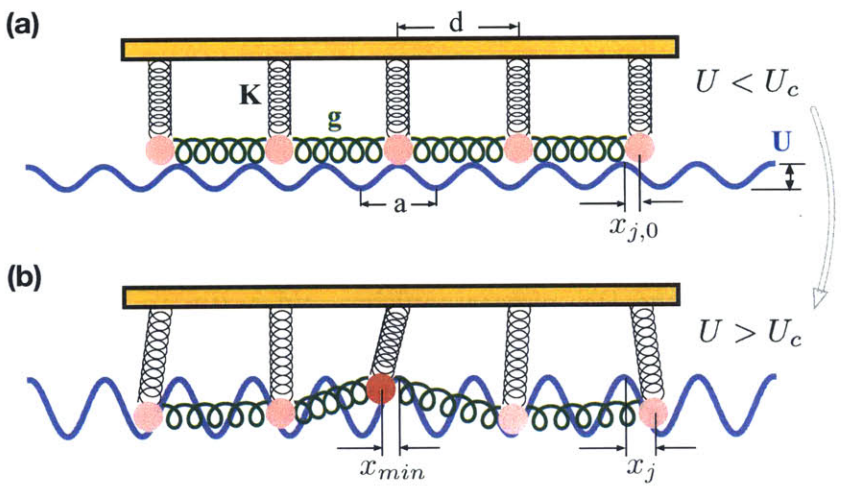

Figure 14-3: The Frenkel-Kontorova-Tomlinson model showing a structural transition in the atomic position distribution. **(a)** When $U < U_c$ the chain is unpinned with atoms at their intrinsic unperturbed positions $x_{j,0}$ relative to the nearest lattice maxima. **(b)** When $U > U_c$ the chain is pinned wit the atoms at their pinned positions x_j relative to the nearest lattice maxima. The distance of the center atom to its closest maximum, denoted x_{min} parametrizes the reflection-symmetry-breaking transition.

hull function [63].) The curve is continuous (analytic) below the pinning transition. Above the transition it has a jump at $x_{j,0} = 0$ from $-x_{min}$ on one side of the PN barrier to $+x_{min}$ on the other side because the global minimum switches from the left local minimum to the right local minimum. In the same way, one of the neighbouring atoms $j \pm 1$ at distance d away is forbidden from a lattice maximum when the intrinsic position of atom j is $x_{j,0} = \pm d (\mathrm{mod}\ a)$, and the forces exerted on it by the neighbours produce smaller jumps in x_j at these points. Another pair of even smaller jumps occurs at $x_{j,0} = \pm 2d (\mathrm{mod}\ a)$ due to next-next neighbours, and so on down the chain. For an infinite incommensurate chain with irrational $d (\mathrm{mod}\ a)/a$, as in the Aubry limit, the curve of x_j forms a fractal staircase with an infinite number of jumps and is nowhere analytic (Fig.14-4a). For a finite mismatched chain, each curve x_j should have N jumps near the points $x_{j,0}$ that put an atom in the chain over a lattice maximum (Fig.14-4b). For the center atom $j = (N+1)/2$ in an odd-N chain, the main jump, which corresponds to displacement of this atom and the rest of the chain to the left or to the right of the symmetry point at a lattice maximum, parametrizes the reflection-symmetry-breaking transition [92, 98, 99, 63].

To visualize the dynamical situation of stick-slip friction, consider an atom's relative position x_j versus the intrinsic position $x_{j,0}$ when the support is moved sufficiently quickly so that the chain does not have time to relax across the PN barrier, and instead follows the local minimum. Above the pinning transition, as $x_{j,0}$ crosses from left to right the value where x_j jumps in the static case, the chain sticks to the left metastable state until the PN barrier vanishes and a slip to the global minimum occurs (Fig.14-4c). When the support is moved in the opposite direction, the chain sticks to the right metastable state before slipping to the global minimum on the left. This dynamical process results in hysteresis loops centered around the jumps in the static x_j (Fig.14-4c,d). Below the pinning transition, there are no PN barriers: the superlubric chain always follows the global minimum and the dynamic curve of x_j coincides with the continuous static curve. Thus, the hysteresis that can be used to measure friction [17, 112] across the boundary between superlubricity and stick-slip, can also be used to measure the opening of gaps in the atomic position distribution across the pinning transition: the two are different aspects of the same physical phenomenon.

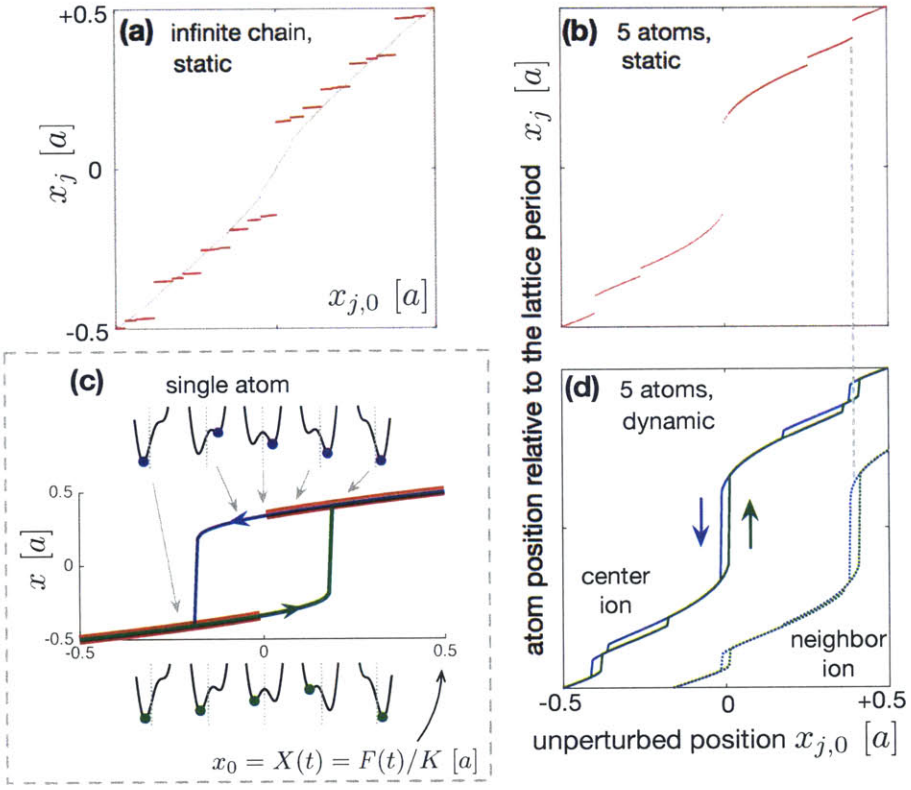

Figure 14-4: Analyticity breaking as formation of gaps in the ground-state position distribution of atoms relative to the lattice. **(a)** In the limit $N \to \infty$, $K \to 0$ corresponding to the Frenkel-Kontorova model, and at $d(\mathrm{mod}\ a)/a = (\sqrt{5}-1)/2$, the curve of allowed ground state positions x_j versus $x_{j,0}$ is continuous below the Aubry transition (grey) and forms a fractal staircase above the Aubry transition (red). (Numerical results shown are for $N = 101$ and $K/g = 0.0078$.) **(b)** For a realistic nanocontact, for example $N = 5$, $K/g = 1$ and $d(\mathrm{mod}\ a) = (\sqrt{5}-1)/2$, a finite staircase forms above the transition. **(d)** In a dynamical situation (fast translation of the support), the gaps in this staircase appear as hysteresis loops in measurements of friction above the superlubricity-breaking transition. The trajectory for a neighboring ion is shown with a dotted line to emphasize that the secondary gaps are due to the primary instabilities of other ions in the chain near their respective lattice maxima. **(c)** Illustrated here for a single ion, the ground-state ion position (red) is given by its position up to the midpoint of a hysteresis loop in a friction experiment, where the global minimum switches from one site to the next.

14.2 Observation of forbidden positions via stick-slip

We perform friction experiments by applying an external electric force F_{app} to quickly move back and forth the position $X(t) = F_{app}(t)/K$ of the axial trapping potential, thus translating the intrinsic ion positions $x_{j,0}(X(t)) = x_{j,0}(0) + X(t)$. The dynamic position curves x_j are then mapped out by monitoring the position of each ion via fluorescence. In the elementary case of a 2-ion partially mismatched chain we observe two hysteresis loops in each ion's position: a large one due to the primary slips of the ion over its lattice maximum, and a smaller one due to secondary slips induced by the primary slips of the other ion (Fig.14-5). These hysteresis loops correspond to the points where analyticity is broken for the finite chain. The heights of the loops give the desired static discontinuities in x_j - forbidden regions in the atomic position distribution. The left and right edges of the loops correspond to the slipping events in the stick-slip process, and as before, half the difference in F_{app} between the forward and reverse slips gives the static friction force F_s required to pull the chain over the corresponding PN barrier and the area enclosed by the loops gives the energy dissipated by stick-slip friction. We observe both the primary and secondary loops to open up from zero with increasing lattice depth, in qualitative agreement with zero-temperature numerical simulations, despite a decreased size and distorted shape of the secondary loop as a result of the finite temperature in our system (chapter 15).

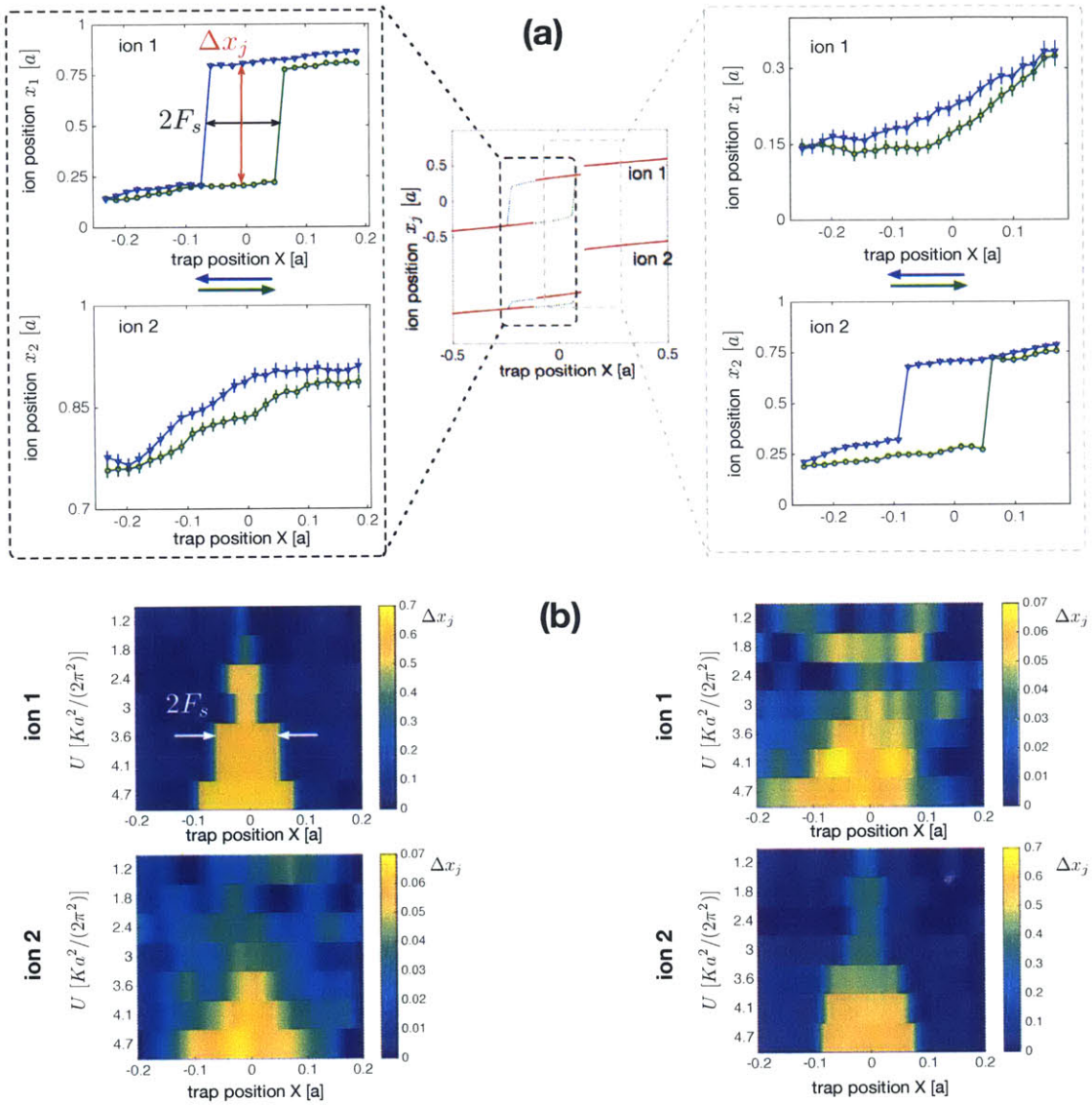

Figure 14-5: Observation of analyticity breaking in a 2-ion chain. **(a)** The measured displacements from lattice maxima x_1, x_2 versus the intrinsic displacements $x_{1,0}, x_{2,0}$ show a secondary hysteresis loop for ion 2 induced by the primary hysteresis loop of ion 1 (left), when the trap position X is quickly moved forward and backward in the vicinity of a Peierls-Nabarro barrier that causes a large gap in the ground-state position distribution of ion 1. Similarly, the primary hysteresis loop on ion 2 induces a secondary hysteresis loop on ion 1 (right). The heights of these loops give measurements of these gaps, and the width of the loops give a measurement of the static friction force F_s. Note the different scales of the primary and secondary loops. The 2 ions in this measurement are partially mismatched to the lattice with $d(\mathrm{mod}\ a)/a \approx 2/3$ and $q \approx 0.5$. The error bars show a statistical uncertainty of 1 standard deviation. **(b)** As the lattice depth U is increased, the measured loops open up as seen in the increasing difference between the forward and backward ion positions Δx_j, shown in colour, and in the increasing static friction force, corresponding to the half-width of the color region $\Delta x_j > 0$.

14.3 Observation of the Aubry transition

To measure quantitatively the transition from analyticity to the gapped pinned phase and from superlubricity to finite friction as a function of lattice depth U, we measure, ion-by-ion, the static friction force F_s, which is the most experimentally reliable measurement of the sizes of the hysteresis loops. As discussed in chapter 12, for chains of $N = 1 - 5$ ions, we clearly observe superlubricity below a critical value of the lattice depth U_c as vanishing of the measured friction force within experimental errors (Fig.14-6). When the ions are matched to the lattice ($q = 1$), superlubricity is observed to break at $U_c \approx Ka^2/(2\pi^2)$ for all N (Fig.14-6b) as in the single-atom limit of FKT corresponding to the Prandtl-Tomlinson model [58]. In other words, anti-confinement by the lattice only needs to overcome the external chain stiffness K, and neither the number of ions N, nor the internal springs g have an effect on friction, because when the ions are in registry with the lattice, they are always subject to same lattice sticking forces. When the ions are mismatched to the lattice ($q = 0$), superlubricity is observed to break at values of $U_c > Ka^2/(2\pi^2)$ (Fig.14-6a) due to structural superlubricity [17] as mismatch activates the stiffness of internal springs g in keeping the ions at their intrinsic positions against the lattice forces. The observed increase of U_c with ion number can be explained by the fact that g increases with N in a harmonic trap as $g/K \approx \frac{1}{4}N^{1.65}$ (see section 10.3). Thus, in the large N limit, the internal springs dominate the chain stiffness and the pinning behaviour, as in the Frenkel-Kontorova limit [91], where the Aubry transition occurs at the largest value $U_c = ga^2/(2\pi^2)$ when the chain and the substrate are maximally incommensurate at a spacing ratio equal to the Golden ratio $d(\mathrm{mod}\ a)/a = (\sqrt{5}-1)/2$. When g and K are comparable in an infinite golden-ratio chain, the Aubry transition should occur [95, 96] at $U_c \gtrsim (g+K)a^2/(2\pi^2)$.

We extract the critical lattice depth U_c at the superlubricity-breaking transition using a piecewise linear fit (Fig.14-6) to the measured static friction force on the central ion(s) in the chain (corresponding to the symmetry-breaking transition in an odd chain). The experimental data points of U_c versus the effective g/K at the chain

center, obtained from chains of different N (Fig.14-7a), agree with the analyticity-breaking Aubry transition in an infinite golden-ratio chain with finite external confinement K. In other words, our finite inhomogeneous system simply tuned to cancel the lattice forces on an unperturbed arrangement of the chain ($q = 0$) is as robust against analyticity and superlubricity breaking as Aubry's upper bound in an infinite, maximally incommensurate chain. To understand this, one must consider the finite periodicity resolution $1/N$ set by the size of a finite system. Indeed, for the mismatched intrinsic chain arrangements that are observed to follow the Aubry transition limit, separations between neighbouring ions $d_{j,j+1}(\text{mod } a)/a$ tend to fall within this resolution of the golden ratio (Fig.14-7c). In fact, for a homogeneous chain, one can show that for any N there exists a choice of spacing $d(\text{mod } a)/a = l/N$, where l is an integer, such that the chain is mismatched to the substrate ($q = 0$) and $d(\text{mod } a)/a$ is within $1/2N$ of the golden ratio. This reconciles the intuitions that a finite system is maximally superlubric when mismatched to the substrate, and that an infinite system is maximally superlubric (statically, largest sliding phase) when maximally incommensurate with the substrate.

I close this chapter by addressing one of the questions posed in the beginning: how the number of contact atoms affects nanofriction. The answer depends on the material properties and the normal load. When the intrinsic arrangement of nanocontact atoms is matched to the substrate crystal lattice, each atom experiences an identical friction force, so the total friction force is proportional to the number of atoms, or the true contact area. However, friction vanishes in superlubricity below a critical normal load which does *not* depend on the number of atoms, but only on the stiffness of the contact. When the arrangement of contact atoms is suitably mismatched, the total friction force is again proportional to the number of atoms in the limit of large normal loads. At low normal loads, but higher than the critical load in the matched case, all the atoms at the nanocontact become superlubric except for the boundary atoms, and friction becomes independent of the number of contact atoms. Surprisingly, this occurs at the same normal loads for small contacts and for infinite contacts, independent of the size and function only of the contact's stiffness to deformation.

At an even lower normal load, which again depends only on the stiffness of the contact, the whole contact becomes superlubric.

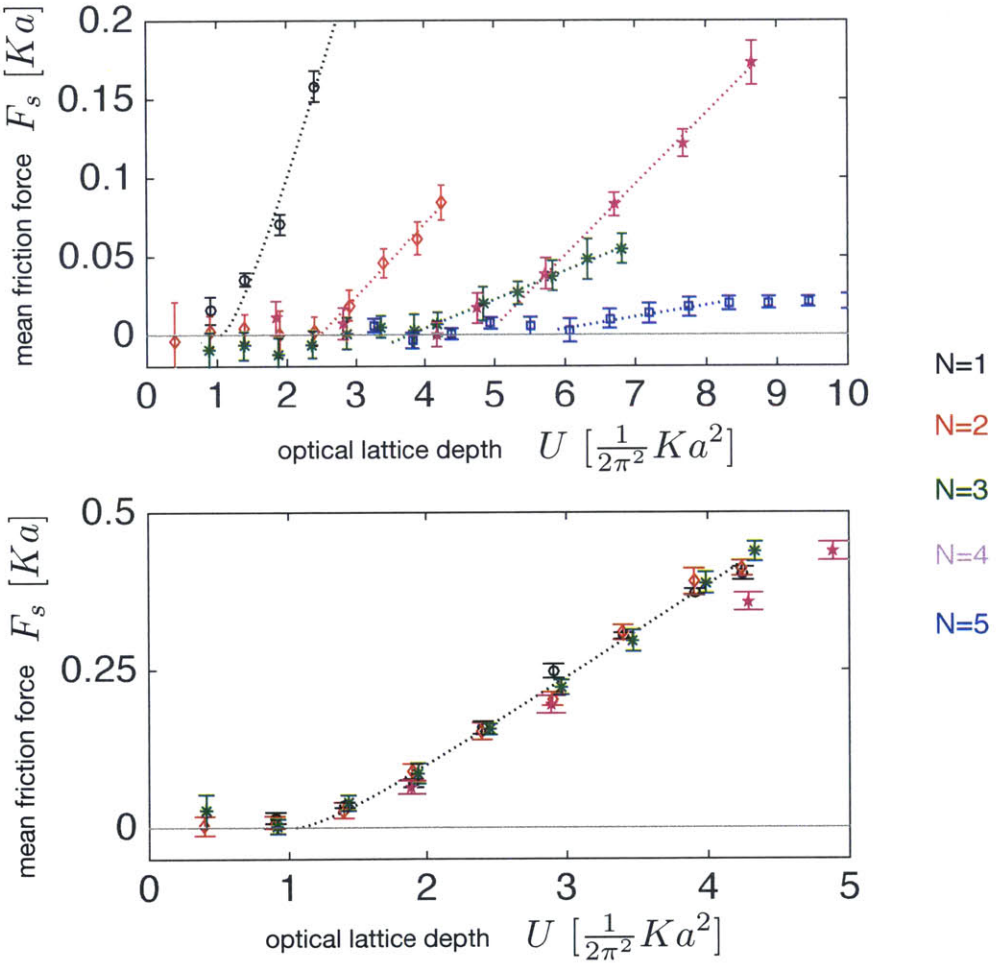

Figure 14-6: In chapter 12, we observed the transition from superlubricity to stick-slip as a function of lattice depth U (normal load η), shown here again for mismatched (top) and matched (bottom) ion chains with $N = 1 - 5$. This observed superlubricity-breaking transition in the mismatched cases (top) corresponds to the Aubry analyticity-breaking transition. This is testified by the agreement of the superlubricity-breaking lattice depth U_c with the expected analyticity-breaking lattice depth in the Aubry limit, as can be seen in Fig.14-7. To extract the values of U_c from the data, here we fit an analytical formula for the PT model to the single-ion and the matched chain results, and for the mismatched chain results we fit the lowest-order piecewise linear model $b + a(U - U_c) \cdot H(U - Uc)$, where H is the Heaviside step function, the measured friction of a central ion in the chain. The part of the fit for $U > U_c$ is shown as dotted lines.

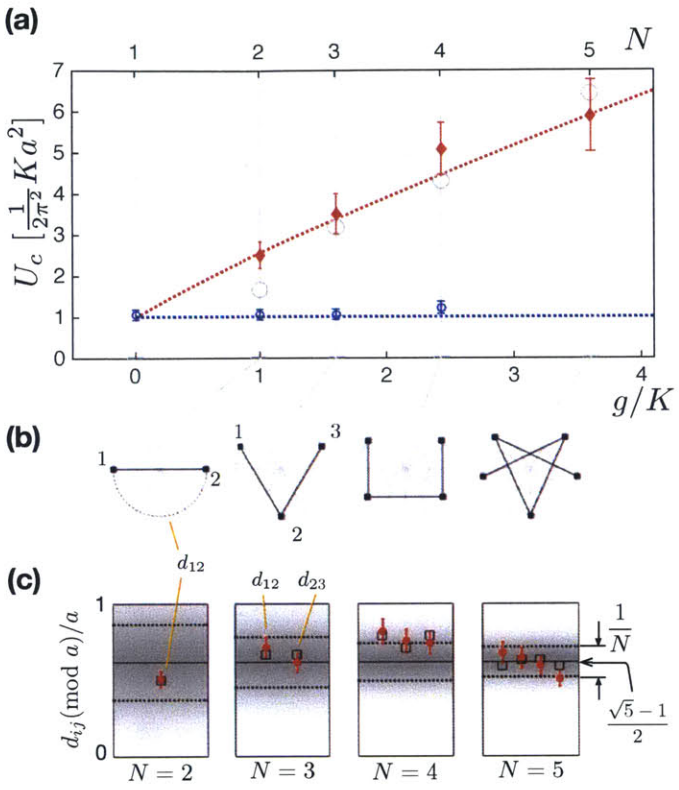

Figure 14-7: **Aubry transition in finite "incommensurate" ion chains. (a)** The measured superlubricity-breaking point U_c for the center ion plotted against the internal spring stiffness (each value of g/K is obtained at a different ion number N plotted on the second horizontal axis at the top). In the matched case (blue open circles), regardless of ion number or internal springs, the breaking point follows the PT limit (blue dotted line). In the mismatched case (red filled diamonds), the breaking point follows the Aubry transition ($N = \infty$, $d(\mathrm{mod}\ a)/a = (\sqrt{5}-1)/2$) modified [95, 96] by the finite external confinement K (red dotted line). The gray open circles are numerical simulations of our finite, inhomogeneous system. The error bars represent a $\pm 12\%$ systematic uncertainty in applying the lowest-order fitting model as obtained by the fidelity of U_c determination on the numerical results. **(b)** For each ion number, mismatching is achieved by placing the ions at the calculated relative phases shown. **(c)** The calculated configurations correspond to ion spacings shown in black: $d(\mathrm{mod}\ a)/a = 1/2$ for $N = 2$, $d(\mathrm{mod}\ a)/a = 2/3$ for $N = 3$, and inhomogeneous spacings close to $d(\mathrm{mod}\ a)/a = 3/4$ for $N = 4$ and close to $d(\mathrm{mod}\ a)/a = 3/5$ for $N = 5$. Shown in red are actual measured spacings, which deviate from the expected due to a 1%-scale asymmetry of the axial trap. One can see that the effects of inhomogeneity and asymmetry still put the ion separations $d_{j,j+1}(\mathrm{mod}\ a)/a$ in our finite chains within the $1/N$ resolution window (gray shading and dotted lines at 1σ) around the Golden ratio $(\sqrt{5}-1)/2$, explaining why the observed superlubricity breaking agrees with the Aubry transition.

Chapter 15

Velocity-dependence of friction and thermal dynamics

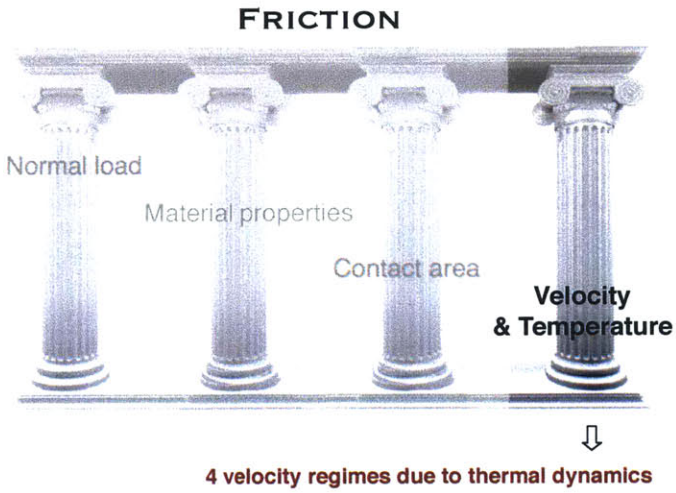

Figure 15-1: In this chapter, I explore the fourth pillar of friction: its velocity and temperature dependence.

Amonton's and Coulomb's empirical "third law" of friction states that kinetic dry friction is independent of velocity. In reality, in many situations, it exhibits complex velocity [77, 78, 79, 80] and temperature dependence [80, 81, 82, 83], which are intimately related at the atomic scale, yet still difficult to understand as a result of non-equilibrium, highly nonlinear dynamics [76]. In the context of stick-slip friction, these phenomena are governed by the interplay of the driven transport and thermal

dynamics time scales, related to dissipation and thermal hopping across energy barriers. While modeling of this at the atomic scale has been extensive [84, 85, 86, 87, 88], pinning down the microscopic mechanisms of velocity and temperature dependence using nanotribology experiments is challenging without full control and independent measurement of all the microscopic parameters of the system including the height of energy barriers and the thermal dynamics timescales. Our model nanofriction interface of trapped ions in an optical lattice affords this microscopic control, and has enabled us to build a clear picture of microscopic thermal dynamics directly corroborated by experiments. In particular, we observe 4 regimes of velocity and thermal dynamics in a single experiment for the first time, enabling us to deconvolve thermal, structural (chapter 13) and load effects (chapter 12) of stick-slip friction experimentally for the first time.

Stick-slip friction subject to thermal dynamics is governed by the interplay of 3 time scales:

1) the inverse velocity time scale, or time to displace the two surfaces by one lattice constant of the substrate

$$\tau_{trans} = a/v \tag{15.1}$$

2) the time scale of thermal hopping across a Peierls-Nabarro energy barrier U_B, given by the Arrhenius thermal activation relation

$$\tau_{th} = \tau_0 \cdot exp(U_B/k_BT) \tag{15.2}$$

3) the time scale of energy dissipation $\tau_c = \gamma^{-1}$.

The thermal activation prefactor $\tau_0(\tau_c, \omega_L^{-1}, \omega_L^{-1})$ is the inverse of the attempt rate A, known as the Arrhenius constant, and is a function of the dissipation time scale and the vibrational motion time scales of the lattice ω_L^{-1} and the harmonic trap ω_0^{-1}.

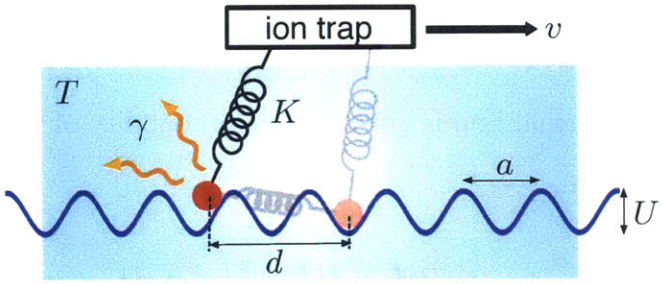

Figure 15-2: The trapped ions interact with an effective bath at temperature T via laser cooling at rate $\gamma = \tau_c^{-1}$. The latter removes frictional heat as the ions stick and slip over the lattice as the trap is moved at speed v. The bath results in fluctuating forces that can cause an ion to slip over the barrier prematurely (thermal hopping).

15.1 Thermal hopping and dissipation

The simple picture of the stick-slip process discussed thus far is deterministic. The ion chain is stuck in a metastable local energy minimum as the shear force is applied, until a critical force when this configuration becomes mechanically unstable, resulting in a slip to a global minimum. This picture is correct in the limit of zero temperature ($T = 0$) and infinite dissipation rate ($\tau_c = 0$). The first condition means that there is no thermal hopping across the energy barrier out of the metastable state ($\tau_{th} = \infty$), and the second condition means that the chain immediately finds the next minimum energy configuration after a slip and ends up there with zero kinetic energy ($T = 0$) instantaneously. This is, of course, unphysical, but is a good approximation in the friction plateau regime identified in this chapter - the regime in which we operated in all the friction experiments described in the previous chapters.

Consider a single ion in the bistable potential of the Prandtl-Tomlinson model being pulled by the applied electric force F_{app} at speed v (Fig15-2). The balance of cooling processes (laser cooling) and heating processes (photon recoil, electric field noise, parametric heating from lattice potential fluctuations) results in an effective bath at temperature T, typically at $k_B T \approx 0.1 \cdot U$ in our system. The ion's motion is coupled to this bath via the laser cooling at rate $\gamma = \tau_c^{-1}$. At thermal equilibrium in the classical limit, the ion's energy relative to its local minimum has a Boltzmann

distribution

$$p_E dE = \frac{1}{k_B T} exp(-E/k_B T) \tag{15.3}$$

The probability of a thermal hop is given by the probability of the ion's energy being above the energy barrier

$$\begin{aligned} p_{hop} = P(E > U_B) &= \int_{U_B}^{\infty} p_E dE \\ &= exp(-U_B/k_B T) \end{aligned} \tag{15.4}$$

The thermal hopping rate R_{hop} is given by this probability times the attempt rate:

$$R_{hop} = A p_{hop} = \tau_{th}^{-1} \tag{15.5}$$

which leads to equation 15.2.

The attempt rate reduces to $A \approx \omega_{loc}$ in the underdamped limit $\gamma << \omega_{loc}$, where $\omega_{loc}/2\pi$ is the vibrational frequency at the metastable local minimum [88, 84]. The attempt rate reduces to $A \approx \omega_{loc}^2/\gamma$ in the overdamped limit $\gamma >> \omega_{loc}$. With typical damping rates of $\gamma \approx 2\pi \times 3$ kHz and vibrational frequencies in the few hundred kHz range, our experiments are most of the time governed by underdamped dynamics.

Thus, the idealized deterministic stick-slip process will occur if thermal hopping is negligible on the time scale of the driven transport $R_{hop} << v/a$ until the potential is very close to the mechanical instability (Fig.15-3a<A>). This is the case if the transport is fast, at high velocities v, or if the hopping probability is low due to $U/k_B T >> 1$ at low temperatures T. In the opposite regime of low velocities v and high temperatures T, the ion thermalizes across the barrier by fast thermal hopping and never sticks to a metastable state; its probability distribution smoothly shifts from one local minimum to the other resulting in a smooth displacement of the mean position known as thermal drift (Fig.15-3a<B>). In a regime of intermediate velocities and temperatures, sticking may occur part of the time, weakened by occasional thermal hopping. Experimentally, the signature of thermal hopping is diminished hysteresis and static friction force as a result of premature hopping of the ion across

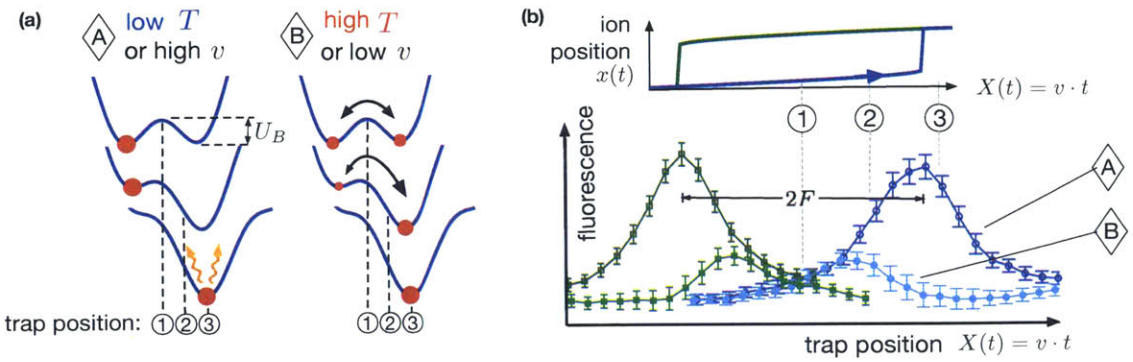

Figure 15-3: **(a)** The deterministic stick-slip process occurs in the limit of low temperature or high velocity and fast damping. **(b)** In the limit of high temperature or low velocity, stick-slip is pre-empted by thermal hopping across the energy barrier as the trap is translated (trap position X is shown 1→2→3). **(b)** The effect of thermal hopping is to reduce the observed hysteresis, resulting in a smaller measured static friction force F_s.

the barrier prior to any mechanical instability (Fig.15-3b). Such reduction of friction due to thermal hopping is known as thermolubricity [86].

To observe deterministic stick-slip, a large damping rate is also required, such that the released energy during a slip is removed faster than the transport time scale $v/a << \gamma$. If this does not happen, the residual kinetic energy results in a higher temperature and large thermal hopping rate; such frictional overheating then reduces stick-slip friction. Experimentally, finite damping is evident in all our observations of slipping events as a decaying fluorescence tail after a slip, corresponding to an exponential decay of the released energy as a result of recooling (Fig.15-4) (infinitely fast damping would result in a sharp jump of fluorescence to the new value corresponding to the new minimum).

These simple pictures of thermal dynamics are corroborated by full dynamics simulations using the Langevin approach where a random fluctuating force is introduced via the fluctuation-dissipation theorem relating it to the effective temperature and dissipation rate [87].

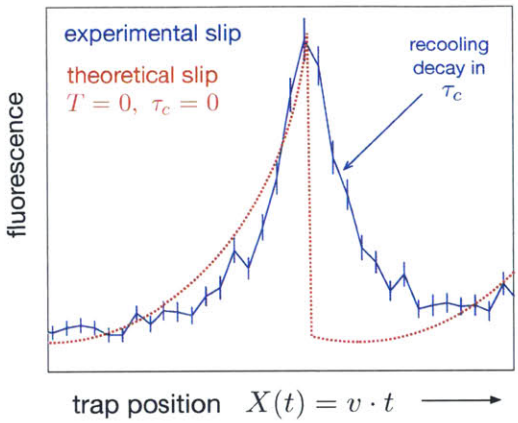

Figure 15-4: An observed fluorescence peak signaling a slipping event (blue) is superimposed on the theoretical result in the zero-temperature, infinite-dissipation limit. The fluorescence decay observed in experiments following a slip gives the dissipation time constant $\tau_c = \gamma^{-1}$.

15.2 Velocity dependence of friction from thermolubricity to velocity weakening

The competition of the transport time scale with the time scales of thermal dynamics described above results in velocity-dependent friction. In this section, we focus on velocity-dependent friction of a single trapped ion. We vary the velocity, with which the harmonic trap position X is translated, over 4 to 5 orders of magnitude, and experimentally observe 4 regimes of stick-slip friction in order of increasing velocity (Fig.15-5a): 1) thermal drift, where friction is zero and velocity-independent; 2) thermal activation, where friction increases logarithmically with velocity; 3) friction plateau, where friction is large and velocity-independent, and 4) velocity weakening, where friction decreases logarithmically with velocity due to frictional overheating.

The observed friction plateau of perfect, maximal stick-slip friction $F_{s,max}$, equal to the applied force required to induce a mechanical instability, occurs for a window of velocities $R_{hop,U} << v/a << \gamma$, where $R_{hop,U} = A \cdot exp(-U/k_BT)$ is the thermal hopping rate over the highest barrier U equal to the depth of the optical lattice potential. As velocity drops from $v/a >> R_{hop,U}$ towards the thermal drift regime of zero friction when $v/a << R_{hop,U}$, in the intermediate regime $v/a \sim R_{hop,U}$ thermal

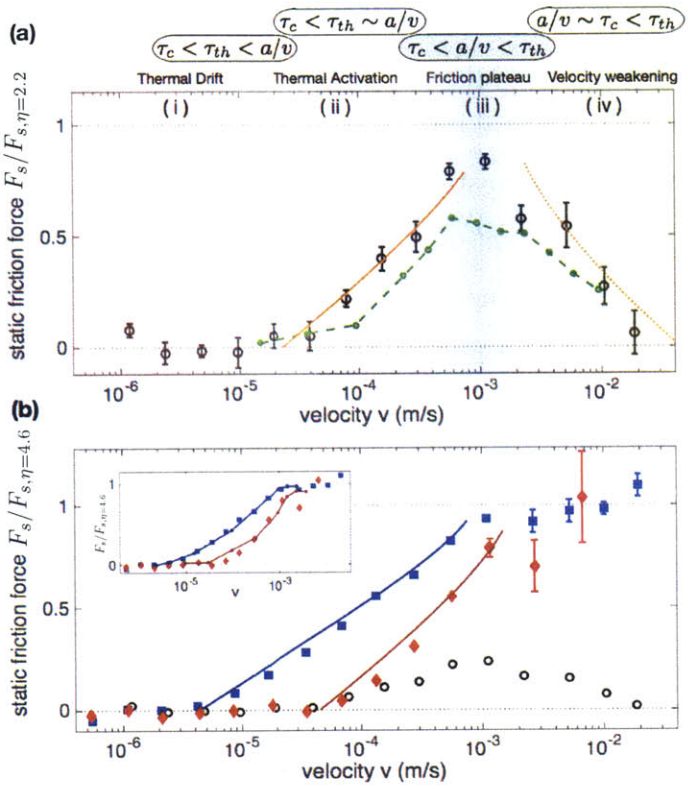

Figure 15-5: **Velocity dependence of stick-slip friction for a single ion.** The transport time a/v should be compared to two time scales: the slowest thermal hopping time between two lattice wells, given by $\tau_{th,U} = R_{hop,U}^{-1} = \tau_0 exp(U/k_BT)$, and the recooling time after a slip $\tau_c = \gamma^{-1}$. This results in four regimes of stick-slip friction that are observed in (a), labeled (i)-(iv). **(a)** Here $\tau_{th,U} \approx 10\mu$s, $\tau_c \approx 100\mu$s and $\eta = 2.2$, resulting in $F_{s,max,\eta=2.2} = 0.14Ka$. ($U = 2\pi\hbar \times 9.5$ MHz and $k_BT/U = 0.14 \pm 0.04$). The solid orange lines show the analytical results of equations 15.9 and 15.10 in the thermal activation and velocity weakening regimes, respectively, where the critical velocities $v_{th} \approx 1$ mm/s and $v_c \approx 2$ mm/s agree with independent measurements of τ_0 and τ_c, respectively (see chapter 8). The Langevin simulation (dashed green line) is in good agreement with the data over all four velocity regimes for the experimental parameters above. Note that an independently measured velocity-dependent temperature correction was used in plotting the analytic formulae and the Langevin results. **(b)** Results at a larger lattice depth $U = 2\pi\hbar \times 18$ MHz where $\eta = 4.6$, $F_{s,max,\eta=4.6} \approx 0.5Ka$, and $\tau_c \approx 50\mu$s, showing the friction plateau regime extend over a wider range of velocities. Increasing the temperature from $k_BT/U = 0.04 \pm 0.01$ (blue squares) to $k_BT/U = 0.17 \pm 0.01$ (red diamonds) reduces the friction in the thermal activation region 10^{-5} m/s $\lesssim v \lesssim 10^{-3}$ m/s while leaving the friction plateau in the region 10^{-3} m/s $\lesssim v \lesssim 10^{-2}$ m/s almost unaffected. Solid lines show the expected results from the analytical thermal activation model 15.9. Data from (a), normalized to $F_{s,max,\eta=4.6}$, is shown as open black circles for comparison. Langevin simulations (inset, solid lines) are in good agreement with the data for the experimental parameters above.

activation begins to reduce the measured static friction force F_s from the plateau value $F_{s,max}$. An applied force reduces the energy barrier U_B to zero at the mechanical instability, but prior to the instability, the barrier becomes sufficiently small that thermal hopping empties the metastable state. Since thermal hopping is exponential in the barrier height $R_{hop} = A \cdot exp(-U_B/k_BT)$, this happens close to a specific barrier height $U_B = k_BT \cdot ln(A \cdot a/v)$ at the associated applied force, which gives the reduced static friction force F_s in the thermolubricated process by an amount ΔF:

$$F_s = F_{s,max} - \Delta F \tag{15.6}$$

Close to a mechanical instability, the barrier height scales as

$$U_B \propto \Delta F^{3/2} \tag{15.7}$$

which leads to

$$F_s = F_{s,max} - C\left(k_BT \cdot ln\left(\frac{1}{v}\frac{a}{\tau_0}\right)\right)^{2/3} \tag{15.8}$$

where C is a parameter determined by the shape of the corrugated potential [88]. This equation can be written as an approximate formula in terms of the experimentally measured parameters of temperature-to-lattice-depth ratio k_BT/U and "thermal velocity" $v_{th} \approx a/\tau_0$:

$$F_s/F_{s,max} = 1 - \left(\frac{3}{2\sqrt{2}}\frac{k_BT}{U} \cdot log\left(\frac{v_{th}}{v}\right)\right)^{2/3} \tag{15.9}$$

Thus, stick-slip friction should scale as $\left(log(v)\right)^{2/3}$ in the thermal activation regime, consistent with our observations (Fig.15-5). Obviously, this formula does not apply to the friction plateau regime, where $F_s/F_{s,max} = 1$ and thermal hopping is negligible regardless of the velocity as long as it is fast enough, or to the thermal drift regime, where $F_s/F_{s,max} = 0$ and thermal hopping dominates regardless of the velocity as long as it is slow enough.

As anticipated in the previous section, we observe that when the velocity becomes faster than the dissipation rate $v/a >> \gamma$, the excess energy released by slips and not removed by laser recooling results in frictional overheating: the temperature increases, resulting again in thermal activation (despite the fast velocity) due to a large value of the thermal hop probability p_{hop}. The observed decrease of the friction force F_s with velocity is logarithmic, and in analogy with equation 15.9, we model this velocity weakening regime with

$$F_s/F_{s,max} = 1 - \left(\frac{3}{2\sqrt{2}}\frac{k_B T}{U} \cdot log\left(\frac{v}{v_c}\right)\right)^{2/3} \tag{15.10}$$

where the "damping velocity" $v_c \approx a/\tau_c$ gives a good agreement with our data (Fig.15-5).

The non-monotonic behaviour of friction with velocity observed in our experiments pertains to the stick-slip frictional mechanism. The laser cooling that removes the released kinetic energy after a slip with rate γ of course does so using an effective viscous drag force roughly linear in velocity

$$F_{visc} = \frac{1}{2} m\gamma v \tag{15.11}$$

This component of friction however, in our system and in dry friction in condensed matter, is significantly smaller than the stick-slip contribution $F_s \sim m\omega_0^2 a$ in the range of available velocities:

$$F_{visc}/F_s \sim \frac{2\gamma v/a}{\omega_0^2} \tag{15.12}$$

At the nominal $\gamma \approx 2\pi \times 3$ kHz and $\omega_0 = 2\pi \times 364$ kHz, this gives $F_{visc}/F_s \sim 10^{-4}$ at the velocity $v/a = \gamma$ when velocity weakening of stick-slip friction sets in. Of course, at larger velocities, when stick-slip friction is wiped out by frictional overheating, viscous drag becomes the dominant mechanism of friction, resulting in friction increasing with velocity again. However, it would require orders of magnitude larger velocities for this viscous frictional mechanism to be within our detection sensitivity via frictional hysteresis.

I conclude this section by noting that the friction plateau regime insensitive to the thermal dynamics is where the dependence of "pure" friction $F_{s,max}$ on structural mismatch and normal load (lattice depth) was investigated in previous chapters. As an example, the full velocity curve is plotted in Fig.15-5b showing the different values of the plateau $F_{s,max}$ for two different values of the lattice depth, corresponding to $\eta = 4.6$ (blue, red filled symbols) and $\eta = 2.2$ (black open circles). It is important to note, however, that the observed plateau regime at the lower lattice depth of $\eta = 2.2$ occurs in a narrower window of velocities. Also, the observed friction force in the plateau regime for $\eta = 2.2$ does not fully reach the plateau value expected from the Prandtl-Tomlinson model, but a value $F_s/F_{s,PT,\eta=2.2} \approx 0.75$. This is due to the fact that at a fixed temperature and reduced barrier height, thermolubricity is enhanced by increased thermal activation over this reduced barrier, since the ratio U_B/k_BT is smaller. This is discussed in more details in the next two sections, together with the observed temperature dependence of friction.

15.3 Temperature and barrier dependence of friction

Stick-slip friction at lower velocities is reduced due to the thermolubricating effect of finite temperature. When we increase the temperature of the system, this effect is increased (Fig.15-5b): friction drops faster with velocity in the thermal activation regime, and the thermal drift regime is extended to higher velocities. The thermal velocity at which friction plateaus, however, does not seem to be affected by temperature, consistent with $v_{th} \approx a/\tau_0$ set by the damping and vibrational time scales.

To investigate more systematically the temperature dependence of friction in the different velocity regimes, we vary temperature and measure friction with velocity either fixed at the boundary between thermal drift and thermal activation, or at the boundary between thermal activation and the friction plateau (Fig.15-6). In the observed $F_s/F_{s,max}$ plotted on a logarithmic scale against $1/T$, the exponential sensitivity of friction to temperature is apparent near the thermal drift regime (yellow), whereas near the friction plateau velocity regime, friction is observed to be nearly

independent of temperature (green). More quantitatively, we fit data to the model

$$F_s/F_{s,max} = f \cdot exp(\zeta U/k_B T) \tag{15.13}$$

where f and ζ are fitted parameters, and ζ represents the sensitivity to temperature. At low velocity ($v \approx 40\mu$m/s), near the thermal drift, we determine $\zeta \approx 0.17$ (expected to be unity for the discussed thermal activation models). At high velocity ($v \approx 1$ mm/s) near the friction plateau, we determine $\zeta \approx 0.016$. This confirms that a nearly zero-temperature stick-slip regime can be experimentally accessed at high transport velocity, as desired for studies of structural and normal load effects on friction.

Since temperature only affects friction via the ratio $U_B/k_B T$, the observed dependence of friction on inverse temperature in Fig.15-6 can also be interpreted as the dependence of friction on the lattice depth U at fixed temperature. The residual sensitivity to temperature even at high velocity then explains the slightly reduced friction plateau $F_s/F_{s,PT,\eta=2.2} \approx 0.75$ at the lower lattice depth corresponding to $\eta = 2.2$. Furthermore, as discussed in chapter 13, structural lubricity in a multi-ion contact with the lattice occurs due to a reduction of the Peierls-Nabarro barriers U_B by interatomic interactions (Coulomb forces), which at fixed temperature then necessarily also means increased thermolubricity. Such structural thermolubricity is discussed in more detail in the next section.

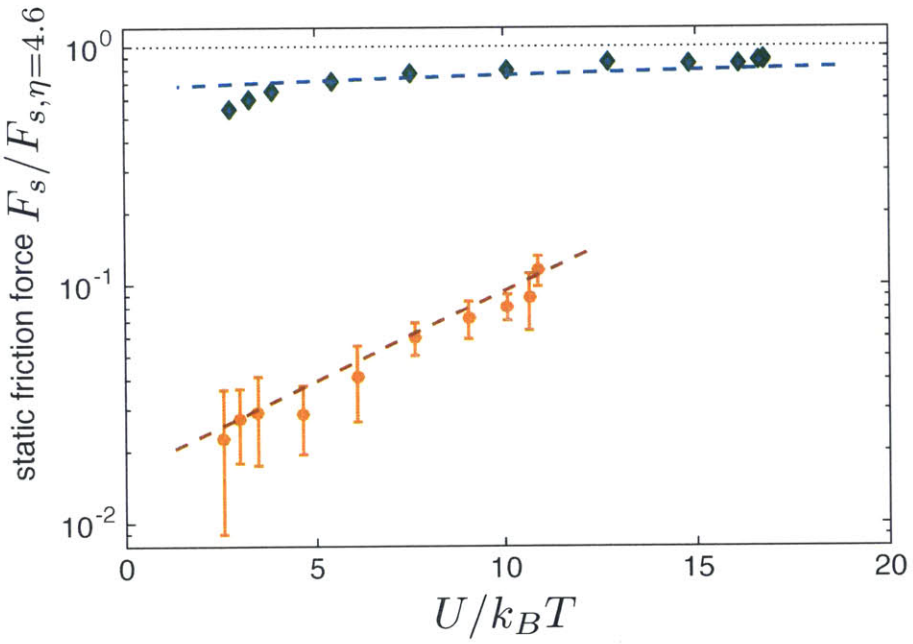

Figure 15-6: Measured sensitivity of friction to temperature at a high velocity ($v \approx 1$ mm/s) near the friction plateau regime (green) and at a low velocity ($v \approx 40\mu$m/s) near the thermal drift regime (orange). Shown here is the measured static friction force divided by the zero-temperature static friction force on a logarithmic scale, plotted versus inverse temperature T^{-1} in units of inverse lattice depth U^{-1}. Alternatively, the measured relation can be interpreted as thermolubricity as a function of the lattice depth U or PN barrier U_B in units of temperature T (at a fixed temperature), which explains the effect of structural thermolubricity in section 15.4. (Experimental parameters for this measurement were $\eta = 4.6$, $U = 2\pi\hbar \times 18$ MHz and $\tau_c \approx 50\mu$s, and temperature was varied by an order of magnitude from $k_BT/U = 0.06$ to $k_BT/U = 0.4$ by introducing additional recoil heating from the near-detuned pumping beam by increasing the π-polarized component as described in section 6.5.)

15.4 Structural thermolubricity

It is easiest to visualize structural thermolubricity for a trapped crystal of 2 ions, where the total potential as a function of the first ion coordinate x_1 and the second ion coordinate x_2 can be visualized in a 3D plot (Fig.15-7). When the two ions are matched to the lattice, with the spacing between them tuned to be an integer number of lattice spacings $d(\mathrm{mod}\ a)/a = 0$, the barrier to common-mode translations is maximal, equal to the Prandtl-Tomlinson barrier determined only by the ratio of lattice depth to external stiffness $\eta = \frac{2\pi^2 U}{Ka^2}$:

$$U_B \approx \frac{1}{2\pi^2}\frac{(\eta-1)^2}{\eta} \tag{15.14}$$

The velocity and temperature dependence of friction for a matched ion crystal is therefore expected to be identical to that for a single ion investigated in the previous sections. Indeed, this is what we observe in the case of a matched 2-ion crystal (Fig.15-8a).

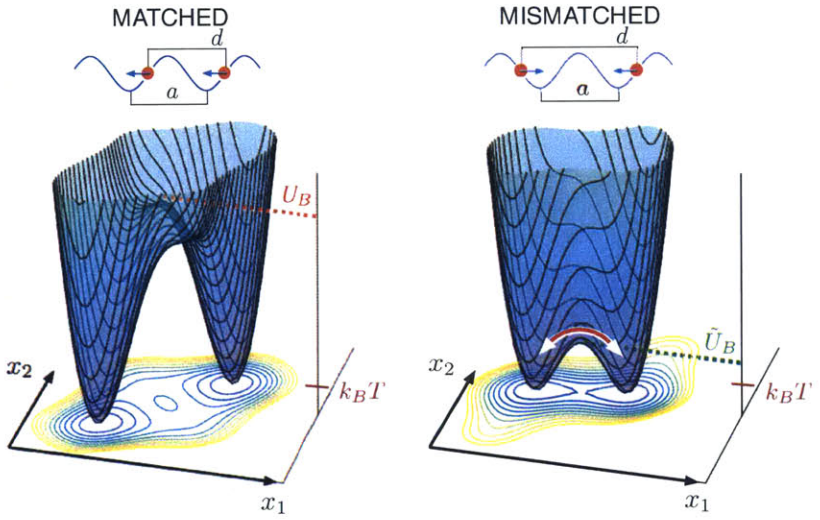

Figure 15-7: The total potential (including the Coulomb interactions) is plotted versus x_1 and x_2 for two ions matched ($q = 1$, left) and mismatched ($q = 0$, right) to the lattice. For a fixed temperature T, the PN barrier U_B in the mismatched case, reduced due to partial lattice force cancellation, results in faster thermal hopping between the local minima of the potential, reducing the observed static friction force beyond the zero-temperature effect of structural lubricity.

When the ions are mismatched, however, the partial cancellation of lattice forces results in a significantly reduced barrier $\tilde{U_B}$, and motion across this barrier corresponds to ions going over lattice maxima one at a time (Fig.15-7). The reduced barrier means a smaller sticking force, and consequently a smaller observed static friction F_s - this is the structural lubricity that we observed in chapter 13. The reduced barrier at fixed k_BT also means faster thermal hopping which reduces friction even further - an effect we call structural thermolubricity. To deconvolve structural thermolubricity, which is velocity-dependent, from structural lubricity, we measure friction versus velocity for a mismatched 2-ion crystal and compare the results with the velocity dependence of a matched 2-ion crystal at the same temperature (Fig.15-8b,c). The ratio of the friction force in the matched case to the friction force in the mismatched case goes to unity in the thermal drift regime, where friction is zero regardless of the barrier height as a result of the dominant thermal hopping, and goes to a factor of ~ 4.8 in the friction plateau regime. In the intermediate thermal activation regime, this ratio spikes as a result of the exponential dependence of thermal activation on the barrier height: at the intermediate velocities, thermolubricity does not yet affect the matched ion crystal, but already significantly diminishes friction over the small barrier in the mismatched case.

The plateau in the friction ratio between the matched and mismatched cases at high velocities suggests that in this regime, the observed factor of 4.8 reduction in friction is due to structural lubricity alone. However, zero-temperature numerical simulations show a reduction of friction by a factor of 2 for a mismatched 2-ion crystal, indicating residual structural thermolubricity reducing friction by another factor of 2.4 even at high velocities. This is not fully consistent with a much smaller measured sensitivity to barrier depth at fixed temperature shown in Fig.15-6, suggesting that temperature actually also increases as a result of structural mismatch. In fact, as mismatch is varied from matched ($q = 1$) to mismatched ($q = 0$) for $N = 1 - 5$ ions, comparison between the experimental data, numerical zero-temperature simulations and Langevin simulations of the full dynamics suggests that in our system, structural lubricity and structural thermolubricity reduce friction by similar factors aided by an

additional temperature increase from $k_BT/U \approx 0.05$ to $k_BT/U \approx 0.35$ (Fig.15-9)).

It is important to note here that structural thermolubricity has not affected the determination of the critical lattice depth U_c of the superlubricity-breaking transition, which is consistent with zero-temeprature simulations and is the basis of our claim of observation of the Aubry transition. Varying temperature in the Langevin simulations confirms that while thermolubricity significantly diminishes friction for $U > U_c$, making the slope of the increase of friction with lattice depth shallower, the crossing of this slope with $F_s = 0$ were stick-slip vanishes is minimally affected. This makes sense: even at large temperatures, some residual stick-slip should be detectable, until it identically vanishes in the superlubric regime.

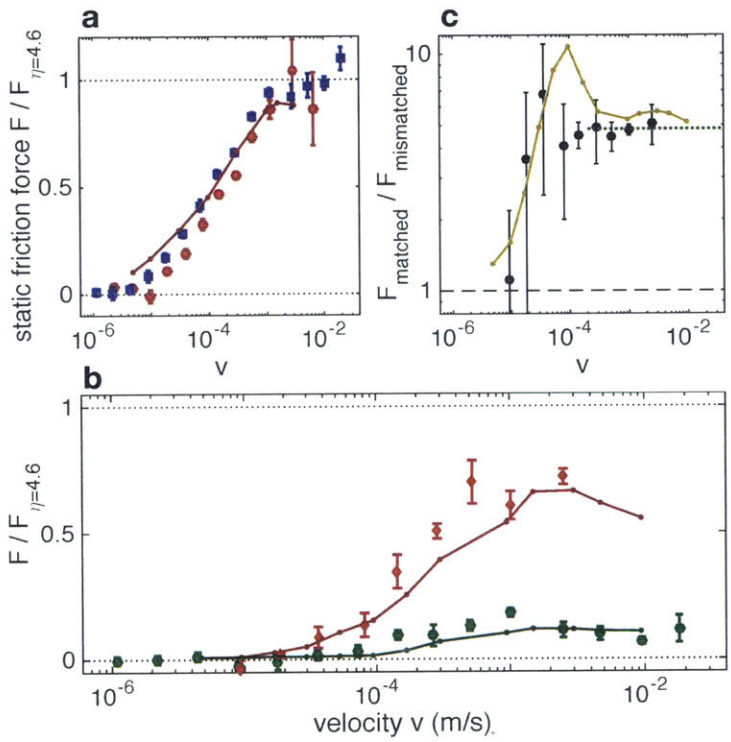

Figure 15-8: **Velocity dependence of friction and structural thermolubricity for a 2-ion crystal. (a)** The velocity dependence of a matched 2-ion crystal (red circles) coincides with the velocity dependence of a single ion (blue squares) at the same experimental parameters $\eta = 4.6$ and $k_BT/U = 0.055 \pm 0.010$; both reach the friction plateau at the maximum value $F_{s,max,\eta=4.6} = 0.5Ka$. **(b,c)** Comparing the velocity dependence of static friction for the matched (red) and mismatched (green) 2-ion crystals, both at a slightly higher temperature than in (a) ($k_BT/U = 0.15 \pm 0.02$), reveals structural friction reduction that goes away in the thermal drift regime, which is obvious in the ratio of matched to mismatched friction in (c). Although barely visible in the data, the peak in simulations is due to structurally-induced thermolubricity: a window of velocities for which the friction in the mismatched case is further reduced from the matched case by thermal effects. In (a)-(c), Langevin simulations for the experimental parameters (solid lines) are in good agreement with the data.

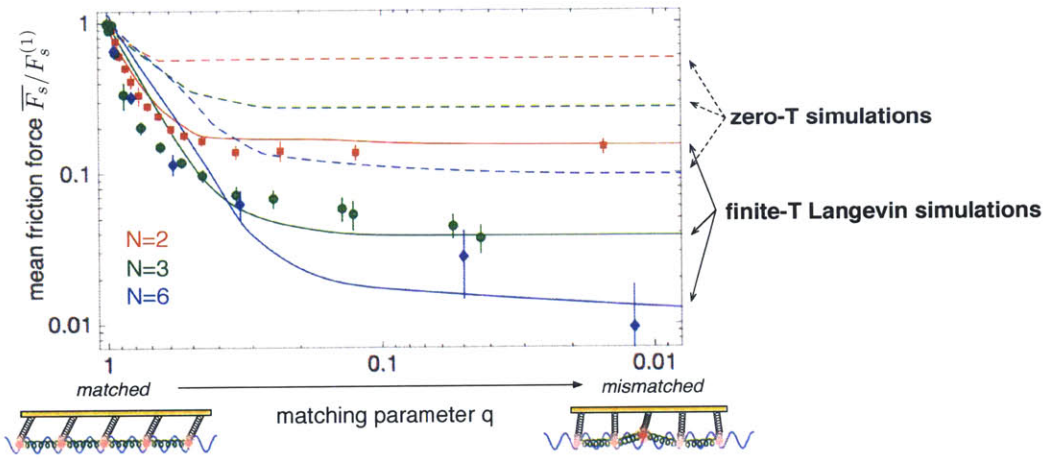

Figure 15-9: Revisiting our measurements of structural lubricity versus the matching parameter q and comparing the results with zero-temperature and finite-temperature simulations, reveals that structural lubricity and structural thermolubricity reduce friction by similar factors in our data for $N = 1 - 6$ trapped ions. This results from an additional increase in temperature from $k_BT/U \approx 0.05$ to $k_BT/U \approx 0.35$ as the ion chain is mismatched, as obtained from fitting Langevin simulations with a q-dependent temperature to our data.

Chapter 16

Multi-slip dynamics

I have so far discussed stick-slip friction in terms of a bistable total potential. As long as the switching of the chain between the two minima of this potential always occurs close to the same value of the applied force, this results in the regular stick-slip pattern that we observe as fluorescence peaks spaced by the lattice constant a in the quickly displaced trap position X. However, at larger corrugations depths $\eta = (\omega_L/\omega_0)^2$, the total potential might have three or more minima. In such a regime, when a slip occurs, it may take the system to the next minimum, two minima over, or more for higher multiplicities of the landscape stability. The multi-slip behaviour has been observed in nanotribology experiments with atomic force microscopes [114, 115] as an irregular pattern of mixed slips of different size and occurring at different times, as a result of the stochastic processes at play. The multi-slip behaviour is intimately tied with the thermal dynamics and velocity of the system [116, 114, 115, 88, 117], and complete understanding of it would require microscopic control of thermal dynamics, and in particular, of the dissipation rate, typically not accessible in AFM experiments [76]. Although in our system, single-shot measurement of slips is not available and the data is obtained by averaging many repetitions of the experiment, the relative abundance of single-slip and double-slip events can still be determined from the average behaviour, and the transition from the single-slip regime to the multiple-slip regime can be identified. Our experiments offer a glimpse into this very important regime of friction relevant for dissipation and wear, and another tool for studying

the thermal dynamics of friction at the microscopic scale. As an example, one could investigate, with single-atom resolution, recipes for stabilizing irregular stick-slip using mechanical excitation [118] - an important approach for controlling and reducing friction [119], or for studying quantum synchronization [120].

16.1 Multistability and stochastic slipping

Let us return to the single-atom Prandtl-Tomlinson model that exactly models a single trapped ion or a commensurate chain of ions in the optical lattice:

$$V_{PT}(x) = \frac{1}{2}(x - X)^2 + \eta\frac{1}{4\pi^2}(1 + \cos(2\pi x)) \tag{16.1}$$

where energies are in dimensionless units of Ka^2, positions are in dimensionless units of the lattice constant a, and $\eta = (\omega_L/\omega_0)^2$ defines the topography of the potential. As discussed in chapter 12, it is always monostable for $\eta < 1$, bistable in a range of trap positions X for $1 < \eta < 4.604$ and multistable for $\eta > 4.604$ (Fig.12-4).

In the tristable regime $4.604 < \eta < 7.788$ [114], when a minimum becomes unstable as a result of applied force, two minima, potentially of different energies, are available for the ion to slip into, and the probability of transitioning to one or the other depends on the temperature T and on the damping rate in the system $\gamma = \tau_c^{-1}$ (Fig.16-1). If the system was overdamped with $\gamma \gtrsim \omega_L$, i.e. if the damping rate was faster than ion motion over a lattice site, bounded by the vibrational frequency in a lattice site, the released kinetic energy as the ion is dumped over the barrier would get dissipated faster than the ion can travel to the other side of the corrugated potential; and it would always end up in the first minimum over [58]. Our system, however, is highly underdamped $\gamma << \omega_L$, and the ion can end up in one of the two available minima after recooling. Assuming an infinitely slow dissipation - the limit of perfect annealing - the probabilities of the two final states are simply weighted by each minimum's Boltzmann factor $exp(-E/k_BT)$. The assumption is not strictly correct, since in our case, dissipation if faster than the hopping rate across the barrier between the two available states $\gamma > \tau_0^{-1}exp(-U_B/k_BT)$, and this should result in an

increased probability to get stuck in the higher-energy metastable state. Nonetheless, this assumption is useful for an initial analysis done here.

An important point is that as long we operate in the velocity- and temperature- insensitive regime of stick-slip friction (see chapter 15) where $v/a > \tau_0^{-1} exp(-U_B/k_B T)$, the ion does not thermally hop out of its initial site prematurely, and the slipping event occurs at a well-defined applied force, or trap position $X = F_{app}/K$. That means that regardless of whether a single- or a double-slip tends to happen, the fluorescence peaks signaling the slipping events will have a regular spacing in X, corresponding to a for single-slip events and to $2a$ for double-slip events. When both types of slip occur with finite probability, they produce a time-averaged fluorescence pattern with varying peak heights, which carries information about the single-slip and double-slip event probabilities (in a way that depends on the initial and final values of X with respect to the lattice in the force ramps). In the next section (16.2), I present the experimental signatures of double-slipping, and in the section after (16.3), I discuss in detail multi-slip dynamics and use a Markov-chain model to extract double-slip probabilities.

16.2 Experimental observation of the single-slip to double-slip transition

As we increase η (by increasing the lattice depth U) and measure the static friction force F_s on a single trapped ion as the hysteretic splitting between the fluorescence peaks (Fig.16-2), we observe that the friction force continues growing linearly after we enter the multislip regime for $\eta > 4.604$ (Fig.16-3). Nothing significant appears to happen at this cross-over point in the measured friction. However, it is evident from the fluorescence traces in Fig.16-2 that the distribution of the observed fluorescence peak heights changes, which is the anticipated signature of the onset of double-slips. Note that the same continued increase in the friction force (Fig.16-3) and the same fluorescence peak patterns are observed for matched crystals of larger N.

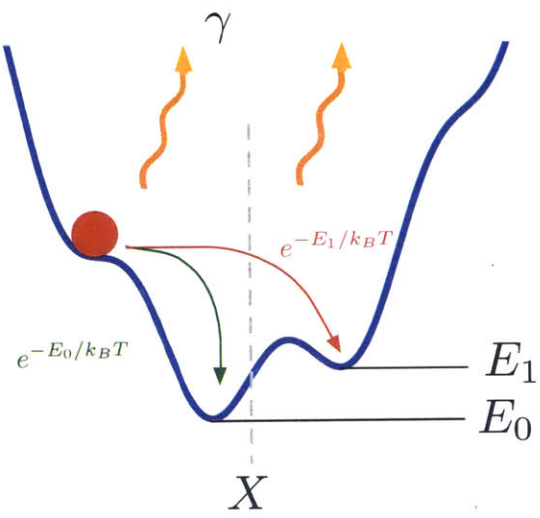

Figure 16-1: The Prandtl-Tomlinson potential can be multistable when $\eta > 4.604$, and a slip can take the ion to one of multiple available minima after recooling, with probabilities weighted by the respective Boltzmann factors. When thermal hopping is negligible, the slips always occur at defined trap positions X that make successive sites unstable, regardless of whether a single or a double slip occurs afterwards, which is determined by a stochastic process.

Plotting in Fig.16-4 the difference in fluorescence between the first and second peak for the forward slips (blue) and backward slips (red) reveals that there is a transition from a regime where the fluorescence is equal to a regime with a difference in fluorescence that increases with η, which can be interpreted as the onset of double slips. This transition appears to happen near $\eta \approx 4$, reasonably close to the expected value of 4.604.

Note that these results were obtained for the force ramp starting and ending at the trap position X centered over a lattice maximum, with a ramp range of $3a$. A different ramp window results in a different distribution of peak fluorescences, which will be important to investigate further systematically. The chosen window, however, gives a nice relation between the observed fluorescence peak heights and the double-slip probabilities, as discussed in the next section.

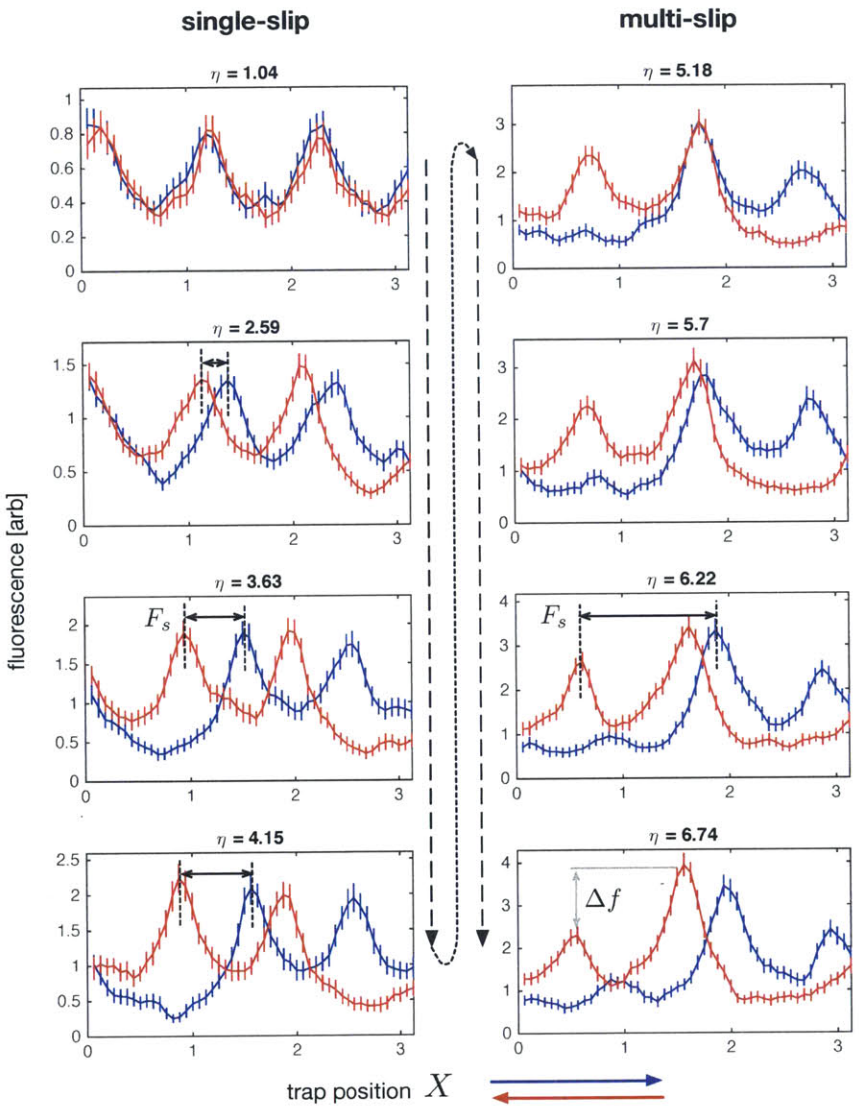

Figure 16-2: Observed fluorescence for a single trapped ion dragged forward (blue) and backward (red) over 3 lattices sites as η is increased from the single-slip to the multislip regime. The forward and backward slips, giving a measurement of the static friction force F_s, continue to separate in the multislip regime, but the peak heights begin to change, indicative of the onset of double slips.

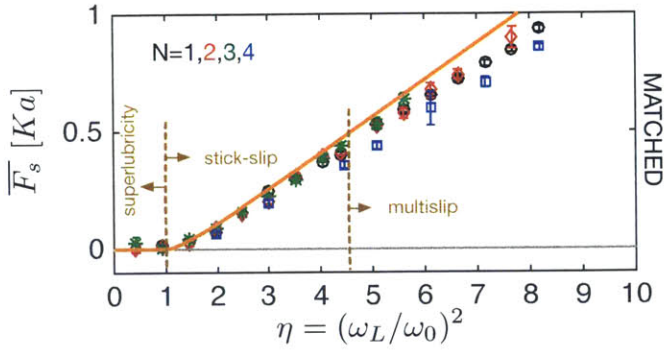

Figure 16-3: The measured friction force for $N = 1 - 4$ ions in a chain matched to the optical lattice continues increasing into the multislip regime $\eta > 4.604$ of the Prandtl-Tomlinson model without a clear change in behavior.

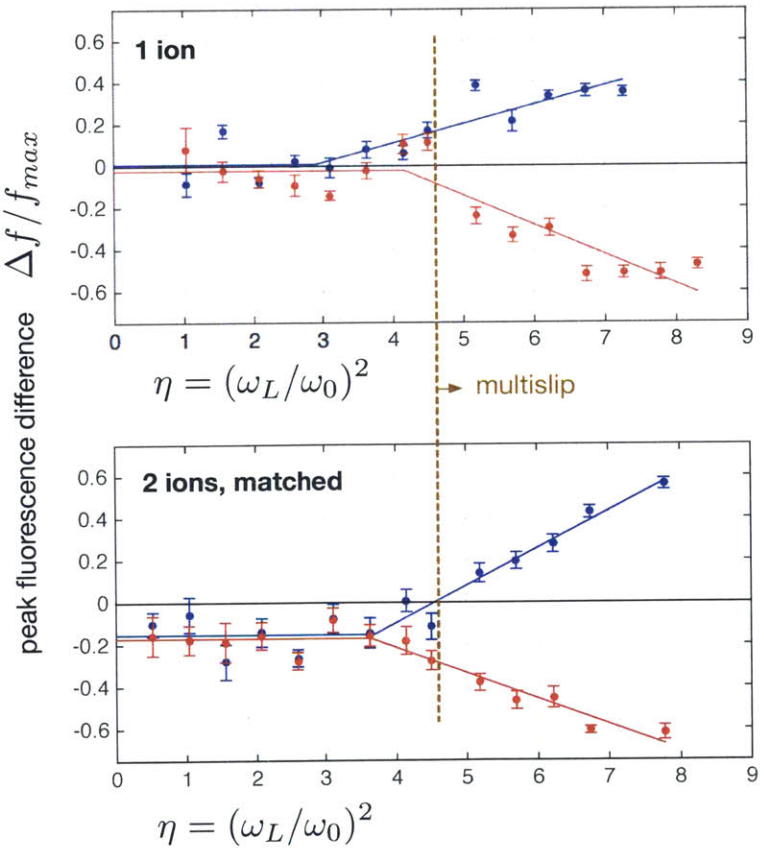

Figure 16-4: The difference in fluorescence Δf between the two peaks normalized by the larger peak starts to increase close the expected crossover to the multislip regime. This fluorescence difference is plotted in blue for forward traces and in red for backward traces, for $N = 1$ ion and $N = 2$ ions matched to the lattice.

16.3 Determination of double-slip probabilities using a Markov model

The best way to visualize multi-slip dynamics is using the hysteresis loops in the position-force trace that we usually experimentally reconstruct from the full fluorescence information. These loops open up around the lattice barriers for $\eta > 1$, and the multi-slip regime is entered when adjacent hysteresis loops begin to overlap (Fig.16-5), resulting at first in tristable regions, creating the possibility for each slip to take the ion(s) either one or two lattice sites over. At steady state (after driving the system over many cycles) and for each trap position $X = F_{app}/K$, there is a probability distribution between the two or three available sites, which determines the time-averaged level of fluorescence at a given slipping point.

One can model this dynamical system as a Markov-chain process with a steady state. The steady state determines the desired probability distribution between the available sites, or "states", labeled in Fig.16-5 as $A, B, \overrightarrow{C}, \overleftarrow{C}, D, E$. The middle site on the way forward, labeled as $\overrightarrow{C}$, and on the way backward, labeled as $\overleftarrow{C}$, are taken as separate states to model the process as a memoryless Markov process. Transitions in this state space are single slips, with probability p_1, and double slips, with probability p_2, where $p_1 + p_2 = 1$ (Fig.16-6). Consider an instantaneous probability distribution over this state space $\vec{p} = \{p_A, p_B, p_{\overrightarrow{C}}, p_{\overleftarrow{C}}, p_D, p_E\}$. In a single time step of the Markov process, this distribution is taken to a new distribution by the transition probability matrix M. After a long enough time for the initial conditions to die out, the steady-state distribution $\vec{p}_{ss}$ is characterized by the fact that it is unchanged by the transition matrix:

$$M\vec{p}_{ss} = \vec{p}_{ss} \tag{16.2}$$

In other words, the steady state is given by the solution to the eigenvalue problem that corresponds to the eigenvalue 1. Diagonalizing the transition probability matrix yields

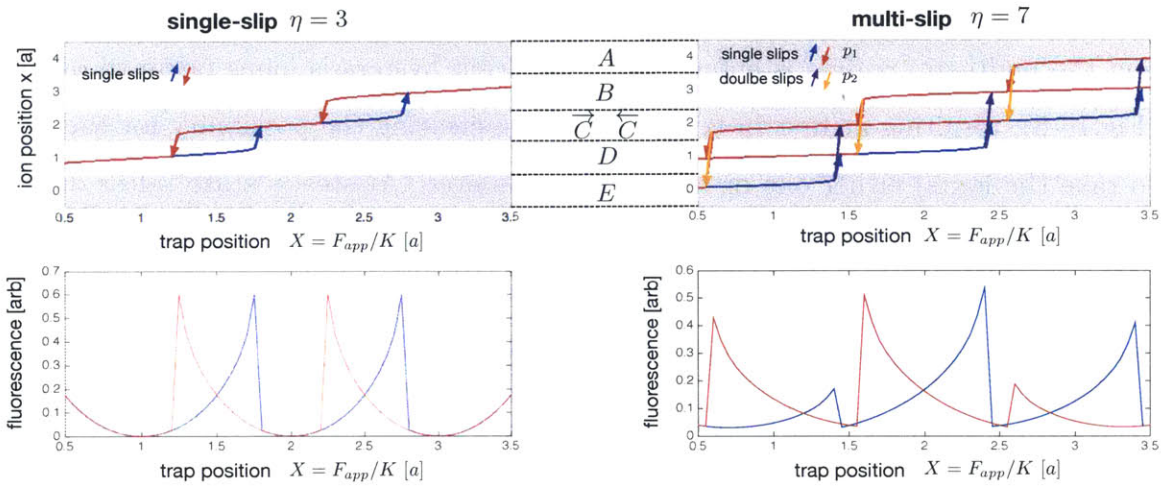

Figure 16-5: As the position of the trap X is ramped by the applied force, hysteresis loops in the ion's position appear over successive lattice maxima. The width of these loops (determined from hysteresis between fluorescence peaks) gives twice the static friction force, so when $F_s > 0.5$, the loops begin to overlap, and multiple slipping possibilities or transitions between different states $A - E$ become available. At finite temperature, each fluorescence peak is proportional to the probability of the state out of which the given slip occurs. The distribution of fluorescence peaks therefore carries information about the probability distribution of the different states. The edges of the ramp in X, break the symmetry of this distribution, enabling us to deconvolve single-slip and double-slip probabilities using a Markov model. In the numerical simulation here, as in the experimental data, the ramp starts and ends over a lattice maximum, and the ratios of peak heights appear to correspond well with the experimental fluorescence traces (Fig.16-2). In the numerical simulation, $k_B T/U \approx 0.23$ was used.

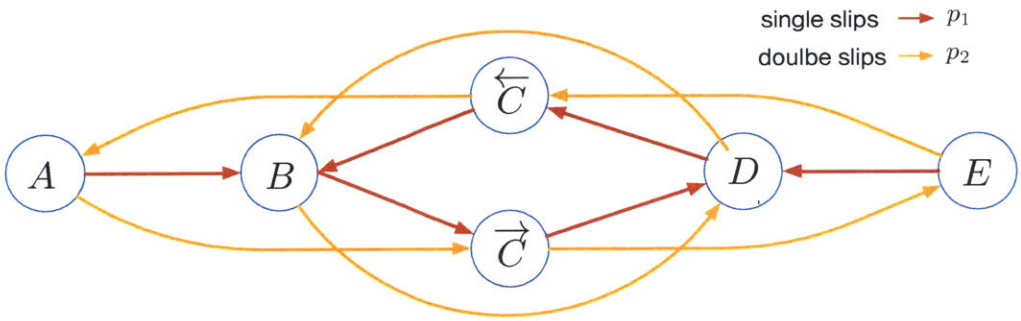

transition matrix $M = \begin{pmatrix} 0 & 0 & 0 & \text{p2} & 0 & 0 \\ \text{p1} & 0 & 0 & \text{p1} & \text{p2} & 0 \\ \text{p2} & \text{p1} & 0 & 0 & 0 & 0 \\ 0 & 0 & 0 & 0 & \text{p1} & \text{p2} \\ 0 & \text{p2} & \text{p1} & 0 & 0 & \text{p1} \\ 0 & 0 & \text{p2} & 0 & 0 & 0 \end{pmatrix}$

Figure 16-6: The states (lattice sites) and possible transitions between them in the Markov chain process modeling the multi-slip dynamics for the ramp range of $3a$ starting and ending at a lattice maximum. Single slips (red) have probability p_1 and double slips (orange) have probability p_2. The corresponding 6×6 transition probability matrix to be diagonalized is shown.

$$
\begin{aligned}
p_A &= \frac{1}{4}\frac{p_2}{1+p_2} \\
p_B &= \tfrac{1}{4} \\
p_{\overrightarrow{C}} &= \tfrac{1}{4}\frac{1}{1+p_2} \\
p_{\overleftarrow{C}} &= p_{\overrightarrow{C}} \\
p_D &= p_B \\
p_E &= p_A
\end{aligned}
\tag{16.3}
$$

As can be seen from Fig.16-5, for the forward transport, the first fluorescence peak is given by slips from state A, so its value (minus the background fluorescence due to the ion already being in states D or $\overrightarrow{C}$ at that X) is proportional to p_A. Similarly, the second fluorescence peak is proportional to p_B, and the third to $p_{\overrightarrow{C}}$. After some algebra, we get

$$
\begin{aligned}
p_2 &= \frac{f_2 - f_3}{f_3 - b} \\
p_1 &= 1 - p_2
\end{aligned}
\tag{16.4}
$$

where f_1, f_2 and f_3 are the values of the three fluorescence peaks observed during forward transport (Fig.16-5 and Fig.16-2) and b is the mentioned background, which can be taken as the minimum fluorescence in the trace. Using equation 16.4, the double-slip probabilities versus η can be extracted from the experimental data (Fig.16-7). (In fact, the double-slip probability p_2 in equation 16.4 is the peak fluorescence difference plotted earlier in Fig.16-4 as evidence of transition from single-slip to multi-slip regime, but normalized by the lower peak rather than the higher peak). According to the PT model, the two available minima during a slip are at equal energy for $\eta = 7.788$, so the curves in Fig.16-7 are in fact expected to not exceed $p_2 = 1/2$ for the range of η values used. The quantitative disagreement solicits more careful modeling (taking into account the non-adiabatic dissipation rate, for example) and further experiments where temperature and the minimum and maximum values of

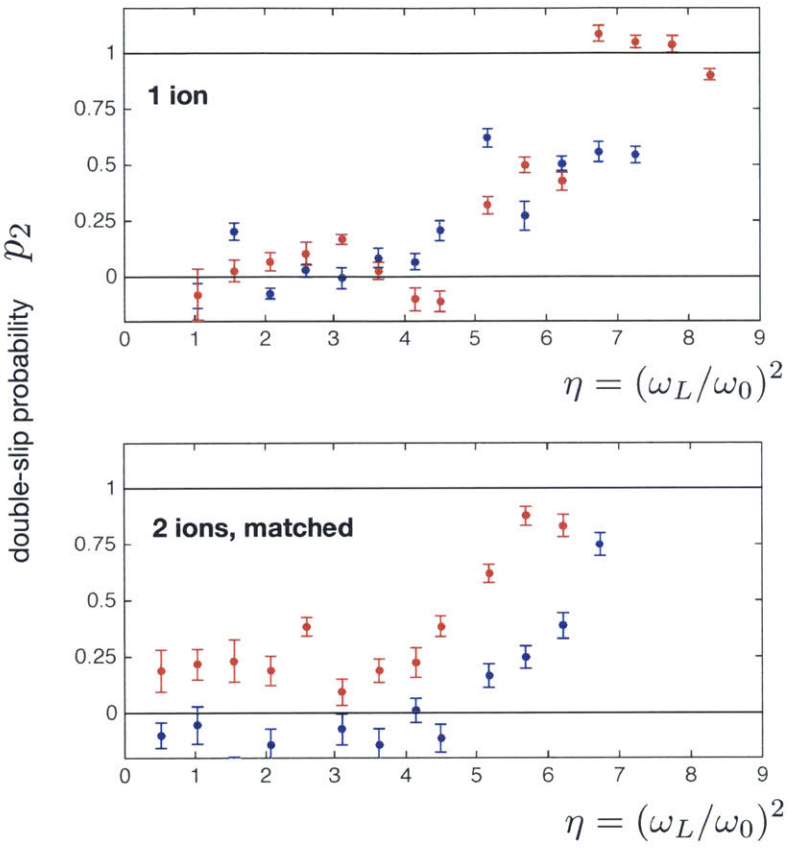

Figure 16-7: Double-slip probabilities versus η extracted from experimental peak fluorescences, again showing a transition from single-slip to multi-slip dynamics (forward slips are shown in blue and backward slips in red).

the X window are varied.

Chapter 17

Friction with trapped ions: conclusions and outlook.

Using the few-ion synthetic frictional interface described in this thesis, we have answered both experimentally and conceptually, with atomic detail, a few key questions about nanofriction, pertaining to the four fundamental pillars. We observed the dependence of friction on the normal load, or substrate interaction strength, and on the structural properties of the frictional interface. We observed the elusive regime of superlubricity at low normal loads and as a result of structural mismatch, related it to the long-standing theoretical concept of the Aubry transition, and very importantly, showed that superlubricity and the Aubry transition occur even in few-atom nanocontacts. Finally, we experimentally elucidated the interplay of different time scales in friction by observing its velocity and temperature dependence with unprecedented systematic control.

These studies, however, have only explored the tip of the iceberg, and friction remains a fascinating and poorly understood phenomenon. I hope that the new set of tools described in this thesis for studying friction with atom-by-atom control can be used in the future to understand this phenomenon even better, at least in the clean controlled system made of cold atoms. For example, a number of open questions can further be studied with these tools: fast-time-scale dynamics of kinks, overdamped multislip dynamics, critical exponents near the Aubry transition, friction

with defects in the substrate lattice or in the contact-layer, friction and superlubricity in 2-dimensional contacts, the effect of different lattice symmetries on friction with 2-dimensional contacts, and the list goes on.

Entering the realm of quantum mechanics, accessible in our system of cold atoms in vacuum, even more fascinating questions present themselves that have barely been addressed by experiment or theory. One such question is spin-dependent friction [21, 121, 122], which could be studied in our system using an optical lattice potential that depends on the internal state of the ion, controllable via lasers. One convenient scheme, for example, would involve hyperfine ground-state sublevels in $^{171}Yb^{+}$. Another possibility is to study the quantum phase transition associated with the Aubry transition [91, 93, 123, 124]. I discuss in part III of my thesis several specific quantum and classical effects at a few-ion level, that, although perhaps digressing from friction, would be intriguing to explore with the current setup.

Part III

Outlook

Chapter 18

Tunneling: towards quantum solids in periodic potentials

An important application of atomic physics is quantum simulation of poorly understood solid-sate phenomena by studying the motion of atoms in periodic optical-lattice potentials. Phenomena in many-body systems with strong inter-particle interactions, such as electrons in certain solids, are particularly interesting and poorly understood. While neutral atoms in optical lattices are promising for emulating the behaviour of electrons in solids, the strength and range of interatomic interactions is limited for neutral atoms. Trapped ions, on the other hand, interact very strongly via the Coulomb forces, just as electrons do, and just as electrons can form a Wigner crystal in a solid [125], trapped ions form Wigner crystals in ion traps. How do these Wigner crystals behave in periodic potentials - i.e. in the crystal lattice of a solid or an optical lattice superimposed on an ion trap? Classically, the same as in the friction problem studied in detail in part II of this thesis. Quantum mechanically, no one knows. Strong interactions combined with strong non-linearities make this a very difficult problem, warranting experimental studies in a well-controlled trapped-ion optical-lattice system achieved in this thesis. The motivation for this is broader than the friction problem studied in our system so far, but understanding the quantum behaviour of solids (Wigner crystals) in periodic potentials can lead to a quantum-mechanical picture of friction and of adsorbed monolayers, possibly relevant at the

nanoscale and at cold surfaces.

Studying the quantum motion of ions in an optical lattice hinges on detecting coherent tunneling of ions between different lattices sites. In the friction language of this thesis, we want to observe quantum mechanical tunneling of an ion chain between two different configurations (local minima) through a Peierls-Nabarro energy barrier. If the chain is matched, this would correspond to common-mode tunneling of the entire chain from one pinned location to the next pinned location one lattice constant a away. An observation of such tunneling of a composite rigid object with individual resolution of its constituent atoms could lead to important studies of decoherence mechanisms as a function of object size (number of atoms). If the chain is mismatched, tunneling through the PN barrier would correspond to tunneling of kinks - solitonic excitations readily detectable in our system (see chapter 13).

To study the quantum coherent processes, laser cooling - the source of dissipation in our system that removes frictional heat - must be turned off for the duration of the experiment. Observation of coherent tunneling is then limited by thermal excitation above the energy barrier by residual heating processes due to environmental fluctuations (T_1 decoherence) and other decoherence processes (T_2 decoherence). In this chapter, I focus on several schemes that might successfully overcome these decoherence time scales, at least for a single trapped ion, the tunneling of which would be the first milestone towards studying quantum solids in periodic potentials in our system.

18.1 Measured heating rate of a single ion in a lattice

Several sources of heating are expected to contribute to T_1 decoherence in our system:

1) anomalous electric field noise [28, 126];

2) electric field noise due to noisy trap electrode drive (multichannel digital-to-analog converter and output amplifiers);

3) parametric heating by lattice intensity fluctuations [127];

4) photon recoil heating from the close-detuned lattice.

Noise due to sources 2-4 can, in principle, be mitigated by passive filtering (on the noisy drive), active feedback (on lattice fluctuations) and larger lattice detuning (to reduce photon recoil heating). Anomalous heating is a more fundamental source of noise and to mitigate it would require rebuilding the experimental setup under a different design (blade trap with distant electrodes, cryogenic cooling of the trap [29, 30], in-situ Ar^+ bombardment cleaning of the trap surface [128] [129], etc.). The anomalous heating rate can be estimated based on published measurements from traps with similar parameters that underwent similar fabrication procedures [30, 130]. Reference [30] reported a heating rate of $\dot{\bar{n}} = 4.2 \pm 0.3$ quanta/ms for a trap with vibrational frequency $\omega_0 = 2\pi \times 1$ MHz and an ion trapped $75\mu m$ from the gold electrode surface. Assuming the commonly accepted d^{-4} scaling of electric field noise with distance from electrode surfaces [28, 126, 131, 25], for ions trapped at 135μm above the gold trap surface in our system this puts the heating rate estimate at $\dot{\bar{n}} = 0.4$ quanta/ms at $\omega_0 = 2\pi \times 1$ MHz, equivalent to $R_{heat} = 2\pi\hbar \times 0.4$ MHz / ms.

The expression for the heating rate in terms of the electric field noise power spectrum $S_E(\omega)$ is given by [28]:

$$R_{heat} = \dot{\bar{n}}\hbar\omega_0 = \frac{e^2}{4m}\left(S_E(\omega_0) + \frac{\omega_0^2}{2\omega_{RF}^2}S_E(\omega_{RF} \pm \omega_0)\right) \tag{18.1}$$

Since $\omega_0 << \omega_{RF}$ and the noise spectrum is typically "pink" $S_E(\omega) \propto \omega^{-1}$ [28], the second term in equation 18.1 is negligible and the heating rate is expected to scale as $R_{heat} \propto \omega_0^{-1}$, and the rate of excitation of vibrational quanta as $\dot{\bar{n}} \propto \omega_0^{-2}$, i.e. heating becomes significantly worse at lower trap vibrational frequencies.

We have performed preliminary measurements of the total heating rate of a trapped ion centered in the site of an optical lattice by switching off laser cooling and observing temperature increase with time as inferred from the ion fluorescence (see section 6.4). Our best measurement (Fig.18-1) gives $\dot{\bar{n}} = 2.5$ quanta/ms at a lattice vibrational frequency of $\omega_L = 2\pi \times 0.635$ MHz, corresponding to a lattice depth of $U = 2\pi\hbar \times 12$ MHz (however, heating rates up to 60 quanta/ms have also been seen, for example, under imperfect compensation). Assuming $\dot{\bar{n}} \propto \omega_0^{-2}$ scaling, this

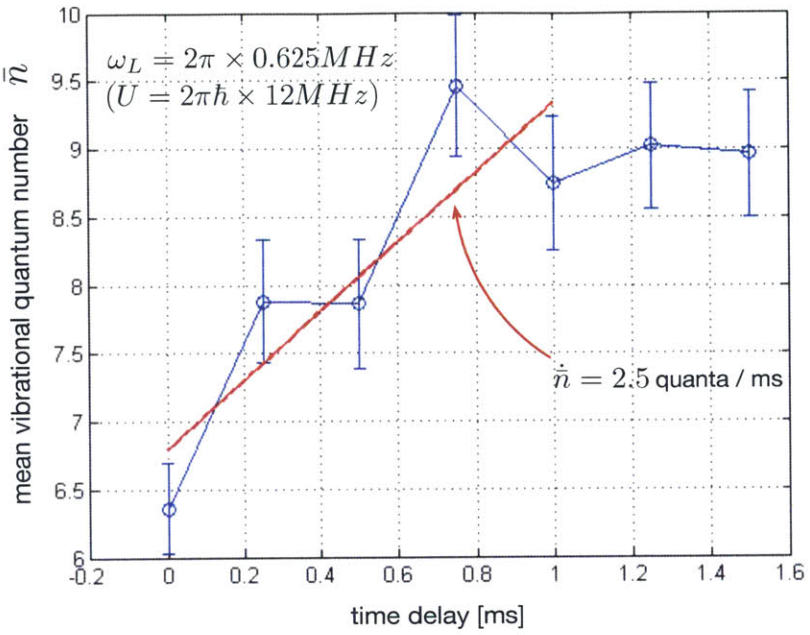

Figure 18-1: Measured heating rate of a single ion in an optical lattice, obtained by switching off cooling and observing temperature increase with time. Temperature is obtained from the ion's fluorescence in its lattice well, a method described in more detail in section 6.4. This temperature measurement saturates at large temperatures, so the heating rate is obtained using a linear fit in the first 1ms of heating.

corresponds to $\dot{\bar{n}} = 1.0$ quanta/ms for a $2\pi \times 1$ MHz vibrational frequency, a factor of 2 larger than the anticipated 0.4 quanta/ms heating rate from anomalous heating, indicating additional heating, potentially due to the lattice.

The parametric heating in a lattice site at twice the vibrational frequency $2f_L = 2\omega_L/2\pi$ is given by [127]

$$\frac{1}{E}\frac{dE}{dt} = \pi^2 f_L^2 S_L(2f_L) \tag{18.2}$$

where the one-sided power spectrum of the fractional intensity noise of the lattice $S_L(f)$, as measured at the cavity transmission, is shown in Fig.18-2a. It results in the heating rate constant $\frac{1}{E}\frac{dE}{dt}$ as a function of lattice vibrational frequency f_L shown in Fig.18-2b. Thus, at $f_L = 0.635$ MHz and at $\bar{n} = 1$, we expect $\dot{\bar{n}} = 0.03$ quanta/ms from paramteric heating due to lattice intensity fluctuations, a negligible contribution to the total 2.5 quanta/ms observed.

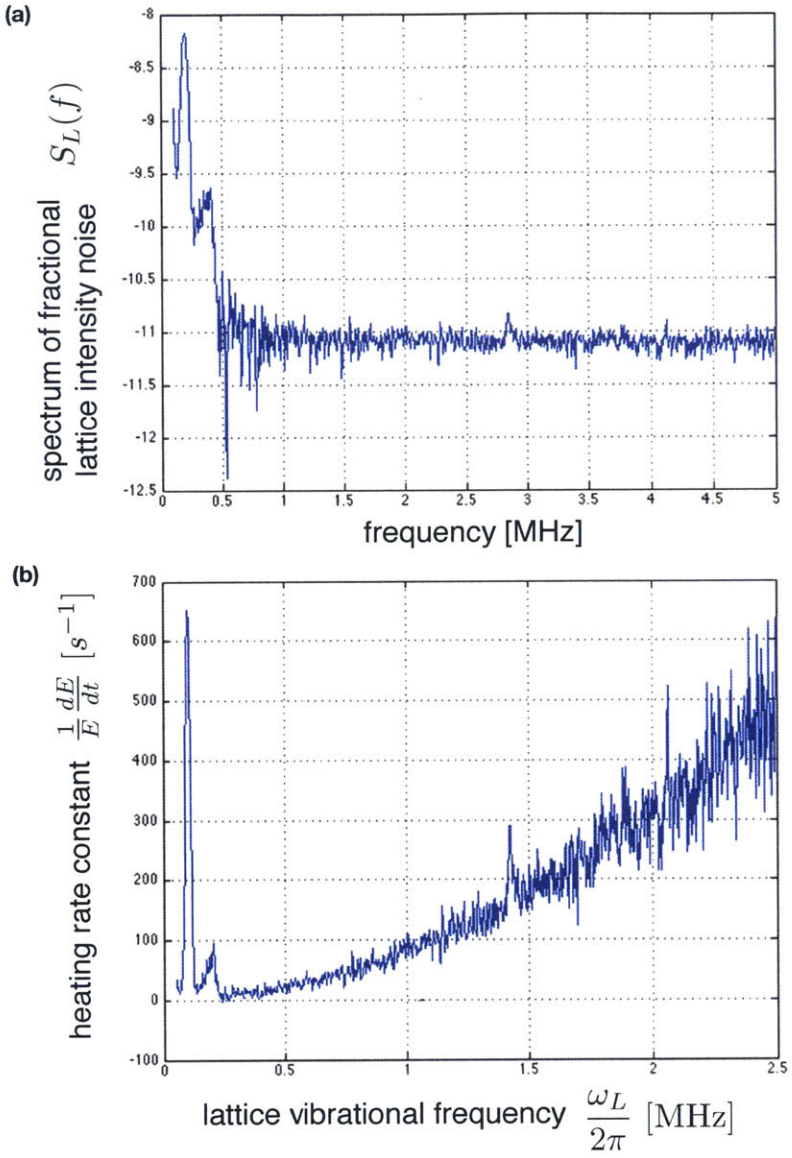

Figure 18-2: **(a)** Measured spectrum of fractional lattice intensity fluctuations at the output of the cavity (normalized by the photodiode DC reading). The noise spectrum appears to be white in the frequency range of relevance. **(b)** Heating rate constant due to parametric lattice intensity noise heating as a function of trap vibrational frequency, obtained from the measured intensity noise spectrum and equation 18.2.

The photon recoil heating by the lattice is given by the recoil energy times the photon scattering rate

$$R_{ph} = \hbar\omega_{rec}\gamma_{sc} \tag{18.3}$$

where the rate of photon scattering by $^{174}Yb^{+}$ from for the far-detuned lattice is given by

$$\gamma_{sc} = \frac{3}{2\hbar}\frac{U}{\Delta/\Gamma} \tag{18.4}$$

Given the large detuning $\Delta/\Gamma = 630$ and the lattice with $U = 2\pi\hbar \times 12$ MHz and $\omega_L = 2\pi \times 0.635$ MHz, we estimate $\dot{\bar{n}} = R_{ph}/\hbar\omega_L \approx 0.4$ quanta / ms, potentially a sizable contribution to the total observed heating rate of 2.5 quanta/ms.

If the observed heating rate is indeed dominated by anomalous electric field noise as this analysis suggests, one way to potentially suppress this heating rate without significant changes to the setup would be to move the minimum of the RF pseudopotential further from the trap chip surface, which is currently 134μm away. With the current set-up, this is limited by the requirement to keep the ions within the cavity waist of 38 μm. In the best case scenario then, the ions would end up at 172μm from the surface, and the d^{-4} scaling would result in heating rate reduction by a factor of 2.7.

18.2 Tunneling in a shallow lattice

The Rabi frequency $2J$ for single-atom tunneling between two sites of a uniform optical lattice with $a = \lambda/2$ can be obtained from the width of the ground band [132] as

$$2J = \tfrac{1}{2}(E_{0,q=\pi/a} - E_{0,q=0}) \approx \tfrac{1}{2}\exp(-\tfrac{1}{4}U) \tag{18.5}$$

where J, E and U are in units of recoil energy $E_{rec} = \frac{\hbar^2k^2}{2m}$, and $k = \frac{2\pi}{\lambda}$. That means that the fastest tunneling proceeds at angular frequency $\frac{1}{2}\omega_{rec} \times 0.82$ at the lowest lattice depth $U = 0.8$ where all ground band energies are below U, and tunneling falls off exponentially with the depth of the lattice U.

The conventional approach to observing ion tunneling in a lattice is to 1) cool the

ion near its vibrational ground state $\frac{1}{2}\omega_L$ (where $\omega_L = 2\sqrt{U}$ in recoil units) at one site of a deep optical lattice, 2) shut off the cooling lasers, 3) adiabatically ramp the lattice down to the recoil energy $U \approx 1$ while keeping it in the motional ground state, 4) let the motional wavefunction of the ion evolve coherently for a variable time T_{exp}, 5) quickly ramp the lattice back up to project the ion into one of the lattice wells, and 6) detect which well the ion is in (via fluorescence modulated by position in the lattice, or via split image detection - see chapter 7).

Cooling of ions to the ground state of the deep optical lattice was demonstrated in section 6.4 and in our paper [16]. For an ion to stay in the ground state as the lattice is ramped down, according to the adiabaticity criterion for avoiding vibrational excitations at ω_L, the rate of fractional change of the vibrational frequency must be smaller than the vibrational frequency:

$$\frac{d\omega_L}{dt}/\omega_L << \omega_L \tag{18.6}$$

That means that during the fastest ramp allowed, $\omega_L(t)$ follows the solution of the differential equation $\frac{d\omega_L}{dt}/\omega_L = \omega_L$ given by

$$\omega_L(t) = \frac{1}{\omega_L(0)^{-1} - t} \tag{18.7}$$

So the total time T for a ramp from $\omega_L(0)$ to $\omega_L(T)$ is

$$T = \frac{\omega_L(0) - \omega_L(T)}{\omega_L(0)\omega_L(T)} \tag{18.8}$$

which for $\omega_L(0) >> \omega_L(T)$ (as in our case where typically $\omega_L(0) \approx 100$ and $\omega_L(T) \approx 1$ in recoil units) reduces to $T = 1/\omega_L(T)$, which in our case is on the order of the inverse recoil frequency ω_{rec}^{-1} for the fastest allowed adiabatic ramp.

As mentioned above, tunneling will also proceed on the time scale of ω_{rec}^{-1} or slower. That means that once the cooling lasers are shut off in step (2), the heating rate due to external noise cannot exceed 1 recoil of energy after one fastest tunneling Rabi

period $\frac{2\pi}{0.41\omega_{rec}}$:

$$R_{heat} \lesssim 0.41\hbar\omega_{rec}^2/(2\pi) \tag{18.9}$$

Given $\omega_{rec} = 2\pi \times 8.4$ kHz for $^{174}Yb^+$ ions, the heating rate in our system must not exceed $2\pi\hbar \times 30$ kHz / ms. Optimistically assuming that the heating rate is independent of the vibrational frequency, as in the case of a white power spectrum of electric field noise [28], our measured heating rates of $\sim 2\pi\hbar \times 1$ MHz / ms already drastically exceed the allowable decoherence rate to observe tunneling. More realistically, noise is not white, but pink, with $1/\omega$ scaling, as observed, for example, in other ion traps [28, 29]. In that case, the heating rate would go up by a factor $\omega_L(0)/\omega_L(T) \approx 100$ after an adiabatic ramp to a recoil-deep lattice, certainly prohibiting ion tunneling experiments in shallow lattices. It is possible, however, that the measured heating rate suffers from a peaked noise spectrum in the vicinity of 1 MHz and the heating rate will go down after an adiabatic ramp. This would need to be confirmed with more careful measurements.

18.3 Enhanced tunneling in a double-well potential

As discussed in the previous section, the fastest tunneling rate scale is set by the recoil angular frequency $\omega_{rec}/(2\pi) = \frac{h}{8ma^2}$ and scales as a^{-2}. This means that it could be made faster by reducing the spacing between lattice wells a. One way is to use a shorter-wavelength optical lattice - which in our case would be deep in the UV wavelengths that are technologically challenging. An alternative approach is to observe tunneling of ions in a double-well potential with a tunable well spacing that can be brought significantly below a. For example, one can observe coherent oscillations of a single ion or a chain of ions matched to the lattice between the left well and the right well of the Prandtl-Tomlinson potential (see section 12.2) obtained by superimposing a deep optical lattice U and the axial harmonic confinement at angular frequency ω_0 of the Paul trap:

$$V_{PT}(x) = \frac{\pi^2}{4}\omega_0^2 x^2 + \frac{1}{2}U\Big(1 + \cos\big(2\pi x\big)\Big) \tag{18.10}$$

This is the same equation as 12.3, but with energies in units of E_{rec} and ω_{rec} respectively, and positions and distances in units of a. Let us introduce again the PT parameter specifying the shape of the potential $\eta = \frac{4U}{\omega_0^2}$ in terms of the ratio of the two potential components expressed in recoil units. (Recall that equivalently, $\eta = \frac{\omega_L^2}{\omega_0^2}$.) Then,

$$V_{PT}(x) = \frac{\pi^2}{4}\omega_0^2 x^2 + \frac{1}{8}\eta\omega_0^2\Big(1 + \cos\big(2\pi x\big)\Big) \tag{18.11}$$

This potential is plotted in Fig.18-3 and the distance between the two wells and the energy barrier are plotted as a function of η. One can see from these plots, that the two wells can be brought arbitrarily close together by choosing the shape of the PT potential via η, and the height of the barrier between the wells can be independently controlled by scaling the energy of the potential via the axial Paul trap confinement ω_0 (the lattice depth U of course needs to be scaled accordingly to maintain a desired η). For example, by dialing in $\eta = 1.11$, the distance between the two wells δ can be made $1/4$ of the underlying lattice spacing a, which should result in a tunneling rate enhancement by a factor of $\delta^{-2} = 16$ from $0.41\omega_{rec}$, assuming that the barrier is adjusted to just barely keep 2 eigenstates below the barrier.

18.3.1 Tunneling rate calculation

To verify this intuition, the tunneling rate in the double-well potential 18.11 can be calculated by diagonalizing the Hamiltonian $H = V_{PT} - \frac{1}{\pi^2}\frac{d^2}{dx^2}$ (dimensionless units) in the eigenbasis of the underlying axial harmonic potential with angular frequency ω_0. The idea is that for large energies, the lattice component of the V_{PT} potential is a perturbation on the harmonic oscillator potential, especially for η close to 1, and the Hilbert space can be cut off at a finite number of basis vectors. The harmonic oscillator eigenvectors are given by Hermite-Gaussian wavefunctions in position space

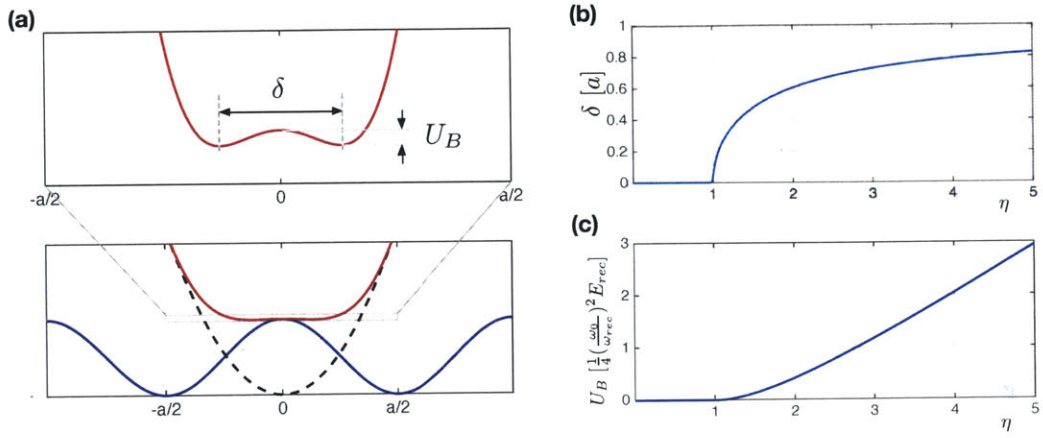

Figure 18-3: **(a)** Tunneling can be significantly enhanced in the Prandtl-Tomlinson double-well potential where the superimposed harmonic trap can squeeze two lattice sites arbitrarily close together. Here, $\eta = 1.11$ is illustrated. **(b)** The distance between the two minima δ in units of the lattice spacing a goes to zero sharply as the corrugation parameter η approaches unity from above. **(c)** The barrier height U_B also goes to zero at $\eta = 1$.

(where h_n are Hermite polynomials):

$$\psi_n(x) = \frac{(\pi\omega_0/2)^{1/4}}{\sqrt{2^n n!}} h_n\left(x\sqrt{\pi^2\omega_0/2}\right)\exp\left(-x^2\frac{\pi^2\omega_0}{4}\right) \tag{18.12}$$

The Hamiltonian matrix elements H_{nm} are then given by $H_{nm} = \int_{-\infty}^{+\infty} \psi_n(x) H \psi_m(x) dx$. Taking basis vectors ψ_n up to n_{max} and diagonalizing the $n_{max} \times n_{max}$ matrix gives the eigenspectrum up to n_{max}. The difference between the lowest two eigenfrequencies gives the tunneling Rabi frequency (equivalent to the width of the ground band giving the tunneling Rabi frequency in a lattice). Fig.18-4 shows the tunneling Rabi frequency calculated this way with increasing n_{max} for $\omega_0 = 119\omega_{rec}$ and two values of η. Thus, for low values of η close to 1, the procedure converges for about $n_{max} = 25$ basis vectors.

With the choice of $\eta = 1.11$ and $\omega_0 = 119\omega_{rec}$, corresponding to $2\pi \times 1$ MHz - the largest axial vibrational frequency attainable in the current set-up (limited by the maximum output of the DAC supplying the DC voltages), this diagonalization procedure gives the first excited state energy equal to the energy barrier. The tun-

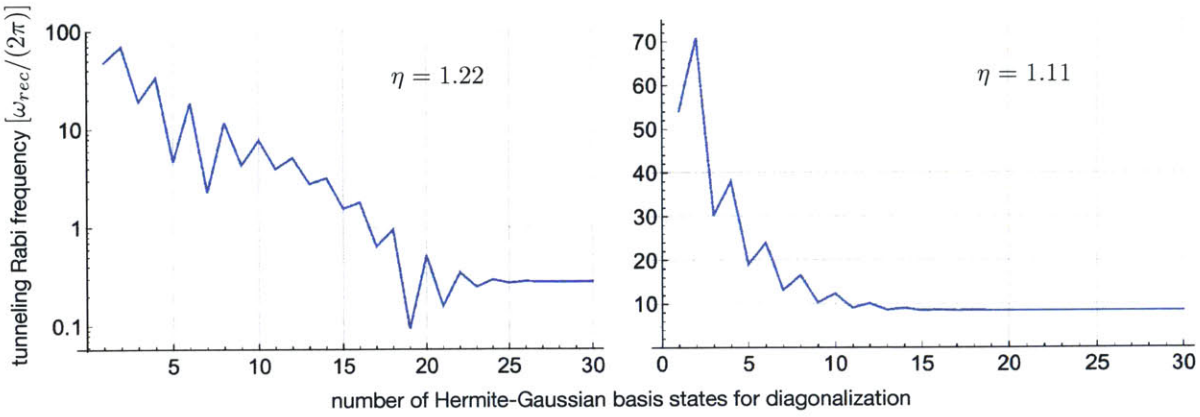

Figure 18-4: Convergence of the diagonalization procedure with the number of basis states for determining the tunneling Rabi frequency. Convergence is faster for η close to 1, since the lattice becomes less of a perturbation to the harmonic oscillator Hamiltonian.

neling Rabi frequency is $\omega_{tun} = 9\omega_{rec}$, a factor of 20 faster than the fastest tunneling in a recoil-deep lattice, attained here in a lattice that is $U \approx 4000E_{rec}$ deep ($2\pi\hbar \times 30$ MHz).

Repeating this procedure for several pairs of η and ω_0 that give the first excited state energy at the energy barrier, confirms that the tunneling rate scales as δ^{-2}, as shown in Fig.18-5a. The solid line that agrees with the results (red points) is

$$\omega_{tun} = \frac{1.34}{\delta^2}(0.41\omega_{rec}) \tag{18.13}$$

In Fig.18-5b the same results are plotted against the axial vibrational frequency ω_0, where the solid line that agrees with the results is

$$\omega_{tun}/\omega_{rec} = 0.37(\omega_0/\omega_{rec})^{2/3} \tag{18.14}$$

This shows that increasing the tunneling rate beyond $9\omega_{rec}$ would be difficult: reaching $14\omega_{rec}$ would require an axial vibrational frequency of $\omega_0 = 2\pi \times 2$ MHz, which means quadrupling the DC voltages for axial confinement and quadrupling the lattice depth U to $2\pi\hbar \times 130MHz$.

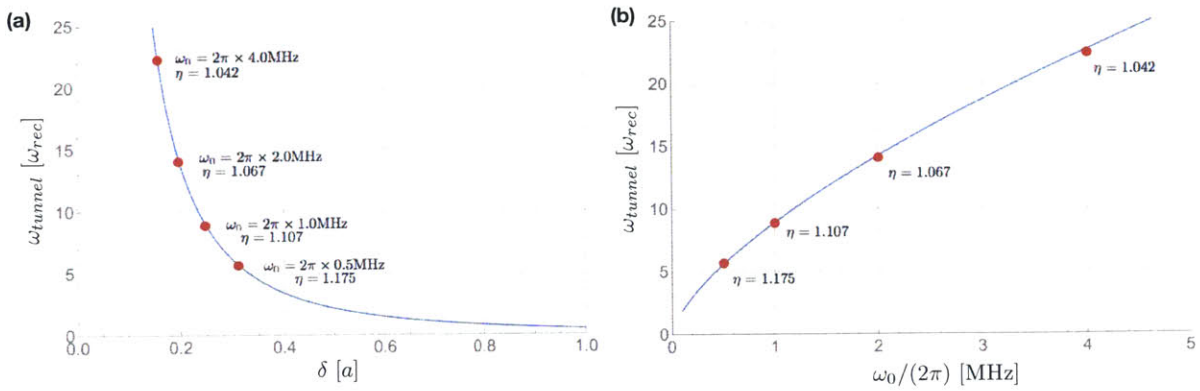

Figure 18-5: **(a)** The tunneling Rabi frequency scales with the distance between the double-well minima as δ^{-2}. **(b)** Scaling of the tunneling Rabi frequency with the overall energy scale represented by the harmonic trap vibrational frequency ω_0.

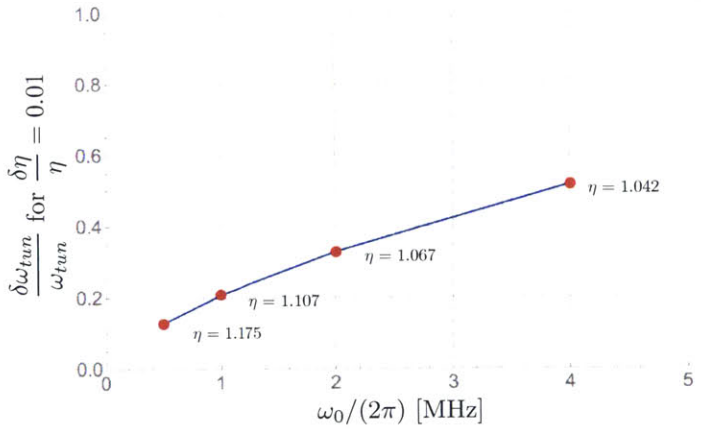

Figure 18-6: Fractional sensitivity of the tunneling Rabi frequency (vs the overall energy scale determined by ω_0) for 1% fractional fluctuations in η (likely to be dominated by fluctuations in the lattice depth).

18.3.2 Limitations

One important consideration for enhancing the tunneling rate with this method is the attainable stability of η limited by the stability of the lattice depth U. The plot versus ω_0 of fractional fluctuations of the tunneling rate for 1% fluctuations in η is shown in Fig.18-6. At $\eta = 1.11$ and $\omega_0 = 2\pi \times 1$ MHz, the tunneling rate fluctuates by 20% for 1% fluctuations in the lattice depth, so U must be stable to better than 1% on a time scale of tunneling for these parameters: $\frac{2\pi}{9\omega_{rec}} = 10\mu$s. This can be achieved by lattice intensity stabilization with a 100 kHz bandwidth lock.

Another important consideration is lattice scattering that begins to contribute

to decoherence at large lattice depths and the 12.6 GHz detuning (corresponding to $\Delta/\Gamma = 630$) that we currently use. The scattering rate from $^{174}Yb^{+}$ is related to the lattice depth as follows:

$$\gamma_{sc} = \frac{3}{2\hbar}\frac{U}{\Delta/\Gamma} \tag{18.15}$$

This means that a lattice $U = 4000E_{rec}$ that gives a tunneling rate of $9\omega_{rec}$ will also scatter about 10 photons and add 10 recoils of energy to the system in one tunneling Rabi period unless the detuning in increased further, which would require a proportional increase in laser power to maintain the desired lattice depth.

The biggest limitation to this scheme is likely to be the stability of axial electric fields. Their drifts or fluctuations even on a small scale result in a significant tilt of the double-well, which becomes more sensitive for lower values of η, which are desired to enhance the tunneling rate. For example, at $\eta = 1.11$, an electric field that displaces the Paul trap position X by only 0.005a already makes one of the wells of the double-well potential disappear.

18.3.3 Experimental protocol

To observe coherent tunneling between the two minima of this double-well potential, we can employ the position-dependent fluorescence that enables single-lattice-site resolution in friction experiments. Fluorescence contrast between the two minima can be achieved by tilting the potential once the lattice is ramped up for position detection. Thus, the proposed experimental scheme is as follows (see Fig.18-7):

<1> Initialize the ion in a single well at $\eta = 2$ (or another value $\eta >> 1$) and trap centered over a lattice minimum $X = -0.5$. Duration: limited by recooling time $\tau_c \approx 50\mu s$.

<2> Move the trap over a lattice maximum $X = 0$ to create the symmetric bistable potential. Duration: limited by trap low-pass filtering $\sim 100\mu s$. Turn laser cooling off.

<3> Adiabatically ramp down the lattice depth to $\eta = 1.11$ to initiate tunneling. Duration: must be between the tunneling time scale of $\sim (10\omega_{rec})^{-1}$ and the inverse

energy gap to the next band of two states $\sim (30\omega_{rec})^{-1}$.

<4> Wait for a variable delay time T_{exp} while the ion tunnels. (Vary T_{exp} between 0 and $(10 \times 2\pi\omega_{rec})^{-1}$ to reconstruct the Rabi flopping.)

<5> Suddenly ramp up the lattice depth back to $\eta = 2$ to freeze the coherent evolution. Duration: much faster than tunneling time scale $\sim (10\omega_{rec})^{-1}$.

<6> Turn laser cooling on and move the trap to tilt the double-well enough to create fluorescence contrast but not enough to cause a slip: $0 < |X| << F_s/K$. Duration: limited by trap low-pass filtering $\sim 100\mu s$.

<7> Collect fluorescence to determine which site of the bistable potential the ion ended up in. Duration: limited by thermal hopping time $\tau_{th} \sim 1 - 10ms$.

Before concluding this section, I emphasize again, that while the double-well potential is described in the context of a single trapped ion, the common mode of an ion crystal which is matched to the lattice will experience an identical double-well potential, and therefore this scheme is suitable for studying quantum coherent tunneling of an ion chain as a rigid composite object.

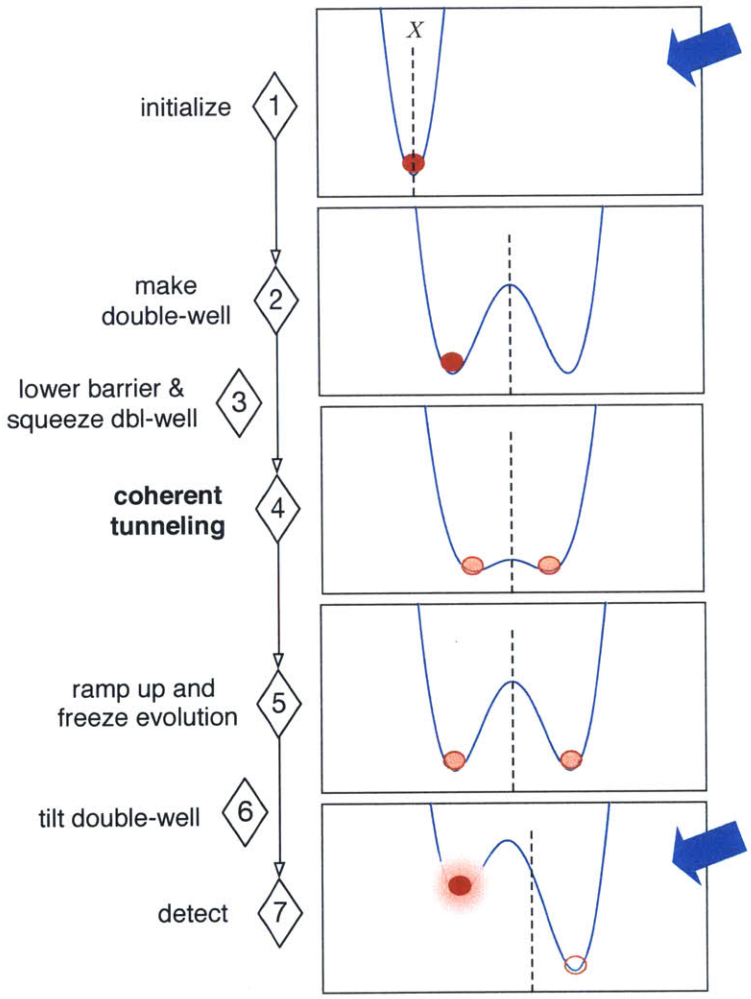

Figure 18-7: Experimental scheme for observing tunneling of a single ion or a matched ion crystal in a double-well potential. Detection of the ion in the left or the right minimum is enabled by a fluorescence contrast between them as a result of a potential tilt which brings one minimum higher up the lattice potential than the other.

18.4 Tunneling assisted by delocalized states

In the previous section, I discussed a way to enhance the tunneling achievable in a lattice by squeezing two wells of a double-well potential close together. Here, I discuss a way in which tunneling could be induced in a deep optical lattice at the original site spacing by using photon-assisted coupling to delocalized motional states.

In the limit of a deep optical lattice, tunneling is exponentially suppressed as can be inferred from the spatial overlap between two ground-state harmonic oscillator wavefunctions displaced by δ (in units of the lattice spacing) and corresponding to angular vibrational frequency ω (in units of ω_{rec}):

$$\langle \phi_0(x) | \phi_0(x-\delta) \rangle = e^{-\frac{\pi^2}{8}\delta^2\omega} \tag{18.16}$$

Taking these harmonic oscillator wavefunctions to be approximations to localized states at two neighbouring lattice sites, gives $\delta = 1$, and for a deep optical lattice $\omega = \omega_L >> 1$, these wavefunction are well localized with a very poor spatial overlap.

A way to address the poor wavefunction overlap is to couple both wavefunctions to a virtual untrapped, or delocalized, motional state, which has good overlap with both wavefunctions. This could be, for example, an internal state of the ion that experiences the opposite sign of the optical lattice potential and has lattice sites in between the sites of the original lattice (Fig.18-8). Coupling to a highly excited motional state of the intermediate site can achieve the desired wavefunction overlap. Let us again consider harmonic oscillator wavefunctions. It turns out that there is a simple closed-form expression for the overlap between the ground-state harmonic eigenfunction and an excited eigenfunction of a displaced oscillator:

$$\langle \phi_0(x) | \phi_n(x-\delta) \rangle = \frac{e^{-\frac{\pi^2}{8}\delta^2\omega} \left(\frac{\pi}{2}\delta\sqrt{\omega}\right)^n}{\sqrt{n!}} \tag{18.17}$$

where again δ is the distance between the two oscillators in units $a = \lambda/2$ and ω is the oscillator frequency in units of recoil frequency. This expression turns out to

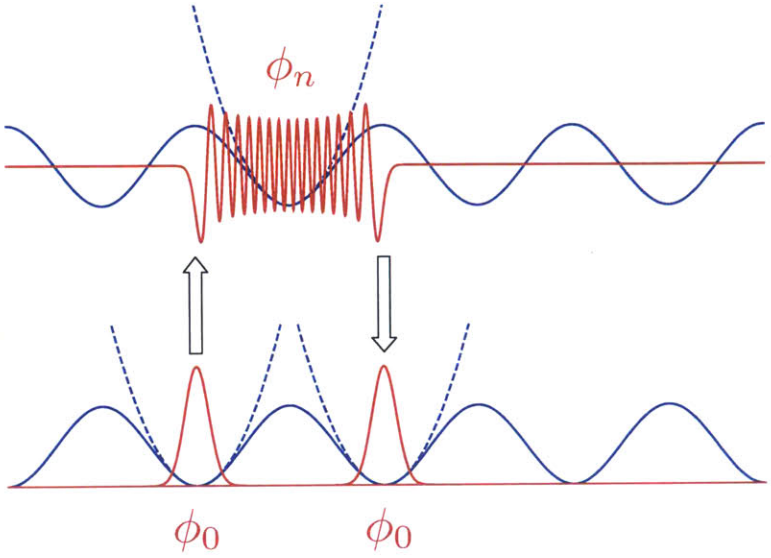

Figure 18-8: Tunneling between two deep lattice wells can be enhanced by two-photon coupling via a highly excited vibrational state in a "flipped" lattice experienced by a different internal state. The highly excited intermediate vibrational state has good spatial overlap with the localized wavefunctions representing the initial and the final state of the tunneling process.

be the square root of the poisson distribution

$$\langle \phi_0(x) | \phi_n(x-\delta) \rangle = \sqrt{\text{Poisson}(n;\nu)} \tag{18.18}$$

with the Poisson distribution mean and variance given by

$$\nu = \frac{\pi^2}{4}\delta^2\omega \tag{18.19}$$

We are interested in the overlap between the ground-state harmonic oscillator wavefunctions at neighouring lattice sites that we want to couple and the n^{th} vibrational state of the "intermediate" oscillator site that is $a/2$ away from each of the primary sites. Given a vibrational frequency of $\omega = 2\pi \times 400$ kHz, reasonable for our system, the overlap peaks at $n = 30$ at a value of 0.25 (see Fig.18-9). This means that if the 30th vibrational state can be resolved spectroscopically, a large tunneling rate can be achieved virtually via this delocalized vibrational state.

To conclude this section, I emphasize that this scheme is fundamentally different

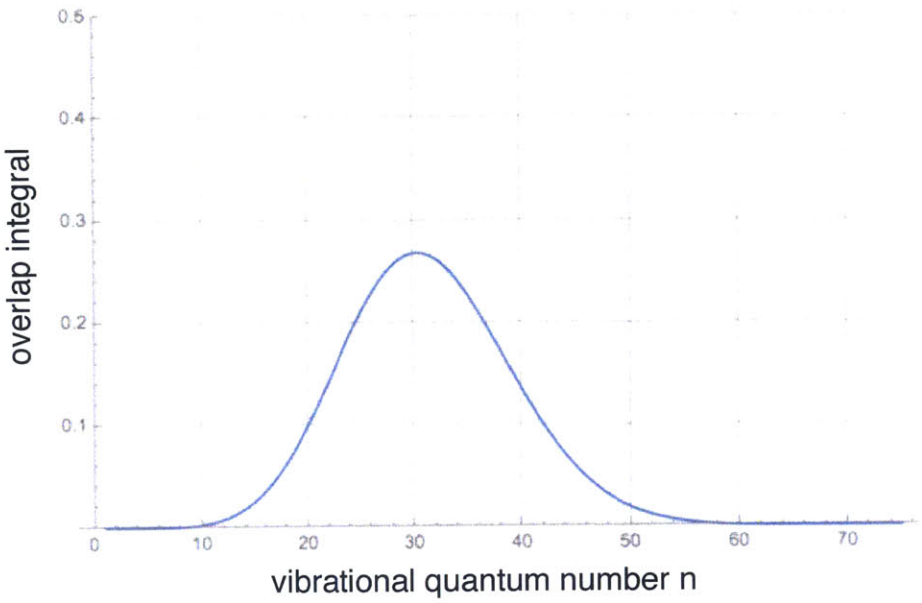

Figure 18-9: The spatial overlap between the localized ground-state wavefunction and an excited intermediate state n follow a Poisson-like function that peaks a particular quantum number n depending on the depth of the lattice (i.e. the vibrational frequency of the effective harmonic oscillator).

from other photon-assisted tunneling schemes [133, 134], which usually serve to control the phase of tunneling and restore a resonant tunneling condition. The scheme here can in addition significantly enhance the tunneling rate itself, and could be used more generally in neutral atom experiments as well.

Appendix A

Publications

A number of publications resulted from this thesis work, shown here by topic.
(* indicates equal author contributions)

Friction:

→ Alexei Bylinskii*, Dorian Gangloff* and Vladan Vuletic, *"Tuning friction atom-by-atom in an ion-crystal simulator"*. **Science**, 348(6239), 1115-1119 (2015)

→ Dorian Gangloff*, Alexei Bylinskii*, Ian Counts, Wonho Jhe, Vladan Vuletic, *"Velocity tuning of friction with two trapped atoms"*. **Nature Physics**, (2015), doi: 10.1038/nphys3459

→ Alexei Bylinskii*, Dorian Gangloff*, Ian Counts and Vladan Vuletic, *"Observation of Aubry transition in finite atom chains via superlubricity breaking"*. Manuscript in preparation

Trapping and cooling of ions in optical lattices:

→ Leon Karpa*, Alexei Bylinskii*, Dorian Gangloff*, Marko Cetina and Vladan Vuletic, *"Suppression of Ion Transport due to Long-Lived Subwavelength Localization by an Optical Lattice"*. **Physical Review Letters**, 111(16), 163002 (2013)

Ion-cavity system:

→ M. Cetina, A. Bylinskii, L. Karpa, D. Gangloff, K. M. Beck, Y. Ge, M. Scholz, A. T. Grier, I. Chuang, and V. Vuletic, *"One-dimensional array of ion chains coupled to an optical cavity"*. **New Journal of Physics**, 15 053001 (2013)

Other:

→ D. Gangloff*, M. Shi*, T. Wu*, A. Bylinskii, B. Braverman, M. Gutierrez, R. Nichols, J. Li, K. Aichholz, M. Cetina, L. Karpa, B. Jelenkovic, I. Chuang, and V. Vuletic, *"Preventing and reversing vacuum-induced optical losses in high-finesse tantalum (V) oxide mirror coatings"*. **Optics Express**, 23, 18014-18028 (2015)

→ P. Samutpraphoot, S. Weber, Q. Lin, D. Gangloff, A. Bylinskii, B. Braverman, A. Kawasaki, C. Raab, W. Kaenders, and V. Vuletic, *"Passive intrinsic-linewidth narrowing of ultraviolet extended-cavity diode laser by weak optical feedback"*. **Optics Express**, 10 11592 (2014)

→ A. M. Eltony, D. Gangloff, M. Shi, A. Bylinskii, V. Vuletic, I. L. Chuang, *"Technologies for trapped-ion quantum information systems"*. Under review at Springer Special Issue on Trapped Ion Quantum Information Processing, arXiv:1502.05739

Bibliography

[1] Michael A. Nielsen and Isaac L. Chuang. *Quantum Computation and Quantum Information.* Cambridge University Press, Cambridge, UK, 2000.

[2] Richard P. Feynman. Simulating physics with computers. *International Journal of Theoretical Physics*, 21(6-7):467–488, June 1982.

[3] D. Leibfried, R. Blatt, C. Monroe, and D. Wineland. Quantum dynamics of single trapped ions. *Reviews of Modern Physics*, 75(1):281–324, March 2003.

[4] Leticia Tarruell, Daniel Greif, Thomas Uehlinger, Gregor Jotzu, and Tilman Esslinger. Creating, moving and merging Dirac points with a Fermi gas in a tunable honeycomb lattice. *Nature*, 483(7389):302–305, 2012.

[5] Markus Greiner, Olaf Mandel, Tilman Esslinger, Theodor Hansch, and Immanuel Bloch. Quantum phase transition from a superfluid to a Mott insulator in a gas of ultracold atoms. *Nature*, 415:39–44, 2002.

[6] Waseem S Bakr, Jonathon I Gillen, Amy Peng, Simon Fölling, and Markus Greiner. A quantum gas microscope for detecting single atoms in a Hubbard-regime optical lattice. *Nature*, 462(7269):74–7, November 2009.

[7] Jacob F Sherson, Christof Weitenberg, Manuel Endres, Marc Cheneau, Immanuel Bloch, and Stefan Kuhr. Single-atom-resolved fluorescence imaging of an atomic Mott insulator. *Nature*, 467(7311):68–72, September 2010.

[8] Christof Weitenberg, Manuel Endres, Jacob F. Sherson, Marc Cheneau, Peter Schauß, Takeshi Fukuhara, Immanuel Bloch, and Stefan Kuhr. Single-spin addressing in an atomic Mott insulator. *Nature*, 471(7338):319–324, March 2011.

[9] Lawrence W. Cheuk, Matthew A. Nichols, Melih Okan, Thomas Gersdorf, Vinay V. Ramasesh, Waseem S. Bakr, Thomas Lompe, and Martin W. Zwierlein. Quantum-Gas Microscope for Fermionic Atoms. *Physical Review Letters*, 114(19):193001, 2015.

[10] Maxwell F. Parsons, Florian Huber, Anton Mazurenko, Christie S. Chiu, Widagdo Setiawan, Katherine Wooley-Brown, Sebastian Blatt, and Markus Greiner. Site-Resolved Imaging of Fermionic Li6 in an Optical Lattice. *Physical Review Letters*, 114(21):213002, 2015.

[11] Elmar Haller, James Hudson, Andrew Kelly, Dylan A. Cotta, Bruno Peaudecerf, Graham D. Bruce, and Stefan Kuhr. Single-atom imaging of fermions in a quantum-gas microscope. *Nature Physics*, 11:738–742, 2015.

[12] Hidetoshi Katori, Stefan Schlipf, and Herbert Walther. Anomalous Dynamics of a Single Ion in an Optical Lattice. *Physical Review Letters*, 79(12):2221–2224, September 1997.

[13] C Schneider, M Enderlein, T Huber, and T Schaetz. Optical Trapping of an Ion. *Nature Photonics*, 4:772–775, 2010.

[14] Martin Enderlein, Thomas Huber, Christian Schneider, and Tobias Schaetz. Single Ions Trapped in a One-Dimensional Optical Lattice. *Physical Review Letters*, 109(23):233004, December 2012.

[15] Rasmus Linnet, Ian Leroux, Mathieu Marciante, Aurélien Dantan, and Michael Drewsen. Pinning an Ion with an Intracavity Optical Lattice. *Physical Review Letters*, 109(23):233005, December 2012.

[16] Leon Karpa, Alexei Bylinskii, Dorian Gangloff, Marko Cetina, and Vladan Vuletić. Suppression of Ion Transport due to Long-Lived Subwavelength Localization by an Optical Lattice. *Physical Review Letters*, 111(16):163002, October 2013.

[17] Alexei Bylinskii, Dorian Gangloff, and Vladan Vuletic. Tuning friction atom-by-atom in an ion-crystal simulator. *Science*, 348(6239):1115–1118, 2015.

[18] Rainer Blatt and David Wineland. Entangled states of trapped atomic ions. *Nature*, 453(7198):1008–15, June 2008.

[19] L. Lamata, D. Leibrandt, I. Chuang, J. Cirac, M. Lukin, V. Vuletić, and S. Yelin. Ion Crystal Transducer for Strong Coupling between Single Ions and Single Photons. *Physical Review Letters*, 107(3):030501, July 2011.

[20] T Fogarty, C Cormick, H Landa, Vladimir M Stojanovic, E Demler, and Giovanna Morigi. Nano-friction in cavity quantum electrodynamics. *arXiv:1504.00275v1*, pages 1–9, 2015.

[21] Boris Wolter, Yasuo Yoshida, André Kubetzka, Saw Wai Hla, Kirsten Von Bergmann, and Roland Wiesendanger. Spin friction observed on the atomic scale. *Physical Review Letters*, 109(11):116102, 2012.

[22] Jens D Baltrusch, Cecilia Cormick, Gabriele De Chiara, Tommaso Calarco, and Giovanna Morigi. Quantum superpositions of crystalline structures. *Physical Review A*, 84(6):063821, 2011.

[23] Jens D. Baltrusch, Cecilia Cormick, and Giovanna Morigi. Quantum quenches of ion Coulomb crystals across structural instabilities. *Physical Review A*, 86(3):032104, September 2012.

[24] R Schmied, T Roscilde, V Murg, D Porras, and J I Cirac. Quantum phases of trapped ions in an optical lattice. *New Journal of Physics*, 10(4):045017, April 2008.

[25] Amira M Eltony, Dorian Gangloff, Molu Shi, Alexei Bylinskii, Vladan Vuletic, and Isaac L Chuang. Technologies for trapped-ion quantum information systems. *arXiv:1502.05739*, 2015.

[26] J.I. Cirac and P. Zoller. A scalable quantum computer with ions in an array of microtraps. *Nature*, 404(6778):579–81, April 2000.

[27] D.A. Hite, Y. Colombe, A.C. Wilson, D.T.C. Allcock, D. Leibfried, D.J. Wineland, and D.P. Pappas. Surface science for improved ion traps. *MRS Bulletin*, 38(10):826–833, 2013.

[28] L. Deslauriers, S. Olmschenk, D. Stick, W. Hensinger, J. Sterk, and C. Monroe. Scaling and Suppression of Anomalous Heating in Ion Traps. *Physical Review Letters*, 97(10):103007, September 2006.

[29] Jaroslaw Labaziewicz, Yufei Ge, Paul Antohi, David Leibrandt, Kenneth Brown, and Isaac Chuang. Suppression of Heating Rates in Cryogenic Surface-Electrode Ion Traps. *Physical Review Letters*, 100(1):013001, January 2008.

[30] Jaroslaw Labaziewicz, Yufei Ge, David Leibrandt, Shannon Wang, Ruth Shewmon, and Isaac Chuang. Temperature Dependence of Electric Field Noise above Gold Surfaces. *Physical Review Letters*, 101(18):180602, October 2008.

[31] Andrew T Grier, Marko Cetina, Fedja Orucevic, and Vladan Vuletic. Observation of Cold Collisions between Trapped Ions and Trapped Atoms. *Physical Review Letters*, 102(22):223201, 2009.

[32] Marko Cetina, Andrew T. Grier, and Vladan Vuletić. Micromotion-Induced Limit to Atom-Ion Sympathetic Cooling in Paul Traps. *Physical Review Letters*, 109(25):253201, December 2012.

[33] Marko Cetina, Alexei Bylinskii, Leon Karpa, Dorian Gangloff, Kristin M Beck, Yufei Ge, Matthias Scholz, Andrew T Grier, Isaac Chuang, and Vladan Vuletić. One-dimensional array of ion chains coupled to an optical cavity. *New Journal of Physics*, 15(5):053001, May 2013.

[34] Marko Cetina. Hybrid Approaches to Quantum Information Using Ions, Atoms and Photons. *Ph.D. Thesis, Massachusetts Institute of Technology*, 2011.

[35] J.H. Wesenberg. Electrostatics of surface-electrode ion traps. *Physical Review A*, 78(6):063410, 2008.

[36] D. J. Berkeland, J. D. Miller, J. C. Bergquist, W. M. Itano, and D. J. Wineland. Minimization of ion micromotion in a Paul trap. *Journal of Applied Physics*, 83(10):5025, 1998.

[37] Shannon X. Wang, Guang Hao Low, Nathan S. Lachenmyer, Yufei Ge, Peter F. Herskind, and Isaac L. Chuang. Laser-induced charging of microfabricated ion traps. *Journal of Applied Physics*, 110(10):104901, 2011.

[38] D T C Allcock, J A Sherman, D N Stacey, A H Burrell, M J Curtis, G Imreh, N M Linke, D J Szwer, S C Webster, A M Steane, and D M Lucas. Implementation of a symmetric surface-electrode ion trap with field compensation using a modulated Raman effect. *New Journal of Physics*, 12(5):053026, May 2010.

[39] a. S. Bell, P. Gill, H. a. Klein, a. P. Levick, Chr Tamm, and D. Schnier. Laser cooling of trapped ytterbium ions using a four-level optical-excitation scheme. *Physical Review A*, 44(1):3–6, 1991.

[40] Marko Cetina, Andrew Grier, Jonathan Campbell, Isaac Chuang, and Vladan Vuletić. Bright source of cold ions for surface-electrode traps. *Physical Review A*, 76(041401):041401(R), 2007.

[41] Chr. Balzer, A. Braun, T. Hannemann, Chr. Paape, M. Ettler, W. Neuhauser, and Chr. Wunderlich. Electrodynamically trapped Yb^{+} ions for quantum information processing. *Physical Review A*, 73(4):041407(R), April 2006.

[42] Andrew T Grier. Interaction of Trapped Ions with Trapped Atoms. *PhD Thesis Massachusetts Institute of Technology*, 2011.

[43] Dorian Gangloff, Molu Shi, Tailin Wu, Alexei Bylinskii, Boris Braverman, Michael Gutierrez, Rosanna Nichols, Junru Li, Kai Aichholz, Marko Cetina, Leon Karpa, Branislav Jelenković, Isaac Chuang, and Vladan Vuletić. Preventing and reversing vacuum-induced optical losses in high-finesse tantalum (V) oxide mirror coatings. *Optics Express*, 23(14):18014, 2015.

[44] Wolfgang Ketterle. 8.421 Atomic and Optical Physics I, 2014.

[45] Wolfgang Ketterle. 8.422 Atomic and Optical Physics II, 2013.

[46] Vladan Vuletić, Cheng Chin, Andrew Kerman, and Steven Chu. Degenerate Raman Sideband Cooling of Trapped Cesium Atoms at Very High Atomic Densities. *Physical Review Letters*, 81(26):5768–5771, 1998.

[47] H. Perrin, A. Kuhn, I. Bouchoule, and C. Salomon. Sideband Cooling Of Neutral Atoms In A Far-Detuned Optical Lattice. *Europhysics Letters*, 42(4):395–400, 1998.

[48] S. E. Hamann, D. L. Haycock, G. Klose, P. H. Pax, I. H. Deutsch, and P. S. Jessen. Resolved-sideband Raman cooling to the ground state of an optical lattice. *Phys. Rev. Lett.*, 80(19):4149–4152, 1998.

[49] S.C. Webster. *Raman Sideband Cooling and Coherent Manipulation of Trapped Ions.* PhD thesis, Oxford, 2005.

[50] Jurgen Eschner, Giovanna Morigi, Ferdinand Schmidt-Kaler, and Rainer Blatt. Laser cooling of trapped ions. *J. Opt. Soc. Am. B*, 20(5):1003–1015, 2003.

[51] B. N. J. Persson. Sliding friction. *Surface Science Reports*, 33(3):83–119, 1999.

[52] J. Sokoloff. Static and dry friction due to multiscale surface roughness. *Physical Review E*, 78(3):036111, September 2008.

[53] B. N. J. Persson. Theory of rubber friction and contact mechanics. *Journal of Chemical Physics*, 115(8):3840–3861, 2001.

[54] B. N. Persson. Elastoplastic contact between randomly rough surfaces. *Physical review letters*, 87(11):116101, 2001.

[55] B. N. J. Persson. Contact mechanics for randomly rough surfaces. *Surface Science Reports*, 61:201–227, 2006.

[56] Michael Urbakh, Joseph Klafter, Delphine Gourdon, and Jacob Israelachvili. The nonlinear nature of friction. *Nature*, 430(6999):525–8, July 2004.

[57] Volker Bormuth, Vladimir Varga, Jonathon Howard, and Erik Schäffer. Protein friction limits diffusive and directed movements of kinesin motors on microtubules. *Science (New York, N.Y.)*, 325(5942):870–3, August 2009.

[58] Andrea Vanossi, Nicola Manini, Michael Urbakh, Stefano Zapperi, and Erio Tosatti. Colloquium: Modeling friction: From nanoscale to mesoscale. *Reviews of Modern Physics*, 85(2):529–552, April 2013.

[59] Christopher H Scholz. Earthquakes and friction laws. *Nature*, 391:37–42, 1998.

[60] L. Prandtl. A Conceptual Model to the Kinetic Theory of Solid Bodies. *Zeitschrift für Angewandte Mathematik und Mechanik*, 8(April):85, 1928.

[61] G. A. Tomlinson. A Molecular Theory of Friction. *Philosophical Magazine*, 7(June):905, 1929.

[62] Ya. I. Frenkel and T. A. Kontorova. No Title. *Zh. Eksp. Teor. Fiz.*, 8:1340, 1938.

[63] Braun and Kivshar. *The Frenkel-Kontorova Model: Concepts, Methods, and Applications*. 2004.

[64] S. Aubry. The twist map, the extended Frenkel-Kontorova model and the devil's staircase. *Physica D: Nonlinear Phenomena*, 7(1-3):240–258, 1983.

[65] Kazumasa Shinjo and Motohisa Hirano. Dynamics of friction: superlubric state. *Surface Science*, 283:473–478, March 1993.

[66] Robert W. Carpick and Miquel Salmeron. Scratching the Surface: Fundamental Investigations of Tribology with Atomic Force Microscopy. *Chemical reviews*, 97(4):1163–1194, June 1997.

[67] G. Binnig, C. F. Quate, and Ch. Gerber. Atomic Force Microscope. *Physical Review Letters*, 56(9):930–933, 1986.

[68] J Krim and A Widom. Damping of a crystal oscillator by an adsorbed monolayer and its relation to interfacial viscosity. *Physical Review B*, 38(17):184–189, 1988.

[69] Jacob N. Israelachvili. Adhesion forces between surfaces in liquids and condensable vapours. *Surface Science Reports*, 14(3):109–159, 1992.

[70] Izabela Szlufarska, Michael Chandross, and Robert W Carpick. Recent advances in single-asperity nanotribology. *Journal of Physics D: Applied Physics*, 41(12):123001, June 2008.

[71] Michael Urbakh and Ernst Meyer. Nanotribology: The renaissance of friction. *Nature materials*, 9(1):8–10, January 2010.

[72] C Mathew Mate, Gary M McClelland, Ragnar Erlandsson, and Shirley Chiang. Atomic-Scale Friction of a Tungsten Tip on a Graphite Surface. *Physical Review Letters*, 59(17):1942–1946, 1987.

[73] A. Socoliuc, R. Bennewitz, E. Gnecco, and E. Meyer. Transition from Stick-Slip to Continuous Sliding in Atomic Friction: Entering a New Regime of Ultralow Friction. *Physical Review Letters*, 92(13):134301, April 2004.

[74] Martin Dienwiebel, Gertjan Verhoeven, Namboodiri Pradeep, Joost Frenken, Jennifer Heimberg, and Henny Zandbergen. Superlubricity of Graphite. *Physical Review Letters*, 92(12):126101, March 2004.

[75] Motohisa Hirano, Kazumasa Shinjo, Reizo Kaneko, and Yoshitada Murata. Observation of Superlubricity by Scanning Tunneling Microscopy. *Physical Review Letters*, 78(8):1448–1551, 1997.

[76] Sergey Yu. Krylov and Joost W. M. Frenken. The physics of atomic-scale friction: Basic considerations and open questions. *Physica Status Solidi (B)*, 251(4):711–736, April 2014.

[77] E Gnecco, R Bennewitz, T Gyalog, C Loppacher, M Bammerlin, E Meyer, and H Guntherodt. Velocity dependence of atomic friction. *Physical Review Letters*, 84(6):1172–5, February 2000.

[78] E. Riedo, E. Gnecco, R. Bennewitz, E. Meyer, and H. Brune. Interaction Potential and Hopping Dynamics Governing Sliding Friction. *Physical Review Letters*, 91(8):084502, August 2003.

[79] Xin-z Liu, Zhijiang Ye, Yalin Dong, Philip Egberts, Robert W Carpick, and Ashlie Martini. Dynamics of Atomic Stick-Slip Friction Examined with Atomic Force Microscopy and Atomistic Simulations at Overlapping Speeds. *Physical Review Letters*, 114(14):146102, 2015.

[80] Qunyang Li, Yalin Dong, Danny Perez, Ashlie Martini, and Robert W. Carpick. Speed dependence of atomic stick-slip friction in optimally matched experiments and molecular dynamics simulations. *Physical Review Letters*, 106(12):126101, 2011.

[81] Xueying Zhao, Simon Phillpot, W. Sawyer, Susan Sinnott, and Scott Perry. Transition from Thermal to Athermal Friction under Cryogenic Conditions. *Physical Review Letters*, 102(18):186102, May 2009.

[82] Lars Jansen, Hendrik Hölscher, Harald Fuchs, and André Schirmeisen. Temperature Dependence of Atomic-Scale Stick-Slip Friction. *Physical Review Letters*, 104(25):256101, June 2010.

[83] I. Barel, M. Urbakh, L. Jansen, and a. Schirmeisen. Unexpected temperature and velocity dependencies of atomic-scale stick-slip friction. *Physical Review B*, 84(11):115417, September 2011.

[84] Yi Sang, Martin Dubé, and Martin Grant. Thermal Effects on Atomic Friction. *Physical Review Letters*, 87(17):174301, October 2001.

[85] S. Krylov, K. Jinesh, H. Valk, M. Dienwiebel, and J. Frenken. Thermally induced suppression of friction at the atomic scale. *Physical Review E*, 71(6):065101, June 2005.

[86] K. Jinesh, S. Krylov, H. Valk, M. Dienwiebel, and J. Frenken. Thermolubricity in atomic-scale friction. *Physical Review B*, 78(15):155440, October 2008.

[87] Martin H. Müser. Velocity dependence of kinetic friction in the Prandtl-Tomlinson model. *Physical Review B*, 84(12):125419, September 2011.

[88] Yalin Dong, Ajay Vadakkepatt, and Ashlie Martini. Analytical Models for Atomic Friction. *Tribology Letters*, 44(3):367–386, September 2011.

[89] Thomas Bohlein, Jules Mikhael, and Clemens Bechinger. Observation of kinks and antikinks in colloidal monolayers driven across ordered surfaces. *Nature materials*, 11(2):126–30, February 2012.

[90] Davide Mandelli, Andrea Vanossi, Michele Invernizzi, S. V. Paronuzzi Ticco, Nicola Manini, and Erio Tosatti. Superlubric-Pinned Transition in Sliding Incommensurate Colloidal Monolayers. *arXiv:1508.00147v1*, pages 1–9, 2015.

[91] I. García-Mata, O. V. Zhirov, and D. L. Shepelyansky. Frenkel-Kontorova model with cold trapped ions. *The European Physical Journal D*, 41(2):325–330, September 2006.

[92] A Benassi, A Vanossi, and E Tosatti. Nanofriction in cold ion traps. *Nature Communications*, 2:236, January 2011.

[93] Thaned Pruttivarasin, Michael Ramm, Ishan Talukdar, Axel Kreuter, and Hartmut Häffner. Trapped ions in optical lattices for probing oscillator chain models. *New Journal of Physics*, 13(7):075012, July 2011.

[94] D Mandelli, A Vanossi, and E Tosatti. Stick-slip nanofriction in trapped cold ion chains. *Physical Review B*, 87(19):195418, 2013.

[95] Michael Weiss and Franz-Josef Elmer. Dry friction in the Frenkel-Kontorova-Tomlinson model: Static properties. *Physical Review B*, 53(11):7539–7549, 1996.

[96] Michael Weiss and Franz-Josef Elmer. Dry Friction in the Frenkel-Kontorova-Tomlinson Model: Dynamical Properties. *Zeitschrift für Physik B Condensed Matter*, 69:55–69, 1997.

[97] Charles Kittel. *Introduction to Solid State Physics*. Wiley, 7th edition, 1996.

[98] S.R. Sharma, B. Bergersen, and Joos B. Aubry transition in a finite modulated chain. *Physical Review B*, 29(1):6335–6340, 1984.

[99] Y. Braiman, J. Baumgarten, Joshua Jortner, and J Klafter. Symmetry-Breaking Transition in Finite Frenkel-Kontorova Chains. *Physical Review Letters*, 65(19):2398–2401, 1990.

[100] Todd P Meyrath, Daniel F V James, and Physics Los Alurnos National. Theoretical and numerical studies of the positions of cold trapped ions. *Physics Letters A*, 240(March):37–42, 1998.

[101] D F V James. Quantum dynamics of cold trapped ions with application to quantum computation. *Applied Physics B*, 66:181–190, 1998.

[102] Masanori Igarashi, Akiko Natori, and Jun Nakamura. Size effects in friction of multiatomic sliding contacts. *Physical Review B*, 78:165427, 2008.

[103] E. C. Zeeman. Catastrophe Theory. *Scientific American*, 234(4):65–83, April 1976.

[104] Motohisa Hirano and Kazumasa Shinjo. Atomistic locking. *Physical Review B*, 41(17):11837, 1990.

[105] S Aubry. Exact models with a complete devil's staircase. *Journal of Physics C: Solid State Physics*, 16:2497, 1983.

[106] S. Aubry and P.Y. Le Daeron. The discrete Frenkel-Kontorova model and its extensions. *Physica D: Nonlinear Phenomena*, 8:381–422, 1983.

[107] M Peyrard and S Aubry. Critical behaviour at the transition by breaking of analyticity in the discrete Frenkel-Kontorova model. *Journal of Physics C: Solid State Physics*, 16(9):1593–1608, 2000.

[108] Ze Liu, Jiarui Yang, Francois Grey, Jefferson Zhe Liu, Yilun Liu, Yibing Wang, Yanlian Yang, Yao Cheng, and Quanshui Zheng. Observation of Microscale Superlubricity in Graphite. *Physical Review Letters*, 108(20):205503, 2012.

[109] Rufan Zhang, Zhiyuan Ning, Yingying Zhang, Quanshui Zheng, Qing Chen, Huanhuan Xie, Qiang Zhang, Weizhong Qian, and Fei Wei. Superlubricity in centimetres-long double-walled carbon nanotubes under ambient conditions. *Nature Nanotechnology*, 8:912–6, 2013.

[110] Ali Erdemir and Anirudha V Sumant. Macroscale superlubricity enabled by graphene nanoscroll formation. *Science*, 348(6239):1118–1122, 2015.

[111] Alexei Bylinskii, Dorian Gangloff, Ian Counts, and Vladan Vuletic. Observation of Aubry transition in finite atom chains via friction. *manuscript in preparation*, 2015.

[112] Dorian Gangloff, Alexei Bylinskii, Ian Counts, Wonho Jhe, and Vladan Vuletić. Velocity tuning of friction with two trapped atoms. *Nature Physics*, doi:10.103, 2015.

[113] S. N. Coppersmith and D.S. Fisher. Pinning transition of the discrete sine-Gordon equation. *Physical Review B*, 28(5):2566, 1983.

[114] Sergey Medyanik, Wing Liu, In-Ha Sung, and Robert Carpick. Predictions and Observations of Multiple Slip Modes in Atomic-Scale Friction. *Physical Review Letters*, 97(13):136106, September 2006.

[115] Raphael Roth, Thilo Glatzel, Pascal Steiner, Enrico Gnecco, Alexis Baratoff, and Ernst Meyer. Multiple slips in atomic-scale friction: An indicator for the lateral contact damping. *Tribology Letters*, 39(1):63–69, 2010.

[116] Jun Nakamura, Shinya Wakunami, and Akiko Natori. Double-slip mechanism in atomic-scale friction: Tomlinson model at finite temperatures. *Physical Review B*, 72(23):235415, 2005.

[117] Mykhaylo Evstigneev and Peter Reimann. Stick-slip statistics in atomic friction. *Physical Review B*, 87(20):205441, May 2013.

[118] Rosario Capozza, Shmuel M. Rubinstein, Itay Barel, Michael Urbakh, and Jay Fineberg. Stabilizing Stick-Slip Friction. *Physical Review Letters*, 107(2):024301, July 2011.

[119] Anisoara Socoliuc, Enrico Gnecco, Sabine Maier, Oliver Pfeiffer, Alexis Baratoff, Roland Bennewitz, and Ernst Meyer. Atomic-scale control of friction by actuation of nanometer-sized contacts. *Science*, 313(5784):207–10, July 2006.

[120] O. V. Zhirov and D. L. Shepelyansky. Quantum synchronization. *The European Physical Journal D*, 38(2):375–379, January 2006.

[121] Dirk Kadau, Alfred Hucht, and Dietrich E. Wolf. Magnetic friction in Ising spin systems. *Physical Review Letters*, 101(13):137205, 2008.

[122] C. Fusco, D. E. Wolf, and U. Nowak. Magnetic friction of a nanometer-sized tip scanning a magnetic surface: Dynamics of a classical spin system with direct exchange and dipolar interactions between the spins. *Physical Review B*, 77(17):174426, 2008.

[123] Bambi Hu, Baowen Li, and Wei-Min Zhang. Quantum Frenkel-Kontorova model: A squeezed state approach. *Physical Review E*, 58(4):R4068–R4071, October 1998.

[124] O. Zhirov, G. Casati, and D. Shepelyansky. Quantum phase transition in the Frenkel-Kontorova chain: From pinned instanton glass to sliding phonon gas. *Physical Review E*, 67(5):056209, May 2003.

[125] Giuseppe Grosso and Giuseppe Pastori Parravicini. *Solid State Physics*. Academic Press, 2000.

[126] N. Daniilidis, S. Narayanan, S. A. Möller, R. Clark, T. E. Lee, P. J. Leek, A. Wallraff, St. Schulz, F. Schmidt-Kaler, and H. Häffner. Fabrication and heating rate study of microscopic surface electrode ion traps. *New Journal of Physics*, 13(1):013032, 2011.

[127] T. Savard, K. O'Hara, and J. Thomas. Laser-noise-induced heating in far-off resonance optical traps. *Physical Review A*, 56(2):R1095–R1098, August 1997.

[128] D. A. Hite, Y. Colombe, A. C. Wilson, K. R. Brown, U. Warring, R. Jördens, J. D. Jost, K. S. McKay, D. P. Pappas, D. Leibfried, and D. J. Wineland. 100-Fold Reduction of Electric-Field Noise in an Ion Trap Cleaned with In Situ Argon-Ion-Beam Bombardment. *Physical Review Letters*, 109(10):103001, September 2012.

[129] D. A. Hite, Y. Colombe, A. C. Wilson, K. R. Brown, U. Warring, R. Jördens, J. D. Jost, K. S. McKay, D. P. Pappas, D. Leibfried, and D. J. Wineland. 100-Fold Reduction of Electric-Field Noise in an Ion Trap Cleaned with In Situ Argon-Ion-Beam Bombardment. *Physical Review Letters*, 109(10):103001, September 2012.

[130] S. Seidelin, J. Chiaverini, R. Reichle, J. J. Bollinger, D. Leibfried, J. Britton, J. H. Wesenberg, R. B. Blakestad, R. J. Epstein, D. B. Hume, J. D. Jost, C. Langer, R. Ozeri, N. Shiga, and D. J. Wineland. A microfabricated surface-electrode ion trap for scalable quantum information processing. *Phys. Rev. Lett.*, 96:253003, January 2006.

[131] A. Safavi-Naini, P. Rabl, P. F. Weck, and H. R. Sadeghpour. Microscopic model of electric-field-noise heating in ion traps. *Physical Review A*, 84(2):023412, August 2011.

[132] Markus Greiner. *Ultracold quantum gases in three-dimensional optical lattice potentials.* PhD thesis, Ludwig-Maximilians-Universitat Munchen, 2003.

[133] Hirokazu Miyake, Georgios A. Siviloglou, Colin J. Kennedy, William Cody Burton, and Wolfgang Ketterle. Realizing the Harper Hamiltonian with Laser-Assisted Tunneling in Optical Lattices. *Physical Review Letters*, 111(18):185302, October 2013.

[134] Colin J. Kennedy, Georgios A. Siviloglou, Hirokazu Miyake, William Cody Burton, and Wolfgang Ketterle. Spin-Orbit Coupling and Quantum Spin Hall Effect for Neutral Atoms without Spin Flips. *Physical Review Letters*, 111(22):225301, November 2013.